

Diss. ETH No. 17840

# **3-D Seismic Velocity Models of the Alpine Crust from Local Earthquake Tomography**

A dissertation submitted to

**ETH ZÜRICH**

for the degree of

**DOCTOR OF SCIENCES**

presented by

**TOBIAS DIEHL**

Diplom-Physiker,

University of Karlsruhe (Germany)

born June 28, 1976

citizen of Germany

accepted on the recommendation of

Prof. Dr. Eduard Kissling, examiner

Dr. Stephan Husen, co-examiner

Dr. Nicholas Deichmann, co-examiner

Dr. Felix Waldhauser, co-examiner

Prof. Dr. Domenico Giardini, co-examiner

Zürich, 2008



# Contents

<b>Zusammenfassung</b>	<b>1</b>
<b>Abstract</b>	<b>3</b>
<b>1 Introduction</b>	<b>5</b>
<b>2 Compilation of Data Set for the Alpine Region</b>	<b>13</b>
2.1 Introduction . . . . .	14
2.2 Networks in Greater Alpine Region . . . . .	14
2.3 Compilation of Combined Waveform Data Set . . . . .	16
2.3.1 Bulletin Data . . . . .	16
2.3.2 Waveform Data . . . . .	17
2.3.3 Station Data . . . . .	18
2.3.4 Iterative Merging Procedure . . . . .	19
2.4 Merged Phase Data: The ISC-Compilation . . . . .	23
<b>3 Consistent Phase Picking for Regional Tomography Models (Paper I - Accepted for Publication in <i>Geophys. J. Int.</i>)</b>	<b>25</b>
3.1 Introduction . . . . .	26
3.2 Routine Hand Phase Picking . . . . .	29
3.2.1 Phase Timing and the Assessment of its Uncertainty . . . . .	29
3.2.2 Phase Identification and the Assessment of its Uncertainty . . . . .	31
3.2.3 Sources of Inconsistencies in Routine Picks . . . . .	33
3.3 Automated Re-picking of P-Phase Data . . . . .	33
3.3.1 Local Earthquake Data Set of the Alpine Region . . . . .	33
3.3.2 The MPX Picking System . . . . .	35
3.3.3 Calibration of the Automatic Weighting Procedure . . . . .	36
3.3.4 Predicted Arrivals for Production Mode . . . . .	40
3.3.5 Results of MPX Production Mode . . . . .	41
3.4 Local Source Tomography with Highly Consistent Data Set . . . . .	43
3.4.1 Consistent Minimum 1-D Model for the Alpine Region . . . . .	44
3.4.2 Preliminary 3-D Results and Comparison with ISC Data . . . . .	46
3.4.3 Consistency of Re-Picked Data Set . . . . .	48
3.5 Discussion and Conclusion . . . . .	49

<b>4</b>	<b>High-Resolution 3-D P-Wave Model of the Alpine Crust (Manuscript to be Submitted to <i>Geophys. J. Int.</i>)</b>	<b>53</b>
4.1	Introduction . . . . .	54
4.2	Local Earthquake Data from Automated Phase Picking . . . . .	56
4.3	Method . . . . .	58
4.4	Solution Quality . . . . .	59
4.5	3-D Tomographic Model of the Alpine Crust . . . . .	68
4.6	Discussion . . . . .	70
4.7	Concluding Remarks . . . . .	75
<b>5</b>	<b>Automatic S-Wave Picker for LET (Paper II - Submitted to <i>Bull. Seism. Soc. Am.</i>)</b>	<b>77</b>
5.1	Introduction . . . . .	78
5.2	Combined Picking Approach . . . . .	79
5.2.1	STA/LTA Detector . . . . .	80
5.2.2	Polarization Detector . . . . .	82
5.2.3	Autoregressive Picker . . . . .	85
5.2.4	Quality Assessment in Combined Approach . . . . .	87
5.3	Case Study: Application to the Alpine Region . . . . .	90
5.3.1	Reference Data Set . . . . .	90
5.3.2	Calibration and Test-Mode . . . . .	91
5.3.3	Production-Mode . . . . .	96
5.4	Discussion and Conclusion . . . . .	96
<b>6</b>	<b>Discussion and Conclusion</b>	<b>99</b>
6.1	3-D Lithological Model of the Alpine Crust . . . . .	100
6.2	Crustal P-Wave Model from Automated Phase Picking . . . . .	102
6.3	Towards a 3-D S-Wave Model of the Alpine Crust . . . . .	107
6.4	Conclusion . . . . .	110
	<b>Appendix</b>	<b>113</b>
<b>A</b>	<b>Supplementary Material for Chapter 3</b>	<b>113</b>
A.1	Sets of Fisher Coefficients for Greater Alpine Region . . . . .	113
<b>B</b>	<b>Supplementary Material for Chapter 5</b>	<b>115</b>
B.1	Character of S-Waves at Local Distances . . . . .	115
B.2	Combined Picking Approach (Supplementary Material) . . . . .	117
B.2.1	STA/LTA Detector . . . . .	117
B.2.2	Polarization Detector . . . . .	120
B.2.3	Autoregressive Picker . . . . .	124
B.2.4	Quality Assessment in Combined Approach . . . . .	129
B.3	Application to Alpine Region (Supplementary Material) . . . . .	131
B.3.1	Average Picking Uncertainty . . . . .	131
B.3.2	Picking Performance for Tomography . . . . .	132



B.3.3	Parameter Search Procedure . . . . .	133
B.4	Outlier Detection (Supplementary Material) . . . . .	134
B.4.1	Outlier-Detection in Test-Mode . . . . .	134
B.4.2	Outlier-Detection in Production-Mode . . . . .	136
<b>C</b>	<b>Users Guide for Consistent Phase Picking</b>	<b>137</b>
C.1	Introduction . . . . .	138
C.2	Routine Hand Picking . . . . .	138
C.2.1	Phase Timing and its Error Assessment . . . . .	139
C.2.2	Phase Identification and its Error Assessment . . . . .	141
C.2.3	First Motion Polarity and its Error Assessment . . . . .	143
C.2.4	Size of Time Window and Amplitude Scaling . . . . .	145
C.2.5	Aliasing and Waveform Filtering . . . . .	146
C.2.6	Additional Comments for S-Wave Picking . . . . .	147
C.3	Consistent Hand Picking Procedure . . . . .	151
C.3.1	Consistent Waveform Filtering . . . . .	151
C.3.2	Consistent Window Size and Amplitude Scaling . . . . .	151
C.3.3	Consistent Phase Identification . . . . .	154
<b>D</b>	<b>Users Guide for MPX Picking System</b>	<b>155</b>
D.1	Introduction . . . . .	156
D.2	Basic Concept of MPX . . . . .	156
D.3	Compilation of Reference Data Set . . . . .	157
D.4	Calibration Procedure . . . . .	158
D.4.1	Adjustment of Search Windows . . . . .	159
D.4.2	Calibration of the Automated Quality Assessment . . . . .	163
D.4.3	Assessment of Calibration Scheme . . . . .	166
D.5	Examples of Production Modes . . . . .	167
D.5.1	Application to the Alpine Region . . . . .	168
D.6	Cookbook Example: MDA via SPSS Software . . . . .	169
<b>E</b>	<b>Miscellaneous</b>	<b>173</b>
E.1	Parameterization and Resolution in 3-D Tomography . . . . .	173
	<b>References</b>	<b>177</b>
	<b>Acknowledgments</b>	<b>187</b>
	<b>Curriculum Vitae</b>	<b>189</b>



# Zusammenfassung

In den vergangen zwei Jahrzehnten wurden erheblich Fortschritte im Verständnis von Lithosphärenstruktur und tektonischer Entwicklung des Alpenbogens erzielt. Mit Hilfe von großangelegten geophysikalisch-geologischen Alpen-Traversen und der Verwendung von hochauflösender teleseismischer Laufzeittomographie wurden wesentliche strukturelle Unterschiede der Kruste und des oberen Mantels zwischen West-, Zentral- und Ostalpen aufgedeckt. Informationen über die Lithologie der gesamten alpinen Lithosphäre sind notwendig um diese ‘nicht-zyklindrische’ 3-D Struktur des Alpenbogens in einem regionalen tektonischen Kontext zu erklären. Unabhängige P- und S-Wellen Geschwindigkeitsmodelle liefern eindeutige Aussagen über die Zusammensetzung und den physikalischen Zustand der Lithosphäre (z.B. Fluidgehalt, Temperatur), da sie, unter anderem, mit petrologischen Labor-messungen verglichen werden können.

Solche regionalen 3-D P- und S-Wellen Modelle können mit Hilfe von Lokalbeben-Tomographie erstellt werden, wobei Resolution und Verlässlichkeit der tomographischen Modelle stark von der Qualität der verwendeten Laufzeitdaten abhängt. Eine gleichmässige Resolution der gesamten alpinen Kruste ist nur durch eine Verküpfung von mehr als 10 seismischen Netzwerken im Alpenraum möglich. Routinemässig bestimmte Einsatzzeiten (Picks) von einzelnen seismologischen Diensten sind oft inkonsistent und in kombinierten Datensätzen fehlt eine gemeinsame quantitative Fehlerangabe meist völlig. Einsatzzeiten von P- und S-Wellen müssen daher erneut bestimmt werden (re-picking), um geeignete Laufzeitdaten für hochauflösende Tomographien zu erhalten. In Anbetracht der Datenmengen, welche für regionale Modelle notwendig sind, stellen automatische Algorithmen zur Einsatzbestimmung (Auto-Picker) die zukünftigen Werkzeuge dar.

In der vorliegenden Arbeit wurden Lokalbebenendaten von 14 seismischen Netzwerken im Alpenraum zusammengetragen. Der endgültige Datensatz enthält Wellenformen und zugehörige Hypozentral-Parameter von mehr als 1500 Ereignissen im Zeitraum von 1996 bis 2007. Darüberhinaus wurden Methoden zur konsistenten manuellen Bestimmung von P- und S-Einsätzen entwickelt. Diese Verfahren wurden verwendet um Referenz-Datensätze von P- und S-Phasen zu erstellen, welche später zur Kalibrierung und zum Test von automatischen Picker-Algorithmen eingesetzt wurden.

Die MPX Software wurde zur automatischen Bestimmung von P-Einsätzen benutzt. Der endgültige Datensatz besteht aus mehr als 13000 konsistent bestimmten P-Wellen Ersteinsätzen, wobei der mittlere Pick-Fehler bei ca. 0.12 s liegt.

Anschliessend wurden diese Laufzeiten für die Lokalbeben-Tomographie verwendet. Das resultierende 3-D P-Wellen Modell bildet den Großteil des Alpen Orogens zwischen 0 und 60 km Tiefe ab. Geschwindigkeitsanomalien erster Ordnung, wie beispielsweise die Krusten-Mantel Grenze (Moho) oder der Ivrea Körper, sind gut aufgelöst und stimmen mit Ergebnissen früherer Untersuchungen überein. Darüberhinaus sind verschiedene (konsistente) kleinskalige Anomalien sichtbar. Eine Fortsetzung der Europäischen Unterkruste unterhalb der Adriatischen Moho in den Zentralalpen ist in dem tomographischen Modell nicht erkennbar. Das Fehlen einer solchen Signatur könnte auf eine Eklogitisierung der subduzierten Europäischen Unterkruste in den Zentralalpen hinweisen.

Die Qualität unseres Modells in Bezug auf Resolution und Verlässlichkeit wird deutlich durch den Vergleich mit einem Tomographie Modell basierend auf routinemäßig bestimmten Einsatzzeiten, welche dem ISC-Katalog entnommen wurden. Das Auflösungsvermögen der ISC-Daten ist deutlich schlechter im unteren Teil des Modells, obwohl es etwa sieben mal mehr P-Laufzeiten umfasst als der qualitativ hochwertige überarbeitete Datensatz. Diese verschlechterte Auflösung wird höchstwahrscheinlich von falsch identifizierten regionalen Pn Phasen verursacht, welche hauptsächlich in routinemäßig bestimmten Einsatzzeiten vorhanden sind.

Die automatische Bestimmung von S-Wellen Einsätzen stellt den nächste Schritt auf dem Weg zu einem lithologischen 3-D Modell der alpinen Kruste dar. Allerdings verlangt die verlässliche Bestimmung von Zweiteinsätzen die Verwendung von komplexen Methoden zur Phasenidentifizierung und Einkomponenten-Ansätze sind deshalb nicht geeignet um S-Phasen zu picken. In dieser Arbeit wurde daher ein Algorithmus entwickelt, der drei verbreitete Detektions- und Picking-Methoden zu einem stabilen S-Wellen Picker kombiniert. Dabei werden Informationen der verschiedenen Methoden zu einer 'in-situ' Abschätzung der Unsicherheiten (Einsatzzeit, Phasenidentifizierung) zusammengefasst. Der kalibrierte S-Picker wurde auf ausgewählte Dreikomponenten-Registrierungen angewendet und der endgültige Datensatz umfasst etwa 2600 S-Wellen Ersteinsätze. Der mittlere Pick-Fehler liegt bei ca. 0.27 s. Aufgrund der geringeren Anzahl von Dreikomponenten-Registrierungen und der wenigen, qualitativ hochwertigen Sn Phasen ist dieser Datensatz momentan noch nicht ausreichend für ein regionales 3-D S-Wellen Modell der alpinen Kruste. Allerdings könnte er in Gebieten mit ausreichender Datenabdeckung, wie z.B. in Süddeutschland oder der Schweiz, für lokale S-Wellen bzw.  $V_P/V_S$  Studien verwendet werden. Eine wesentlich Verbesserung der S-Wellen Datenabdeckung im Alpenraum setzt eine vergrößerte Anzahl von Dreikomponenten-Registrierungen voraus. Zudem ist eine Weiterentwicklung von Methoden zur Identifizierung von regionalen Sn Phasen notwendig, wofür der in dieser Arbeit entwickelte S-Wellen Picker eine ausgezeichnete Grundlage bildet.

# Abstract

Important progress has been made over the last two decades to unravel the lithospheric structure and tectonic evolution of the Alpine arc. Large-scale geophysical-geological transects and high-resolution teleseismic tomography have revealed substantial differences between Western, Central, and Eastern Alps in terms of crustal and upper mantle structure. To integrate the ‘non-cylindric’ 3-D structure of the orogen into a regional tectonic context, detailed information on the lithology of the entire Alpine lithosphere is required. Independent models of P- and S-wave velocities can provide unique information on composition and physical state of the lithosphere (e.g. fluid content, temperature), since they allow the comparison with petrological measurements.

Local earthquake tomography can be used to derive such regional 3-D P- and S-wave velocity models. The resolution and reliability of such tomographic images strongly depend on the quality of the available arrival-time data. A uniform resolution of the entire Alpine crust requires compilation and merging of local earthquake data of more than ten national and regional networks in Austria, France, Germany, Italy, Slovenia, and Switzerland. Since routine picks provided by single networks usually include a high degree of inconsistencies, and a common quantitative error assessment is not available for merged phase data, re-picking of P- and S-phases has to be performed to obtain arrival-time data appropriate for high-resolution seismic tomography. Considering the amount of data necessary for regional models, new algorithms combining accurate picking with an automatic quality assessment represent the future of tools required to derive large suitable data sets.

In this work, local earthquake data were compiled from 14 seismic networks in the greater Alpine region. The final data base includes digital waveform data and information on associated hypocenters (bulletin data) of more than 1500 events for the period of 1996 to 2007. Procedures for consistent routine hand picking were developed and applied to derive reference data sets of accurate P- and S-phase picks, which were later used for calibration and testing of automatic picking algorithms.

The MPX software was used for automated re-picking of P-waves. The final data set consists of more than 13’000 consistently picked first arriving P-phases with an average picking error of about 0.12 s. Subsequently, the high-quality phase data was used for local earthquake tomography. The resulting 3-D P-wave model images major parts of the Alpine orogen between 0 and 60 km depth. First order anomalies like crust-mantle boundary (Moho) and the Ivrea body in the Western

Alps are well resolved and in good agreement with previous studies. In addition, several (consistent) small-scale anomalies are visible in the tomographic image. A clear continuation of the lower European crust beneath the Adriatic Moho in the Central Alps is not observed. The absence of such a signature may indicate eclogitization of the subducted European lower crust in the Central Alps.

The comparison with a tomography model derived from routine picks of the ISC data base clearly demonstrates the achievements of the automated re-picking approach. Though the model based on ISC data comprises almost seven times more P-phases than the re-picked data set, the resolution in the lower parts of the model is significantly blurred. This lack of resolution is most probably related with the larger number of misidentified regional Pn phases present in routine data.

The automatic re-picking of S-waves represents the next step towards a 3-D lithological model of the Alpine crust. Reliable picking of later arrival phases requires sophisticated phase identification procedures and single-component approaches are therefore not appropriate for S-phase picking. The algorithm developed in this work combines three commonly used phase detection and picking methods to a robust S-wave picking tool. Information from the different techniques provides an ‘in-situ’ estimate of timing uncertainty and phase identification of the automatic pick. The calibrated S-wave picker was applied to a subset of three-component recordings and the final data set consists of about 2600 first arriving S-phase picks. The average picking error is about 0.27 s. Due to the fewer amount of three-component recordings and the low number of high-quality Sn phases, this data set is not yet sufficient for a regional 3-D S-wave model of the Alpine crust. In areas of increased data coverage like southern Germany and Switzerland, it might be used for local S-wave or  $V_P/V_S$  studies. A further improvement of the S-wave data coverage in the Alpine region will require more three-component data. In addition, enhancement in picking of regional Sn phases is necessary and the S-picking approach developed in this work represents an excellent base for this purpose.

# Chapter 1

## Introduction

## The Structure of the Alpine Lithosphere - State of the Art

Important progress has been made over the last two decades to unravel the lithospheric structure and tectonic evolution of the Alpine arc. Several large-scale geophysical-geological transects - the European Geotraverse (EGT) (*Blundell et al.*, 1992), the Swiss National Research Project 20 (NRP-20) (*Pfiffner et al.*, 1997), the French-Italian Etude Continentale et Oceanique par Reflexion et Refraction Sismique - Progetto Strategico Crosta Profonda (ECORS-CROP) (*Roure et al.*, 1990), and the East-Alpine Reflection Seismic Traverse (TRANSALP) (*Transalp Working Group*, 2001) - have been integrated with high-resolution teleseismic tomography images (*Lippitsch et al.*, 2003) to a detailed three-dimensional (3-D) model of the lithosphere and asthenosphere beneath the Alpine arc (*Kissling et al.*, 2006; *Schmid and Kissling*, 2000; *Schmid et al.*, 1996).

Substantial structural differences were discovered between the western, central, and eastern Alps. Beneath the western Alps, subduction of European continental lithosphere occurs in SE direction beneath the Adriatic microplate (Fig. 1.1a). The Ivrea body in the western Alps forms a backstop, against which the European lower crust is upfolded and backthrusts resulting in a duplication of European lower crust (*Schmid and Kissling*, 2000). In the central part of the Alps, SE directed subduction of European lithosphere still persists but lower Adriatic crust is wedged into lower European crust (Fig. 1.1b) as described by *Ye et al.* (1995) or *Schmid and Kissling* (2000). Thick piles of folded upper crustal material (the Alpine nappes) overly the lower crust beneath the western and central Alps (Fig. 1.1). In the eastern Alps a reversal of subduction occurs: Adriatic lithosphere subducts beneath European lithosphere in NE direction (*Lippitsch et al.*, 2003; *Kissling et al.*, 2006).

Furthermore, differences in seismicity are observed between central and western Alps as described by *Deichmann and Baer* (1990), *Sue et al.* (1999), *Deichmann et al.* (2000b) and *Schmid and Kissling* (2000). The lower crustal wedge beneath the central Alps appears aseismic (Fig. 1.1b) whereas the lower crustal wedge is seismically active beneath the western Alps (Fig. 1.1a).

The 3-D seismic velocity structure of the lower crust and the lithosphere-asthenosphere boundary in the range of the Alpine suture represents a key parameter to integrate these differences into improved tectonic models. Independent models of P- and S-wave velocities can provide unique information on composition and physical state of the lithosphere (fluid content, temperature, etc.), since they allow the comparison with petrological measurements. Existing models of the Alpine lower crust as summarized in *Schmid et al.* (2004), however, are mainly based on results from Controlled Source Seismology (CSS). In terms of seismic velocities, these models are poorly resolved in the depth ranges of the lower crust and large parts of the associated structure and composition is based on extrapolation. Likewise, teleseismic tomography is not appropriate to resolve crustal structure due to the sub-vertical incidence of rays.



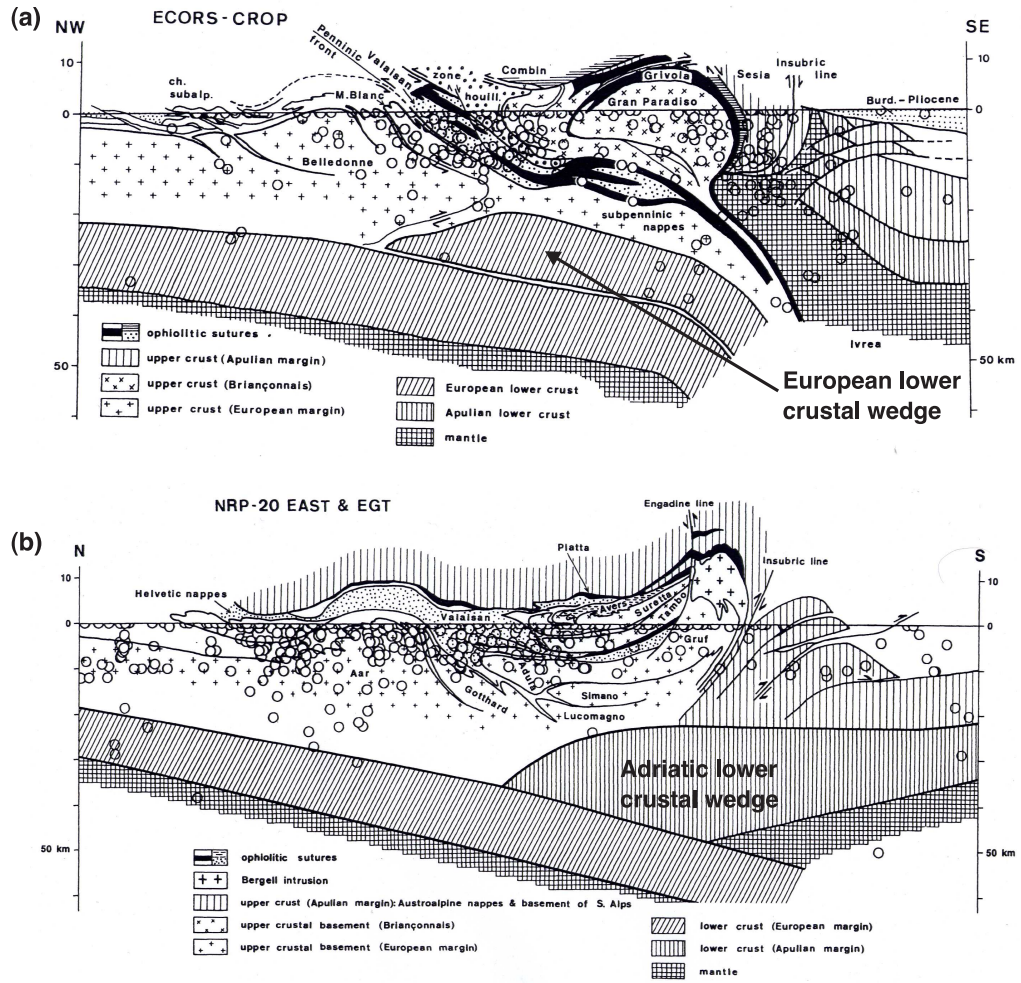


**Figure 1.1:** Schematic geophysical-geological cross section through the western and the central Alps (modified after *Schmid and Kissling, 2000*). (a) ECORS-CROP (western) transect. (b) NRP-20 East/EGT (central) transect. Superimposed circles indicate well-locatable hypocenters for the 1980-1995 time period (*Solarino et al., 1997*) from within a 30 km wide corridor, orthogonally projected onto the transects.

## Method and Data

Although local earthquake tomography can be used to derive high-resolution 3-D regional seismic models of the lithosphere, most of the existing models in the Alps suffer from the small aperture of the networks (e.g. *Solarino et al.*, 1997b; *Eva et al.*, 2001; *Paul et al.*, 2001; *Husen et al.*, 2003), low quality of travel-time data (e.g. *Solarino et al.*, 1997) or a combination of both. In case of the Alps, seismicity is dominated by shallow focal depths within the upper crust. Therefore, the lower crust is only illuminated by long distance regional (Pn) phases and the depth resolution depends mainly on the aperture of the network. Thus, to achieve an evenly dense data coverage for local source tomography encompassing the entire Alpine crust, phase data from more than 10 national and regional networks have to be compiled.

Merging routine phase data from several networks usually goes along with a variety of difficulties as described by *Solarino et al.* (1997). The identification of common events complicates the merging process and the lack of a common and consistent error assessment for phase data provided by different networks definitely limits the quality of such compilations. Figure 1.2 presents the result of the local source tomography of *Solarino et al.* (1997), which is based on merged routine phase data

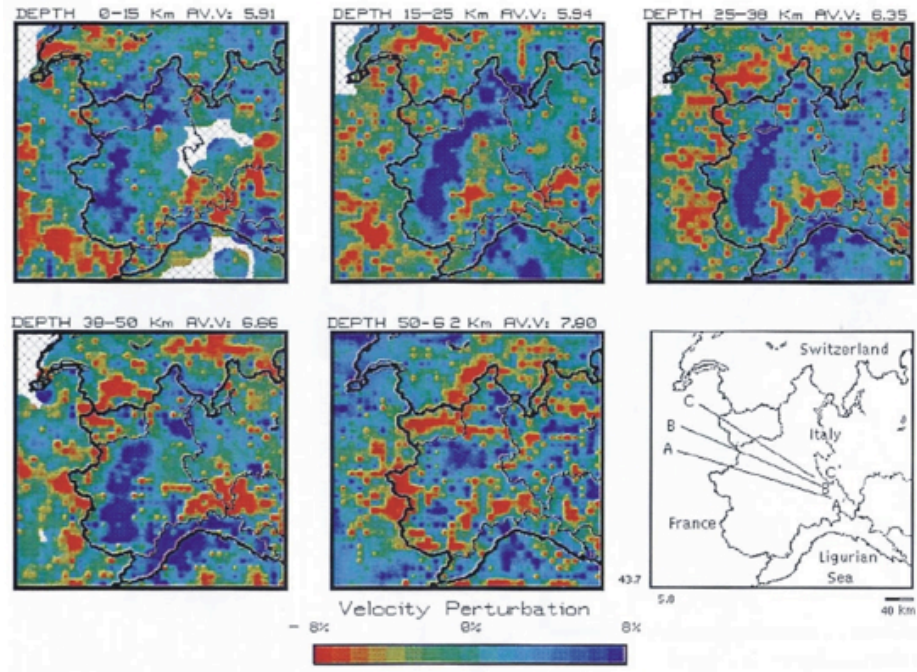


**Figure 1.2:** Tomographic image based on merged routine phase data of networks in the greater Alpine region (*Solarino et al.*, 1997). The high noise level present in the phase data significantly blurs the image and leads to a reduced resolution.

---

from permanent networks in the greater Alpine region. Besides the pronounced high-velocity anomaly in the western Alps, associated with the Ivrea geophysical body, only few coherent structures are visible in the tomographic images.

Thus, to improve the resolution and reliability of the tomographic image, large and consistent sets of phase data are required. A common and consistent quality assessment can only be achieved through re-picking of P- and S-wave arrival times from the original seismograms. Considering the amount of data necessary for regional high-resolution tomography, algorithms combining accurate picking with an automated error assessment represent the future of tools used to derive large suitable data sets. Recently, *Aldersons* (2004) developed the MPX software, which integrates the robust Baer-Kradolfer picker (*Baer and Kradolfer*, 1987) with a pattern recognition technique to estimate the uncertainty of the arrival time. It was successfully applied for re-picking first arriving P-phases from waveform data of the Italian national seismic network by *Di Stefano et al.* (2006).

Automated picking of secondary arrivals represents the next challenge in the development of accurate and reliable phase pickers. Especially the onset determination of S-waves is difficult due to the character of the later arriving shear wave. Even manual picking and phase identification is often uncertain, especially at larger epicentral distances. Single-component approaches like the Baer-Kradolfer algorithm are certainly not sufficient for reliable identification and picking of later arrival S-phases. Therefore, polarization analysis of three-component (3C) recordings have to be included to distinguish S body waves from P and surface waves.

In addition, the reliable (automatic) picking of S-arrivals requires a minimum information on the first arriving P-phase. Most picking algorithms are applied within a time window around the expected phase onset and pick the earliest well-defined signal in this window. Therefore, the width and the position of the time window affects the phase identification and, on the other hand, its choice strongly depends on the accuracy of the available travel-time curves. To avoid phase misidentification caused by wide or misplaced search windows, quality weighted P-arrival times are necessary to achieve appropriate velocity models and hypocenter locations prior to the S-picking. Furthermore, details on the first arriving P-phase is necessary for the directivity operator commonly used for S-wave detection.

A data set suitable for a re-picking approach has to include waveform data and informations on associated hypocenters (bulletin data). In addition, information on stations has to be gathered to avoid inconsistencies in terms of coordinates and station codes. As mention before, a uniform resolution of the entire Alpine crust requires the compilation and merging of local earthquake data from all available networks in Austria, France, Germany, Italy, Slovenia, and Switzerland. Due to the absence of a common standard for data exchange of digital waveforms and bulletin data, the compilation of a complete data set of the Alpine region represents a rather challenging task and requires the development of tools for automated data requests and data processing. Furthermore, procedures for merging waveform and bulletin data have to be setup.

## Agenda

Local source tomography can be used to image the seismic velocity structure of the Alpine crust. To obtain a set of high-quality P- and S-wave arrival times for the entire region, consistent re-picking of seismograms has to be performed.

The compilation of a local earthquake data set suitable for our re-picking approach is described in the second chapter. The corresponding data set comprises earthquake catalogs (bulletins), digital waveform data and station information of more than ten networks in the greater Alpine region. An iterative merging procedure was setup to combine data from several networks to one common data base. For a later comparison between our re-picked data and ‘standard’ routine phase data, additional arrival times were extracted from the data base of the International Seismological Center (ISC).

The third chapter presents procedures for consistent phase picking and their application to the Alpine region. Common problems in routine hand-picking at local to regional epicentral distances are summarized and a procedure for consistent manual P-phase picking is proposed. The MPX software of *Aldersons* (2004) is used for re-picking first arriving P-phases from the Alpine local earthquake data. The proposed hand-picking procedure is used to derive a reference data set consisting of a limited number of consistently picked P-phase arrival times. The reference data set is used to calibrate and test the performance of MPX. Furthermore, an iterative application of automatic pickers and minimum 1-D travel-time inversions (*Kissling*, 1988) is necessary to obtain appropriate travel-time curves for MPX. Subsequently, the calibrated MPX is applied to the complete Alpine local earthquake data set in the ‘production-mode’. The final P-phase data set consists of more than 13’000 high-quality first arrivals from 552 well-locatable earthquakes in the Alpine region. This data set is used to calculate a minimum 1-D model for the greater Alpine region, including a 1-D velocity model, station corrections and corresponding hypocentral solutions.

The P-phase data set and the regional 1-D model achieved in this chapter represent the basis for a 3-D P-wave model of the Alpine crust and serves as initial information for the automated re-picking of S-wave arrivals. Chapter 3 was accepted for publication by the *Geophysical Journal International* (GJI).

The high-quality P-phase data set derived from automated re-picking with the MPX software is used for 3-D local earthquake tomography as presented in the fourth chapter. A model parameterization of 25 x 25 km (horizontal) x 15 km (vertical) in combination with a average picking error of about 0.12 s allows the resolution of velocity perturbations of at least 5% in the lower crust. But also Moho topography and small scale structure in the upper crust is resolved in this model. The solution quality is assessed in detail by several sensitivity and resolution tests using checkerboard models and synthetic crustal models.

The general Moho topography in our tomographic model agrees very well with

---

the results derived from CSS (*Waldhauser et al.*, 1998) and recent receiver function studies (*Lombardi et al.*, 2008). Furthermore, first order anomalies such as the Ivrea body in the western Alps, as well as the crustal roots of the Alps and the northern Apennines are clearly resolved in our model. In addition, we found some indications for eclogitization of the lower European crust in the Central Alps. Chapter 4 will be submitted as a manuscript to the *Geophysical Journal International* (GJI).

Confirmed by the success of quality weighted re-picking of first arriving P-phases, we setup a concept for an automated S-wave picker, which is suitable for local earthquake tomography. In our approach, as described in the fifth chapter, we combine two S-wave detectors with an autoregressive picking algorithm. The detectors are based on a combined short-term to long-term average ratio (STA/LTA) of horizontal components and on a polarization detector exploiting the particle motion of a 3C recording. Information from the different techniques provides an ‘in-situ’ estimate of timing uncertainty and phase identification of the automatic pick.

Similar to the procedure described for P-phases in chapter 3, we use a set of hand picked S-arrivals to calibrate and test the automatic picker. P-wave velocities and station corrections of the minimum 1-D model of chapter 3 are converted in S-wave velocities using a constant  $v_P/v_S$  ratio. Hypocenter locations of the minimum 1-D model of chapter 3 are then used to calculate rather accurate travel-time curves to estimate the onsets of first arriving S-waves. P-phase picks derived in chapter 3 were used to setup appropriate S-wave search windows and to calculate back-azimuth and incidence angle of the incoming P-wave, required for wavefield decomposition and directivity analysis. Chapter 5 was submitted as a manuscript to the *Bulletin of the Seismological Society of America* (BSSA) and supplementary material is provided in Appendix B.

The results are summarized and discussed in the sixth chapter. Tomography results based on re-picked data are compared with results based on phase data extracted from the ISC data base. Furthermore, we discuss the potential 3-D resolution of the S-phase data set obtained from chapter 5.

The ‘*Users Guide for Consistent Phase Picking*’ in Appendix C complements chapter 3. It summarizes in more detail problems in routine phase picking of P- and S-phases and illustrates them with a series of examples. In addition, procedures for consistent phase picking are proposed. Although this users guide is mainly focused at local to regional distances, most of its principles apply likewise also to teleseismic observations.

The ‘*Users Guide for MPX Picking System*’ in Appendix D represents another complement to chapter 3. It basically describes the fundamental concept of MPX and the necessary calibration procedure. Particularly, the pattern recognition

approach and the corresponding Multiple Discriminant Analysis (MDA) are explained in further detail.

Appendix E.1 includes some theoretical considerations concerning the parameterization and resolution in 3-D tomography. Examples for P, S, and  $v_P/v_S$  illustrate the dependencies of the minimum resolvable perturbation from model parameterization, background velocity, and data error.

## Chapter 2

# Compilation of a Local Earthquake Data Set for the Alpine Region

## 2.1 Introduction

As already mentioned in the general introduction of chapter 1 the seismicity in the Alps is dominated by shallow focal depths within the upper crust. To illuminate the lower crust, we have to rely on long distance regional phases (mainly Pn) and the resolution in depth strongly depends on the aperture of the used network. To achieve an uniform ray-coverage suitable for local source tomography of the entire Alpine crust, local earthquake data (including bulletin, waveform, and station data) of more than 10 national and regional networks have to be compiled. Merging such a heterogeneous data set goes along with a variety of difficulties. Especially the identification of common events in bulletins of different networks can become ambiguous, since a majority of events in the Alpine region is located in the boarder region between networks (see *Solarino et al.*, 1997). Hypocenters of events at the edge or even outside of a network usually denote a large uncertainty. Moreover, differences in the network geometry can bias the location significantly. Since we focus on re-picking of arrival times, only waveform and event data are merged. Routine phase data provided by the single networks is not considered in the merging process.

In this chapter we give an overview of the available permanent networks in the greater Alpine region used in this study. Furthermore, common problems present in waveform data like timing errors and data formats are summarized. Subsequently, the iterative procedure used to merge waveform data with identified common events is described. To compare the results derived from re-picking of arrival times against commonly used compilations of routine picks, we extracted phase data for the Alpine region from the International Seismological Center (ISC). The corresponding data set is presented at the end of this section.

## 2.2 Networks in Greater Alpine Region

Figure 2.1 presents the national and regional networks used in this study. All networks except the TOMOCH array are based on permanent stations. The TOMOCH network consists of 7 broad-band stations temporary installed and deployed by ETH Zurich between 2004 and 2006 in southern Germany and France. Table 2.1 and 2.2 summarize the associated networks in detail. Accessibility, availability, and format of waveform and bulletin data differs for most networks. Only few data bases are completely accessible via AutoDRM (Automatic Data Request Manager, *Kradolfer* 2000) and often only low sampled channels (e.g. BH with sampling frequency of 20 Hz) or recent data is available online. A large part of high sampled waveform data for the entire period of 1996 to 2007 is available only on request. The majority of networks provide digital waveform data in GSE2 or SAC format and almost each network has its own event-bulletin format.



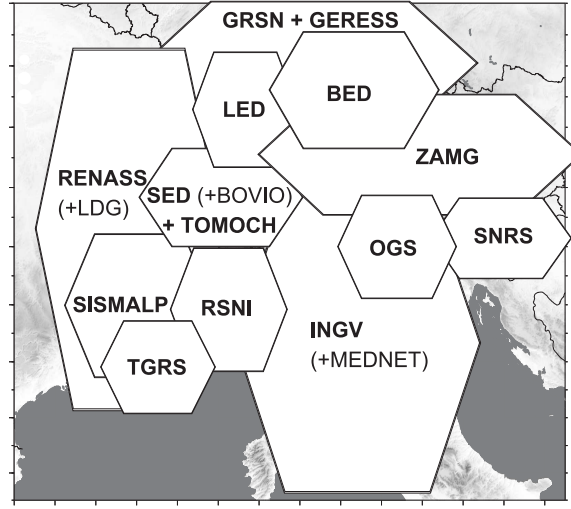


**Figure 2.1:** National and regional networks in the greater Alpine region used in this study. Data of networks marked by thin labels is only embedded in one (or several) of the bold labeled networks. For further description see Tab. 2.1 and 2.2.

Network Label	Institution	Available Waveform Data	Retrieved by	Format
BED	Ludwig-Maximilians-University, Munich, Germany	local & regional event data	request, on-site	GSE1/2
GRSN, GERESS	SZGRF Erlangen, BGR Hannover, Germany	continuous data	AutoDRM	GSE2
INGV, MEDNET	Istituto Nazionale di Geofisica e Vulcanologia, Rome, Italy	local & regional event data (including MEDNET data)	web interface, request, FTP	SAC
LDG	LDG/CEA, Paris, France	some local & regional event data included in SED data base		
LED	Landes-Erdbebendienst Baden-Württemberg, LGRB Freiburg i. B., Germany	local & regional event data	request	GSE2
OGS	Istituto Nazionale di Oceanografia e di Geofisica Sperimentale, Trieste/Udine, Italy	local & some regional event data ( $M \geq 3.5$ )	request	SAC
RENASS	Réseau National de Surveillance Sismique, EOST, Université Louis Pasteur Strasbourg, France	local & regional event data	web interface	GSE2
RSNI	Regional Seismic Network of Northwestern Italy, Dip.Ter.Ris., Università di Genova, Italy	local & regional event data	request, on-site	ASCII

**Table 2.1:** Waveform and bulletin data from regional and national networks in the greater Alpine region used in this study (Part I).

## 2 COMPILATION OF DATA SET FOR THE ALPINE REGION

Network Label	Institution	Available Waveform Data	Retrieved by	Format
SED	Swiss Seismological Service, ETH Zurich, Switzerland	Local & regional events, continuous data	internal access, AutoDRM	Binary, GSE2
SISMALP	Réseau Sismologique des Alpes, Laboratoire de Géophysique Interne et Tectonophysique (LGIT), Université Joseph Fourier Grenoble, France	local & regional event data	request, on-site	Binary
SNRS	Seismic Network of the Republic of Slovenia, Environmental Agency of the Republic of Slovenia - Seismology Office (ARSO), Ljubljana, Slovenia	local & regional event data	request, recent data: AutoDRM	GSE2
TGRS, ROSALP	Très Grande Résolution Sismique, Université de Nice, France	continuous data (including 2 ROSALP stations)	AutoDRM	SAC
TOMOCH	Temporary stations in France & Germany deployed by ETH Zurich, Switzerland	continuous data	internal access	Y-Format
ZAMG	Zentralanstalt für Meteorologie und Geodynamik, Vienna, Austria	continuous data	AutoDRM	GSE2

**Table 2.2:** Waveform and bulletin data from regional and national networks in the greater Alpine region used in this study (Part II).

## 2.3 Compilation of Combined Waveform Data Set

Bulletin and waveform data of 14 networks in the greater Alpine region were compiled for the period of 1996 to 2007. Station information like coordinates and instrument type are included in a master-station list (MSL). Associated waveforms are merged with waveforms of other networks for same events in an iterative procedure.

### 2.3.1 Bulletin Data

Event bulletin data from 9 networks in the greater Alpine region were compiled. Regional bulletins are completed by bulletins of the National Earthquake Information Center (NEIC) for events  $M_l \geq 4.0$  (complete except clusters and aftershocks) to ensure no major event is missed. All extracted bulletin information is converted to a common bulletin format (ECB) to simplify comparison of events between different networks. The basic information for each event consists of origin time,

epicenter location, focal depth, magnitude, magnitude type, agency, and an event identification flag (event-ID). The event-ID is derived from the associated origin time (date and time up to minute).

The 9+1 bulletin lists are used to select the waveform data extracted for each network. The base for all networks is the NEIC list with events  $M_l \geq 4.0$  since we expect that the majority of stations in the region should be triggered for this magnitude. We define a geographical outline for each network and depending on seismicity and accessibility, a minimum magnitude  $M_l^{min}$  for the network is selected (between 2.5 and 3.0 for most networks). Within the outlined area all events with  $M_l \geq M_l^{min}$  are selected for waveform extraction. Outside the area, we accept only selected events with larger magnitudes.

To account for incompleteness, we compare the bulletin of the current network with neighboring bulletins. We use a definition for common events similar to *Solarino et al.* (1997). Events are clearly identified as common if the difference in source time is  $\leq 15$  s and the distance between hypocenters is  $\leq 40$  km. For five networks, only external bulletins were used for event selection.

### 2.3.2 Waveform Data

Based on event lists derived from bulletin data, digital waveforms of 14 networks (bold labels in Fig. 2.1) were compiled for the period of 1996 to 2007. Accessibility, availability, and format of waveform data from different networks is summarized in Tab. 2.1 and 2.2.

Waveform data is converted to GSE2-format (Group of Scientific Experts, Geneva, 1990) via codes listed in Tab. 2.3. Besides network specific problems as illustrated by examples in Tab. 2.3 (delays due to DCF synchronization, swapped polarities of amplitudes, wrong or incomplete GSE2 headers, etc.) the most common problem is represented by multiple channel pairs for same events caused by multiple triggers or short gaps in the data base. When merging data sets, we have to account for shared stations, which are often included in two or more networks. In case of several channels (e.g. short period and broad-band or velocity and acceleration) available for the same station code, the most appropriate has to be selected. To avoid inconsistencies due to multiple data, we checked the waveforms of each network for identical channels in a semi-automatic procedure. If an identical channel-station pair is identified, all available seismograms are displayed and the most appropriate is selected for further use. The merging procedure accounts for identical data of shared stations and selects appropriate channels in case of different available instrument types for same stations (see 2.3.4). In addition, recordings of 3C instruments are often incomplete (missing Z-, E-, or N-component). In such cases, incomplete 3C recordings are reduced to vertical components if at least a Z-component is available. If Z is missing the recording is rejected. Finally, the name of each waveform file is associated with the corresponding event-ID in the bulletin list of the network.

Much effort was put in identifying incorrect time synchronization and correction of systematic time shifts caused by DCF systems or filters. Unfortunately, it was

## 2 COMPILATION OF DATA SET FOR THE ALPINE REGION

Network Label	Original Format	Conversion Code	Problems/Remarks
BED	GSE1/2	modified codeco <sup>3</sup>	DCF, filter delays
INGV	SAC	modified codeco <sup>3</sup>	SAC header not consistent and not compatible with GSE2
OGS	SAC	modified codeco <sup>3</sup>	SAC amplitudes in floating representation, not compatible with GSE2/CM6
RSNI	ASCII	geno2gse2_osx <sup>2</sup>	Time depending corrections for time (DCF delays) and amplitude polarity, multiple station codes
SED	Binary, GSE2	signalhandler <sup>3</sup>	-
SISMALP	Binary	sis2gse <sup>2</sup>	Time and instrument depending check of timing quality
TGRS	SAC	modified codeco <sup>3</sup>	-
TOMOCH	Y-format	y2gse <sup>3</sup>	Data gaps between 5 min blocks, wrong channel ID

**Table 2.3:** Overview about codes used for conversion to GSE2 format and specific problems present in waveform data. <sup>1</sup> Code provided by U. Kradolfer, K. Koch, K. Stammer, modified by T. Diehl. <sup>2</sup> Fortran codes provided by N. Deichmann, modified by T. Diehl. <sup>3</sup> Codes provided by M. Baer.

not possible to obtain complete information on transfer functions and gains for all instruments. To avoid inconsistencies due to aliasing, we require a minimum sampling frequency of 40 Hz for local and regional earthquake data. Data with sampling below 40 Hz is not considered.

### 2.3.3 Station Data

Information on station locations (latitude, longitude, and elevation) was compiled for all networks. Station lists provided by the network owners were cross-checked against each other and against regional station lists of *Solarino et al.* (1997), *Lippitsch* (2002), *Di Stefano* (2005), and the ISC online station-book (<http://www.isc.ac.uk/IR/stationbook.html>). All available information was compiled to a master-station list similar to the procedure described by *Solarino et al.* (1997). In case of inconsistent information, the station owner was consulted. A station is flagged as unusable in the MSL, if the conflict could not be clarified. Finally, all usable stations are associated with a reference location used for all further applications (merging, tomography, synthetic travel times for automatic pickers, etc.). In addition, channels identifiers provided in the waveform files were analyzed to get basic information about instrument type (corner frequency, number of components) for each station. Figure 2.2 presents reference locations for all stations flagged as usable in the MSL. Triangles denote three component stations, circles denote one component (vertical) instruments and colors indicate the corresponding network affiliation. Of course, not all of the displayed stations operated

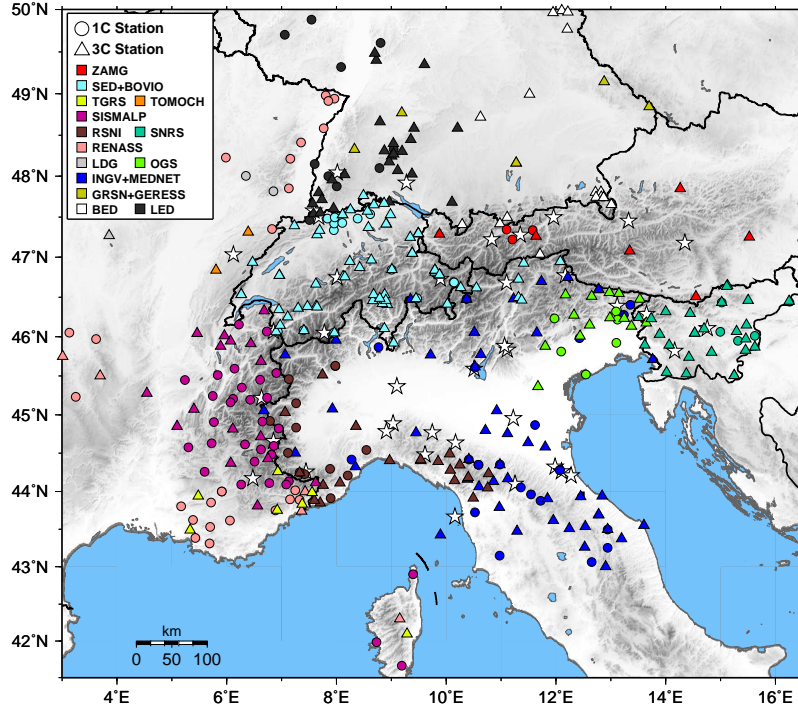


**Figure 2.2:** Networks and stations in greater Alpine region used in this study. Locations correspond to reference locations in MSL. Triangles denote three component stations, circles denote one component (vertical) instruments. Colors indicate the corresponding network affiliation. Not all of the stations operated at the same time.

at the same time.

### 2.3.4 Iterative Merging Procedure

The iterative merging procedure for bulletin and waveform data is summarized in the flow chart of Figure 2.3. For each network an updated (extended) bulletin is derived from the network bulletin (if existing) and several external bulletins (neighboring networks, NEIC) as described in 2.3.1.

Events included in the updated bulletin are extracted from the waveform data base of the network as described in 2.3.2. The event-ID links the waveform file with event parameters (location, magnitude, etc.) provided in the updated bulletin. Furthermore, the updated network bulletin is compared with the master-event list (MEL) from the previous iteration step, using differences in location and origin time as criteria to identify common events. If an event from the updated network bulletin is identified in the MEL, the corresponding location is included as additional bulletin information to the existing reference location. Events not identified in the MEL will be added as new reference location to the MEL.

The event-ID of the reference location is used to identify the merged waveform file from the previous iteration (reference file). Waveforms from the current network are merged with the reference file from the previous iteration. In a first step, the

sampling rate  $\Delta f$  of the current trace is verified. If it is below 40 Hz, the trace is not considered in the merging procedure. In addition, it is checked whether the station code is flagged as usable in the MSL. Subsequently, the station/channel

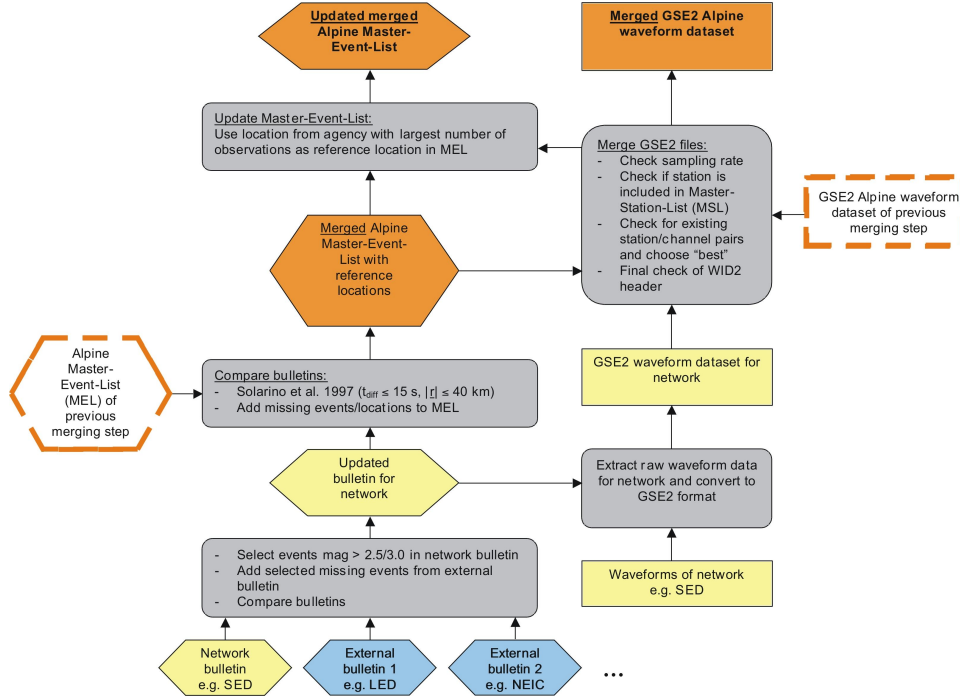


**Figure 2.3:** Flow chart of iterative merging procedure used to derive combined waveform data set for Alpine region.

IDs from the network file are compared with the available data in the reference file. We define a hierarchy of channel-IDs for the merging procedure. HH (broad-band,  $\Delta f \geq 80$  Hz) channels have highest priority, followed by BH (broad-band,  $\Delta f < 80$  Hz), EH (short-period,  $\Delta f \geq 80$  Hz), and finally SH (short-period,  $\Delta f < 80$  Hz). If a higher-quality channel for the same station is identified in the network file, it replaces the existing trace in reference file. If a higher-quality channel for the same station already exists in the reference file, the trace from network file is not considered. Finally, the GSE2 header is checked for completeness and missing information is replaced by default values.

This merging procedure is repeated for all networks and subsequently a final reference location for each event is determined from all available locations. If a NEIC location is available it is used as reference location. For all other events we use the location provided by the agency with the largest number of recordings (stations in GSE2 file) as reference location. Figure 2.4 shows the resulting ray-coverage for the final data set. Hypocenters correspond to reference locations in the final MEL. The data set includes 1C and 3C recordings of about 1500 local earthquakes recorded at about 400 stations (not all stations were operating at the same time). The final waveform data set consists of more than 70'000 seismograms, whereas about 50% are 3C recordings.

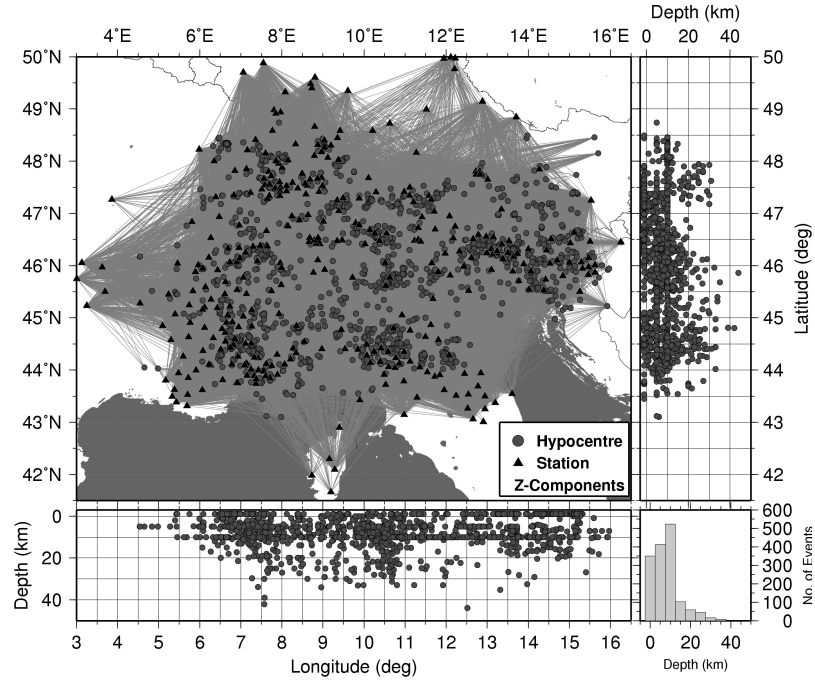


**Figure 2.4:** Ray-coverage for 70'000 seismograms. The data set consists of more than 1500 local and regional earthquakes recorded at about 400 different stations in the greater Alpine region. Hypocenter locations correspond to reference locations in Master-Event list.

To assess the potential of the waveform data set in terms of P-wave tomography studies, Figure 2.5 displays the number of vertical recordings for each station. Stations with more than 100 vertical recordings are indicated as black circles. For the majority of stations we have a rather high number of recordings, which results in a dense data coverage especially for the western and central Alps and the northern Apennines. North-eastern Italy, the Po plain, the Bavarian Molasse basin, eastern Austria, and the Jura mountains represent areas with less dense station and/or data coverage.

Figure 2.6 displays the analog results for potential S-wave tomography studies. Circles denote 3C stations and the color indicates the number of complete 3C recordings. The amount of 3C recordings and stations is significantly lower. If we consider that S-phases above 100 km epicentral distance (transition from S<sub>g</sub> to S<sub>n</sub> as first arriving S-phase) are usually difficult to pick, the resulting data coverage becomes even worse as demonstrated in Figure 2.7. The number of 3C recordings of epicentral distances < 100 km is rather low and only regions with dense 3C station spacing and increased nearby seismicity represent potentially resolved areas.

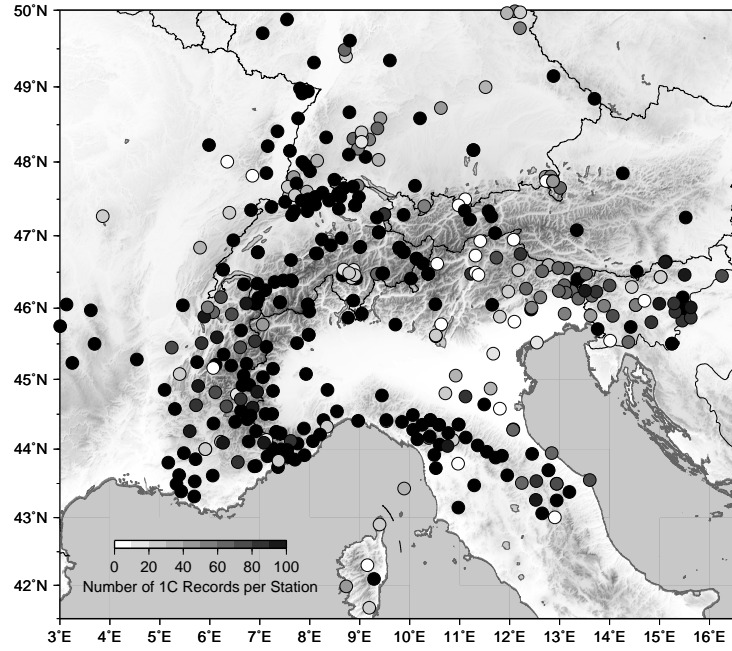


**Figure 2.5:** Circles denote stations with more than one vertical component recording. The filling of the circles indicate the number of recordings for each station. Stations with more than 100 vertical recordings are black colored.

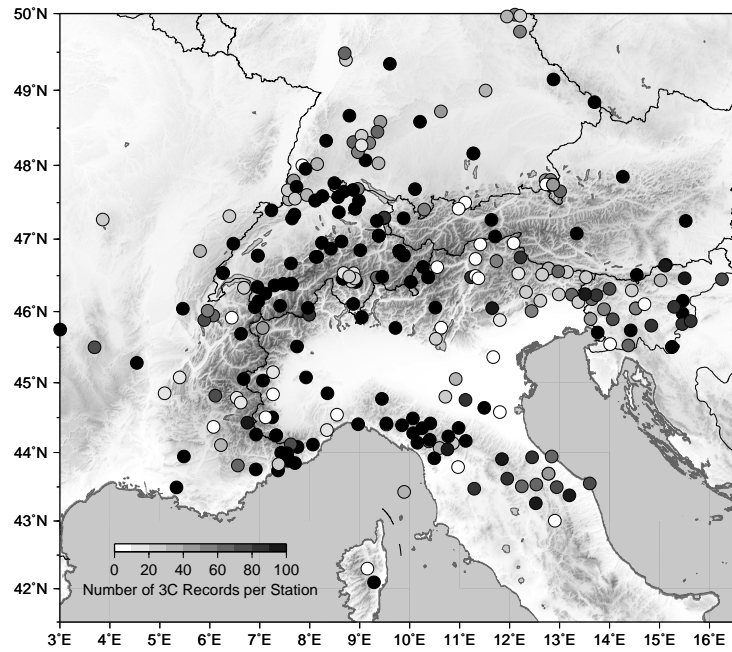


**Figure 2.6:** Circles denote stations with more than one three component recording. The filling of the circles indicate the number of recordings for each station. Stations with more than 100 three component recordings are black colored.



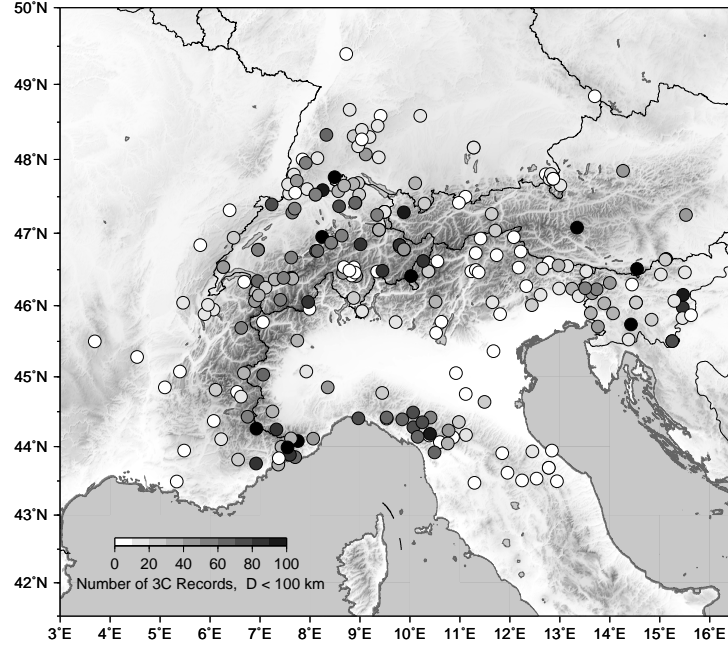


**Figure 2.7:** Circles denote stations with more than one three component recording with epicentral distance  $\Delta < 100$  km (dominated by Sg). The filling of the circles indicate the number of recordings for each station. Stations with more than 100 three component recordings are black colored.

## 2.4 Merged Phase Data: The ISC-Compilation

The International Seismological Center (ISC) compiles bulletin and phase data provided by different national and regional seismic networks to a common data base. ISC data is commonly used for global and regional tomographic studies, since it represents one of the largest compilations of seismic phases in the world. Although the phase data includes a significant degree of noise (see e.g. *Röhm et al.*, 2000), ISC data has also recently been used for local source tomography. To compare local earthquake tomography models derived from high-quality re-picked data with standard routine compilations, ISC phase data was extracted from CDs and online requests for the period of 1996 to 2007.

The phase data was converted from IMS format (International Monitoring System) to the CNV format (VELEST phase format, for description see *Kissling et al.* 1995). Phase readings of stations not flagged as usable in the MSL are rejected. Events identified as non-tectonic events (rock bursts, explosions, landslides) are not considered. The valid latitude range for extracted events goes from  $43.0^\circ$  to  $49.0^\circ$  north, the longitude range encompasses  $4.0^\circ$  to  $16.0^\circ$  east. The minimum magnitude is  $M_l = 1.5$ .

Usually, hypocenters of several agencies are available for the same event. Locations provided by ISC have highest priority, followed by NEIC. If neither ISC nor NEIC location is available, we use the location associated with the smallest azimuthal gap

as reference location, since a small gap usually indicates higher location quality. For each station the earliest possible P and S phase is assumed to be the first arriving body wave. However, we consider only phases labeled as Pg, P\*, Pb, Pn, P, Sg, S\*, Sb, Sn, or S. Observations classified as ‘Q’ (questionable) are rejected. Since the error assessment is assumed to be not consistent for the majority of readings we weight all other qualities (‘I’ for impulsive, ‘E’ for emergent or no quality information at all) equal. Events with less than 6 usable P observations are rejected.

The final data set contains about 10’000 events (at least 6 P-observations per event) recorded at 267 stations. This results in more than 190’000 P- and more than 110’000 S-phases. It is remarkable that almost one third of the stations reported in the MSL is missing in the ISC data set.

## Chapter 3

# Consistent Phase Picking for Regional Tomography Models: Application to the Greater Alpine Region

T. Diehl, E. Kissling, S. Husen and F. Aldersons

Originally submitted to *Geophys. J. Int.*, April 15, 2008  
Accepted for publication September 17, 2008

## Abstract

The resolution and reliability of tomographic velocity models strongly depends on quality and consistency of available travel-time data. Arrival times routinely picked by network analysts on a day-to-day basis often yield a high level of noise due to mispicks and other inconsistencies, particularly in error assessment. Furthermore, tomographic studies at regional scales require merging of phase picks from several networks. Since a common quality assessment is not usually available for phase data provided by different networks, additional inconsistencies are introduced by the merging process. Considerable improvement in the quality of phase data can only be achieved through complete re-picking of seismograms. Considering the amount of data necessary for regional high-resolution tomography, algorithms combining accurate picking with an automated error assessment represent the best tool to derive large suitable data sets. In this work, we present procedures for consistent automated and routine picking of P-wave arrival times at local to regional scales including consistent picking error assessment. Quality-attributed automatic picks are derived from the MPX picking system. The application to earthquakes in the greater Alpine region demonstrates the potential of such a re-picking approach. The final data set consists of more than 13'000 high-quality first-arrivals and it is used to derive regional 1-D and preliminary 3-D P-wave models of the greater Alpine region. The comparison with a tomographic model based on routine phase data extracted from the ISC Bulletin illustrates effects on tomographic results due to consistency and reliability of our high-quality data set.

## 3.1 Introduction

Due to increasing computational power and major improvements in forward and inverse algorithms over the past two decades, seismic tomography is by now able to provide 3-D velocity images with spatial resolution of up to a few kilometers at local to regional scales. The development of sophisticated forward solution methods (e.g., ray tracing) for complex 3-D media (e.g., *Um and Thurber, 1987; Virieux et al., 1988; Podvin and Lecomte, 1991*) and their implementation in local earthquake tomography algorithms (e.g., *Thurber, 1983; Haslinger and Kissling, 2001; Husen and Kissling, 2001*) have led to a significant increase in the computational accuracy of inversion techniques. The enlarged memory capacity of modern computer systems allows a fine grid for the model parametrization as described e.g., in *Kissling et al. (2001)*.

The minimum resolvable velocity perturbation in tomographic models, however, depends directly on the model parametrization, the background velocity, and the timing accuracy of forward solvers and data. To resolve a velocity perturbation of  $\Delta v = 5\%$  in the mid crust ( $v_P \approx 6.0$  km/s) along a ray segment of  $\Delta x = 15$  km requires a timing error  $\varepsilon_t$  not greater than 0.12 s. The same perturbation amplitude along the same ray segment in the uppermost mantle ( $v_P \approx 8.0$  km/s) requires an even higher timing accuracy of  $\varepsilon_t < 0.09$  s.

Although modern forward solvers for complex 3-D structure are able to achieve such precision, the limiting factor of most present day tomographic studies is represented by the accuracy and consistency of the available phase data (i.e., phase picks). In this context, a ‘phase pick’ is defined as the arrival time of a seismic phase as determined from picking the onset of a wave at a particular station. Furthermore, we define ‘routine pick’ as the arrival time estimated by network analysts on a day-to-day basis for the purpose of locating earthquakes in near real-time. Differences in the picking behavior of the various analysts of a network leads to inconsistencies in routine phase picks in terms of absolute timing (e.g., *Leonard, 2000*), timing uncertainties and phase interpretations.

Additional inconsistencies across networks have to be considered for tomographic studies at regional scales. A uniform resolution of the entire Alpine orogen requires data of more than 10 national and regional permanent networks (e.g., *Solarino et al., 1997*; *Lippitsch et al., 2003*). Merging such a heterogeneous data set presents several difficulties, since no common error assessment for timing and phase interpretation is available. Furthermore, identification of common events can be difficult because of significantly different hypocenter locations (*Solarino et al., 1997*). Figure 3.1 denotes examples of inconsistencies and obvious phase misidenti-

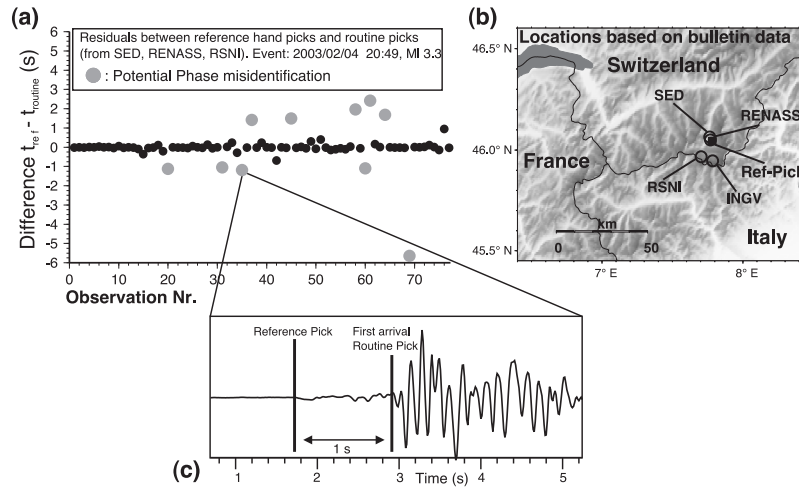


**Figure 3.1:** Example of phase misidentification in routine phase data. (a) Difference between (revised) reference hand picks and routine picks provided by SED (Switzerland), RENASS (France), and RSNI (Italy). Grey dots indicate probable phase misidentifications in routine phase data. (b) Locations of the same earthquake, as reported in different national and regional bulletins. ‘Ref-Pick’ denotes location resulting from reference picks and regional minimum 1-D model. (c) Waveform and corresponding routine and reference picks for an obvious phase misidentification. The routine pick is located at the secondary Pg phase.

fications in routine phase data of several networks in the Alpine region, which may result in errors up to several seconds. To benefit from recent improvements in the quantity and quality of seismic stations (digital transmission, high sampling rates, accurate timing with GPS-systems, increasing number of broadband sensors, etc.), the existing inconsistencies in seismic phase data must be significantly reduced.

Due to the steadily increasing amount of available digital waveform data, automatic picking algorithms are required to measure phase arrival times with a high level of consistency for large data sets. Several automatic approaches have been developed over the past decades. Traditionally, characteristic functions from STA/LTA ratios of energy, envelopes, frequency, and particle motion are used to detect and pick the onset of a seismic phase (e.g., *Allen*, 1978, 1982; *Baer and Kradolfer*, 1987; *Earle and Shearer*, 1994; *Withers et al.*, 1998). More recently, autoregressive (AR) pickers based on the Akaike information criterion (AIC, *Akaike*, 1973) were developed as described e.g., in *Takanami and Kitagawa* (1988) or *Leonard and Kennett* (1999). Usually, implementations of AR-AIC pickers have to be combined with phase detectors from STA/LTA ratios (e.g., *Sleeman and van Eck*, 1999; *Leonard*, 2000) or other techniques such as wavelet analysis (*Zhang et al.*, 2003).

To enhance the consistency of phase picks of similar or repeating events (e.g., swarms) waveform-correlation can be used as described e.g., by *Aster and Rowe* (2000) and *Rowe et al.* (2002). Primarily, waveform-correlation provides only relative arrival times. Absolute arrival times can be obtained from applying an AR-AIC picker to a stack of aligned waveforms of a specific cluster as shown by *Rowe et al.* (2004). Such refined and adjusted phase picks provide an excellent base for high-resolution relocation of seismic sources (e.g., *Rowe et al.*, 2004) and tomography studies (e.g., *Satriano et al.*, 2008). Since correlations-pickers assume waveform similarity, their application is mainly limited to repeating seismicity at local scales.

Although accuracy of automatic picks is comparable to manual picks as demonstrated e.g., by *Sleeman and van Eck* (1999), *Leonard* (2000) or *Zhang et al.* (2003), most of the existing algorithms do not provide an assessment on the absolute uncertainty of the automatic pick. Since consistent data quality weighting is crucial for most travel-time inversions, the automatic error assessment represents an essential component of the phase picking procedure. Among the existing methods, the *MannekenPix* (MPX) picking software (*Aldersons*, 2004) is one of only a few algorithms that include an automatic quality weighting. *Di Stefano et al.* (2006) applied the MPX picking system successfully to the data of the Italian national seismic network.

To achieve an appropriate aperture to resolve the deep crustal structure of the Alps at a regional scale, a data set derived from several seismic networks has to be compiled. Furthermore, the low seismicity of this region requires data from a long recording period. Consequently, this results in a rather heterogeneous data set in terms of waveform characteristics and hypocentral information. The lower seismicity also demands more of the automatic picking and classification procedure, since a simple discrimination of very good from bad picks, as is typically done when automatic picking is used, would not be sufficient to provide enough phase picks.

In this work, we first present a consistent picking and error assessment for local and regional P-phases and identify common problems and inconsistencies in rou-

tine hand picking. Subsequently, we will give a brief introduction to the general concept of MPX and present calibration procedures suitable for local to regional scales. These procedures are applied to the greater Alpine region and the resulting high-quality automatic phase picks are inverted for 3-D velocity structure. The comparison with regional tomography models based on routine phase data extracted from the ISC Bulletin demonstrates the potential improvement of our re-picking approach.

## 3.2 Routine Hand Phase Picking

Although travel-time based earth models and hypocentral solutions strongly depend on the accuracy of phase data, the description of consistent phase picking has received little attention in the literature. *Simon* (1981), *Kulháněk* (1990), and *Kulháněk* (2002) provide a general overview about seismogram interpretation from local to teleseismic scales. They focus mainly on basic descriptions of phases observable in common seismograms. The assessment of timing uncertainty and phase interpretation, however, is barely discussed. The fundamentals of digital signal processing and their influence on onset properties are described e.g., in *Seidl and Stammer* (1984), *Scherbaum* (2001), and *Scherbaum* (2002). Among the few recent guidelines, the *New Manual of Seismological Observatory Practice* (NMSOP) of *Bormann et al.* (2002) provides an introduction to basic picking principles for local, regional and teleseismic seismograms. Although they propose to quantify the onset-time reliability, a detailed description for consistent quality assessment is missing.

In the following section, we present a hand picking procedure, which includes a consistent quality assessment for timing uncertainty and phase interpretation. It is focused on crustal phases of local to regional distances, but its principles apply likewise to teleseismic observations.

### 3.2.1 Phase Timing and the Assessment of its Uncertainty

The basic quantities associated with a picked phase are usually the absolute arrival time and the corresponding observation uncertainty. Common qualification of timing uncertainties differentiate signals into ‘impulsive’ and ‘emergent’ phase onsets as e.g., used by the International Seismological Center (ISC). Such qualitative error assessment, however, no longer satisfy the resolution capability of modern digital waveform data. In addition, it is difficult or even impossible to give a general predictive definition of a seismic onset time, which could be used for the actual measurement of first arrival time from a sampled band-limited signal in the presence of noise (*Seidl and Stammer*, 1984).

Consequently, a physical consistent formulation can only be achieved by a probabilistic point of view as suggested e.g., in *Bormann et al.* (2002). Such an approach directly relates the measured arrival time with the corresponding observation uncertainty. Considering the onset of a seismic phase as a probabilistic function  $P_a(t)$ ,

the arrival time is expressed as the ‘most likely’ time  $t_A$ , with  $P_a(t_A) = \text{Max}(P_a)$ . On the other hand, the ‘earliest’ possible time for the phase onset is defined as  $t_E$ , where the likelihood for onset is approaching zero. Thus  $P_a(t_E) \geq 0$ . Similarly, the ‘latest’ possible time for the phase onset  $t_L$ , is defined as  $P_a(t_L) \geq 0$ . Figure 3.2 illustrates the proposed concept in further detail. Although the onset of the phase

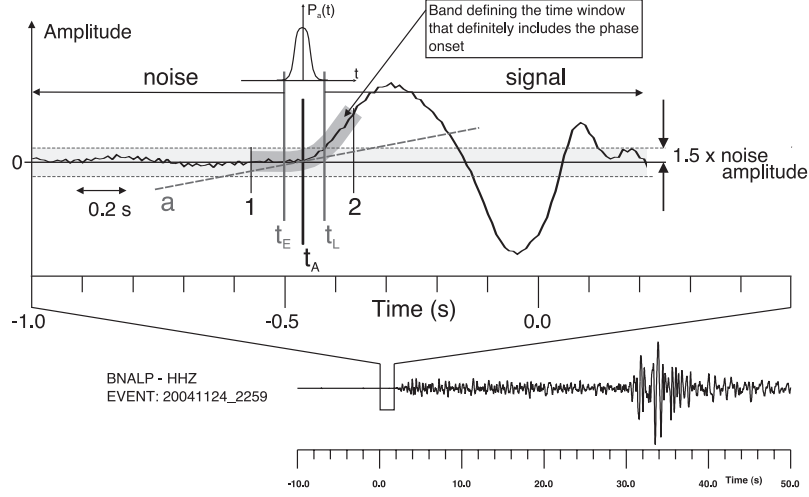


**Figure 3.2:** Probabilistic phase picking approach: the ‘earliest’ possible pick corresponds to  $t_E$ , the ‘latest’ possible pick corresponds to  $t_L$ . The most likely arrival time  $t_A$  is located within this interval. Primarily amplitude is used for the determination of  $t_E$  and  $t_L$ . See text for further details.

(mainly characterized by a change in amplitude) is rather impulsive and exhibits an almost ideal signal to noise ratio, it is difficult to determine an arrival time consistent with picks of waveforms from the same seismic source recorded at other stations. The thick grey band between position ‘1’ and ‘2’ defines the time window that definitely includes the onset of the wavelet, while position ‘1’ is certainly too early to be picked as  $t_E$  and ‘2’ is too late as  $t_L$ . The band outlined by two broken lines denotes the possible threshold of the noise amplitude (arbitrarily defined as 1.5 times pre-signal amplitude).

In practice, we first determine the position of  $t_L$  and  $t_E$ . For a consistent determination of  $t_L$  and  $t_E$ , we have to setup a common procedure. Since the amplitude exceeds the threshold several times at position ‘2’, the end of the grey band is certainly too late to be picked as  $t_L$ . Therefore, we define the intercept between signal amplitude and the *a priori* noise threshold as  $t_L$ . Usually, the consistent determination of  $t_E$  is more difficult. In Figure 3.2 we fit a tangent (dashed line ‘a’) to the slope of the onset. If we shift the tangent from  $t_L$  towards earlier times, the slope decreases. The earliest possible time  $t_E$  corresponds to the first zero slope from  $t_L$  towards earlier time. Therefore, the start of the grey band (position ‘1’) is certainly too early, whereas  $t_A$  would be too late to be picked as  $t_E$ . To ensure  $t_E$  includes the zero slope time in the presence of higher background noise, we could shift it earlier by approximately half the dominant noise period. Subsequently, we pick the arrival of the phase at the most likely position  $t_A$ , within the error



interval of  $t_E$  and  $t_L$  (e.g., on the seismogram's leading edge). For the special case of a delta-pulse,  $t_E$  and  $t_L$  would coincide with  $t_A$ . In addition, a quantitative weighting scheme has to be defined where the assigned discrete weighting classes depend only on measured time error intervals ( $t_L - t_E$ ). This procedure allows the adjustment of the weighting class definitions even after the picking process, whilst remaining consistent.

### 3.2.2 Phase Identification and the Assessment of its Uncertainty

Although phase misinterpretation can result in significantly large errors (as demonstrated in Fig. 3.1), phase identification is typically not supplied with any observation error or uncertainty attribute at all (unlike the arrival time of a phase). Particularly for local earthquake studies in orogenic areas with significant lateral crustal structure variations, phase identification can become ambiguous. As an example, Figure 3.3 presents a velocity reduced record section of a local earthquake near Walenstadt, Switzerland, with a focal depth of 13 km. Based on waveform characteristics alone, phase interpretation appears rather difficult for some stations in the distance range of phase triplication (e.g., SPAK and SIERE). In addition, the amplitude ratio between Pg and Pn exhibits strong variations between some stations (e.g., EMV and HEI) probably due to 3-D Moho topography. In these cases, Pn is likely to be missed and Pg will be picked as first-arrival phase. Since most applications like hypocentral localization and travel-time tomography are still based on first-arrivals only, we have to setup an error assessment for phase identification to avoid such gross inconsistencies. For use in routine first-arrival studies and subsequent special studies, we define an error assessment for phase identification as shown in Table 3.1. In addition, synthetic travel-time curves for

Phase label	Phase is ...	Phase used for routine 1 <sup>st</sup> arrival studies
Pg, Sg	Direct (crustal)	Yes (if first arrival)
Pn, Sn	Moho-refracted	Yes (if first arrival)
PmP, SmS	Moho-reflected	No
P1, S1	Unknown type, but certainly first arrival	Yes
P2, S2	Unknown type, second arrival	No
P3, S3	Unknown type, third arrival	No
P, S	Unknown type, uncertain if first arrival	No

**Table 3.1:** Glossary used for phase identification of P- and S-waves at local to regional distances. The glossary implies a first order uncertainty assessment for phase identification.

main crustal phases (as demonstrated in Fig. 3.3) can be used to identify phases or crosscheck phase interpretations. Inconsistent picking of arrival times and phase

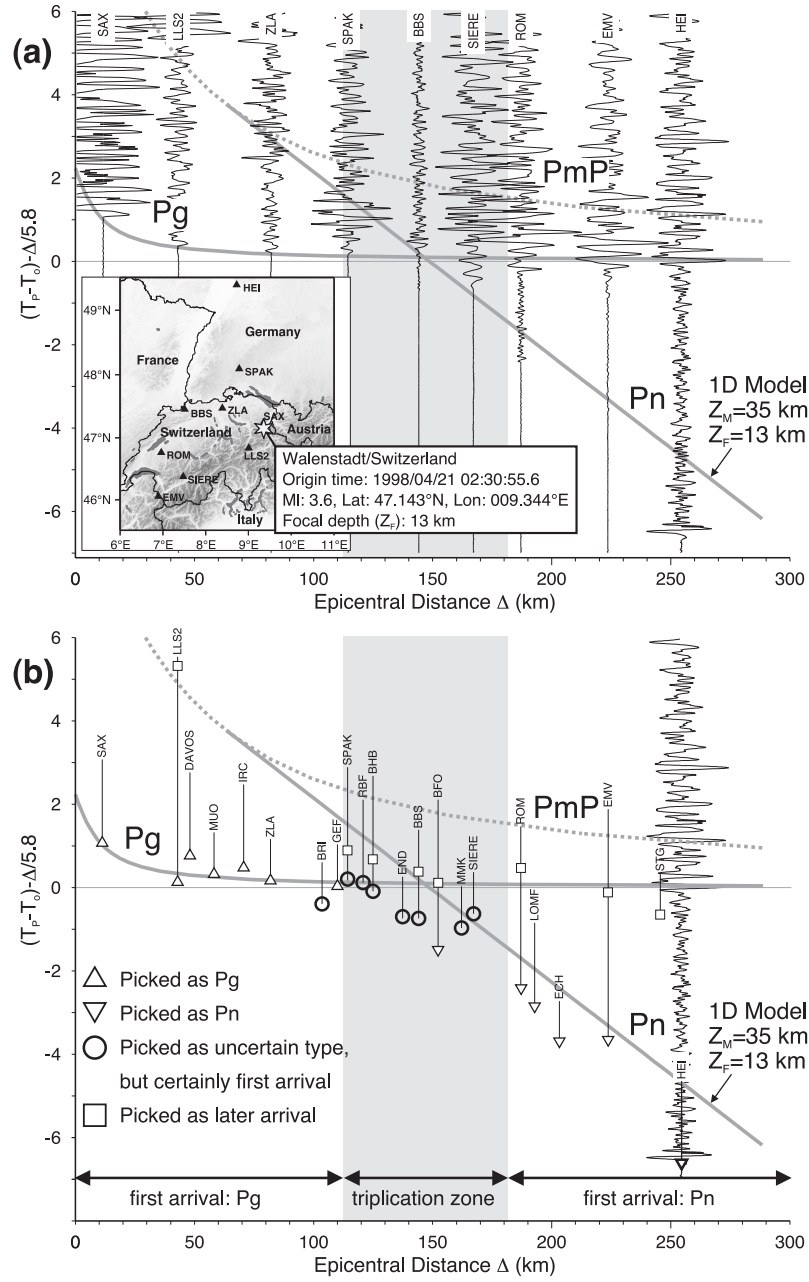


**Figure 3.3:** (a) Velocity reduced record section of a local earthquake near Walenstadt, Switzerland. Amplitudes are normalized to maximum amplitude of each trace. Synthetic travel-time curves for  $P_g$ ,  $P_n$ , and  $PmP$  are indicated by solid and dashed lines. Discrimination of phase type purely from waveform characteristics might be difficult for stations in triplication range (e.g., SPAK and SIERE). Denote differences in amplitude ratio between  $P_g$  and  $P_n$  for station EMV and HEI. Deviations between expected and observed  $P_n$  arrival are related to 3-D Moho topography. (b) Velocity reduced phase picks, crosschecked against synthetic travel time curves derived from a simplified crustal model.

identification can also bias the determination of first motion polarities and therefore directly affects the quality of fault plane solutions.

#### 3.2.3 Sources of Inconsistencies in Routine Picks

Besides insufficient error assessment of timing and phase identification, the picking procedure itself can induce a significant amount of inconsistency, which can result in errors up to several hundred milliseconds. A prominent example is the random choice of window size and amplitude scaling in phase picking (*Douglas et al.*, 1997). Another common problem is the inconsistent usage of filters and misinterpretation of artifacts caused by digital filters. The application of acausal anti-aliasing filters in modern recording systems as described in *Scherbaum* (2001) can lead to oscillations prior to impulsive onsets often interpreted as precursory phases.

Such inconsistencies can be reduced by using pre-defined window lengths for picking, uniform amplification of amplitudes, and consistent application of filters. For reference picking of P-phases we used a 1 Hz 2<sup>nd</sup> order high-pass (HP) filter for broad-band data in order to simulate a short period transfer function. Short period data is only HP filtered if obvious low frequency noise is present. Low-pass (LP) filters are only applied if significant high-frequency noise is observed. LP filters can also be used to somewhat attenuate precursory oscillations caused by acausal anti-aliasing filters.

### 3.3 Automated Re-picking of P-Phase Data: Application to the Greater Alpine Region

#### 3.3.1 Local Earthquake Data Set of the Alpine Region

Waveform and bulletin data from about 1500 events with  $M_l \geq 2.5$  recorded between 1996 and 2007 were compiled from 13 national and regional networks in the Alpine region. Waveforms provided by the different networks were all converted to common GSE2-format (Group of Scientific Experts, Geneva, 1990). Obvious timing and polarity problems present in some data were checked for and - where possible - corrected or the data were removed. To avoid inconsistencies in terms of station codes and station coordinates, information provided by the networks were compiled to a master station list similar to the procedure described by *Solarino et al.* (1997). The resulting data set comprises of more than 70'000 seismograms recorded at about 400 stations shown as triangles and circles in Figure 3.4. This data set represents a unique compilation of digital waveforms from local earthquakes within the Alpine region.

From this data set we select a reference data set consisting of a subset of 39 events, representative of the different tectonic regions and the range of magnitudes and focal depths. These reference events (locations indicated by white stars in Fig.

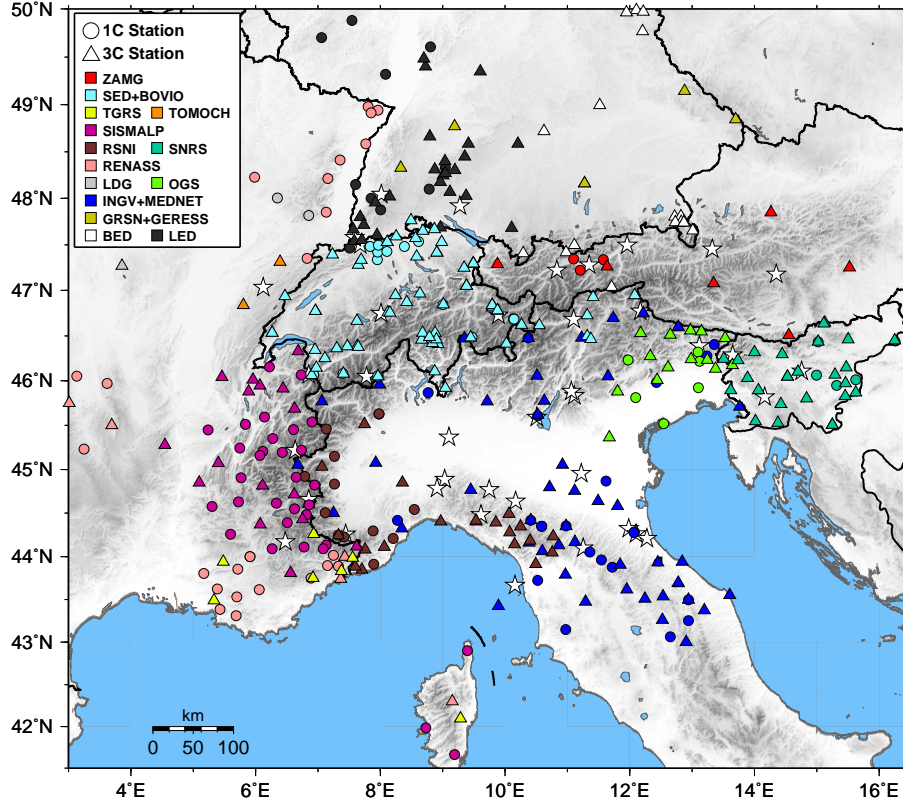


**Figure 3.4:** Networks and stations in greater Alpine region used in this study. Triangles denote three component stations, circles denote one component (vertical) instruments. Colors indicate the corresponding network affiliation. Not all of the stations operated at the same time. Additional white stars indicate location of reference events used for calibration of MPX.

3.4) were consistently and accurately hand picked with the above described routine picking procedure. Table 3.2 shows the weighting scheme used for reference P-phase picking and the number of P-picks in each class. Epicentral distances for

P-Quality class $qP$	Error $\varepsilon_{qP}$ (s)	Weight (%)	# Observations
0	$\pm 0.050$	100	755
1	$\pm 0.100$	50	905
2	$\pm 0.200$	25	876
3	$\pm 0.400$	12.5	481
4	$> 0.400$	0.0 (rejected)	769

**Table 3.2:** Error assessment used for reference P-phase picking and number of P-picks for each quality class derived from 39 reference events.

reference picks vary between 1 km and about 700 km. We used this reference data set for MPX calibration and test of the calibration scheme.

### 3.3.2 The MPX Picking System

The concept of MPX is described in detail by *Aldersons* (2004) and *Di Stefano et al.* (2006). Here, we summarize only the basic principles of the algorithm. Although more recent versions of MPX are not limited to re-picking, the version we used was designed only for re-picking. As such, it requires an initial pick to guide the picking engine to an approximate phase onset time. The initial pick can be provided by an existing routine pick or a predicted time from a theoretical travel-time curve. The latter assumes the existence of an appropriate regional velocity model (preferably a minimum 1-D model e.g., *Kissling et al.* 1994) and an approximate hypocentral location. If routine picks are used as initial picks, we have to ensure that the number of gross misidentifications like the example in Figure 3.1 is small.

The MPX picking algorithm represents an extended version of the robust Baer-Kradolfer picker (*Baer and Kradolfer*, 1987). The threshold for the picker is derived in a adaptive way by comparing apparent noise and signal characteristics. A noise window and a signal window are centered around the initial pick and are separated by safety gaps  $g_N$  and  $g_S$  as demonstrated in Figure 3.5. The length

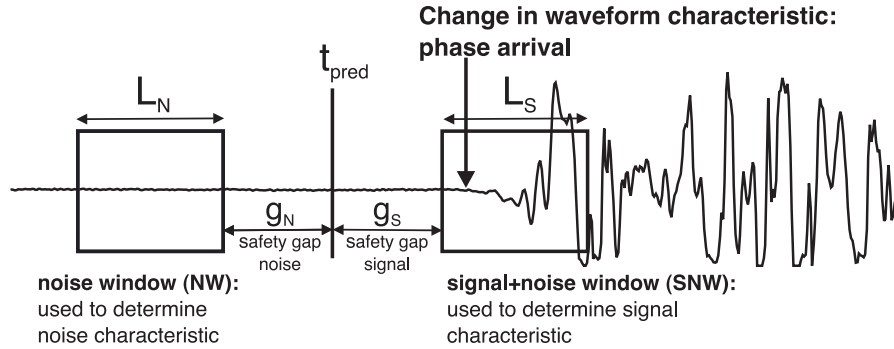


**Figure 3.5:** MPX search window configuration: The noise window  $NW$  and the signal+noise window  $SNW$  are centered around the initial pick (here predicted  $t_{pred}$ ) and are separated by safety gaps  $g_N$  and  $g_S$ .

of the safety gaps mainly depends on the expected maximum difference between initial pick and actual phase onset. Large safety gaps allow picking even from imprecise initial picks. However, mispicks and misinterpretation of later phases as first-arrivals become more likely.

A pattern recognition scheme weights different waveform attributes (predictors) obtained in the time window around the automatic pick and classifies the pick in discrete quality classes. The corresponding weighting factors are called ‘Fisher coefficients’ (*Fisher*, 1936, 1938), which have to be calibrated with a set of reference hand picks (reference data). A multiple discriminant analysis (MDA) is used to derive appropriate Fisher coefficients from the reference picks.

### 3.3.3 Calibration of the Automatic Weighting Procedure

The data set of 39 reference events was used to derive appropriate Fisher coefficients for automatic quality classification. The MDA compares the predictor values around the automatic pick with the associated reference quality class. The Fisher coefficients represent the optimum weighting of each predictor to estimate the corresponding quality class membership. This relationship between predictors and reference quality class is based on the assumption that automatic and reference picks are located at the same phase. However, the autopicker often misses the first-arrival and picks a later more impulsive phase as shown in the example of Figure 3.6. To account indirectly for phase misinterpretation, we associate the pre-

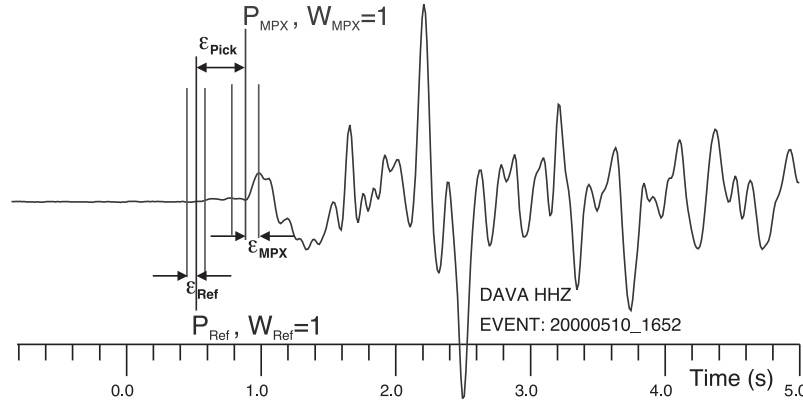


**Figure 3.6:** Example for misinterpretation of an impulsive later phase as first arriving P-phase by the automatic picker. Although automatic classification  $W_{MPX}$  corresponds to the reference weight  $W_{Ref}$ , the error  $\epsilon_{Pick}$  between automatic and reference pick is several times larger than the error  $\epsilon_{MPX}$  associated with quality class  $W_{MPX}$ .

dictors with a ‘target’ class instead of the reference class in the MDA. The ‘target’ class coincides with the reference class if the error  $\epsilon_{Pick}$  between automatic and reference pick is within the error interval of the reference class. If it is larger, the ‘target’ class corresponds to the next lower class, where the error interval includes  $\epsilon_{Pick}$  analogous to the procedure described by *Di Stefano et al.* (2006). However, this will result in a larger number of actual high-quality picks downgraded to lower classes by MPX.

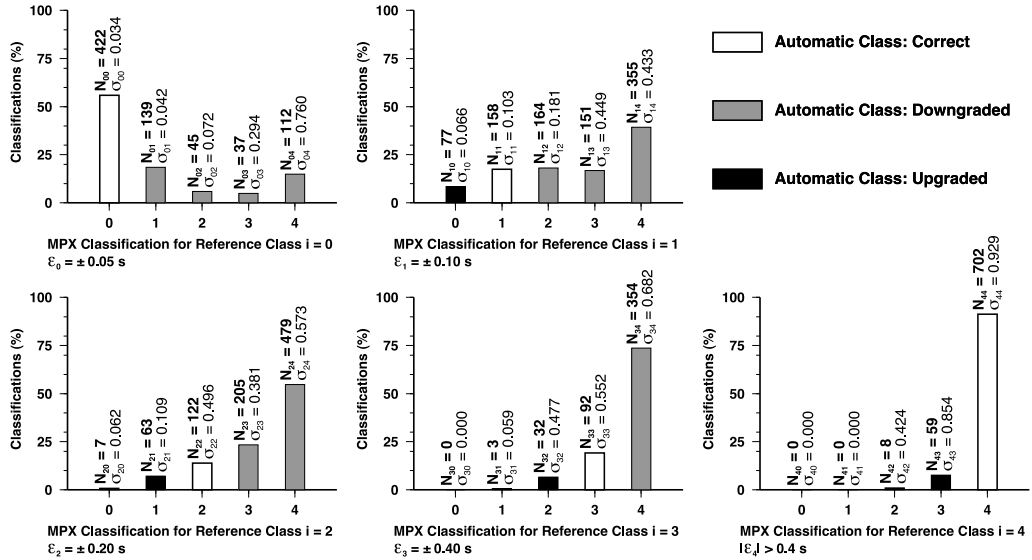
In addition, the choice of reference picks used for the MDA can have a significant influence on the Fisher coefficients and the stability of the resulting automatic classification. Subsets dominated by higher quality picks result in a conservative but robust error assessment in our tests. Fisher coefficients derived from a subset of reference events with  $M_l \geq 4.0$  are given in Table A.1 of appendix A.1. This magnitude threshold leads to an average quality that is biased towards higher signal-to-noise (SN) ratios, since first arriving Pn and Pg phases at distances  $\geq 100$  km have SN ratios comparable to first arriving Pg phases at distances  $< 100$  km.

Figure 3.7 illustrates the performance of the corresponding weighting scheme in

### 3.3 AUTOMATED RE-PICKING OF P-PHASE DATA

terms of accuracy and classification when applied to all reference events.  $N_{ij}$  denotes the number of picks of reference class  $i$  classified by the pattern recognition scheme as automatic class  $j$ . The  $\sigma_{ij}$  represent the standard deviation for differences between reference picks of class  $i$  and corresponding automatic picks of class  $j$ . A satisfactory automatic picking and quality assessment is achieved if the deviation between automatic and reference picks is within the error interval of automatic quality classification ( $\sigma_{ij} \leq \varepsilon_j$ ) and if only few low quality reference picks are moderately upgraded to higher quality classes by MPX. However, upgrades from worst to top quality classes lead to a serious distortion of the data error estimate for seismic tomography and may generate artifacts in tomographic images. Both requirements are satisfied for automatic class  $j = 0$  and  $j = 1$  for the weighting scheme in Figure 3.7. All  $\sigma_{ij}$  are less than or close to  $\varepsilon_j$  and none of the reference class ‘4’ picks (rejected class) are upgraded to high-quality class ‘0’ or ‘1’. For this weighting scheme, automatic picks of class ‘0’ and ‘1’ satisfy the requirements for use in tomographic inversion.

The weighting scheme derived from using ‘target’ classes and reference picks of stronger events results in a robust but rather conservative classification. This pro-



**Figure 3.7:** Performance of MPX for a weighting scheme derived from reference events with  $M_l \geq 4.0$ . The  $N_{ij}$  denote the number of picks of reference class  $i$  classified by MPX as automatic class  $j$ . The  $\sigma_{ij}$  represent the standard deviation for differences between reference picks of class  $i$  and corresponding automatic picks of class  $j$ . White bars indicate correct classification, gray bars indicates downgrading, and black bars identify upgrading of picks by MPX. The automatic weighting classifies more than 55% of the class ‘0’ picks correctly. For classes  $\geq 1$  MPX downgrades a large number of picks to lower or lowest classes.

cedure is necessary to minimize the number of misidentifications present especially at larger regional distances where weak emergent Pn phases are followed by impulsive Pg or PmP phases. In addition, the generally lower signal-to-noise ratio increases the likelihood of mispicks at these distances.

For short distances dominated by first arriving Pg phases we expect less complex waveforms and larger signal-to-noise ratios. Fisher's coefficients given in Table A.2 of appendix A.1 are derived from reference picks at epicentral distances  $\Delta < 100$  km (dominated by first arriving Pg phases). The corresponding classification performance of MPX for distances  $< 100$  km is shown in Figure 3.8. The performance of the automatic classification is much higher for this distance range as indicated by the larger number of correctly predicted qualities (white bars). The  $\sigma_{ij}$  are less-equal or close to  $\varepsilon_j$  for all usable automatic classes (0-2) and none of the rejected picks of class '4' are upgraded to high-quality classes. Although most of the actual class '3' reference observations are rejected by MPX, we recover downgraded picks of class '0', '1', and '2' in the automatic class '3'. Since none of the quality class '4' picks are upgraded and all  $\sigma_{i3} \leq \varepsilon_3$ , automatic picks of class '0' to '3' can be used in this distance range. The higher recovery rate within this distance range

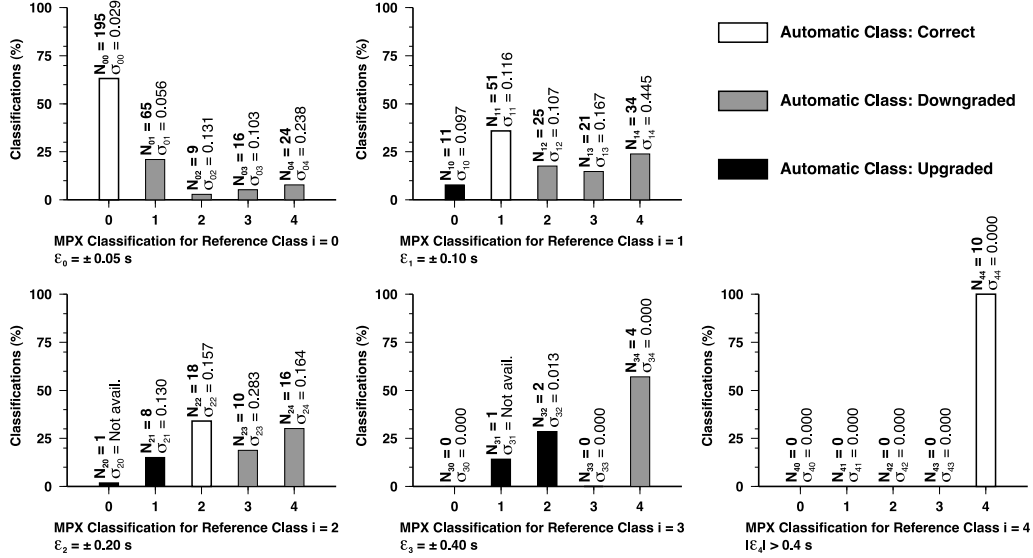


**Figure 3.8:** Performance of MPX for epicentral distances  $< 100$  km (predominantly Pg phases) similar to Figure 3.7. The used weighting scheme is derived from reference picks with  $\Delta < 100$  km.

can provide essential picks to reduce azimuthal gaps or to increase the number of observations per event and may allow the retention of otherwise rejected events. Since *a priori* information about hypocenters exists, we calculate an approximate epicentral distance for each waveform. To achieve the maximum performance of MPX in the so-called ‘production stage’ (application of calibrated MPX to the complete data set) we split the data set into two parts: Fisher coefficients of Table A.2 are used for  $\Delta < 100$  km, whilst the robust coefficients of Table A.1 are used for waveforms with  $\Delta \geq 100$  km. With such a distance-dependant calibration scheme we achieve a first order discrimination between Pg and Pn phases. Accordingly, automatic picks of class 0-3 from the first part can be used for tomographic inversion, whereas, from the second part only class 0-1 have sufficient quality. Figure 3.9 summarizes the performance of MPX for three different calibration



### 3.3 AUTOMATED RE-PICKING OF P-PHASE DATA

schemes using the matrix representation introduced by *Di Stefano et al.* (2006). Automatic picks are compared to reference picks similar to Figure 3.7 and 3.8. The

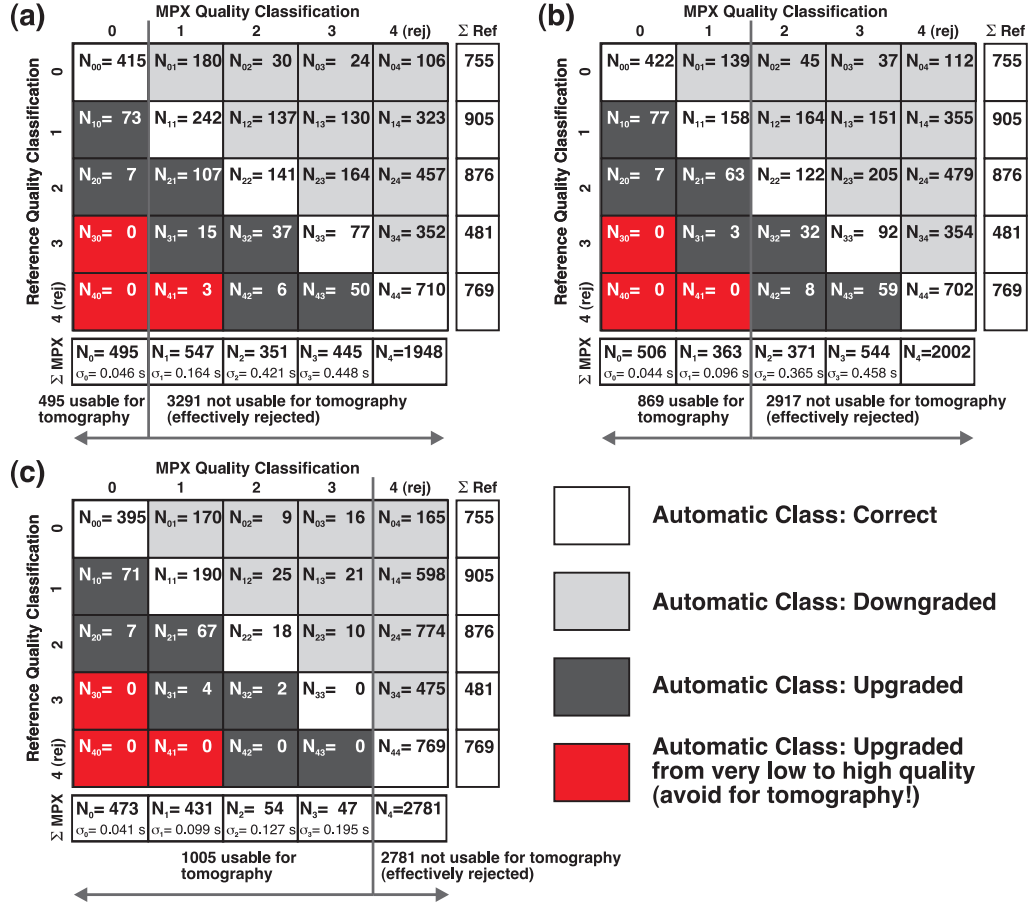


**Figure 3.9:** Performance of MPX for three different calibration schemes using a matrix representation. **(a)** Similar to *Di Stefano et al.* (2006), all reference picks are used for the MDA. For our data set, only automatic picks of class 0 satisfy the requirements for use in tomography (see text). **(b)** Only waveforms of events with  $M_l \geq 4.0$  are used for the MDA. Automatic picks of class 0 and 1 can be used for tomography. **(c)** Distance-dependant calibration as used in this work. Automatic picks of class 0-2 and, in this case, also class 3 (see text) can be used for tomography.

number of reference picks of quality class  $i$  classified by the pattern recognition scheme as automatic class  $j$  is represented by  $N_{ij}$ . The total number of automatic picks classified as class  $j$  is described by  $N_j$  and the standard deviation for differences between automatic picks of class  $j$  and corresponding reference picks is indicated by  $\sigma_j$ . By using all reference picks for the MDA similar to the procedure suggested by *Di Stefano et al.* (2006), only automatic picks of class 0 satisfy the requirements for application in tomography (Fig. 3.9a). Automatic picks of class 1 exhibit a standard deviation  $\sigma_1$  significantly greater than  $|\varepsilon_1| = 0.1 \text{ s}$  and in addition, they contain three picks upgraded from the lowest quality class 4.

In Figure 3.9b only waveforms of events with  $M_l \geq 4.0$  are used for the MDA. Au-

tomatic classes 0 and 1 can be used for tomography, which leads to a significantly increased number of picks. An even higher number of usable picks is obtained with the distance-dependant calibration scheme shown in Figure 3.9c.

### 3.3.4 Predicted Arrivals for Production Mode

Since we do not have reliable routine picks for most of the waveform data, we can only rely on predicted arrival times as initial picks. This represents the standard case for most regional data sets. In a first run, we used the minimum 1-D model of *Solarino et al.* (1997) and catalog locations to calculate predict P-arrivals. Figure 3.10a shows the differences between calculated predicted arrivals and corresponding reference picks ( $tP_{pred} - tP_{ref}$ ) for reference picks identified as first-arrivals (Pg, Pn, P1) and usable quality class. The differences show a broad scatter and the mean indicates a systematic bias of predicted arrival times. Since the model

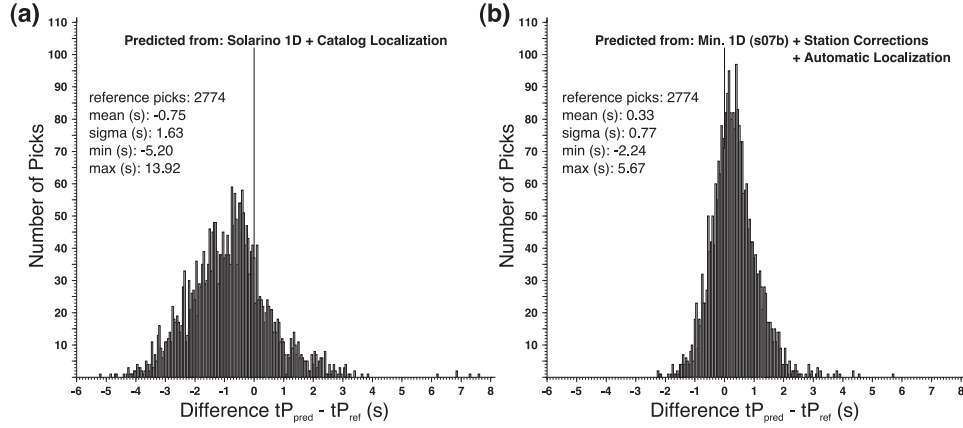


**Figure 3.10:** Difference between predicted and corresponding reference hand picks ( $tP_{pred} - tP_{ref}$ ). **(a)** Predicted arrival times calculated from the minimum 1-D model of *Solarino et al.* (1997) (obtained from a different data set) and catalog locations. **(b)** Predicted arrival times calculated with a true minimum 1-D model (specifically calculated for our data set) and usage of corresponding station corrections. Localizations used to derive predicted arrival times are based on unweighted automatic picks and are relocated in the same minimum 1-D model. Usage of a minimum 1-D model with station corrections and relocated hypocenters significantly improves the accuracy of predicted arrival times.

of *Solarino et al.* (1997) denotes a minimum for a similar area but a largely different data set of local earthquakes, the model predicts systematically biased arrival times indicated by the negative mean. The broad scatter in predicted arrivals requires the use of wide safety gaps, to ensure that the actual phase can be reached by the signal window  $SNW$ . Safety gaps of e.g.,  $\pm 4.0$  s result in a large number of mispicks, especially in the range of the crossover distance between Pn and Pg. To overcome this problem, the accuracy of predicted arrival times had to be improved.

In our approach, we first inverted the reference data set to derive a coarse regional minimum 1-D model as described by *Kissling* (1988). The model of *Solarino et al.*

(1997) was used as initial model for the inversion. To improve and stabilize the station corrections of the minimum 1-D model, we extended the reference data set by using unweighted automatic picks. The low quality automatic picks were derived from the pure Baer-Kradolfer picker applied without any quality weighting to the complete data set of 1533 events. Hypocenters were relocated in the coarse minimum 1-D model and obvious mispicks were identified by residuals  $|\delta t| > 2.0$  s. High quality events (azimuthal gap  $< 100^\circ$ , minimum number of observations = 20, rms  $\leq 0.8$  s) from this data set were combined with the reference data. In this combined data set, we kept the original weights for the reference picks and weighted all automatic picks by only 25% to account for the lower quality. The combined phase data were used to derive the updated regional minimum 1-D model *s07b* and the corresponding station corrections by simultaneous inversion. The unweighted automatic picks were used to relocate all events within *s07b* (station corrections applied). Again, we removed all picks associated with residuals  $|\delta t| > 2.0$  s and rejected low quality events with azimuthal gap  $> 180^\circ$ , minimum number of observations  $< 6$ , and rms  $> 1.0$  s. The remaining 930 events were selected for re-picking with the calibrated MPX in production stage. Figure 3.10b shows the differences between predicted arrivals from model *s07b* (applied station corrections and relocated hypocenters based on unweighted automatic picks) and reference picks. The standard deviation is reduced by a factor of two and the significantly higher accuracy of the minimum 1-D model allows the use of narrower safety gaps.

#### 3.3.5 Results of MPX Production Mode

As previously mentioned, we split the data set into two distance ranges and apply different sets of corresponding Fisher coefficients to each subset. Waveforms associated with distances  $\Delta \leq 20$  km are LP filtered (15 Hz, 2<sup>nd</sup> order) to remove possible high-frequency precursors generated by acausal anti-alias filters. For  $20 < \Delta < 100$  km we apply a HP filtered (1 Hz, 2<sup>nd</sup> order) to remove possible low-frequency noise. The same configuration of filters was used for the calibration of the weighting scheme shown in Figure 3.8.

Non-seismic signals like spikes and step-functions (caused e.g., by problems in transmission) are commonly present in large heterogeneous data sets. The identification of such signals is crucial for reliable automatic picking, since they are often misinterpreted as high-quality arrivals by the picking algorithms. To avoid mispicks due to quality problems present in the data set, we perform an automatic quality check around the predicted arrival time in a pre-picking stage and reject obvious low-quality seismograms. A de-spiking routine was used to detect and remove possible spikes. Steps in the seismograms caused by data gaps filled with zeros are identified by an running average detector applied around the predicted arrival time.

The final result of the production mode is summarized in Table 3.3. The left part shows the number of automatic picks for each class after merging picks from all 930 events at both distance ranges. These picks were used to relocate all events

in the minimum 1-D model *s07b*. After rejecting low-quality events with an az-

2F All Events (930)			2F Locat. Events (551)			1F Locat. Events (356)		
Class	#	Auto-Picks	Class	#	Auto-Picks	Class	#	Auto-Picks
0		5793	0		5046	0		4746
1		5242	1		4340	1		2513
2		1191	2		906	2		-
3		1131	3		862	3		-
$\Sigma$		13357	$\Sigma$		11154	$\Sigma$		7259

**Table 3.3:** Results of MPX Production Mode. Left: Automatic picks derived from all 930 events used for production mode with two distance-dependant sets of Fisher coefficients (2F). Middle: Corresponding automatic picks left after removal of low-quality events ( $\text{gap} > 180^\circ$  and  $N_{obs} < 8$ ). Right: Automatic picks of locatable events using only one set of robust Fisher coefficients for the entire distance range (1F).

imuthal  $\text{gap} > 180^\circ$  or less than 8 observations, 551 events were left. The middle part of Table 3.3 summarizes the number of automatic picks corresponding to the 551 events. The right part of Table 3.3 shows the results if only one set of robust Fisher coefficients (1F) for the entire distance range is used. In this production mode we used the Fisher coefficients listed in Table A.2. By splitting the data set into two distance ranges, we gain about 200 events and 4000 additional phases. Finally, we merged the automatic picks with the extended reference data set (hand picks of 49 events). If an automatic and reference pick is available for the same observation, we replace the automatic by the reference pick, since its weighting is expected to be less conservative. The combined data set is then relocated in minimum 1-D model *s07b* one more time. To identify gross mispicks, travel-time residuals of  $|\delta t| > 0.8$  s (twice the error of lowest usable class) were visually cross-checked against waveforms in a semi-automatic procedure. From 1373 cross-checked picks, 103 are identified as mispicks. After removing identified mispicks from the data set and a last check of event quality ( $\text{gap} < 180^\circ$ ,  $N_{obs} \geq 8$ ) 552 events remain. Table 3.4 summarizes the final high-quality P-phase data set for the Alpine region. The

Quality	Class	$qP$	Error $\varepsilon_{qP}$ (s)	# MPX+REF Picks
	0		$\pm 0.050$	5387
	1		$\pm 0.100$	4875
	2		$\pm 0.200$	1822
	3		$\pm 0.400$	1225
	$\Sigma$			13309

**Table 3.4:** Final high-quality P-phase data set for the Alpine region consisting of MPX automatic picks and reference hand picks of 552 events.

average picking error can be estimated from the number of picks for each class and the error interval of each class. For our final data set we obtain an average picking

error of  $\varepsilon_t \approx 0.12$  s with maximum errors not exceeding 0.8 s. The corresponding ray-coverage for the final data set is shown in Figure 3.11. Reference events used for calibration of MPX are indicated by white stars and gray stars denote additional reference events.

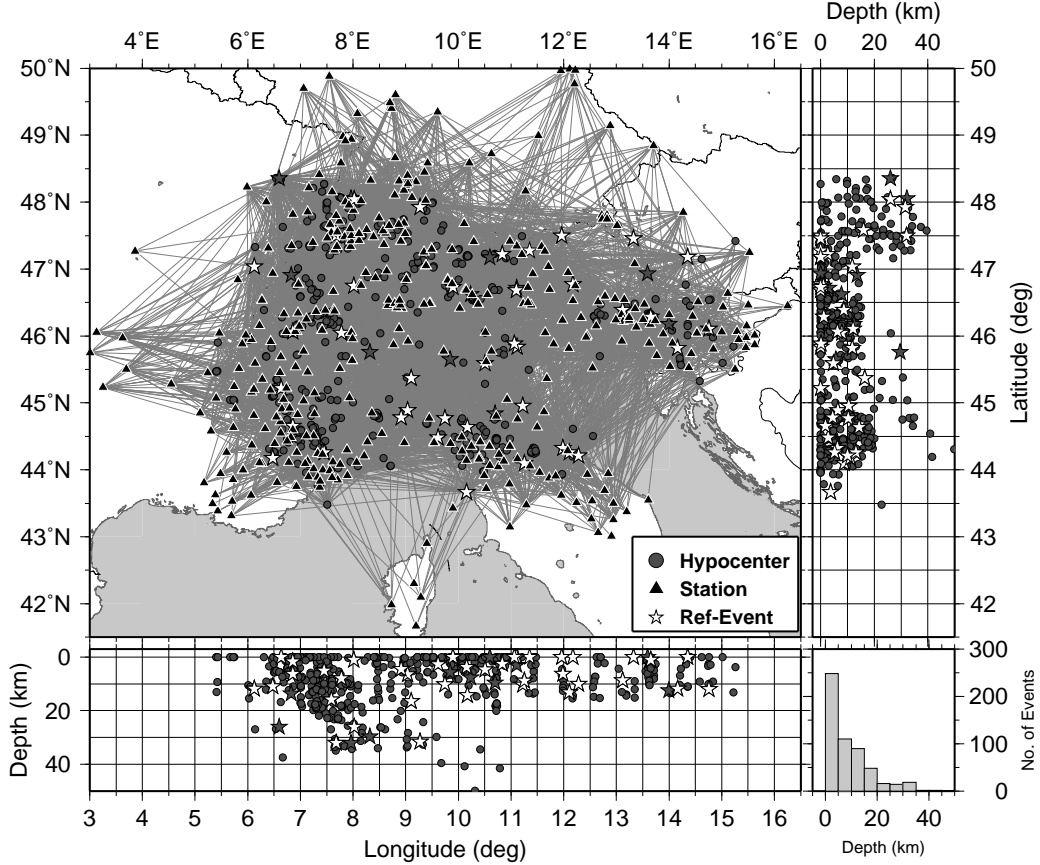


**Figure 3.11:** Ray-coverage of the combined high-quality P-data set consisting of 552 local earthquakes. Triangles denote stations, circles represent hypocenters, white stars indicate locations of reference events used for calibration of MPX (similar to Fig. 3.4), and gray stars denote additional reference events. Hypocenters correspond to locations in minimum 1-D model *s12c*.

## 3.4 Local Source Tomography with Highly Consistent Data Set

The combined arrival times of the 552 well located events are used for local earthquake tomography. According to the procedure recommended by *Kissling et al.* (1994) we determine a regional minimum 1-D model, which will be used as initial model for the 3-D inversion.

### 3.4.1 Consistent Minimum 1-D Model for the Alpine Region

The regional minimum 1-D model is derived in an iterative inversion procedure as described by *Kissling* (1988). The initial model for the inversion is the preliminary model *s07b*, which is based on unweighted automatic picks and reference hand picks. The model is indicated by dashed line in Figure 3.12. The final high-quality regional minimum 1-D model *s12c*, based on quality-weighted automatic and reference picks, agrees quite well with *s07b* for the upper and mid crust. In the depth range of the lower crust to upper mantle (35-50 km) *s12c* indicates higher velocities. The lower velocities of *s07b* might result from the large number of delayed picks present in low-quality automatic picks. In such a procedure, weak

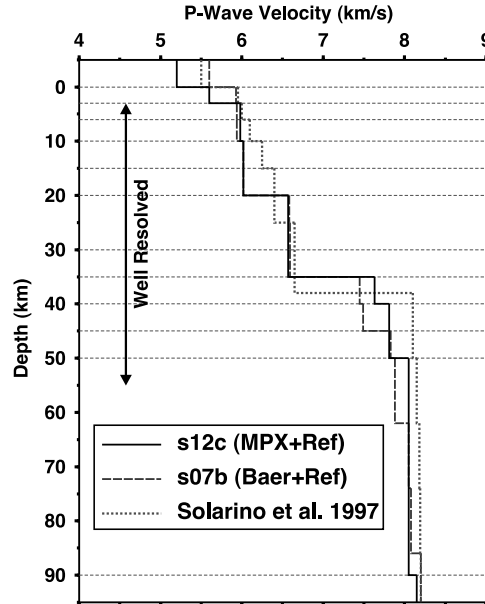


**Figure 3.12:** Different (minimum) 1-D Models for Alpine region. Dotted line indicates the regional model of *Solarino et al.* (1997) derived from merged phase data. Higher velocities within the upper and mid-crust reflect the influence of the Ivrea body in the western Alps. Model *s07b* (dashed line) is based on unweighted automatic picks mixed with reference hand picks. Model *s12c* is derived from MPX quality-weighted automatic picks mixed with reference hand picks.

Pn phases are often missed and later phases are therefore misinterpreted as first-arrivals, leading to lower velocities.

Figure 3.13 presents the station corrections of the minimum 1-D model *s12c*. Station corrections express deviations from the 1-D model due to 3-D structure with respect to a reference station (e.g., *Kissling*, 1988). The correction of the reference station is defined as zero. Negative corrections (circles) indicate higher velocities compared to reference station and positive corrections (crosses) indicate lower velocities. Corrections in a large regional model usually represent a mixture of site effects close to the surface (e.g., sediments) and Moho topography (especially for stations located at the edge of the network). Therefore, the detailed interpretation

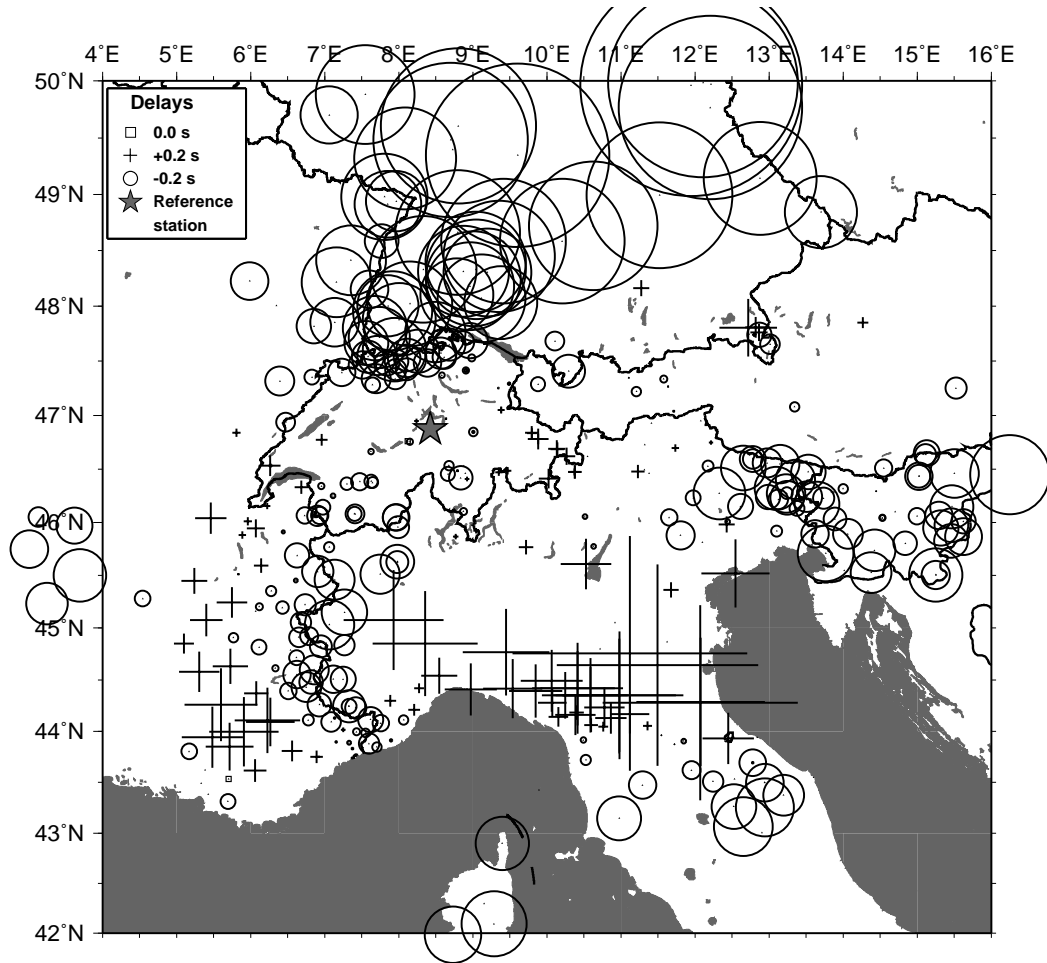


**Figure 3.13:** Station corrections of minimum 1-D model *s12c* for stations with at least 5 observations. Reference station BNALP is represented by a gray star. Negative corrections (circles) indicate higher velocities compared to reference station. Positive corrections (crosses) indicate lower velocities. Symbol size corresponds to correction amplitude.

can become ambiguous whereas the general pattern of corrections is an indication of consistency of the phase data. The corrections of model *s12c* denote a very consistent and sensible distribution for the entire region. Station BNALP in the central swiss Alps was chosen as reference station. As expected, stations at the edge of the network dominated by mantle phases from a limited range of back-azimuths denote negative corrections. This effect can add up to several seconds in places like southern Germany, where the Moho is much shallower than the average value of 35 km indicated in model *s12c*. In addition, negative delays are observed throughout the western Alps, in the area of the Ivrea body, parts of the south-eastern Alps, and for massifs like the Black Forest. Positive delays associated with reduced velocities are mainly observed in the Provence area, within the Apennine Mountains, and throughout the Po plain. Station corrections in Switzerland and surrounding areas agree very well with the results obtained by *Husen et al.* (2003).

### 3.4.2 Preliminary 3-D Results and Comparison with ISC Routine Phase Data

We inverted the high-quality data set of 552 events for 3-D structure using the SIMULPS14 code (e.g., *Thurber*, 1983; *Eberhart-Phillips and Michael*, 1993; *Hasslinger and Kissling*, 2001). Initial hypocenters and P-wave velocities were taken from *s12c*. The horizontal spacing of inversion nodes is 25 x 25 km and the vertical distance between node planes is 15 km. In-between these nodes, velocities are interpolated by the inversion code. The rather coarse parameterization turned out to be the finest possible parameterization without showing strongly heterogeneous ray coverage and results in a uniform resolution for major parts of the Alpine lithosphere. The left column of Figure 3.14 shows horizontal cross sections through the preliminary 3-D model at two different depths.

The Bulletin of the ISC represents the largest compilation of routine phase picks reported by seismological agencies around the globe and therefore allows the direct comparison between routine data and re-picked data at regional scales. All events extracted from the ISC Bulletin (about 10'000 between 1996 and 2007) were relocated in the minimum 1-D model *s12c* prior to the 3-D inversion. As demonstrated e.g., by *Grand* (1990), *Spakman et al.* (1993), or *Röhm et al.* (2000), ISC phase data contain a considerable amount of random and systematic errors up to the order of minutes. Therefore, P-phases indicating travel-time residuals  $|\delta| > 5.0$  s are considered as outliers and were removed from the data set. Subsequently, all remaining phases were used to relocate the events again. Finally we selected well-locatable events with at least 10 P-phase observations and an azimuthal gap  $< 150^\circ$ . The remaining data set consists of about 95'000 P-phases from 3400 events in the Alpine region. Hence, the ISC data set includes about six times more events and about seven times more phases than our re-picked data set. Based on the study of *Röhm et al.* (2000) we estimate the minimum average timing error of the filtered data set to be in the order of 0.3 s.

We used the same initial model and the same inversion parameters (damping value



### 3.4 LOCAL SOURCE TOMOGRAPHY WITH HIGHLY CONSISTENT DATA SET

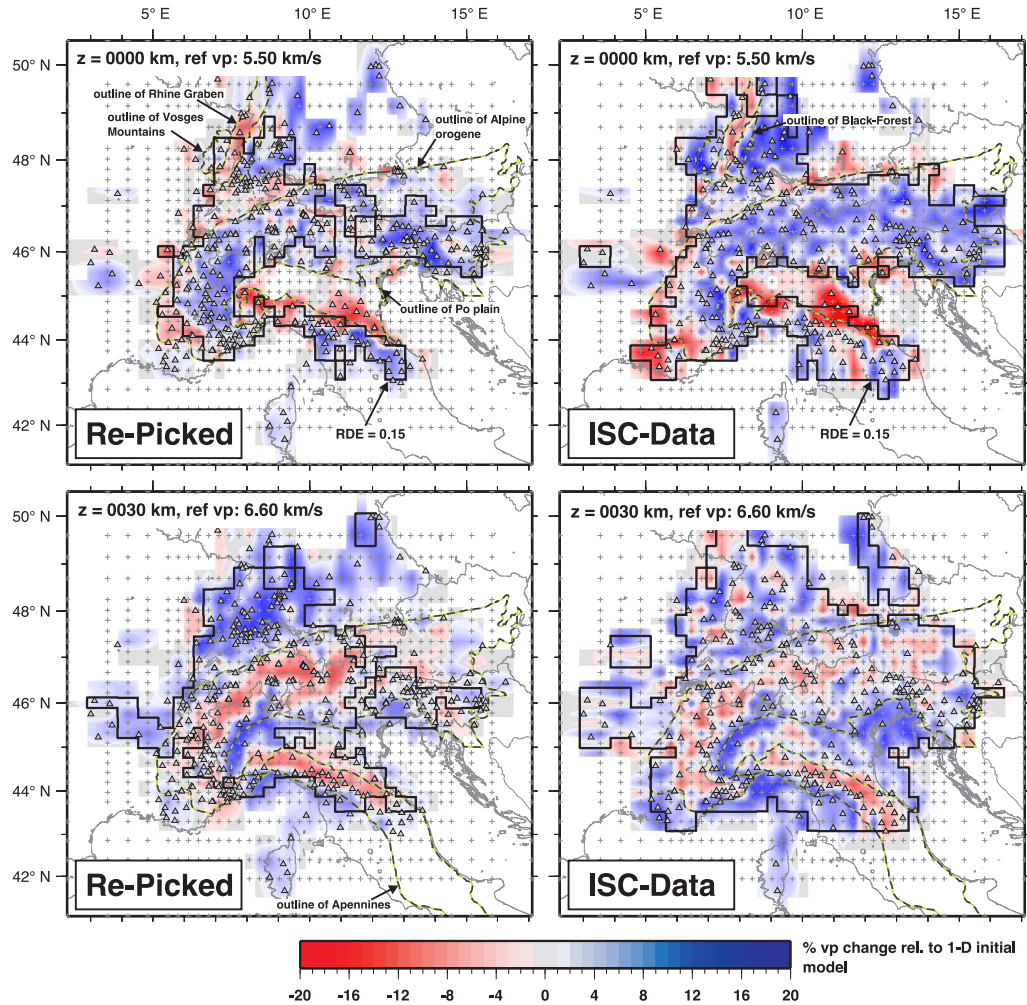


**Figure 3.14:** Comparison of tomographic images based on high-quality re-picked phase data (left column, total of 13'300 P-phases with an average estimated timing error of 0.12 s) and standard ISC phase data (right column, total of 95'000 P-phases with an average estimated timing error of at least 0.3 s) at 0 and 30 km depth. The  $v_P$  velocity structure is shown as percentage change relative to the 1-D initial reference model (same for re-picked and ISC). Bold black contours outline resolution diagonal element (RDE) of 0.15 and green-black dashed lines outline major tectonic units as indicated. Triangles denote location of stations and crosses denote inversion grid nodes. Note how the tomographic image of 30 km depth obtained from re-picked phase data is much more reliable in the well-resolved region - showing much fewer single cell anomalies of checkerboard type - while for very shallow depth, the performance of the two data sets is virtually the same with the larger ISC data set resolving a significantly larger region.

100, five iterations, RKP-raytracing) for the 3-D inversion of the ISC data set as we used for the re-picked data. The right column of Figure 3.14 shows the corresponding cross sections through the ISC based 3-D model. The bold black contours in Figure 3.14 outline the resolution diagonal element (RDE) of 0.15, which is used as a first order assessment of the solution quality in both models.

The uppermost part of the model seems to be rather well resolved by ISC data set (Fig. 3.14, 0 km depth) due to the higher data coverage compared to the re-picked data set (indicated by enlarged area of  $RDE = 0.15$  in the ISC data). Tectonic units like massifs (Black-Forest, Vosges mountains), sedimentary deposits (southern Rhine Graben, Po plain, partly Molasse basin), and the Alpine orogen are clearly resolved by the ISC data. The higher noise level of the ISC data becomes obvious in 30 km depth (Fig. 3.14), where the crustal root of the Alps and the northern Apennines are much more clearly imaged by the re-picked data set. The tomographic image derived from the ISC data shows only few coherent structures and, in addition, it denotes a multitude of checkerboard type single cell anomalies where a smooth P-wave structure is expected. The reduced resolution of the ISC data in the deeper part of the model might result from the increased number of inconsistently picked or misidentified regional Pn phases.

Considering the higher noise level of the ISC data, stronger damping might be in order and this would likely reduce the amplitude of single cell anomalies that lead to the checkerboard appearance. This, however, would obviously also reduce the amplitude of the fair and well resolved anomalies making any interpretation of deep structure such as the Alpine crustal root even more difficult. In conclusion, ISC data is of significantly lower quality than our compiled and selected local earthquake data set and higher quality data leads to better resolution. Neither of these conclusions comes as a surprise.

### 3.4.3 Consistency of Re-Picked Data Set

The consistency of the preliminary 3-D model is demonstrated in Figure 3.15. The  $v_P = 7.25$  km/s iso-surface (gray color code) of the 3-D model is compared with the Moho topography from Controlled Source Seismology (CSS) modeling of *Waldhauser et al.* (1998). Topography of the CSS model is indicated as colored contour lines, representing European-, Adriatic-, and Ligurian-Moho. The dashed line in Figure 3.15 outlines the well-resolved parts of the 3-D model. Poorly resolved or unresolved areas are masked. The tomographic model agrees very well with the CSS model for the major parts of the region. We observe steep gradients in the western Alps and a wider trough in the eastern Alps. Crustal roots below the Alps and the Apennines are pronounced features. Furthermore, we compared the tomographic model with the recent receiver functions study of *Lombardi et al.* (2008). The color of the triangles in Figure 3.15 represent Moho depth derived from a grid-search technique. Results of both methods show a high degree of agreement.

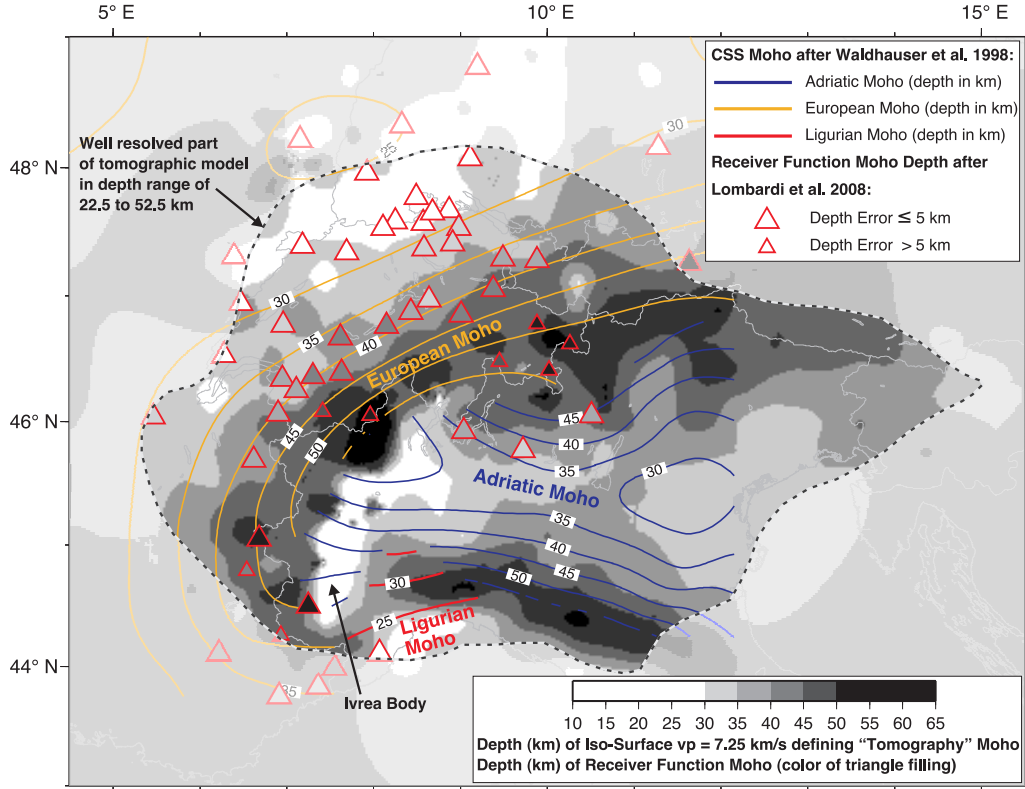


**Figure 3.15:** Moho topography derived from iso-surface of  $v_P = 7.25$  km/s in our preliminary 3-D model. Contour lines indicate Alpine Moho derived from CSS after Waldhauser et al. (1998). Color code of triangles denote Moho depth from receiver function study of Lombardi et al. (2008). The dashed line outlines the well-resolved parts of the 3-D model.

### 3.5 Discussion and Conclusion

Compilation of high-quality phase data for regional tomography typically requires the re-picking of seismograms, since routine picks contain a large number of mis-picks. In addition, error assessment of merged routine data is usually inconsistent. A uniform assessment of phase identification and timing uncertainty, however, is essential for travel-time inversion. The routine hand picking procedure presented in this work leads to highly consistent phase picks and allows a flexible quality weighting. Since the error intervals of the onsets (defined by  $t_E$  and  $t_L$ ) are explicitly picked, the weighting scheme can be adjusted posterior to the picking, if necessary.

Considering the amount of waveform data necessary for regional studies, hand picking does not represent a feasible alternative to automated re-picking approaches. The MPX picking system provides quality-weighted automatic picks with an accuracy and consistency comparable to manually picked data. Automatic quality classification achieved by the MDA leads to excellent assessment for picks at local distances (Pg phases exclusively) but only a satisfactory assessment for mixed picks at local to regional distances. By splitting the data set into two distance

ranges and by using a regional minimum 1-D model, we achieve a first order discrimination between Pg and Pn phases. Therefore, different settings for MPX (Fisher coefficients and waveform filters) have to be used for the two subsets. For reliably picking Pn phases, a more conservative weighting scheme avoids misidentification of later arrivals, though the conservative weighting results in a smaller recovery rate of medium quality picks. The separate treatment of Pg and Pn phases during automated picking and subsequent merging of picked phases leads to a significantly increased number of automatic picks of high overall assessment quality. The good agreement between the reference and these automatic picks indicates that the phase association is correct for the majority of picks.

To further improve the performance of MPX, an automatic assessment of the various phase onsets will have to be included in the picking algorithm, since the MDA cannot account for it directly. As any other such algorithms, MPX picks the earliest well-defined signal as the first arriving phase. However, beyond the crossover distance the first arriving Pn is often less well-defined than secondary arriving phases such as Pg or PmP. To correctly identify the picked phase multiple picking approaches, as suggested by *Bai and Kennett* (2000), have to be considered. They propose the use of attributes provided by short-term to long-term average ratios, autoregressive modeling and polarization analysis to pick and identify series of P- and S-phases.

The iterative use of an automatic picker and minimum 1-D models are necessary to obtain consistent sets of regional phase data, since the accuracy of the automatic picks strongly depends on the reliability of predicted arrival times. Particularly for locations in-between networks, catalog locations provided by agencies can differ significantly from the true location. In addition, 3-D structure as expected in an orogen region requires the use of station corrections.

The combined data set of reference picks and quality-weighted automatic picks suggests an average picking error of about 0.12 s. In combination with a 3-D model parametrization of 25 x 25 x 15 km, the average accuracy allows the resolution of at least 5% P-wave perturbations in the mid crust. The 1-D inversion of the combined data leads to a robust regional minimum 1-D model with rather consistent station corrections, reflecting subsurface geology and Moho topography of the Alpine region. Results of the preliminary 3-D inversion indicate satisfactory lateral resolution for about 80% of the Alpine arc. The resolution in depth encompasses the entire crust and the uppermost mantle up to depths of 50 to 60 km for the most parts of the Alps. The Moho topography derived from the iso-surface of  $v_P = 7.25$  km/s in the preliminary 3-D model agrees very well with models from CSS and recent receiver function studies.

The comparison between re-picked phase data and routine picks extracted from the ISC Bulletin clearly demonstrates the impact of a high-quality data set on the resolution and reliability of the tomographic image. The resolution of lower crustal structures with local earthquake tomography requires a consistently picked data set. Inconsistencies in picking and the lack of a common quality assessment cannot be compensated by an increased quantity of phase data.

## Acknowledgments

We are grateful to the following networks who provided us with digital recordings and bulletin data used in this study: BED (Ludwig-Maximilians-University, Munich), GERESS (Hannover), GRSN/SZGRF (Erlangen), INGV/MEDNET (Rome), Landes-Erdbebendienst (Freiburg i. B.), OGS/CRS (Udine/Trieste), RENASS (Strasbourg), RSNI/DipTeris (Genova), SED (Zurich), SISMALP (Grenoble), SNRS (Ljubljana), TGRS (Nice), ZAMG (Vienna). Furthermore, we thank the ISC for their tremendous effort in collecting arrival times in the ISC Bulletin. The reference picking was performed with the *SeismicHandler* package (*Stammer, 1993*). Most of the plots were generated using the Generic Mapping Tool by *Wessel and Smith (1995)*. We thank C. Rowe and F. Waldhauser for their constructive reviews, and Manfred Baer and Ben Edwards for their helpful comments and proof-reading. This research was supported by the Swiss National Fund grant 200021-103698.



## Chapter 4

# High Resolution 3-D P-Wave Model of the Alpine Crust

T. Diehl, S. Husen, E. Kissling and N. Deichmann

## Abstract

The 3-D P-wave velocity structure of the Alpine crust has been determined from local earthquake tomography using a set of high-quality travel-time data. The application of an algorithm combining accurate phase picking with an automated quality assessment allowed the re-picking of first arriving P-phases from the original seismograms. The quality and quantity of the re-picked phase data used in this study allows the 3-D imaging of large parts of the Alpine lithosphere between 0 and 60 km depth. Our model represents a major improvement in terms of reliability and resolution compared to any previous regional tomographic studies of the Alpine crust. First order anomalies like crust-mantle boundary (Moho) and the Ivrea body in the Western Alps are well resolved and in good agreement with previous studies. In addition, several (consistent) small-scale anomalies are visible in the tomographic image. A clear continuation of the lower European crust beneath the Adriatic Moho in the Central Alps is not observed in our results. The absence of such a signature may indicate the eclogitization of the subducted European lower crust in the Central Alps.

## 4.1 Introduction

The Alpine arc results from continental collision between plates or micro plates of Eurasian, African, and Iberian origin. The orogene reveals substantial differences between Western, Central, and Eastern Alps in terms of crustal and upper mantle structure. Based on controlled-source seismic reflection and refraction profiles (see e.g., *Blundell et al.*, 1992; *Pfiffner et al.*, 1997; *Roure et al.*, 1990; *Transalp Working Group*, 2002) several large-scale geophysical-geological transects of the Alpine crust were recently compiled (*Schmid and Kissling*, 2000; *Schmid et al.*, 2004). The locations of the most prominent transects (ECORS-CROP, NFP-20 West, NFP-20 East/EGT, and TRANSALP) are indicated in the tectonic sketch map of Figure 4.1.

In the Western Alps the European Moho dips eastwards and continental European lithosphere is subducted east to SE beneath the Adriatic microplate as revealed by high-resolution teleseismic tomography of *Lippitsch et al.* (2003). The Ivrea body located at the western end of the Po plain (Fig. 4.1) acted as a buttress in the collision process of the European and Adriatic plates and caused the back-thrusting and doubling of the European lower crust under the Western Alps (*Schmid and Kissling*, 2000).

In the Central Alps the structure of the lower crustal wedge is reversed. Adriatic lower crust indents the European middle crust as described by *Ye et al.* (1995) and *Schmid and Kissling* (2000). According to models of *Schmid and Kissling* (2000) and *Kissling et al.* (2006) lower European crust and European lithosphere are subducted southward beneath the Adriatic plate.

The upper mantle structure in the Eastern Alps derived from teleseismic tomography of *Lippitsch et al.* (2003) indicates a change in the subduction regime between



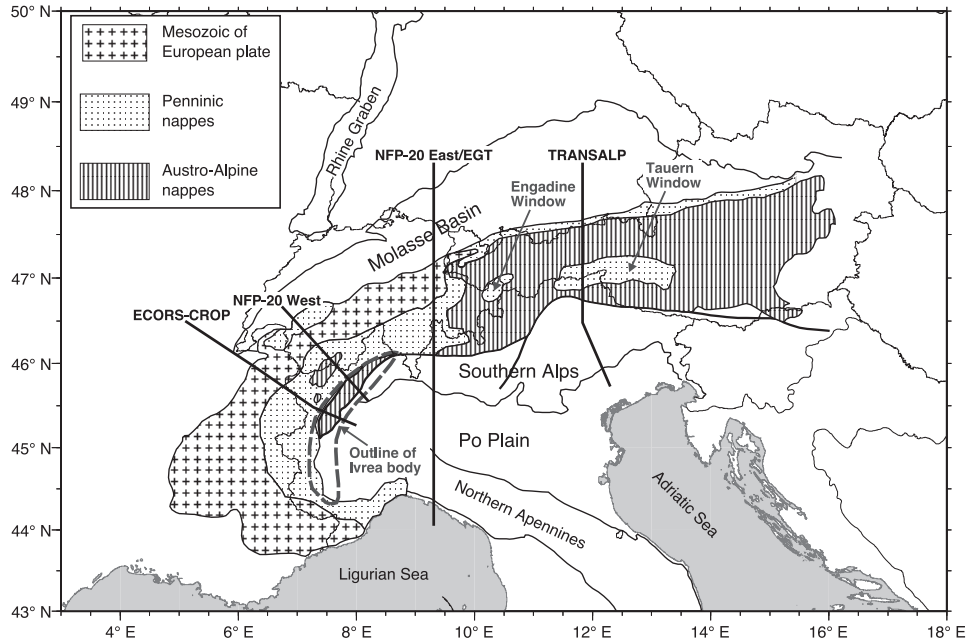


**Figure 4.1:** Tectonic sketch map of the Alpine region (modified from *Carpena and Caby* 1984) with locations of four crustal geophysical transects ECORS-CROP, NFP-20 West, NFP-20 East (EGT), and TRANSALP. The gray dashed contour outlines the Ivrea geophysical body.

Central and Eastern Alps in the realm of the Tauern Window (Fig. 4.1). The subducted lower lithosphere in the Eastern Alps is part of the Adriatic lithosphere and dips NNE beneath the European plate. In addition, differences in seismicity are observed between Central and Western Alps as described by *Deichmann and Baer* (1990), *Sue et al.* (1999), and *Schmid and Kissling* (2000). The lower crustal wedge beneath the Central Alps appears aseismic whereas the lower crustal wedge is seismically active beneath the Western Alps.

The seismic velocity structure of the lower crust and across the lithosphere-asthenosphere boundary represents a key parameter to integrate these differences into improved tectonic models. Independent models of P- and S-wave velocities can provide unique information on composition and physical state of the lithosphere (fluid content, temperature, etc.), since they allow the comparison with petrological measurements. Existing models of the Alpine crust as summarized e.g., in *Schmid and Kissling* (2000), *Schmid et al.* (2004), and *Kissling et al.* (2006) are mainly based on results from Controlled Source Seismology (CSS). In terms of seismic velocities, these models are poorly resolved in the depth ranges of the lower crust. Likewise, teleseismic tomography is not appropriate to resolve crustal structure due to the sub-vertical incidence of rays. In addition, teleseismic usually provides only relative velocity models.

Local Earthquake Tomography (LET) can be used to derive three-dimensional velocity images of the lithosphere with a spatial resolution up to a few tens of kilometers. Recent tomographic studies in the Alps, however, were restricted to image mostly the upper crust due to the limited aperture of the seismic network

used (e.g., *Solarino et al.*, 1997b; *Eva et al.*, 2001; *Paul et al.*, 2001; *Husen et al.*, 2003). Furthermore, the resolution of existing models often suffers from low data quality, especially if routine phase data was merged from several networks (e.g., *Solarino et al.*, 1997). The impact of a high-quality data set on the resolution of the tomographic image was demonstrated by *Diehl et al.* (2008). Recent developments in phase picking algorithms (e.g., *Aldersons*, 2004) allow for automated re-picking of large waveform data sets with a high degree of consistency. These new tools automatically assign an observation weight to each phase to quantify the uncertainty of the timing. *Di Stefano et al.* (2006) applied such a procedure to the Italian national network and improved on existing regional 3-D models for the lithosphere system beneath Italy (*Di Stefano*, 2005). A similar automated approach was used by *Diehl et al.* (2008), who re-picked P-phase data of local earthquakes in the greater Alpine region.

In this article we present a consistent 3-D P-wave velocity model of the Alpine crust derived from the inversion of the high-quality phase data set of *Diehl et al.* (2008). Besides the lower crustal seismic velocities and the Moho geometry, the target area of this study is the P-velocity structure in the suture zone regions beneath the Alps.

## 4.2 Local Earthquake Data from Automated Phase Picking

The arrival-time data set used for local earthquake tomography was derived from automated re-picking of waveform data as described in *Diehl et al.* (2008). Waveforms from about 1500 events with  $M_l \geq 2.5$  recorded between 1996 and 2007 were compiled from 13 national and regional networks. The MPX software of *Aldersons* (2004) was used for consistent and quality weighted re-picking of first arriving P-phases. Our final data set comprises more than 13'000 phases from 552 well locatable local earthquakes with a minimum number of 8 observations per event and azimuthal gap  $< 180^\circ$ . Epicentral distances of Pg and Pn phases in this data set vary between 1 km and about 700 km. The resulting ray-coverage and the station configuration is shown in Figure 4.2, where hypocenters correspond to the location in the regional minimum 1-D model of *Diehl et al.* (2008).

Table 4.1 summarizes the quality weighting scheme used for the automated picking of P-phases. The highest quality class 0 is associated with an error interval of  $\pm 0.05$  s and the lowest quality class used for 3-D tomography corresponds to an uncertainty of  $\pm 0.4$  s. As demonstrated by *Diehl et al.* (2008) the average picking error of the data set is about 0.12 s and no significant outlier picks (misidentified phases etc.) are included. The quality of this data set represents a major improvement in terms of accuracy and consistency compared to any compilation based on routine picks (*Diehl et al.*, 2008).

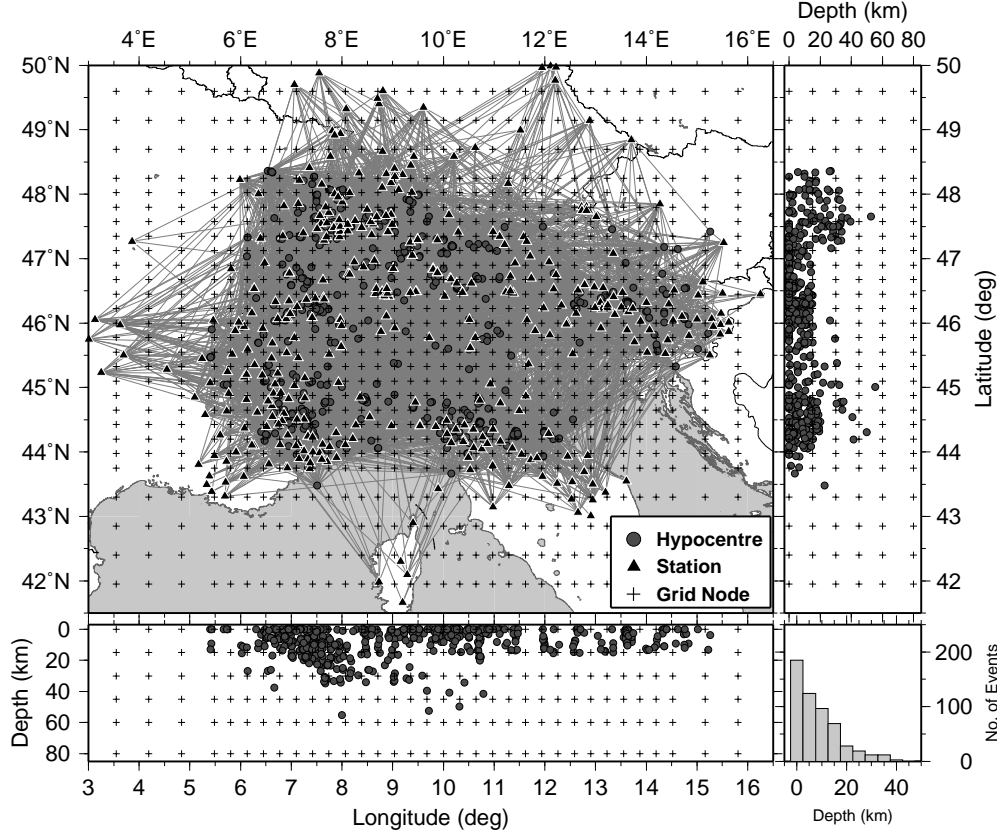


**Figure 4.2:** Ray-coverage of 552 earthquakes selected for 3-D local earthquake tomography of the Alpine region. Triangles denote location of 391 seismic stations. Hypocenters (grey circles) correspond to the location in the minimum 1-D model of *Diehl et al.* (2008). Crosses mark position of inversion grid nodes of the 3-D model.

Quality class	Error $\varepsilon_{qP}$ (s)	Weight (%)	# Observations
0	$\pm 0.050$	100	5387
1	$\pm 0.100$	50	4875
2	$\pm 0.200$	25	1822
3	$\pm 0.400$	12.5	1225
4	$> 0.400$	0.0	not considered

**Table 4.1:** Weight assignments and associated uncertainty intervals used for the automated re-picking of P-phases.

### 4.3 Method

We used the well-established SIMULPS14 software (*Thurber, 1983; Eberhart-Phillips, 1990*), extended by a full 3-D ray shooting technique (*Haslinger and Kissling, 2001*), to invert simultaneously for hypocenter locations and 3-D P-wave velocity structure. Since SIMULPS14 solves the non-linear, coupled hypocenter-velocity problem by a linearized, iterative, damped, least-square approach, the solution depends on the choice of initial model (velocities, hypocenters), damping values, and model parameterization (see *Kissling et al., 2001*). SIMULPS14 includes a seismic grid (representing the 3-D velocity structure) and a forward grid used by the 3-D shooting ray-tracer as described by *Kissling et al. (2001)*. In the seismic grid, seismic velocities are linearly interpolated between grid nodes.

As suggested by *Kissling et al. (1994)*, hypocenters and P-wave velocities from the minimum 1-D model of *Diehl et al. (2008)* are used as initial values. The parameterization of the 3-D seismic grid is chosen to guarantee uniform and fair resolution in most parts of the model volume. The final parameterization is selected from several single-iteration inversions for different model parameterizations similar to the procedure described in *Husen et al. (2003)*. The rather coarse grid of 25 x 25 km (horizontal) x 15 km (vertical) for the central part of the model turned out to be the finest possible model parameterization without showing a strongly heterogeneous ray coverage. The corresponding grid nodes of the final model parameterization are indicated as crosses in Figure 4.2 and the initial P-wave velocities are given in Table 4.2.

Considering the trade-off between model parameterization, minimum resolvable velocity perturbation, and average data error, the chose grid represents an appro-

Depth of Grid Plain (km)	$v_P$ (km/s)
0	5.50
15	6.10
30	6.60
45	7.70
60	8.00
80	8.10

**Table 4.2:** Initial P-wave velocities at nodes of 3-D gradient model. Velocities are based on minimum 1-D model of *Diehl et al. (2008)*.

priate parameterization to reliably resolve lower crustal structure with at least 5% velocity perturbation, assuming  $v_P = 6.5$  km/s, an average ray length of  $\Delta x = 25$  km, and the given data error of 0.12 s.

The appropriate damping value was selected empirically from a series of inversions similar to the procedure proposed by *Eberhart-Phillips (1986)*. The trade-off curves were calculated for a large range of damping values (1, 10, 100, 1000, 10'000) and, in contrast to single-loop inversions as originally suggested by *Eberhart-Phillips (1986)*, seven iterations were performed for each damping value. The multi-loop

procedure provides additional information on the behavior of trade-off curves for increasing model variance and also allows a decision on the maximum number of iterations reasonable for a chosen damping value. Data variance is compared against model variance for each iteration and damping value as shown in Figure 4.3a. The preferred damping value is associated with the best compromise between data misfit reduction and model variance. As demonstrated in Figure 4.3a, the damping value 100 leads to a high data reduction with a moderate model variance for our data set and model parameterization. Lower damping values (e.g. 10) require more iterations steps to achieve similar data reduction and lead to a large model variance (complex models). Figure 4.3b shows the reduction of the weighted RMS after each iteration using an optimal damping value of 100. After iteration 5

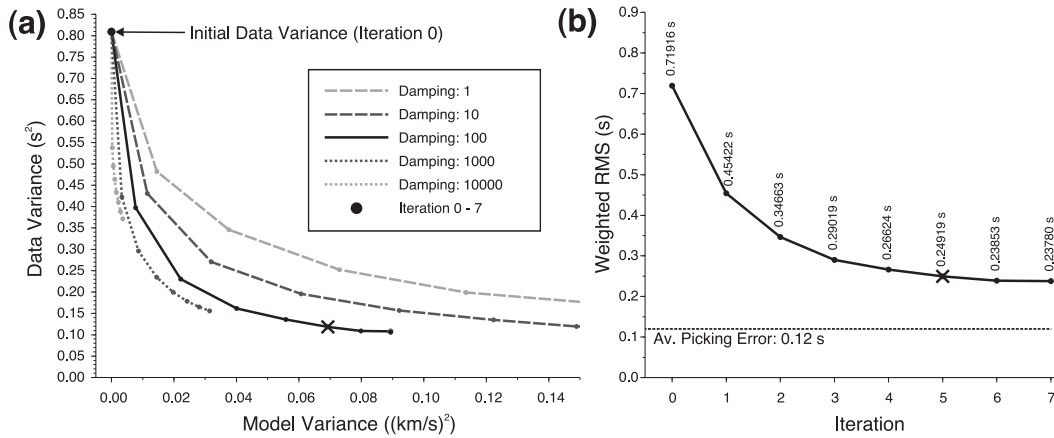


**Figure 4.3:** Trade-off curves to determine appropriate damping for inversion and the number of necessary iteration steps. **(a)** Data misfit versus model variance. Each curve represents trade-off for different damping values over 7 iterations. The optimum misfit reduction is achieved for damping value 100 after 5 iterations (cross). **(b)** Reduction of weighted RMS after each iteration using a damping value of 100. After iteration 5 (cross) the improvement becomes insignificant.

the weighted RMS is reduced by 65% compared to the initial weighted RMS. Further iterations lead to insignificant improvement of the data fit and therefore the inversion is terminated after 5 iterations (cross in Fig. 4.3). The fact that the final RMS is still remarkably larger than the average picking error of 0.12 s indicates that the inversion was not able to resolve small scale anomalies due to the chosen relatively coarse model parameterization. A finer model parameterization would allow resolving these small scale anomalies but ray coverage does not support this.

## 4.4 Solution Quality

The assessment of the solution quality is a crucial component of any seismic tomography study. Areas of fair and good resolution have to be separated from poorly or none resolved regions. In addition, the inversion process may introduce artifacts in areas of low resolution or even in areas of good resolution (*Kissling*

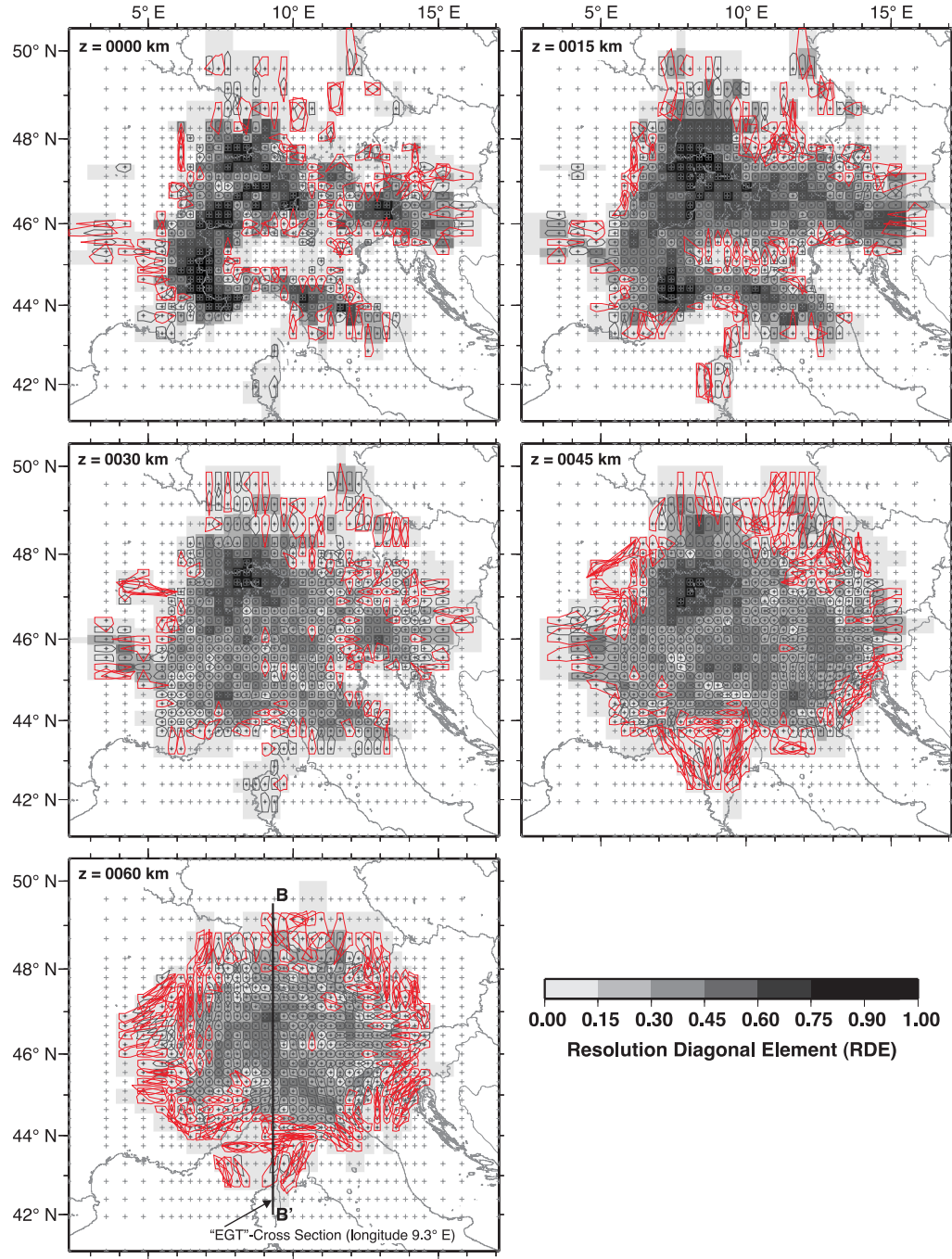
*et al.*, 2001). Primarily, the resolution of a specific volume depends on the associated ray-coverage (density and geometric distribution of rays). Distribution of hit count or derivative weighted sum (DWS) can be used as a first order assessment of the ray-coverage. Hit count and DWS, however, are not sensitive to the geometric distribution of rays. The diagonal element of the resolution matrix (RDE) provides additional information on the independence of one model parameter as described e.g., by *Husen et al.* (2000). The larger the RDE value is for one model parameter the more independent the solution is for this parameter.

Figure 4.4 displays the RDE of the final 3-D  $v_P$  model for several layers between 0 km and 60 km depth. For the uppermost layer the RDE is primarily dominated by station distribution and seismicity. In general, the distribution of RDE values is rather uniform, suggesting an appropriate model parameterization. However, one can observe systematically increased RDE values approximately below the territory of Switzerland. Figure 4.5 displays the RDE distribution in a vertical cross section along the southern segment of the EGT transect. The location of this depth section is indicated by the bold black line in Figure 4.4. Increased RDE in a certain volume usually goes along with the presence of seismicity in or close to this volume. Furthermore, Pn phases lead to an increase of RDE values in the depth range between 45 and 60 km in the central part of the model.

Additional information on the solution quality can be derived from the full resolution matrix. A common diagnostic tool is the spread function (*Toomey and Foulger*, 1989; *Michellini and McEvilly*, 1991), which summarizes the information contained in a row of the full-resolution matrix. Thus, possible smearing (i.e. non-zero off-diagonal elements) will be indicated by increased spread values. However, the spread function does not show the direction of smearing. An alternative representation is proposed by *Reyners et al.* (1999), which maps the decay of the diagonal elements in each row of the resolution matrix in 2D as smearing or resolution contours. These resolution contours visualize the orientation and the spatial bias of potential smearing. Horizontal and vertical resolution contours of the final 3-D  $v_P$  model are shown in Figure 4.4 and 4.5, respectively. The contour lines outline the area in which the values of the resolution matrix decay to 70% of the value of the RDE. Black contour lines denote grid points with no or minor smearing, red contour lines indicate grid points with significant smearing (resolution contour includes a neighboring grid point). Significant smearing as suggested by the resolution contours is mainly restricted to grid nodes of  $RDE < 0.15$ .

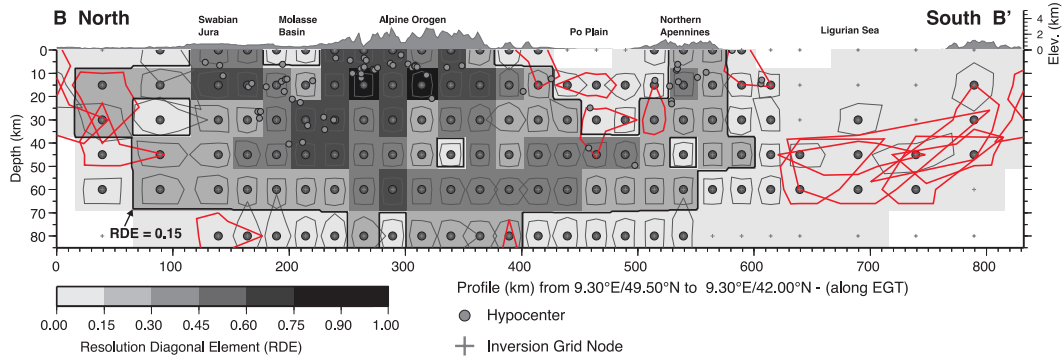
As demonstrated by *Eberhart-Phillips and Reyners* (1997), *Kissling et al.* (2001), and *Toomey and Foulger* (1989), resolution estimates based on RDE or spread values strongly depend on damping and model parameterization. Therefore, no universally applicable cut-off values are available, which define the range of acceptable RDE or spread values. A RDE threshold for the resolution assessment has to be obtained from tests with synthetic data. Checkerboard sensitivity tests (e.g., *Zelt*, 1998) or preferable synthetic characteristic models as proposed by *Haslinger et al.* (1999) and *Husen et al.* (2000) can be used for such a RDE calibration.

Figure 4.6 shows the result of a sensitivity test with a synthetic checkerboard model



**Figure 4.4:** Diagonal elements of the resolution matrix (RDE) and resolution contours (*Reyners et al., 1999*) of the  $v_P$  solution at different depths. Crosses denote grid nodes, black dots denote grid nodes with  $RDE \geq 0.01$ . The contour lines outline the area in which the values of the resolution matrix decay to 70% of the value of the RDE. Black contour lines denote grid points with no or minor smearing, red contour lines indicate grid points with significant smearing. Black bold line indicates location of the vertical cross section of Figure 4.5.





**Figure 4.5:** NS vertical cross section of diagonal elements of the resolution matrix (RDE) and resolution contours (*Reyners et al.*, 1999) of the  $v_P$  solution similar to Figure 4.4. Grey dots indicate hypocenters as derived from the simultaneous 3-D inversion. Profile is situated approximately along the EGT transect (for exact location see black bold line in Fig. 4.4.)

similar to the one proposed by *Husen et al.* (2004). To identify potential vertical leakage, only every second layer is perturbed by alternating high (+10%) and low (-10%) input anomalies (indicated by blue and red rectangles in Fig. 4.6). To identify additional horizontal smearing, a gap of two grid nodes between the input anomalies is inserted. To distinguish upward from downward leakage, the polarities of the input anomalies are swapped for each perturbed layer. The 1-D initial velocity model as shown in Table 4.2 is used as background for the checkerboard model. As for all sensitivity and resolution tests in this study, synthetic travel-times through the input model are calculated using a finite difference solution to the Eikonal equations (*Podvin and Lecomte*, 1991) and the same source-receiver distribution as the real data set. Random noise is added to the synthetic travel-times using an equally distributed error for each quality class. The corresponding range is defined by the error interval of the associated quality class as shown in Table 4.1. We use the same inversion parameters (initial model, parameterization, damping and number of iterations) for the inversion of the synthetic travel-times as we used for the ‘real’ data.

The recovery of the high/low input anomalies is good to fair for grid nodes with RDE values  $\geq 0.15$  as demonstrated in Figure 4.6. Within the area outlined by the RDE contour of 0.15 only minor vertical and horizontal smearing is observed down to 60 km depth. The layer at 80 km depth shows significant leakage from the overlaying high velocity anomalies (Fig. 4.6). Although geometries of the input anomalies are well recovered by the inversion, the amplitudes are reduced by several percent, especially at deeper layers (Fig. 4.6). In a similar second sensitivity test (not shown here), the anomalies are placed in 15, 45, and 80 km depths and the layers at 0, 30, and 60 km remain undisturbed. The result of the inversion is comparable to the one of Figure 4.6. Within the RDE contour of 0.15 the checkerboard is well resolved without showing major vertical or horizontal smearing. Below 60 km, the checkerboard cannot be recovered anymore.

The RDE value of 0.15 represents a reasonable cut-off to separate well to fairly



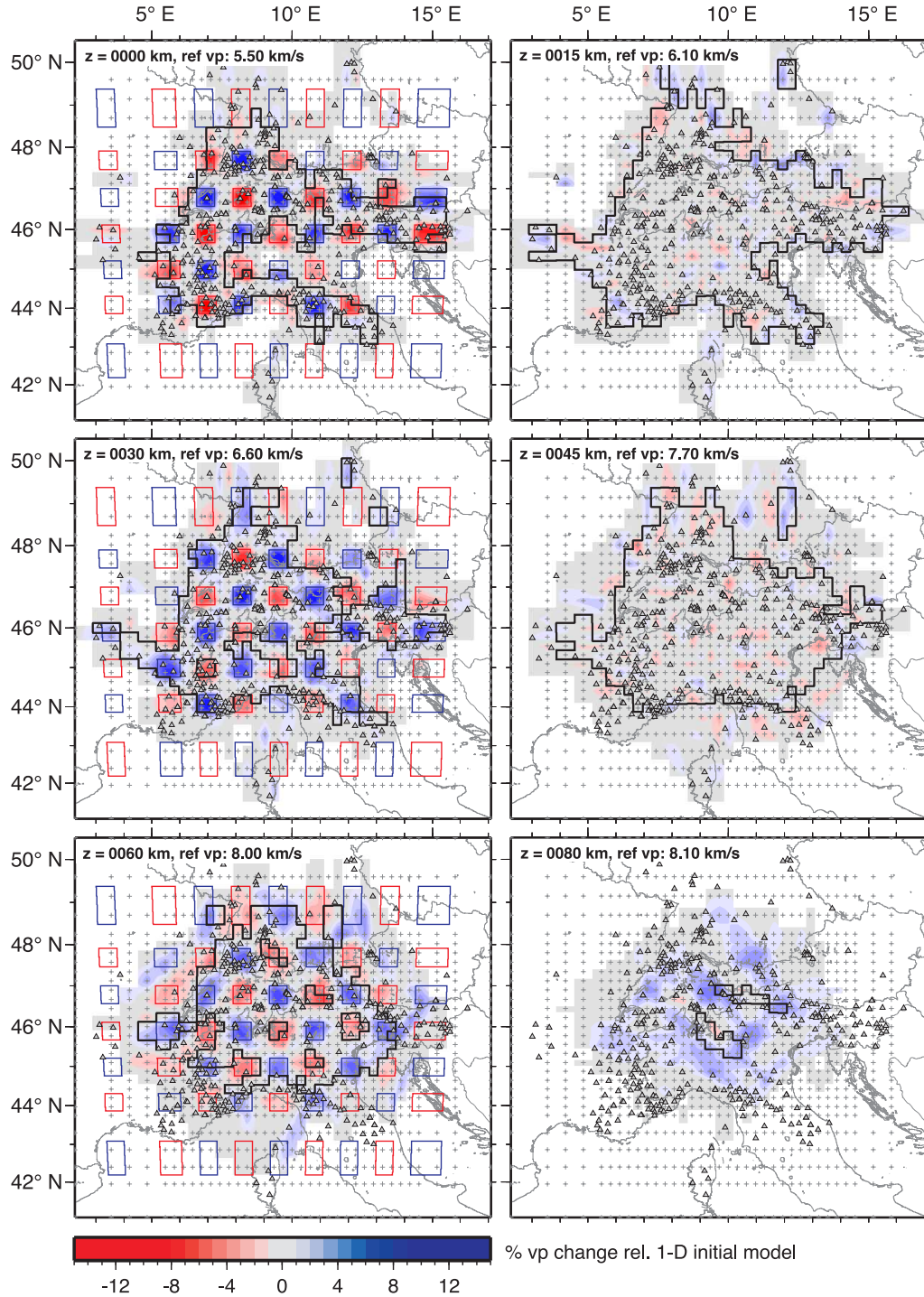


**Figure 4.6:** Sensitivity test with a checkerboard model similar to *Husen et al. (2004)*. Recovered model after five iterations is shown in plane view at different depths. Alternating high (+10%) and low (-10%) input anomalies are indicated by blue and red rectangles, respectively. The thick black line corresponds to the RDE contour of 0.15. Crosses indicate grid nodes and triangles represent seismic stations.

resolved regions from poor resolution, considering the results of Figure 4.4, 4.5, and 4.6 complemented by several additional sensitivity and specific resolution tests not shown here. Single exclaves of RDE values  $\geq 0.15$ , however, are not considered for interpretation.

## Resolution of Lower Crust and Alpine Moho

The specific resolution test shown in Figure 4.7 is designed to estimate the potential recovery of geometry and amplitudes of anomalies in the range of the suture between European and Adriatic lower crust in the Central Alps. The continuation of lower European crust beneath the Adriatic mantle wedge, as proposed in models of e.g., *Schmid and Kissling* (2000), is poorly documented by the available CSS data. On the other hand, temperature fields derived from kinematic modeling predict eclogitization of the subducted lower crust at a depth of 55 to 60 km in the Central Alps (*Bousquet et al.*, 1997). The input anomalies of the synthetic models in Figure 4.7 are extended in east-west direction parallel to the strike of the Central and Eastern Alps and are placed at 45 km depth. The NS vertical cross section of Figure 4.7 is located along the EGT transect (similar to Fig. 4.5) and cut the input anomalies perpendicularly. Amplitudes of the synthetic anomalies with respect to the background model of Table 4.2 are -10% (Fig. 4.7a) and +10% (Fig. 4.7b). The location of the input anomalies are indicated by red and blue rectangles, respectively.

The geometry of the low-velocity anomaly is well recovered by the inversion (Fig. 4.7a) and the vertical leakage is minor. The amplitude, however, is only partly recovered and for the major part it is diminished by more than 4%. The recovery of the high-velocity anomaly denotes significant vertical leakage, especially towards greater depths (Fig. 4.7b). The upward leakage can partly be identified by increased resolution contours, the downward leakage is indicated neither by spread nor by resolution contours, due to the focusing effect of the high-velocity anomaly and the low degree of ‘cross-firing’ of Pn phases in this region.

This example clearly illustrates the necessity of specific resolution tests for the assessment of the solution quality in 3-D tomography. Unmodified European crust subducted beneath the Adriatic mantle should be imaged as a low-velocity anomaly by our data set. The resolution of an eclogitized European lower crust will be rather difficult, since  $v_P$  of eclogite is expected to be comparable or even higher than  $v_P$  of the surrounding peridotite mantle rocks (e.g., *Holbrook et al.*, 1992) and in this case upward and downward leakage has to be considered as demonstrated in Figure 4.7b.

Since the Alpine region shows a strong 3-D Moho topography (see e.g., *Waldhauser et al.*, 1998; *Lombardi et al.*, 2008), its potential resolution with local earthquake tomography is examined in an additional synthetic test. Unlike CSS refraction and reflection methods, local earthquake tomography resolves seismic velocities averaged within a volume, which is defined by the model parameterization. Therefore, sharp and well-defined seismic discontinuities like the Moho are imaged as velocity

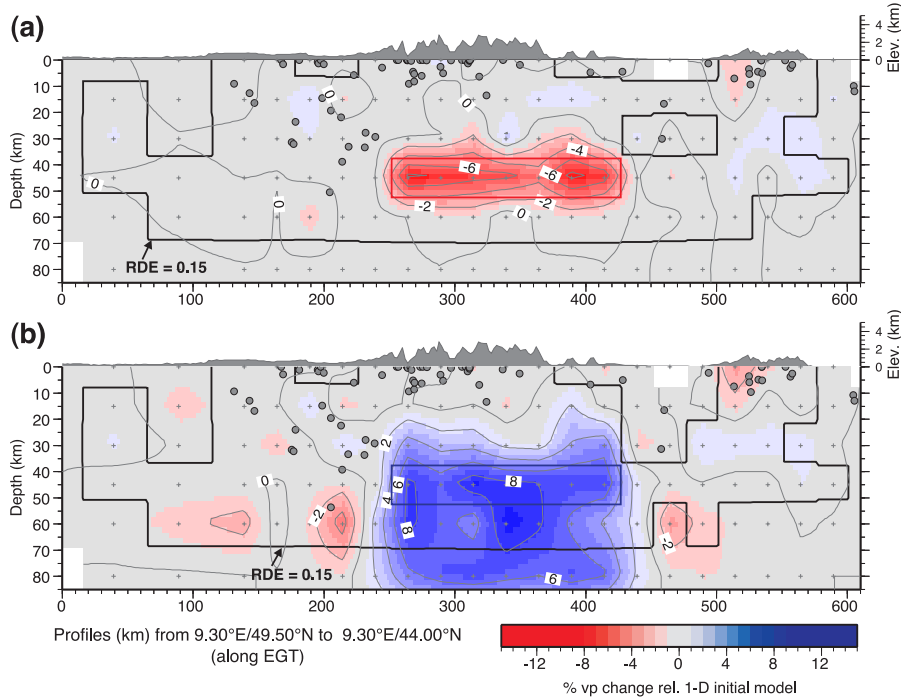


**Figure 4.7:** Assessment of resolution in the region of the expected suture between European and Adriatic lower crust below the Central Alps. NS vertical cross section through synthetic model along EGT transect. Input anomalies are extended in EW-direction. **(a)** Low input anomaly (-10 %). **(b)** High input anomaly (+10 %). Location of input anomalies are indicated by blue and red rectangles, respectively. Contour lines denote percentage  $v_P$  change with respect to initial 1-D model.

gradients in local earthquake tomography. Depending on the model parameterization, the associated velocity gradient is more or less broadened. This effect has to be taken into account for interpretation of lower crustal velocities derived from local earthquake tomography as demonstrated in Figure 4.8a-c.

For a synthetic test we interpolated the velocities from the Alpine crustal model of *Waldhauser et al.* (2002), which is mainly based on CSS data, on a dense grid of 5 x 5 km (horizontal) x 2 km (vertical) nodes. Figure 4.8a represents a vertical cross section through the interpolated synthetic model along the EGT transect. The Moho is defined by a sharp velocity gradient in the range of 6.5 km/s to 8.0 km/s. The dense grid is used to calculate synthetic travel-times using the same source-receiver configuration as the ‘real’ data set, similar to previous sensitivity and resolution tests. After adding random noise, synthetic travel-times are inverted with the same coarse model parameterization, initial velocities, and inversion parameters as used for the ‘real’ data.

The result of the inversion is shown in Figure 4.8b. Fairly to well resolved parts are outlined by the  $RDE = 0.15$  contour line. Compared to the steep velocity gradient defining the Moho in the input model of Figure 4.8a, the output of the inversion denotes an obviously flatter gradient, indicated by the less dense velocity contour lines between 6.5 km/s and 8.0 km/s. This broadening of the velocity gra-

dient is mainly caused by the coarse parameterization of our model. Furthermore, the initial 1-D model (Fig. 4.8c) used for the inversion might not be the optimum choice, since it does not represent the minimum 1-D model of the CSS input model (higher velocities in the upper crust compared to CSS model).

Although the  $v_P = 6.0$  km/s contour line indicates some vertical leakage problems (e.g. at 200 km and 310 km), it seems not affected by the Moho topography. From this we conclude that velocities between 6.5 and 8.0 km/s are mainly associated with the Moho gradient in our model parameterization. On the other side, we observe a very good agreement between the  $v_P = 7.25$  km/s contour line of the input model (solid red line in Fig. 4.8a,b) and the  $v_P = 7.25$  km/s contour line of the inversion result (dashed light grey line in Fig. 4.8b). Therefore we define the  $v_P = 7.25$  km/s contour line as the ‘tomography’ Moho in our model. Moho offsets (European/Adriatic and Adriatic/Ligurian) as indicated by kinks in the CSS model (Fig. 4.8a) are smoothed out in the coarse model (Fig. 4.8b).

Figure 4.8d shows the result from the inversion of the ‘real’ data set as vertical cross section along the same EGT transect (for location see Fig. 4.10). Poor and unresolved areas are masked. Tectonic transect after *Schmid et al.* (2004) is represented by black lines and positions of CSS Mohos after *Waldhauser et al.* (1998) are indicated by solid yellow lines. Solid light grey line denotes the  $v_P = 7.25$  km/s contour (tomography Moho) as derived from the ‘real’ data set, dashed light grey line corresponds to  $v_P = 7.25$  km/s contour from the inversion of the synthetic data (same as in Fig. 4.8b). In general, a rather good agreement is observed between tomographic and CSS Moho. Southward dipping of European Moho, up-doming of the Adriatic Moho and the offset between Adriatic and Ligurian Moho are clearly visible in the tomography Moho.

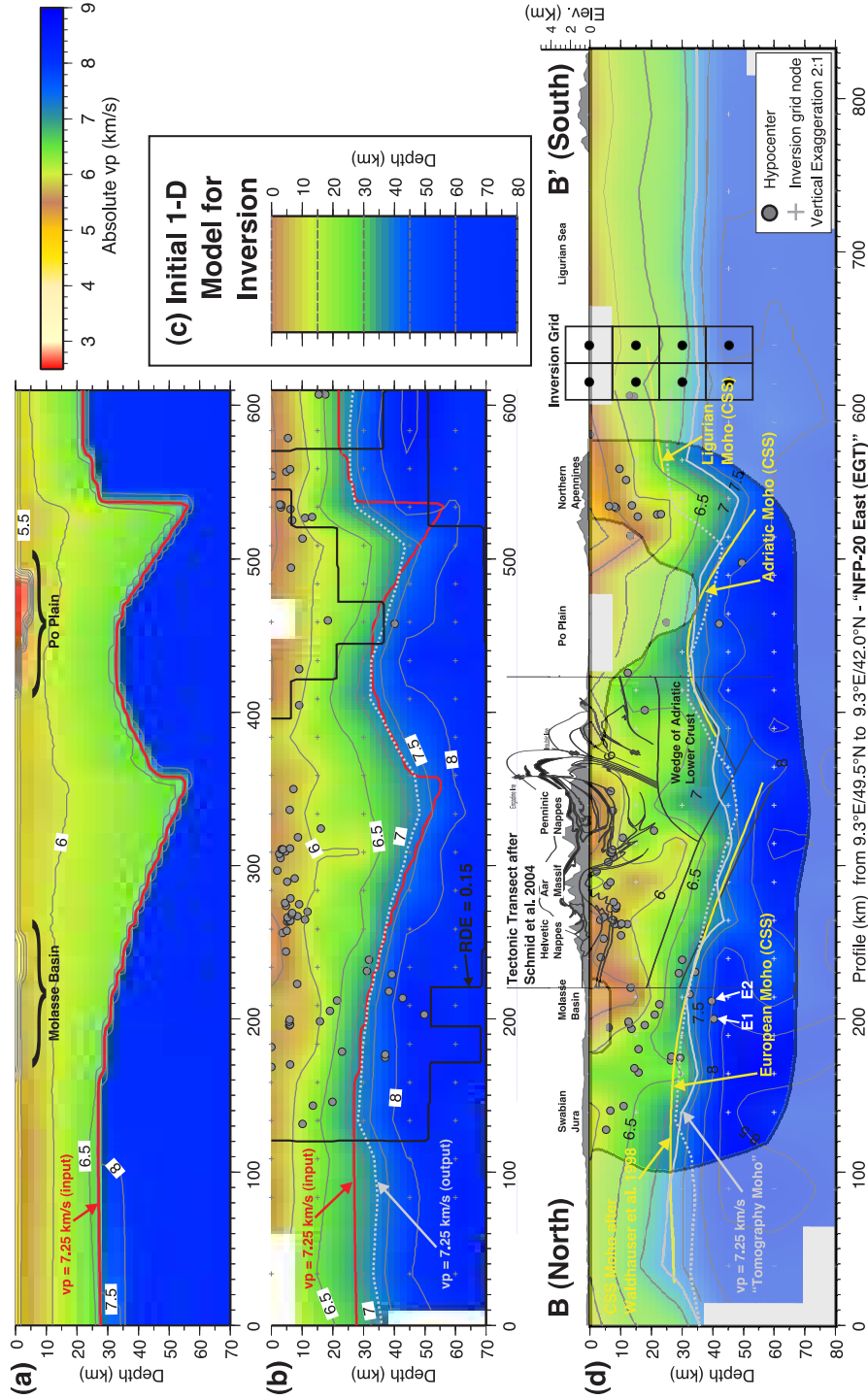


**Figure 4.8:** Resolution test and tomographic result as cross sections along the NFP-20 East/EGT transect (see Fig. 4.4 for location). (a) Crustal model of Waldhauser *et al.* (2002) used as input for resolution test. (b) Recovered model after inversion of synthetic travel-times. (c) Initial 1-D model used for all 3-D inversions. (d) Final inversion result of 'real' data set. Poor and unresolved areas are masked. Black lines represent tectonic transect after Schmid *et al.* (2004). Position of CSS Mohos after Waldhauser *et al.* (1998) is indicated by solid yellow line. Projected hypocenters (grey dots) are located within  $\pm 50$  km distance off the profile. Focal depths of events labeled as E1 and E2 are discussed in section 4.6. Vertical exaggeration for all cross sections is 2:1.

Compared to the  $v_P = 7.25$  km/s contour predicted by the synthetic model (dashed light grey line in Fig. 4.8b,d) the tomography Moho of the ‘real’ data (solid light grey line in Fig. 4.8d) indicates slightly higher velocities in the suture zone between European and Adriatic lower crust. The structure of the lower crust will be discussed in detail in section 4.6.

## 4.5 3-D Tomographic Model of the Alpine Crust

Figure 4.9 shows the tomographic result of the 3-D  $v_P$  model as horizontal cross sections at different depths. The  $v_P$  velocity structure is shown as percentage change relative to the 1-D initial reference model. As shown before, perturbations  $\geq 5\%$  are reliably resolved with our data. Bold black contours include well to fairly resolved regions. Areas outside these contours are associated with low resolution or are not resolved at all. These outlines are mainly based on the  $RDE = 0.15$  contour as described in the previous section. In addition, results of sensitivity and resolution tests are considered for the definition of resolved and unresolved regions. Green/grey dashed contours in Figure 4.9 outline major tectonic units such as the Alpine orogen, the Apennines mountains, sedimentary basins (Molasse basin, Po plain) and external massifs in the northern Alpine foreland (Black-Forest, Vosges Mountains).

Due to the large vertical node spacing of our model, the layer at  $z = 0$  km (Fig. 4.9) is dominated by near-surface and shallow upper crustal structures. Increased  $v_P$ , as indicated by bluish colors, is observed throughout the Western Alps, where the uppermost crust is dominated by the crystalline basement (Fig. 4.9, 0 km). In addition, high  $v_P$  can be found in the south-eastern Alps probably associated with the occurrence of compact limestones in this area. Further regions of increased  $v_P$  are the north-eastern Apennines mountains as well as the southern Black-Forest. Reduced velocities as indicated by reddish colors are mainly associated with sedimentary deposits and basins such as the southern Rhine Graben, the Molasse basin, and the Po plain (although latter two are mostly outside of the resolved part of the model).

The upper to mid crust (Fig. 4.9, 15 km depth) is dominated by the high-velocity anomaly of the Ivrea body in the Western Alps. West and south-west of the Ivrea body, a region of reduced  $v_P$  is observed. Furthermore, low velocities below the Apennines are identified, which can be associated with Po sediments over-thrust by the Apennines mountains.

Besides these first-order anomalies, several small-scale features can be observed such as the high-velocity anomaly north of the Lago Maggiore in southern Switzerland (marked as ‘T’ in Fig. 4.9), whose location agrees very well with the Ticino-anomaly present in the gravity model of *Kissling* (1984). Another striking high-velocity anomaly is located in the range of the Engadine window (marked as ‘E’ in Fig. 4.9) in the border region between Austria, Italy, and Switzerland.

Reduced velocities in the mid to lower crust section (Fig. 4.9, 30 km depth) are mainly associated with the crustal root of the Alps and the northern Apennines.



## 4.5 3-D TOMOGRAPHIC MODEL OF THE ALPINE CRUST

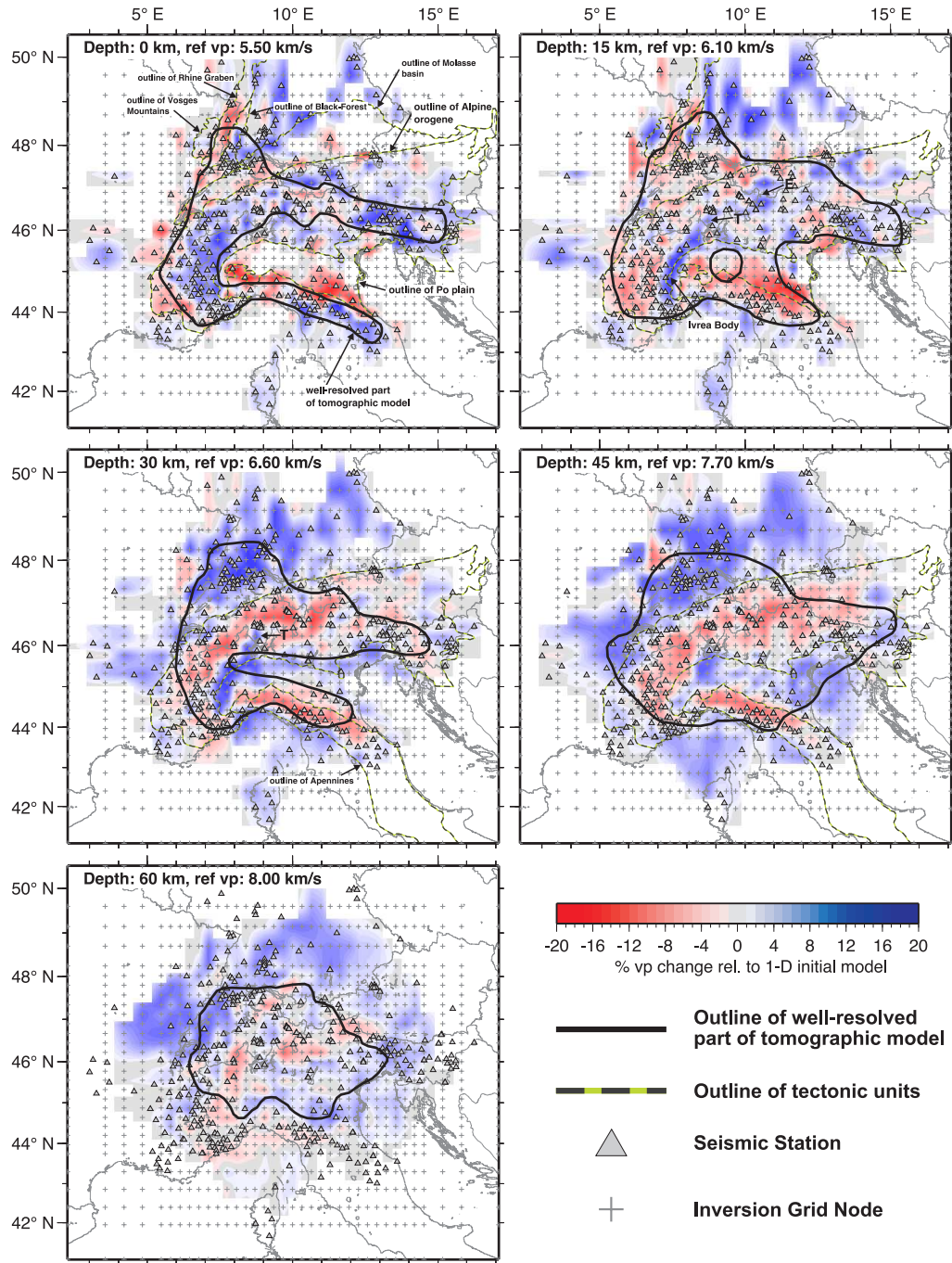


**Figure 4.9:** Tomographic results of 3-D  $v_P$  model. Results are in horizontal cross sections at different depths as indicated. The  $v_P$  velocity structure is shown as percentage change relative to the 1-D initial reference model. Bold black contours include well to fairly resolved regions. Areas outside these contours are associated with low resolution or are not resolved at all. Major tectonic units are outlined as indicated. ‘E’ and ‘T’ mark positions of small-scale anomalies as discussed in the text.

On the other hand, significantly increased velocities indicate the transition to upper mantle velocities in regions of crust of average normal thickness of about 30 km (e.g. northern foreland, Ligurian Sea). The signature of the Ivrea body is still observable at this depth range as well as the small scale Ticino anomaly.

Likewise, lower velocities at 45.0 km depth (Fig. 4.9) clearly reveal the thickening of the crust beneath the Alpine and Apennine orogens. Increased  $v_P$  correlates with upper mantle velocities of European, Adriatic, and Ligurian plates. The signature of Ivrea body is not observed anymore.

The zones of slightly reduced velocities at 60 km depth (Fig. 4.9) correlate largely with the deepest parts of the crustal root as reported in the CSS model of *Waldhauser et al.* (1998) and in the recent receiver function study of *Lombardi et al.* (2008).

## 4.6 Discussion

Figure 4.10 shows further vertical cross sections located perpendicular to the strike of the Alpine orogen as indicated in the map view. Profiles AA', DD', and EE' are located along prominent geophysical-geological transects also marked in Figure 4.1. Like in Figure 4.8d the tomographic Moho is indicated by solid light grey lines and locations of the CSS Mohos after *Waldhauser et al.* (1998) are indicated by solid yellow lines (Fig. 4.10). As demonstrated by *Diehl et al.* (2008), the general topography of the tomographic Moho ( $v_P = 7.25$  km/s iso-surface), is in good agreement with the CSS model of *Waldhauser et al.* (1998) and with the recent receiver function study of *Lombardi et al.* (2008). In the Western and Central Alps the European Moho dips towards south-east to south. The suture between the European and Adriatic lower crust is of asymmetric nature mainly caused by the Ivrea body in the Western Alps (profile EE', DD', CC', BB' in Fig. 4.10 and 4.8d). Although *Behm et al.* (2007) recently compiled a Moho map for the Eastern Alps, the transition between Central Alps and Eastern Alps is still less well documented by CSS data. Profile AA' (Fig. 4.10) along the TRANSALP transect suggests a rather symmetric Moho topography, although a major part of the European Moho is outside the resolved volume. Compared to our result, the location of the European Moho on the TRANSALP transect of *Schmid et al.* (2004) seems to be too deep.



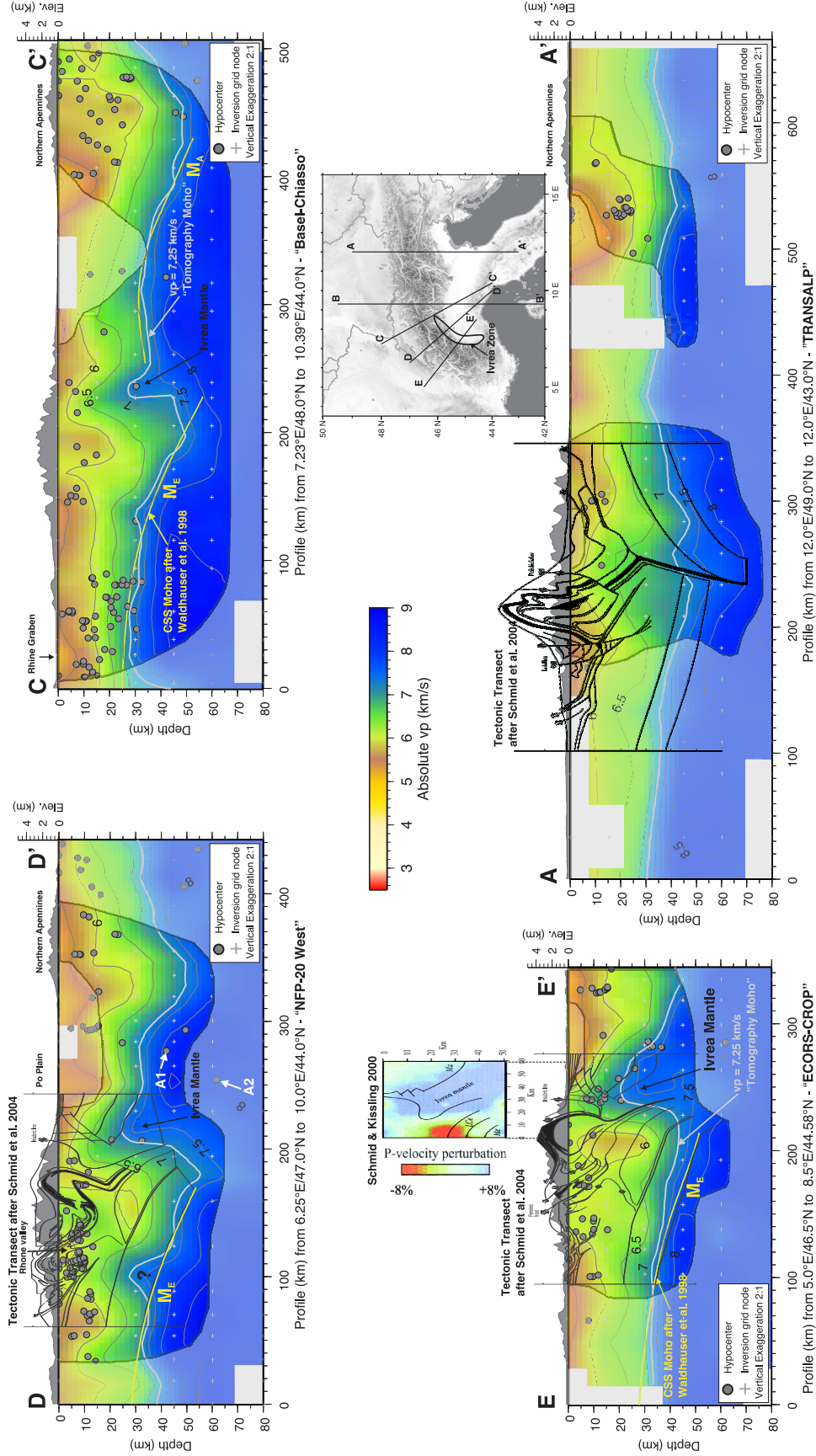


**Figure 4.10:** Final P-wave velocity model. Vertical cross sections perpendicular to the strike of the Alpine orogen as indicated in map view. Profiles AA', DD', and EE' are located along prominent geophysical-geological transects. Poor and unresolved areas of the tomographic model are masked. Tectonic interpretations of Schmid *et al.* (2004) are indicated by black lines.  $M_E$  denotes European Moho,  $M_A$  denotes Adriatic Moho as derived from the CSS model of Waldhauser *et al.* (1998). Projected hypocenters (grey dots) are located within  $\pm 50$  km distance off the profile. Profile BB' is shown in Figure 4.8d. Focal depths of events labeled as A1 and A2 in profile DD' are discussed in section 4.6.

The structure of the Ivrea body in the Western Alps is well resolved from its north-eastern end down to its southern end. Profile EE' in Figure 4.10 represents a cross section along the ECORS-CROP transect. The location of the high-velocity anomaly in our model agrees well with the tomography study of *Solarino et al.* (1997) superimposed for comparison in Figure 4.10 (vertical cross section as published in *Schmid and Kissling* 2000). Similar to the result of *Solarino et al.* (1997) a pronounced low-velocity anomaly is present north-west of the Ivrea body (EE' in Fig. 4.10), probably associated with European upper crust wedged into the suture zone. Likewise, a low-velocity anomaly is observed in the range of the expected doubled lower crust (*Schmid and Kissling*, 2000) along the NFP-20 West transect (profile DD' in Fig. 4.10). Profile CC' in Figure 4.10 marks the north-eastern end of the Ivrea body.

In the Central Alps reduced P-wave velocities between 5.5 and 6.0 km/s reach almost to the suture between the European lower crust and the Adriatic lower crustal indenter in 25 km depth (profile BB' in Fig. 4.8d), indicating thickening of the upper European crust. However, vertical leakage as demonstrated in Figure 4.8b cannot be entirely excluded in this part of the model. Likewise, the low-velocity zone in the upper crust below the Molasse basin is most probably stretched by vertical leakage or inappropriate model parameterization (Fig. 4.8d). Helvetic nappes and Penninic nappes are characterized by P-wave velocities around 5.5 km/s in the upper crust. Realms of Helvetic nappes and Penninic nappes are separated by a zone of slightly increased  $v_P$  located in the area of the Aar Massif (around km 290 on profile BB' in Fig. 4.8d). These observations are in very good agreement with the velocity model of *Ye et al.* (1995) derived from seismic refraction data of the EGT transect.

## Structure of the Lower Crust in the Central Alps

In the region of the expected Adriatic lower crustal wedge (Adriatic indenter) upward bending of the  $v_P = 6.5$  km/s contour can be observed (around km 340 on profile BB' in Fig. 4.8d). Since this feature is not present in the synthetic model of Figure 4.8b, we associate the increase in  $v_P$  in this area with the Adriatic lower crustal indenter.

As mentioned earlier, a clear continuation of the lower European crust beneath the Adriatic Moho is not visible in our tomographic image of Figure 4.8d. The absence of the lower European crust beneath the Adriatic mantle wedge might be an indication for eclogitization of lower crustal material as proposed e.g., by *Bousquet et al.* (1997). To check the hypothesis of existing subducted European lower crust beneath the Adriatic mantle wedge, an additional resolution test was performed as shown in Figure 4.11a-c. Similar to Figure 4.8a the synthetic input model for our test is based on the CSS model of *Waldhauser et al.* (2002), however, in this case a coarser grid was used for interpolation. Unmodified lower European crust ( $v_P = 6.5$  km/s) is extrapolated beneath the Adriatic mantle wedge assuming a constant dip and thickness of the subducted lower crust as indicated by dashed lines in Figure 4.11a.

The result of the inversion of synthetic travel-times for this model is shown in Figure 4.11b. The solid red line denotes the  $v_P = 7.25$  km/s contour of the

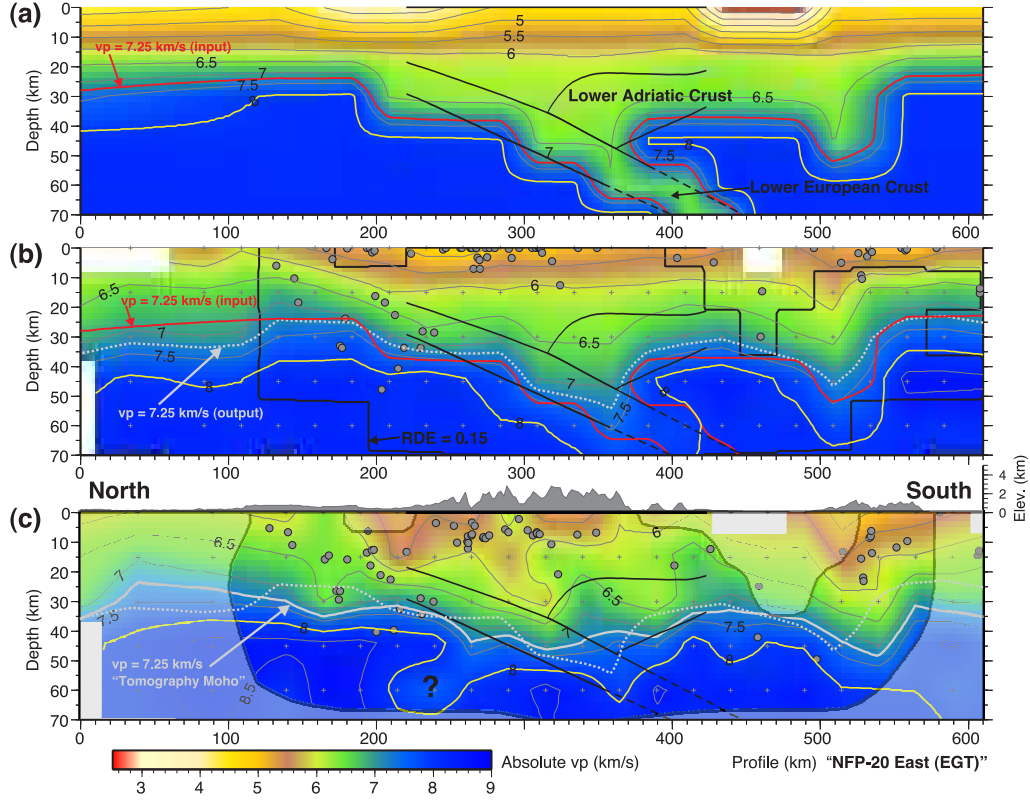


**Figure 4.11:** Resolution assessment for lower crustal subduction in the Central Alps. (a) Synthetic model based on CSS crustal model with European lower crust subducted below Adriatic microplate. (b) Recovered model after inversion of synthetic travel-times. (c) Inversion result of 'real' data set identical to Figure 4.8d.

input model (Fig. 4.11a,b) and the  $v_P = 7.25$  km/s contour recovered by the inversion is indicated by the dashed light grey line (Fig. 4.11b,c). As expected from the previous resolution test in Figure 4.7a, recovered amplitudes of low-velocity anomalies in the lower crust are significantly attenuated compared to their input. In case of the absolute velocity representation in Figure 4.11b, the presence of subducted lower crust is therefore primarily indicated by the downward deflection of the 8.0 km/s contour (solid yellow line) below the Adriatic mantle wedge. In the 'real' data (Fig. 4.11c) no such deflection of the 8.0 km/s contour (solid yellow line) is observed below the Adriatic mantle wedge. In addition, the tomography Moho (solid light grey line) of the 'real' data clearly differs from the  $v_P = 7.25$  km/s contour derived from the inversion of synthetic travel-times (dashed light grey line) in Figure 4.11c, indicating increased P-wave velocities beneath the Adriatic indenter.

The cause of the low-velocity anomaly visible in the European mantle at a depth of about 60 km (downward deflection of 8.0 km/s contour), labeled by a question-

mark in Figure 4.11c, is probably associated with a numerical artifact, caused by the inhomogeneous resolution in this part of the model (see Fig. 4.5).

## Focal Depth Distributions in the Greater Alpine Region

The distribution of earthquake focal depths within the continental lithosphere provides important information on its mechanical strength and rheology as demonstrated e.g., by *Chen and Molnar* (1983), *Maggi et al.* (2000), or *Jackson* (2002). Since then, the issue of a seismogenic continental mantle and its implications for continental geodynamics are intensively discussed (see e.g., *Priestley et al.*, 2007, and references therein). Although the lower European crust in the northern Alpine foreland is known to be seismically active, no evidence exists for earthquakes in the European mantle in this area (*Deichmann et al.*, 2000a). The presence of fluids might play a key role for the occurrence of the lower crustal seismicity as proposed by *Deichmann* (1992). In contrast, there are several indications for a seismogenic Adriatic upper mantle in northwestern Italy (e.g., *Cattaneo et al.*, 1999).

As visible in the cross sections of Figure 4.8d and 4.10 the simultaneous inversion yields a couple of hypocenters which are apparently located within the upper European (e.g., events E1, E2 in Fig. 4.8d) and Adriatic (e.g., events A1, A2 in Fig. 4.10) mantle. A final decision whether these events really occurred in the continental mantle has to consider uncertainties of the Moho model as well as uncertainties in the hypocenter locations. Since the uncertainties of the tomographic Moho are less well known than the uncertainty of the CSS Moho (minimum uncertainty  $\pm 3$  km, *Waldhauser et al.* 1998), we examined only events which were located below the CSS and the tomographic Moho. In total, we found 11 events apparently situated in the European (7 events, all in the northern foreland) and Adriatic (4 events, all in northwestern Italy) mantle. To assess the uncertainty of the hypocenter solutions we relocated the 11 events in our 3-D P-wave model using the NonLinLoc package of *Lomax et al.* (2000). This approach provides a probabilistic solution to the earthquake location problem, including information on uncertainty and resolution. In addition, the corresponding waveforms contain crucial information on the origin of an earthquake. Events above the Moho can be identified by the presence of both PmP and Pn phases. Events located in the mantle are characterized by the lack of PmP phases. Phase identification can be significantly improved by the use of velocity reduced record sections as shown e.g., by *Deichmann* (1987), *Deichmann and Rybach* (1989), or *Diehl et al.* (2008).

Considering the relocated hypocenters and the corresponding uncertainties of focal and Moho depths, nine of the events could also be located just above the Moho (Table 4.3). Only two events in northwestern Italy (A1, A2 in Fig. 4.10) suggest locations in the Adriatic mantle. The additional assessment of velocity reduced record sections showed that all apparent mantle-events in the northern foreland (including events E1, E2 in Fig. 4.8d) have occurred in the lower European crust, only few kilometers above the Moho. The same conclusion holds for the events in northwestern Italy with the exception of event A1 and A2. Waveforms and focal depth suggest that event A1 (few kilometers south-west of Milan) occurred in the

Adriatic mantle. Due to its large uncertainty in focal depth, a final decision on the origin of event A2 is not possible.

Since hypocenter parameters are separated from velocity parameters in the simultaneous inversion, the resolution estimate of the velocities is sufficient for the entire model and independent from the location-accuracy of a single earthquake.

Date	Time	Lat. N	Lon. E	$Z_F$ (km)	$Z_M$ (km)	Final Origin in
1997/09/02	00:30:52.82	47.599	7.824	$29 \pm 02$	27	Eur. crust
2000/04/21	04:12:11.17	45.021	8.764	$51 \pm 10$	44	Adr. crust
2000/09/16	22:04:05.56	45.028	8.016	$67 \pm 13$	43	Adr. mantel? (A2)
2002/01/10	19:27:25.78	47.565	9.052	$31 \pm 02$	30	Eur. crust
2002/05/17	07:19:39.78	47.675	8.476	$29 \pm 03$	28	Eur. crust
2002/07/06	14:09:56.85	47.711	9.700	$36 \pm 11$	31	Eur. crust (E1)
2003/08/24	12:43:40.61	47.805	7.971	$30 \pm 02$	26	Eur. crust
2004/04/18	03:21:05.03	47.594	9.678	$40 \pm 04$	33	Eur. crust (E2)
2005/05/12	01:38:05.39	47.296	7.636	$30 \pm 02$	29	Eur. crust
2005/11/20	10:48:59.95	45.378	9.058	$40 \pm 03$	33	Adr. mantel (A1)
2007/04/02	09:10:33.28	45.777	8.300	$33 \pm 03$	27	Adr. crust

**Table 4.3:** Apparent upper-mantle events relocated in the 3-D model using the NonLinLoc package. Focal depths are indicated by  $Z_F$ . Moho depths  $Z_M$  are taken from the CSS-model of *Waldhauser et al.* (1998). Final origins are based on  $Z_F$ ,  $Z_M$ , corresponding uncertainties, and waveform analysis. Eur. = European, Adr. = Adriatic. Labels in brackets denote events discussed in the text.

## 4.7 Concluding Remarks

The quality and quantity of the automatically re-picked arrival-time data used in this study allows the 3-D imaging of large parts of the Alpine lithosphere. The new P-wave model represents a major improvement over existing model in terms of reliability and resolution of the resulting tomographic image (*Diehl et al.*, 2008). First order anomalies such as the crustal roots of the Alps and the northern Apennines are clearly resolved. Several additionally small scale features like the Ticino-anomaly north-west of the Ivrea body are visible in the tomographic image. Different sensitivity and resolution tests were performed to assess the solution quality of the resulting velocity model in detail. Synthetic tests using a realistic 3-D crustal model were performed to assess the resolution of the crust-mantle boundary (Moho). It is shown, that the general Moho topography can be recovered even with a rather coarse model parameterization.

The Alpine Moho topography derived from local earthquake tomography agrees very well with existing models from CSS methods and receiver function studies. Steep gradients are found in the Western Alps and a wider trough in combination with a rather symmetric suture between European and Adriatic crust is observed in the Eastern Alps.

The Ivrea body is clearly resolved in our model and its position and structure agrees very well with previous studies (e.g., *Solarino et al.*, 1997; *Schmid and*

*Kissling*, 2000). Several low-velocity anomalies are imaged in the upper and mid crust north-west of the Ivrea zone as well as in the Central Alps. These structures are probably associated with wedges of upper crustal material present north of the Insubric line.

Continuation of the lower European crust beneath the Adriatic mantle wedge in the Central Alps is not visible in our tomographic image. By comparing results of the synthetic modeling with the velocity model derived from our ‘real’ data set in Figure 4.11, we can exclude the subduction model for the Central Alps presented in Figure 4.11a. The presence of unmodified European lower crust beneath the Adriatic mantle wedge should lead to an observable signature in the tomographic image. The lack of such signature might be explained by a thinner subducted crustal layer not resolved with our parameterization or by mineral transition due to metamorphic processes. *Laubscher* (1990) discussed the role of eclogitization of subducted crustal material in the Alps and *Bousquet et al.* (1997) proposed eclogitization of the lower European crust in the depth of 55 to 60 km in the Central Alps. Considering the average picking error and the vertical leakage associated with high-velocity anomalies as observed in Figure 4.7b, the discrimination of an eclogitized lower crust from the surrounding mantle would not be possible, since  $v_P$  of both rock types is expected to be about 8 km/s. In agreement with the results of *Bousquet et al.* (1997)  $v_P = 8.0$  km/s is reached in a depth of 55 to 60 km in the realm of the lower European crust (Fig. 4.11c). However, due to the described effects of model parameterization and leakage in this part of the model, the uncertainties in terms of absolute velocities are rather high.

## Acknowledgments

We are grateful to the responsables of the following networks who provided us with digital recordings and bulletin data: BED (Ludwig-Maximilians-University, Munich), GERESS (Hannover), GRSN/SZGRF (Erlangen), INGV/MEDNET (Rome), Landes-Erdbebedienst (Freiburg i. B.), OGS/CRS (Udine/Trieste), RENASS (Strasbourg), RSNI/DipTeris (Genova), SED (Zurich), SISMALP (Grenoble), SNRS (Ljubljana), TGRS (Nice), ZAMG (Vienna).

Most of the plots were generated using the Generic Mapping Tool by *Wessel and Smith* (1995). This research was supported by the Swiss National Fund grant 200021-103698.

# Chapter 5

## Automatic S-Wave Picker for Local Earthquake Tomography

T. Diehl, N. Deichmann, E. Kissling and S. Husen

Originally submitted to *Bull. Seism. Soc. Am.*, April 3, 2008  
Revised version submitted, September 27, 2008

## Abstract

High-resolution seismic tomography at local and regional scales requires large and consistent sets of arrival-time data. Algorithms combining accurate picking with an automated quality classification can be used for re-picking of waveforms and the compilation of large arrival-time data sets suitable for tomographic inversion. S-wave velocities represent a key parameter for petrological interpretation, improved hypocenter determination, as well as for seismic hazard models. In our approach, we combine three commonly used phase detection and picking methods in a robust S-wave picking procedure. Information from the different techniques provides an ‘in-situ’ estimate of timing uncertainty and of the reliability of the automatic phase identification. Automatic picks are compared against manually picked reference picks of selected earthquakes in the Alpine region. The average accuracy of automatic picks and their classification is comparable with the reference picks, although a higher number of picks is downgraded to lower quality classes by the automatic picker. In the production-mode, we apply the picker to a data set of 552 earthquakes in the Alps recorded at epicentral distances  $\leq 150$  km. The resulting data set includes about 2’500 S-phases with an upper error bound of 0.27 s.

## 5.1 Introduction

Resolution and reliability of travel-time-based inversion techniques, like tomography and hypocenter determination, depend strongly on the consistency of the available arrival times. Due to an increasing number of available digital waveform data, modern re-picking algorithms represent a possibility to derive consistent and large sets of arrival-time data. Since quality assessment is crucial for tomography applications, it represents an essential component of any automatic algorithm. Recent studies with re-picked and automatically weighted P-phase data in Italy (*Di Stefano et al.*, 2006) and within the Alpine orogen (*Diehl et al.*, 2008) demonstrated the significant gain of resolution and reliability for tomographic velocity models at local to regional scales.

In terms of composition and physical state of the lithosphere, additional S-wave velocity models represent one of the key parameters. Independent measures of P- and S-wave velocities allow, for instance, the computation of the  $v_P/v_S$  ratio, which is proportional to the Poisson’s ratio (*Holbrook et al.*, 1992; *Christensen*, 1996), and allow also better estimates on subsurface temperature (*Goes et al.*, 2000). Therefore, the quality-weighted automated re-picking of S-waves represents the next step towards three-dimensional petrological models derived from seismic tomography. In addition, appropriate S-wave models and reliable S-arrivals add important constraints to the earthquake location problem; in particular focal depth depends critically on the use of S-arrivals as demonstrated e.g., by *Gomberg et al.* (1990).

Onset determination of S-waves, however, is difficult due to the character of the later arriving shear wave as described in the electronic supplement. Even manual



picking and phase identification is often uncertain, especially at larger epicentral distances. On the other hand, we can make use of the characteristics of an S-wave by exploiting the information of three-component (3C) recordings. The product of different polarization filters applied to a 3C recording, as presented by *Cichowicz* (1993), combines the major characteristics of an S-wave arrival into one single characteristic function. Such a characteristic function can be used for detection and picking of S-phases, since it is not sensitive to P-phases. However, the method described by *Cichowicz* strongly depends on the assumption that incidence angle  $\varphi$  and back-azimuth  $\beta$  can be derived from polarization analysis of the incoming P-wave and that the S-wave is linearly polarized.

*Wang and Teng* (1997) combined the approach of *Cichowicz* (1993) with additional S-wave attributes, like a change of autoregressive (AR) coefficients and the comparison of a short-term average (STA) against a long-term average (LTA). They use a pattern recognition technique to identify and pick S-waves. A similar combined approach is used by *Bai and Kennett* (2000) to detect and identify regional P- and S-phases in three-component seismograms. They implement a polarization analysis based on complex traces derived from the Hilbert transform of the real part of the signal. The method proposed by *Akazawa* (2004) includes an iterative application of envelope functions, STA/LTA detectors and autoregressive picking algorithms based on the Akaike Information Criterion (AIC) (*Akaike*, 1973). Although these combined approaches result in high detection rates and acceptable accuracy, they do not provide any uncertainty estimate of identification and timing, which is required for travel time inversions.

In our approach we combine an S-wave detector similar to *Cichowicz* (1993) with an STA/LTA detector, which is applied to the original horizontal components and which therefore does not require a correct rotation of components. In addition, a predictive AR-AIC picking algorithm is used on single (original and rotated) components and on a combination of both horizontal components as described e.g., in *Takanami and Kitagawa* (1991) or *Leonard and Kennett* (1999). The information provided by the different picking techniques are combined to yield robust S-wave arrival times and are used to derive ‘in-situ’ estimates of the uncertainty and quality of the corresponding phase pick.

We apply our S-wave picking approach to a data set of 3C recordings of local earthquakes in the Alpine region. Since our approach should mimic the manual picks of an analyst, a consistently hand picked reference data set is used to calibrate the parameters and to check the performance of the automatic picker in terms of accuracy and quality assessment. Subsequently the calibrated picker is applied in the production-mode to a data set of 552 events.

## 5.2 Combined Picking Approach

For stable and reliable S-wave picking, different S-wave attributes have to be combined. Our approach to an automatic S-picker is based on three different detection and picking methods. An STA/LTA energy-detector and a polarization-detector

are used to identify the first arriving S-phase. The information provided by the detectors is used to setup the search windows of the AR-AIC picker. Finally, information from detectors and AR-AIC picker is combined to yield the arrival time  $tS_{me}$  of the first arriving S-phase and its corresponding uncertainty interval defined by  $tS_{lo}$  and  $tS_{up}$ .

As minimum *a priori* information, the presented picking procedure requires an existing P-phase pick  $tP_{obs}$  (hand picked or high-quality automatic pick) and a predicted S-arrival time  $tS_{pre}$  (theoretical arrival time in an appropriate regional velocity model, usually 1-D P-wave velocities divided by a constant  $v_P/v_S$  ratio). The picking procedure is summarized in the flow chart of Figure 5.1. Prior to any application, each component of the combined picking approach has to be calibrated with a set of reference S-picks by a trial-and-error procedure as demonstrated in section 5.3.2.

In the following paragraphs we describe the basic principles of the detectors, the AR-AIC picker, and the quality assessment. A more detailed documentation on the

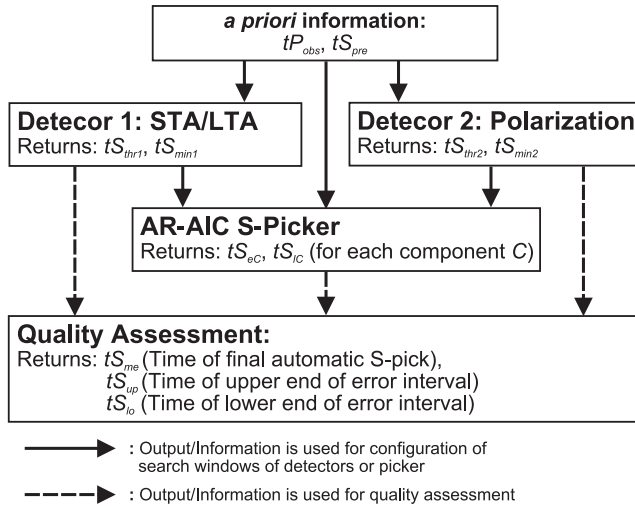


**Figure 5.1:** Flow chart of proposed automatic S-wave picking approach. The procedure requires *a priori* information on the P-wave arrival time  $tP_{obs}$  and on the predicted S-arrival time  $tS_{pre}$ . Information provided by detectors are used to setup the search windows of the AR-AIC picker and for the automatic quality assessment. See Tables 5.1 for further description of variables.

methodology is presented in an electronic supplement. To facilitate the reader's orientation, the most important variables used in the following description are summarized in the glossary of Table 5.1.

### 5.2.1 STA/LTA Detector

The STA/LTA picker represents a very common and simple technique for phase detection. It is implemented in many online-detection algorithms and its principles are described e.g., by *Allen (1978)*, *Allen (1982)*, *Berger and Sax (1980)*, or *Ruud and Husebye (1992)*. Detectors based on STA/LTA are mainly sensitive to a change in amplitude (energy) and therefore discrimination between P and S phases is critical, even if applied only to horizontal components. In our implementation, we calculate running short-term and long-term averages from the originally horizontal components (E, N), as described in the electronic supplement. The lengths of short-term ( $\Delta st$ ) and long-term ( $\Delta lt$ ) average windows basically control the

Variable	Description
<b>General Variables</b>	
$tP_{obs}$	Time of <i>a priori</i> (known) P-arrival (e.g., from high-quality autotpick)
$tS_{pre}$	Time of predicted S-arrival (e.g., from velocity model)
$t_{MHA}$	Time of Maximum Horizontal Amplitude $y_{MHA}$
$tS_{me}$	Time of final automatic S-pick (from quality assessment)
$tS_{up}$	Time of upper bound of error interval (from quality assessment)
$tS_{lo}$	Time of lower bound of error interval (from quality assessment)
<b>Variables used/returned by STA/LTA Detector</b>	
$tS_{thr1}$	Time of threshold-based STA/LTA S-pick ('latest possible')
$tS_{min1}$	Time of minimum-based STA/LTA S-pick ('earliest possible')
<b>Variables used/returned by Polarization Detector</b>	
$tS_{thr2}$	Time of threshold-based polarization S-pick ('latest possible')
$tS_{min2}$	Time of minimum-based polarization S-pick ('earliest possible')
<b>Variables used/returned for AR-AIC Picker</b>	
$t_{AC}$	Time of initial pick for AIC configuration (from detectors or $tS_{pre}$ )
$AIC^C$	AIC function for component $C$ ( $C=N, E, T, Q$ , or $H$ ); $H=E+N$
$tS_{AC}$	Time of AIC-minium for component $C$ ( $C=N, E, T, Q$ , or $H$ )
$tS_{eC}$	Time of 'earliest possible' AIC-pick for component $C$
$tS_{lC}$	Time of 'latest possible' AIC-pick for component $C$

**Table 5.1:** Glossary of the most important variables used and returned by the different detectors and pickers.

resolution of the characteristic function of the STA/LTA detector and have to be determined in the calibration procedure.

To restrict the detection to possible S-phases, we have to ensure that no P-wave is present in the S-detection window. The proposed setup of the S-phase search windows uses  $tP_{obs}$  and  $tS_{pre}$  to determine a first coarse S-picking window. The coarse S-window is used to determine the position of the maximum horizontal amplitude  $y_{MHA}$  at time  $t_{MHA}$  as illustrated in Figure 5.2. We expect the actual S-phase onset to occur certainly prior to  $t_{MHA}$  and therefore, the lower and upper end of the search window ( $SW1$ ,  $SW2$ ) can be determined from the position of  $tP_{obs}$  and  $t_{MHA}$  as described in the electronic supplement.

The picking algorithm applied to the characteristic STA/LTA function within the search window is similar to the method proposed by *Baer and Kradolfer* (1987). We extended their threshold-based method by a 'minimum-picking' approach also suggested by *Cichowicz* (1993), where a (global) minimum of the characteristic function (CF) prior to the threshold-based pick is determined. The threshold  $thr_1$  is determined from the standard deviation  $\sigma_1$  of the STA/LTA function within the search window as described in the electronic supplement. A pick is declared if the actual STA/LTA exceeds the threshold  $thr_1$  and remains above the threshold for a minimum time  $t_{up}$ . To account for roughness and singularities present in characteristic functions derived from complex seismic signals, *Baer and Kradolfer* (1987)

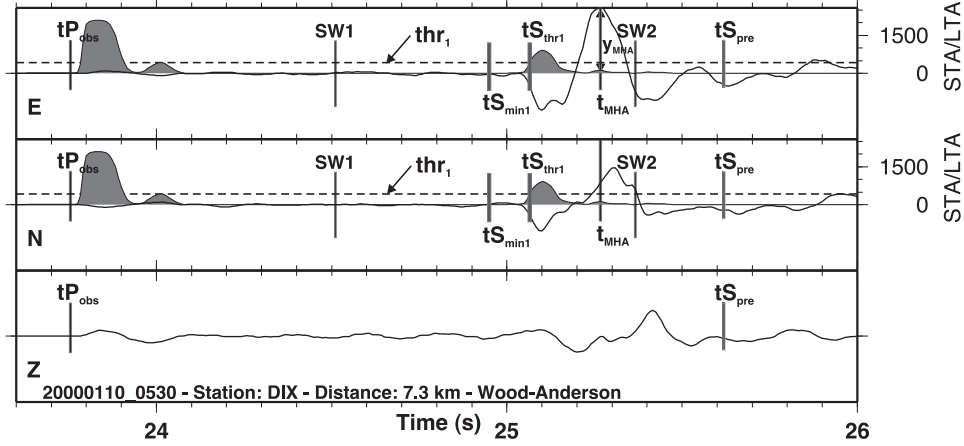


**Figure 5.2:** Combined STA/LTA approach used for S-wave detection on horizontal components. Black solid lines represent the Wood-Anderson filtered 3C seismograms (amplitudes normalized by station maximum) of a local earthquake in Switzerland ( $M_l=3.1$ , focal depth of 9 km). The gray shaded trace denotes the combined STA/LTA ratio derived from N and E components.  $tP_{obs}$  represents the known P-arrival time and  $tS_{pre}$  indicates the position of theoretical S-arrival predicted from a regional 1-D model. The dashed horizontal line denotes the dynamic threshold  $thr_1$  for the picking algorithm. The S-wave arrival time based on the STA/LTA detector in the potential S-window (SW1 to SW2) is most likely located in the interval between  $tS_{min1}$  (minimum pick) and  $tS_{thr1}$  (threshold pick). See text and Tables 5.1 for further description.

introduced the additional parameter  $tdw$ . The pick flag is not cleared if the CF drops below the threshold for a time interval less than  $tdw$ . Values for  $tup$  and  $tdw$  are determined in the calibration procedure. The corresponding threshold-based pick in Figure 5.2 is represented by  $tS_{thr1}$ .

Our ‘minimum-picking’ approach determines the minimum value of the CF prior to  $tS_{thr1}$  and is equivalent to a delay correction usually necessary for threshold-based picks. The corresponding ‘minimum’ pick is represented by  $tS_{min1}$  in Figure 5.2. Further details on the ‘minimum-picking’ are provided in the electronic supplement.

### 5.2.2 Polarization Detector

Polarization filters as described e.g., by *Flinn* (1965) and *Montalbetti and Kanase-wich* (1970) are commonly used to enhance the signal to noise ratio of seismic body waves. Rectilinearity (degree of linear polarization) and directivity of the particle motion are derived from eigenvalue analysis of the covariance matrix over small time intervals. Moreover, these time-domain filter operators can also be applied for identification of body phases, since compressional and shear waves exhibit a high degree of linear polarization in contrast to any Rayleigh-type wave. For known azimuth and incidence of the incoming wavefield, directivity of particle motion can be used to distinguish between compressional and shear waves. *Cichowicz* (1993) combined rectilinearity, directivity, and the ratio between transverse and total energy into one characteristic function  $CF_S$ , which is merely sensitive to S-wave

energy and omits all P phases (Pg, PmP, Sp, etc). The implementation of our polarization detector is mainly based on the approach of *Cichowicz* (1993) and its principles are briefly summarized in the following paragraphs.

As a first step, we determine the direction  $\vec{L}$  of the incoming P-wave. We compute the three-component covariance matrix within a narrow window around the known first arriving P-phase  $tP_{obs}$ . The back-azimuth  $\beta$  and the angle of incidence  $\varphi$  are derived from the eigenvector corresponding to the maximum eigenvalue of the covariance matrix. To separate P from SV and SH-energy, we rotate the observation system (ZEN) into a ray-coordinate system (LQT) using rotation angles  $\beta$  and  $\varphi$  (*Plešinger et al.*, 1986).

Finally, we calculate the directivity  $D(t)$ , rectilinearity  $P(t)$ , ratio between transverse and total energy  $H(t)$ , and a weighting factor  $W(t)$  within a centered window for each sample of the rotated time series. The length of the polarization filter used to analyze a seismogram is derived empirically from the observation-quality  $qP$  of the P-phase (for further details on window lengths see electronic supplement). The covariance matrix is determined from the centered window for each sample.

Directivity  $D(t)$  is defined as the normalized angle between  $\vec{L}$  and eigenvector  $\vec{\epsilon}_{max}$  corresponding to the maximum eigenvalue of the covariance matrix. The directivity operator is expected to be close to zero for the first arriving P-wave ( $\vec{\epsilon}_{max}$  parallel to  $\vec{L}$ ) and close to one for the first arriving S-wave ( $\vec{\epsilon}_{max}$  perpendicular to  $\vec{L}$ ). Rectilinearity  $P(t)$  is calculated using the formulation of *Samson* (1977) and it is expected to be close to one for both first arriving P- and S-waves. The ratio between transverse and total energy  $H(t)$  within the centered window is expected to be close to one for the first arriving S-wave and zero for the first arriving P-wave. As an addition to the original method of *Cichowicz* (1993), we calculate a weighting factor  $W(t)$  for each window, which accounts for the absolute amplitude within the centered window with respect to the maximum amplitude derived from the coarse S-window.

The product of the three squared filter operators with the weighting factor  $W(t)$  yields the modified characteristic function for S-wave detection  $CF_S$ :

$$CF_S(t) = D^2(t) \cdot P^2(t) \cdot H^2(t) \cdot W(t) \quad (5.1)$$

Figure 5.3 shows the LQT components of the same local earthquake from Figure 5.2 and the corresponding S-wave operators  $D(t)$ ,  $P(t)$ , and  $H(t)$ . The arrival of the S-wave (gray band) goes along with the simultaneous increase of  $D(t)$ ,  $P(t)$ , and  $H(t)$  and leads to a well-defined signature on  $CF_S$ .

The picking algorithm applied to  $CF_S$  is almost identical to the one used for the STA/LTA detector described above. A detailed description of the picking algorithm can be found in the electronic supplement. The threshold  $thr_2$  for the picker is derived from the standard deviation and the mean of  $CF_S$  within a defined window similar to the procedure proposed by *Cichowicz* (1993). An additional ‘water-level’ term  $cw$  was introduced, which stabilizes the picking in case of a large signal-to-noise ratio. Values for  $cw$ ,  $tup$ , and  $tdw$  are determined in the calibration procedure. The threshold-based pick on  $CF_S$  is represented by  $tS_{thr2}$

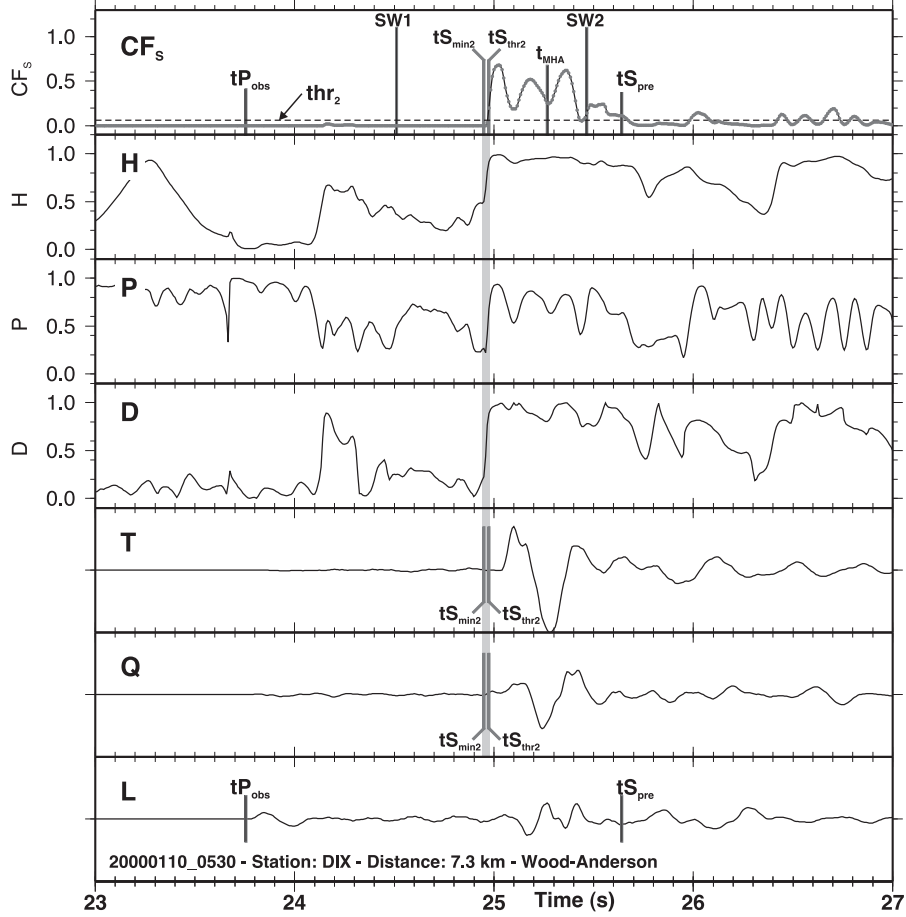


**Figure 5.3:** Example for the polarization detector applied to the same local earthquake of Figure 5.2. L, Q, T denote the rotated components. The corresponding S-wave operators are  $D(t)$  (directivity),  $P(t)$  (rectilinearity), and  $H(t)$  (transverse to total energy ratio). The uppermost trace represents the amplitude weighted characteristic S-wave function  $CF_s$ . The arrival of the S-wave (gray band) goes along with the simultaneous increase of  $D(t)$ ,  $P(t)$ ,  $H(t)$ , and  $CF_s$ . Compared to the actual arrival on T, the S-wave detection is shifted by approximate 0.1 s to earlier times. This time-shift is caused by the finite length of the polarization filter.  $CF_s$  is not affected by the P-wave. See text and Tables 5.1 for further description.

in Figure 5.3. In addition, we perform the minimum-picking prior to  $tS_{thr2}$  as described earlier to account for smaller precursory signals. The position of the minimum-pick is marked as  $tS_{min2}$  in Figure 5.3. Compared to the actual arrival on the transverse component,  $tS_{thr2}$  and  $tS_{min2}$  are shifted by approximate 0.1 s to earlier times (Fig. 5.3). This time-shift is caused by the finite length of the polarization filter. For emergent arrivals the time-shift is less significant.

### 5.2.3 Autoregressive Picker

Autoregressive (AR) models are very useful for the analysis of stationary time series. The non-stationary character of seismic signals can be approximated by dividing a time series into locally stationary segments each modeled as an AR process (*Kitagawa and Akaike, 1978*). Since the corresponding models are expected to be different before and after the arrival of a signal, such AR models can be used to automatically pick the arrival time of seismic phases by finding the time which attains the minimum AIC (Akaike Information Criterion, *Akaike 1973*) value of a locally stationary AR model.

Theory and implementation of different AR-AIC picking algorithms are described e.g., in *Takanami and Kitagawa (1991)*, *Leonard and Kennett (1999)*, or *Sleeman and van Eck (1999)*. Although multivariate AR approaches appear to be slightly more appropriate for robust S-wave picking (e.g., *Takanami and Kitagawa, 1993*; *Leonard and Kennett, 1999*), the application of the univariate method to single components (N, E, Q, T) and combined components (E+N) provides additional details about uncertainty of timing and phase identification. Our implementation is mainly based on the method of *Takanami and Kitagawa (1988)*, which uses an univariate AR fitting approach to derive automatic arrival times. A detailed description of the AR modeling is provided in the electronic supplement.

In practice, the method of *Takanami and Kitagawa (1988)* requires a noise model  $AIC_i^{forw}$  calculated forward in time starting at  $t_{NS}$  and ending at  $t_{SS}$ , assuming the noise part is included in the window from  $t_{NS}$  to  $t_{NE}$  as illustrated in the lower box of Figure 5.4. In addition, the signal model  $AIC_i^{back}$  is calculated backward in time starting at  $t_{SE}$  and ending at  $t_{NE}$ , where parts of the signal are expected to be included in the window between  $t_{SS}$  and  $t_{SE}$ . By simply adding  $AIC_i^{forw}$  and  $AIC_i^{back}$  for common samples of the time series, we obtain the  $AIC_i$  of the locally stationary AR model. If  $i_{min}$  corresponds to the sample of the minimum  $AIC_i$  value, then  $i_{min} + 1$  represents the best estimate of the arrival time. Moreover,  $AIC_i$  from different components can be added to give combined AIC functions, e.g.  $AIC^H$  represents the sum of the horizontal components N and E. In Figure 5.4 the AIC functions have the typical shape with well developed minima around the actual onset of the S-wave. The AR-AIC estimated picks  $tS_{AQ}$  and  $tS_{AT}$  agree very well with the arrival observed on the different components. The onset appears more impulsive on the T component, which is also indicated by the sharper minimum on  $AIC^T$  compared to the one observed on  $AIC^Q$ .

Due to their fundamental concept, predictive AR-AIC pickers always require an initial pick  $t_{AC}$  to setup a noise model window  $\Delta LN$  and signal model window

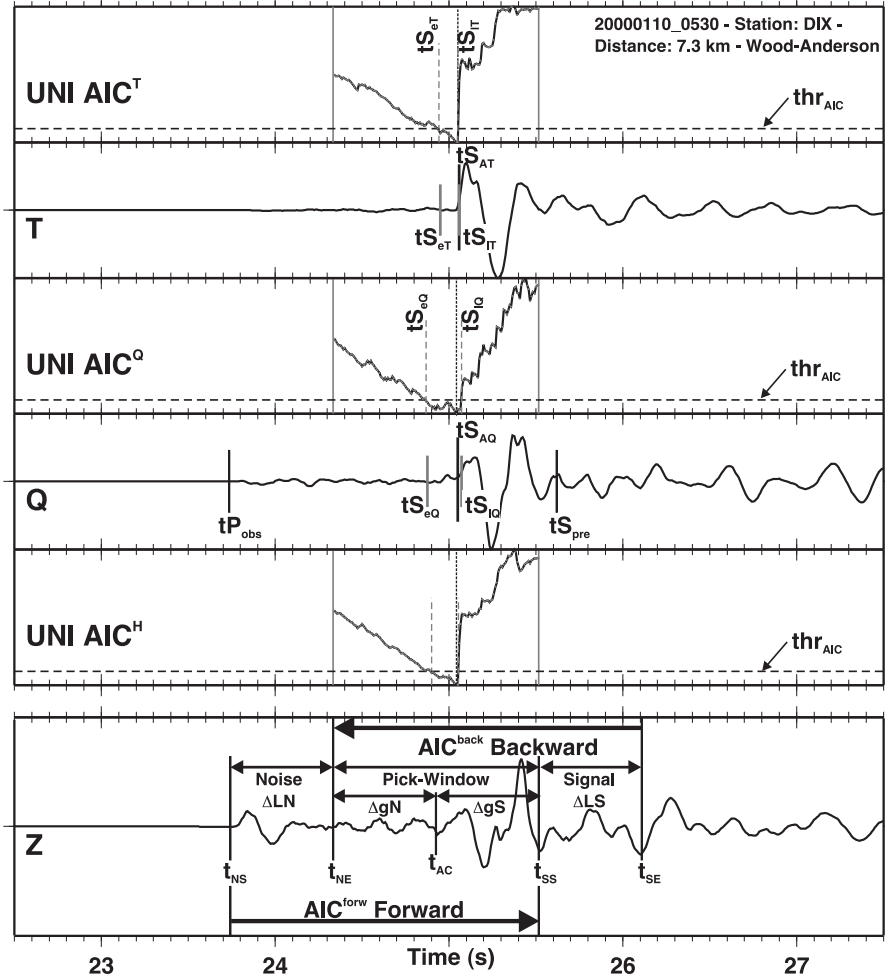


**Figure 5.4:** Example for the AR-AIC picker applied to the same local earthquake of Figure 5.2. All amplitudes are trace normalized. The lower box illustrates the search window configuration centered around  $t_{AC}$ . The corresponding univariate AIC functions are shown for the combination of original E+N components ( $AIC^H$ ) and for the rotated components Q ( $AIC^Q$ ) and T ( $AIC^T$ ). AR-AIC picks  $t_{SAQ}$  and  $t_{SAT}$  derived from the minimum on the AIC functions agree very well with the actual arrival of the S-wave visible on the seismograms. The uncertainty of the AR-AIC pick is expressed by the ‘earliest’ and ‘latest’ possible arrival times  $t_{SeQ}$ ,  $t_{SeT}$ ,  $t_{SIQ}$ , and  $t_{SIT}$  derived from intersection of threshold  $thr_{AIC}$  (dashed horizontal lines) with the corresponding AIC functions. See text and Tables 5.1 for further description.



$\Delta LS$  separated by the picking window  $\Delta gN + \Delta gS$  (Fig. 5.4). Previous implementations of AR-AIC pickers such as *Sleeman and van Eck* (1999) or *Akazawa* (2004) mainly use triggers from STA/LTA detectors and fixed window lengths for this purpose. The quality of AR-AIC pickers, however, depends strongly on the degree of separation between noise and signal in the analysis window from  $t_{NS}$  to  $t_{SE}$  as discussed by *Zhang et al.* (2003). This can be critical if several phases are present within the window (e.g., Pg and Sg at very short epicentral distances or Sn and Sg at larger distances). Figure B.4 and B.5 present examples of such misconfigured AR-AIC search windows.

To avoid such misconfigured windows, minimum *a priori* information is required to guide the picker to the correct phase and to setup the AR-AIC search windows properly. We implemented a distance-dependant procedure for a dynamic configuration of AR-AIC search windows as described in the electronic supplement. Basically,  $tP_{obs}$  and information from both detectors are used for AR-AIC configuration at near-by epicentral distances. For distances  $\geq \Delta_{AIC_1}$  the AR-AIC configuration is mainly based on the predicted arrival time  $tS_{pre}$ . Above  $\Delta_{AIC_3}$  the usually weak Sn-phase is expected to be the first arriving S-wave. The correct identification requires a modified setup using information from detectors and  $tS_{pre}$ . Values for  $\Delta_{AIC_1}$  and  $\Delta_{AIC_3}$  have to be determined in the calibration procedure.

### 5.2.4 Quality Assessment in Combined Approach

Quality assessment implemented in automatic picking procedures have to provide realistic estimates on the timing uncertainty of a pick, as well as a minimum information on actual phase identification. Sophisticated pattern recognition methods used e.g., by *Aldersons* (2004) usually classify the quality of the onset based on wavelet characteristics in the close vicinity of the automatic pick. These methods, however, do not yet provide information on the phase type, in particular, if it is a first or later arriving phase.

Robust uncertainty estimates for automatic S-arrivals can be obtained by combining picking information from different techniques to define lower  $tS_{lo}$  and upper  $tS_{up}$  limit of the error interval. The mean position of this interval  $tS_{me} = (tS_{up} + tS_{lo})/2$  is defined as the S-arrival time. In our approach, the earliest and latest possible pick from the STA/LTA detector ( $tS_{min1}, tS_{thr1}$ ), polarization detector ( $tS_{min2}, tS_{thr2}$ ), and the different AIC minima ( $tS_{AC}$ , with  $C = N, E, Q, T, H$ ) constitute the lower and upper limits of the corresponding error interval.

In addition, the width of the AIC minimum is usually related to the quality of the onset. Impulsive wavelets like the S-arrival on the T component in Figure 5.4 lead to a distinct AIC minimum, whereas emergent wavelets produce broader minima (Q component in Fig. 5.4). The width of the AIC minimum can therefore be used as an additional quality information about the arrival time and is also a good indicator for the presence of possible precursory phases. We define the earliest possible arrival derived from the AIC function as the first sample where AIC drops below the threshold  $thr_{AIC}$  and the latest possible arrival as the last sample below  $thr_{AIC}$  (see Fig. 5.4). The definition of threshold  $thr_{AIC}$  is provided

in the electronic supplement. The corresponding positions of ‘earliest-possible’ and ‘latest-possible’ arrivals are represented by  $tS_{eT}$ ,  $tS_{eQ}$ ,  $tS_{lT}$ , and  $tS_{lQ}$ . The usage of the AIC-quality assessment becomes especially important for appropriate uncertainty estimates at larger epicentral distances. In the following, we define the distance  $\Delta_{AIC_2}$  above which the AIC quality assessment is considered for the overall quality assessment.

Since detectors and components are sensitive to different phase types in different distance ranges, we setup four different weighting scenarios based on tests with the reference data set. The weighting scenarios are described in further detail in the electronic supplement. The basic principles are summarized in Table 5.2. The

		Scenario 1	Scenario 2	Scenario 3	Scenario 4
Epicentral distance $\Delta_{epi}$		$< \Delta_{AIC_3}$	$< \Delta_{AIC_3}$	$\geq \Delta_{AIC_3}$	$\geq 0$ km
Expected first S-phase		Sg	Sg	Sn	any
STA/LTA detection		?	+	?	-
Polarization detection		+	-	?	-
<b>STA/LTA</b>	$tS_{min1}$		X		<b>Rejected</b>
	$tS_{thr1}$		X		
<b>Polarization</b>	$tS_{min2}$	X			
	$tS_{thr2}$	X			
<b>AR-AIC</b>	$tS_{AH}$	X	X	X	
	$tS_{eH}$	O	O	X	
	$tS_{lH}$			X	
	$tS_{AT}$	x	X	X	
	$tS_{eT}$	o	O	X	
	$tS_{lT}$			X	
	$tS_{AQ}$	x	X	X	
	$tS_{eQ}$	o	O	X	
	$tS_{lQ}$			X	
	$tS_{AN}$		X	X	
	$tS_{eN}$		O	X	
	$tS_{lN}$			X	
	$tS_{AE}$		X	X	
	$tS_{eE}$		O	X	
	$tS_{lE}$			X	

**Table 5.2:** Summary of quality weighting scenarios. Detector flags: (+) detection of S-wave, (?) detection of S-wave possible, (-) no detection of S-wave. Time used for quality assessment: (X) use time, (x) use time if time is closest to  $tS_{min2}$ , (O) use time if  $\Delta_{epi} \geq \Delta_{AIC_1}$ , (o) use time if  $\Delta_{epi} \geq \Delta_{AIC_1}$  and if time is closest to  $tS_{min2}$ . See text and electronic supplement for further details on how final S-pick and associated quality class is computed. For further description of variables see Tables 5.1 and 5.4.

error interval derived from the appropriate weighting scenario is used to calculate the mean position of the S-wave arrival and to assign a discrete quality class according to an *a priori* user defined weighting scheme.

Finally, a minimum amplitude signal-to-noise ratio  $S2N_{min}(m)$  is defined for each

quality class  $m$ . If the signal-to-noise ratio of the current pick is less than  $S2N_{min}(m)$ , the pick is downgraded to the next lower quality class and its signal-to-noise ratio is checked again for the new class. Since we expect smaller signal-to-noise ratios for potential Sn phases, we define different sets of  $S2N_{min}(m)$  above and below  $\Delta_{AIC_3}$ . Figure 5.5 shows examples for different automatic S-wave arrival picks and their corresponding error intervals at local to regional distances (further examples are provided in Figure B.6). The mean position and the error intervals of the

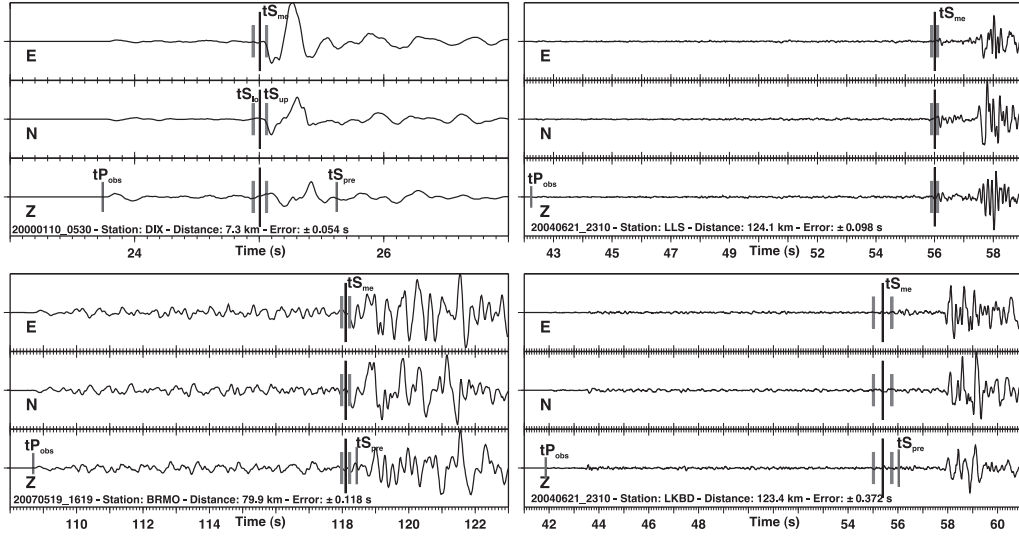


**Figure 5.5:** Examples of automatic S-wave picks at epicentral distances dominated by first arriving Sg phases (left column) and first arriving Sn phases (right column) for different error intervals. The error interval derived from the automatic quality assessment is represented by the vertical gray bars. The vertical long black bars denote the mean position of the S-wave onset. Error interval and mean position agree very well with the actual S-wave arrival observed on the seismograms.

automatic picks agree very well with the actual S-wave arrival observed on the seismograms.

Provided that a reliable origin time  $t_0$  exists, we can define an expected S-window from the arrival time of the P-phase  $tP_{obs}$ , a minimum  $v_P/v_S$  ratio  $\kappa_{min}$ , and a maximum  $v_P/v_S$  ratio  $\kappa_{max}$ . Assuming a similar ray-path for the P and S-waves, the earliest possible S-arrival is defined by  $S_{lo} = (tP_{obs} - t_0) \cdot \kappa_{min}$  and the latest possible S-arrival is defined by  $S_{up} = (tP_{obs} - t_0) \cdot \kappa_{max}$ . Automatic picks outside this expected S-window will be rejected. Such a  $v_P/v_S$ -filter reduces the number of mispicks due to phase misidentification. Since we expect larger variations in  $v_P/v_S$  for crustal phases at smaller epicentral distances (major part of ray-path within heterogeneous upper crust) we define different  $v_P/v_S$  ranges above and below  $\Delta_{AIC_3}$ .

## 5.3 Case Study: Application to the Alpine Region

Before an automatic picker can be applied to a large (unpicked) data set in a ‘Production-Mode’, its performance has to be tested and compared with a smaller number of consistent reference hand picks in a ‘Test-Mode’ as described e.g., by *Di Stefano et al. (2006)* and *Diehl et al. (2008)*. This procedure also involves the iterative calibration of the previously described picker components. The reference data set and the calibration procedure are summarized in the following sections. Subsequently, we present results of the production-mode applied to 552 local earthquakes in the Alpine region.

### 5.3.1 Reference Data Set

Our reference data set consists of three-component recordings of 49 local earthquakes in the greater Alpine region (white stars in Fig. 5.6). We considered

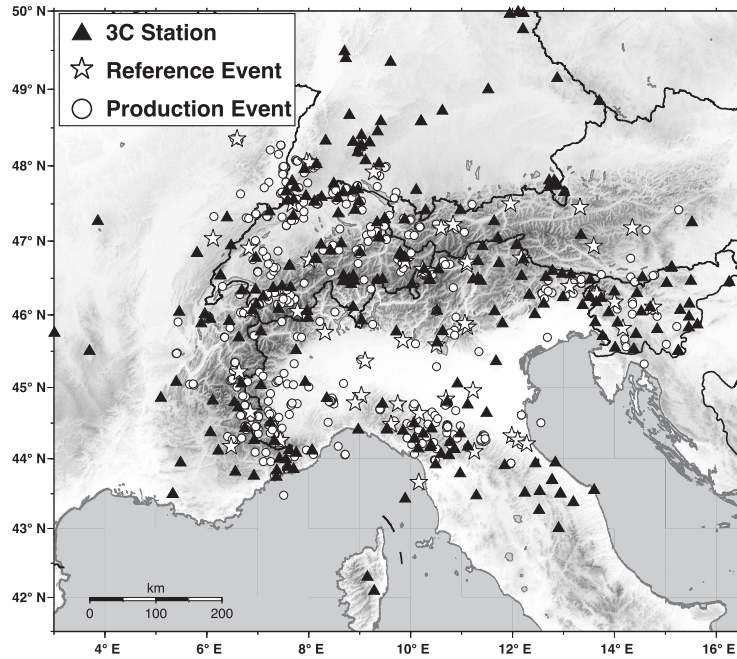


**Figure 5.6:** Map of three-component stations and earthquakes in the Alpine region used for the case study. Black triangles indicate stations, white stars denote locations of reference events used for the calibration of the picker, and white circles correspond to events used for the production-mode.

epicentral distances  $\Delta_{epi} \leq 150$  km for this test. Above 150 km distance, visual identification and picking of S-waves becomes rather uncertain and therefore, it is difficult to compare manual picks with automatic picks.

For the reference S-picking we considered ZNE as well as rotated RT-components.

Each phase pick is associated with an uncertainty in timing and phase identification as described in *Diehl et al.* (2008). The reference data set features certainly a higher level of consistency than routinely determined S-wave picks provided in standard bulletin data. However, particular quality checks (e.g., Wadati diagrams) were not performed, and as a consequence the reference data may contain also some misidentified arrivals.

Table 5.3 shows the weighting scheme used for reference S-wave picking and the numbers of reference picks for each class. From 797 potential S-waves to pick

S-Quality class $qS$	Error $\varepsilon_{qS}$ (s)	Weight (%)	Nr. of Reference Picks
0	$\pm 0.10$	100	153 (19.2%)
1	$\pm 0.20$	50	280 (35.1%)
2	$\pm 0.40$	25	176 (22.1%)
3	$> 0.40$	0 (rejected)	188 (23.6%)
Usable classes: 0 - 2 (76.4% of potential S-phases)			
Average picking uncertainty of usable reference phases: 0.23 s			

**Table 5.3:** Weight assignments based on picking errors for reference S-waves from 49 local and regional earthquakes in the greater Alpine region. Numbers of reference picks refer to epicentral distances  $\leq 150$  km and potential S-phases to pick (3C recording, existing P-pick).

( $\Delta_{epi} \leq 150$  km, 3C recording, existing P-pick), 609 (76.4%) are classified as usable qualities (class 0-2). The rest are rejected (class 3). The estimated average picking uncertainty can be derived from the number of picks and the uncertainty interval of each class as described by Eq. B.17. If we consider only picks of usable quality classes, the average picking uncertainty of the reference data set is about 0.23 s.

### 5.3.2 Calibration and Test-Mode

The calibration of our picking approach basically consists of an iterative trial-and-error procedure. Parameters of the picking components have to be iteratively adjusted until the resulting performance fulfills the requirements for use in high-resolution tomography as described by *Di Stefano et al.* (2006) and *Diehl et al.* (2008). The assessment of the picker-performance for a given set of (appropriate) parameters is described in the following section. Some guidelines on how a set of appropriate parameters is derived for a certain data set is provided at the end of this paragraph.

#### Assessment of Picker-Performance

We applied the automatic picking approach to the waveforms of the reference data set and compared timing and error assessment against reference picks. Predicted S-arrival times are calculated in the regional minimum 1-D P-wave model

of *Diehl et al.* (2008) divided by a constant  $v_P/v_S$  ratio of 1.70. The corresponding hypocenters are relocated in the same minimum 1-D model as described by *Kissling* (1988) or *Husen et al.* (1999) using only P-arrivals. The optimal performance was obtained with the picking parameters summarized in Table 5.4. The suggested values are derived from a parameter search, which is described below. The resulting performance of the automatic picker and the error assessment can be displayed in matrix form, as illustrated in Table 5.5. A satisfactory automatic

Parameter	Description	Value
<b>General Parameters</b>		
$\Delta_{epi}^{max}$	Maximum epicentral distance	150 km
$\Delta_{AIC_3}$	Distance above which Sn is expected as first-arrival	100 km
<b>Parameters for STA/LTA Detector</b>		
$\Delta_{st}$	Length of short-term window	0.2 s
$\Delta_{lt}$	Length of long-term window	2.0 s
$tup$	Minimum time $CF$ above threshold	0.05 s
<b>Parameters for Polarization Detector</b>		
$cw$	‘Water-level’ to stabilize the picking	0.06
$tup$	Minimum time $CF_S$ above threshold	0.10 s
$tdw$	Maximum time $CF_S$ drops below threshold	0.05 s
<b>Parameters for AR-AIC Picker</b>		
$\Delta_{AIC_1}$	Distance above which predicted S is used for configuration	70 km
$\Delta_{gN}, \Delta_{gS}$	Initial length of picking window (before/after $t_{AC}$ )	1.0 s
$\Delta_{LN}, \Delta_{LS}$	Initial length of noise/signal model window	1.0 s
<b>Parameters for Quality Assessment</b>		
$\Delta_{AIC_2}$	Distance above which AIC-quality is considered	50 km
$S2N_{min}^1(0)$	Minimum signal to noise ratio for class 0 ( $\Delta_{epi} < \Delta_{AIC_3}$ )	3
$S2N_{min}^1(1)$	Minimum signal to noise ratio for class 1 ( $\Delta_{epi} < \Delta_{AIC_3}$ )	3
$S2N_{min}^2(0)$	Minimum signal to noise ratio for class 0 ( $\Delta_{epi} \geq \Delta_{AIC_3}$ )	3
$S2N_{min}^2(1)$	Minimum signal to noise ratio for class 1 ( $\Delta_{epi} \geq \Delta_{AIC_3}$ )	2

**Table 5.4:** Summary of basic parameters which have to be adjusted for the described picking approach. The suggested values are derived from a parameter search that compares automatic picks with reference picks of local earthquakes within the greater Alpine region as described at the end of section 5.3.2.

picking and quality assessment is achieved if the deviation between the automatic and reference picks is within the error interval of the corresponding automatic quality classification ( $\sigma_{ij} \leq \varepsilon_j$  and  $\sigma_j \leq \varepsilon_j$ ), and if only a few low quality reference picks are upgraded to higher quality classes by the automatic picker (Table 5.5). Both requirements are satisfied with our automatic picker. All  $\sigma_j$  are less-than or equal  $\varepsilon_j$  (lowermost row of Table 5.5) and none of the reference class ‘3’ picks (rejected class) is upgraded to high-quality class ‘0’ or ‘1’ (dark shaded matrix-fields in Table 5.5). Only two reference picks that were rejected (not picked due to complicated waveforms) were upgraded to class ‘2’ by the automatic picker.

### 5.3 CASE STUDY: APPLICATION TO THE ALPINE REGION

		Automatic Quality Classification				
		0	1	2	3 (rej)	$\Sigma$ Ref
Reference Quality Classification	0	$N_{00} = 59$ 38 % $\sigma_{00} = 0.06$ s	$N_{01} = 38$ 25 % $\sigma_{01} = 0.12$ s	$N_{02} = 24$ 16 % $\sigma_{02} = 0.24$ s	$N_{03} = 32$ 21 % $\sigma_{03} = 1.07$ s	$N_0^{Ref} = 153$ $ \varepsilon_0  \leq 0.1$ s
	1	$N_{10} = 14$ 5 % $\sigma_{10} = 0.10$ s	$N_{11} = 31$ 11 % $\sigma_{11} = 0.14$ s	$N_{12} = 78$ 28 % $\sigma_{12} = 0.33$ s	$N_{13} = 157$ 56 % $\sigma_{13} = 1.24$ s	$N_1^{Ref} = 280$ $ \varepsilon_1  \leq 0.2$ s
	2	$N_{20} = 0$ 0 % $\sigma_{20} = 0.00$ s	$N_{21} = 13$ 7 % $\sigma_{21} = 0.17$ s	$N_{22} = 35$ 20 % $\sigma_{22} = 0.33$ s	$N_{23} = 128$ 73 % $\sigma_{23} = 1.60$ s	$N_2^{Ref} = 176$ $ \varepsilon_2  \leq 0.4$ s
	3 (rej)	$N_{30} = 0$ 0 % $\sigma_{30} = 0.00$ s	$N_{31} = 0$ 0 % $\sigma_{31} = 0.00$ s	$N_{32} = 2$ 1 % $\sigma_{32} = \text{Not av.}$	$N_{33} = 186$ 99 % $\sigma_{33} = 0.69$ s	$N_3^{Ref} = 188$ $ \varepsilon_3  > 0.4$ s
	$\Sigma$ Aut	$N_0^{Aut} = 73$ $\sigma_0 = 0.07$ s $\overline{\Delta AR}_0 = -0.03$ s	$N_1^{Aut} = 82$ $\sigma_1 = 0.15$ s $\overline{\Delta AR}_1 = 0.02$ s	$N_2^{Aut} = 139$ $\sigma_2 = 0.31$ s $\overline{\Delta AR}_2 = 0.11$ s	$N_3^{Aut} = 503$	

**Table 5.5:** Performance of automatic S-wave picker (4 quality classes) in matrix presentation similar to *Di Stefano et al. (2006)*. The number of picks of reference class  $i$  classified by the automatic picker as class  $j$  is represented by  $N_{ij}$ . Percentages correspond to the number of automatic picks per reference quality class. Diagonal elements represent correctly classified automatic picks (reference and automatic weight are the same). Off-diagonal elements represent picks up- or downgraded by the automatic picker.  $N_i^{Ref}$  for each row is equal to the sum over  $j$  of the corresponding  $N_{ij}$ ;  $N_j^{Aut}$  for each column is equal to the sum over  $i$  of the corresponding  $N_{ij}$ . The  $\sigma_{ij}$  denote the standard deviation of the difference  $\Delta AR$  between automatic and reference pick for each matrix element. The  $\varepsilon_i$  refer to the error of quality class  $i$  used for reference picking and  $N_j^{Aut}$ ,  $\sigma_j$ , and  $\overline{\Delta AR}_j$  represent number, standard deviation, and mean of  $\Delta AR$  for all automatic picks classified as  $j$ , respectively.

Furthermore, we observe no significant systematic bias between automatic picks and reference picks (lowermost row of Table 5.5). The mean value of  $\Delta AR$  seems slightly negative (automatic earlier than reference pick) for highest quality class ‘0’. For lower quality classes, automatic picks tend to be marginally delayed in comparison to reference picks. The upper limit of the average uncertainty for all usable automatic picks can be estimated as described earlier. We obtain an average uncertainty of 0.27 s, which is only 40 ms larger than the average uncertainty derived from the reference picks.

Although the accuracy of the automatic picker is comparable to the reference picks, the automatic picker downgrades a large number of potential high-quality picks to lower classes (Table 5.5). Especially for class ‘1’ and ‘2’ more than half of the reference picks are rejected by the automatic picker. In addition, the recovery rate of 11% for class ‘1’ is rather low compared to class ‘0’ (38%) and ‘2’ (20%).

As discussed in the electronic supplement, an appropriate weighting scheme for seismic tomography can be achieved by merging class ‘0’ and ‘1’. The simplified weighting scheme contains only two usable (‘0’ and ‘1’) and one reject class (‘2’) as illustrated in Table B.3. The highest quality represents the largest populated class, and the average picking uncertainty adds up to about 0.29 s in this new weighting scheme (only slightly higher than the average uncertainty in the original

weighting scheme). Such a well-balanced weighting scheme facilitates the model parametrization for tomography. On the other hand, the original weighting scheme of Table 5.5 is more suitable for earthquake location problems, since it contains S-arrivals of high accuracy (class ‘0’,  $\pm 0.1$  s), which are assigned with a higher uncertainty of  $\pm 0.2$  s in the merged weighting scheme. In the earthquake location problem, S-arrivals of high accuracy significantly reduce the location uncertainty. To assess the performance of the automatic picker especially regarding systematic mispicks and outliers present in the test-mode, we display the difference between automatic and reference S-picks ( $\Delta AR$ ) for usable automatic picks against epicentral distance in Figure 5.7. In general, the number of outliers is low and the corresponding errors are large. The number of gross outliers increases in the dis-

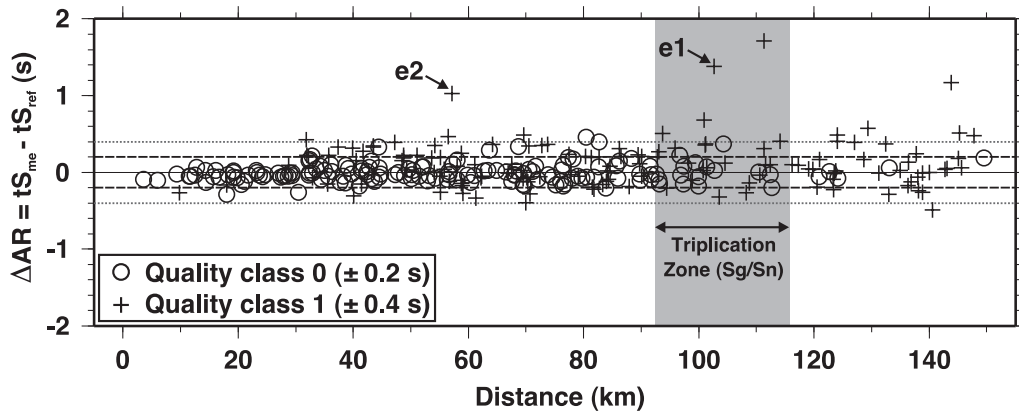


**Figure 5.7:** Difference between automatic and reference pick  $\Delta AR$  against epicentral distance for usable automatic picks of class 0 (circles) and 1 (crosses) in simplified weighting scheme. Dashed lines represent the error interval of class 0 ( $\pm 0.2$  s), dotted lines indicates error interval of class 1 ( $\pm 0.4$  s). The number of gross outliers increase in the distance range of the triplication zone. In this distance range the first arriving weak Sn is followed by an impulsive Sg and a mispick on a later phase is likely.

tance range of the triplication zone (Fig. 5.7), due to misinterpretation of later arriving phases such as Sg or SmS.

An additional technique to identify mispicked S-arrivals is the use of Wadati diagrams as described, for example, by *Kisslinger and Engdahl* (1973) or *Maurer and Kradolfer* (1996). Examples and results of such procedures are provided and discussed in the electronic supplement. The modified Wadati diagram of Figure B.7b suggests difficulties and ambiguity in manually picking and identification of S-waves, especially beyond the cross-over distance between Sn and Sg. On the other hand, the more conservative quality assessment of the automatic approach significantly reduces the scatter in S-phase arrivals (Fig. B.7a) at the cost of a lower number of usable picks. Finally, we point out that prior to any final velocity model estimation, the consistency of the automatic S-picks have to be evaluated in an iterative inversion procedure as described e.g., by *Kissling* (1988) or *Diehl et al.* (2008). Identified mispicks have to be removed from the data set.



### Parameter Search Procedure

To derive a satisfactory picker-performance for a certain data set, appropriate values of the parameters listed in Table 5.4 have to be evaluated from a trial-and-error procedure. The picker is applied to the reference data for each set of parameters and its resulting performance has to be assessed as described in the previous section. To facilitate the parameter search we provide some guidelines on how the parameter have to be evaluated.

The general parameters  $\Delta_{epi}^{max}$  and  $\Delta_{AIC_3}$  depend mainly on the Moho topography of a region and the data quality. Initial values can be estimated from the analysis of reference or routine picks versus epicentral distance. The break-off of reliable Sn observations indicates  $\Delta_{epi}^{max}$ , the characteristic kink in regional travel-time curves indicates the approximate crossover distance  $\Delta_{AIC_3}$ .

Subsequently, both detectors should be separately adjusted aiming at a compromise between hit-rate and accuracy and at avoiding large numbers of false detections. As for the combined approach, the performance of detectors has to be checked against the reference data. The choice of  $\Delta_{st}$  and  $\Delta_{lt}$  mainly controls the degree of resolution of the CF. A lower resolution usually results in more stable detection. Time thresholds  $tup$  and  $tdw$  control the sensitivity of the detectors and depend mainly on the expected dominant frequency of the signal. For  $tup$  we suggest initial values between half and twice the smallest error interval  $\varepsilon_0$  used for the reference picking. Since  $tdw$  accounts for short singularities in the CF we suggest a value between 0 and  $tup$ . The water-level  $cw$  should be estimated from a few high signal-to-noise S-phases. Before choosing our preferred value of 0.06 we tested a range between 0 and 0.1 with our data set.

Due to the dynamic configuration of search windows in our AR-AIC picker, the choice of initial picking windows ( $\Delta_{gN}, \Delta_{gS}$ ) and model windows ( $\Delta_{LN}, \Delta_{LS}$ ) is less critical. The model and noise window depend mainly on the maximum expected period and the initial picking window can be estimated from the maximum deviation between predicted arrival and actual arrival time in the reference data. Values about 0.5 to 2 s should be appropriate. The initial value of  $\Delta_{AIC_1}$  can be estimate from the distance above which detectors become less reliable. Initially, it can also be set to  $\Delta_{AIC_3}$  and then stepwise reduced until a satisfactory accuracy is achieved.

Initially, all parameters related to the quality assessment can be ‘disabled’ by using a corresponding default value ( $\Delta_{AIC_2} = \Delta_{epi}^{max}$ , minimum  $S2N = 1$  for all classes, etc.). If the resulting performance does not fulfill the requirements,  $\Delta_{AIC_2}$  should be gradually reduced. If there are still single mispicks present in the resulting automatic picks, certain minimum signal-to-noise thresholds have to be defined. Of course, highest quality classes should denote higher thresholds. After final consistency checks like Wadati diagrams, additional  $v_P/v_S$ -filters can be defined by  $\kappa_{min}$  and  $\kappa_{max}$ . Eventually, the performance for different frequency bands should be tested by applying specific waveform filters. Further information is provided in the electronic supplement.

### 5.3.3 Production-Mode

In the production-mode the calibrated automatic picker is applied to a data set of 552 local earthquakes in the Alpine region (white circles in Fig. 5.6). The majority of the approximately 13'300 P-arrivals in this data set were picked with the MPX picking tool of *Aldersons* (2004) as described in *Diehl et al.* (2008). Predicted S-arrival times are calculated in the same 1-D velocity model used for the test-mode. Within this data set, 4986 seismograms satisfy the minimum requirements for automatic S-phase picking (P-pick available, 3C recording,  $\Delta_{epi} \leq 150$  km). Since our picking approach assumes the S-wave arrival before and close to the maximum horizontal amplitude  $y_{MHA}$ , it requires that spikes and clipped amplitudes are detected and removed from the data. We implemented a running average despiking routine and a clipping detector, which are applied prior to the picking procedure. Waveforms with clipped amplitudes are rejected by default. The despiking routine and the clipping detector were calibrated during the test-mode. From the 4986 potential 3C recordings, 453 (9%) are rejected due to clipped amplitudes.

The production-mode yields 1618 class '0' ( $\pm 0.2$  s) and 973 class '1' ( $\pm 0.4$  s) automatic picks. Hence, 57% of the (non-clipped) potential S-phases could be picked with our approach. If outliers are disregarded, the average picking uncertainty amounts to about 0.27 s. Since outliers are associated with errors up to several seconds, they lower the average accuracy of the automatic picks significantly. Therefore, outliers from the production-mode have to be identified and removed from the data set as described in the electronic supplement. S-picks indicating  $v_P/v_S$  ratios  $> 1.75$  were cross-checked against waveforms for distances  $> 50$  km in a semi-automatic procedure to assess the number of outliers due to misinterpreted phases. From 450 analyzed automatic picks, 42 (9%) were identified as obvious mispicks or highly questionable automatic picks. Most of these mispicks resulted from phase misinterpretation analogous to example *e1* in Figure 5.7 in the distance range of the triplication zone (90-110 km). The 42 clearly identified mispicks represent about 2% of all automatic picks.

## 5.4 Discussion and Conclusion

The approach presented in this work integrates three of the most commonly used techniques for automatic S-wave detection and picking. If applied independently, none of the described methods is able to provide robust automatic picks at local to regional distances. STA/LTA pickers are rather sensitive to later P-wave energy present in the coda, polarization pickers can fail due to uncertainty in rotation or an insufficient degree of linear polarization, and the reliability of AR-AIC pickers depend strongly on the setup of the corresponding search windows.

By combining different picking techniques we improve the stability of the automatic picking, and in addition we derive 'in-situ' information about timing uncertainty and phase identification of the automatic picks. Our automatic approach

provides timing accuracy comparable with manually picked S-arrivals. More important, classification of impulsive high-quality S-waves agrees very well with the manual error assessment. Compared to the reference picks, emergent and complex S-arrivals are classified rather conservatively by the automatic picker. On the other hand, only very few poor-quality S-arrivals are upgraded by the automatic picker to usable quality classes. The conservative quality assessment of the automatic picker results in a lower number of usable picks but with less outliers as compared to the reference picks.

The number of automatic mispicks due to misinterpretation of impulsive later-arrivals increases especially in the range of the crossover distance between the Sg and the Sn phase. Detectors as well as predictive AR-AIC picker often miss the preceding weak Sn phase. The main difficulty for the predictive AR-AIC picker is the proper configuration of the noise and the signal model windows. If parts of the impulsive later arriving phase are included in the signal window, a detection of the preceding small Sn is usually impossible. A first step to overcome this problem is the proposed dynamic configuration of the windows utilizing additional information from the STA/LTA function. Although this method avoids already some of the misinterpretation, it still fails for a large number of Sn phases. A possible future approach could include an AR-modeling window, moving from the noise part towards the expected Sn signal as proposed e.g., by *Bai and Kennett* (2000). The onset of a seismic signal is then characterized by increased order and values of the AR coefficients. Furthermore, multivariate AR-modelling might improve the success rate of the AR-AIC component. As an addition, the polarization analysis can be extended to include the uncertainty in the rotation angles and by the use of complex traces as suggested e.g., by *Vidale* (1986), *Bai and Kennett* (2001), or *Greenhalgh et al.* (2005). Such further developments might lead to an improved performance of the polarization detector at larger distances. Future extensions should also include adaptive techniques to facilitate the calibration of the presented approach. Accounting for the dominant frequencies of the signals and pattern recognition techniques might reduce the number of user-defined parameters.

The outliers present in the reference data demonstrate that incorrect identification of S-phases (especially Sn) is also a significant problem in hand picked data sets. The implementation of characteristic functions provided by detectors and AR-modeling into routine picking tools could facilitate and improve the visual identification and picking of S-waves.

The resolution and reliability of tomographic models is strongly dependent on the quality and consistency of the inverted arrival-time data. To derive consistent and large data sets for regional models we have to apply automated re-picking to waveform data, since routine phase data from different networks usually do not contain a common quality assessment. Considering the large amount of data necessary for high-resolution regional tomographic models, manually re-picking of waveforms does not represent a feasible alternative. As mentioned before, the average accuracy of our automatic approach is comparable to the average accuracy

of manually picked S-arrivals. In 3-D body wave tomography the minimum resolution of a velocity perturbation depends mainly on the model parametrization and the data error. A  $v_P/v_S$  perturbation of +5% within the mid-crust in a volume of  $25 \times 25 \times 15$  km, results in an  $S - P$  residual of  $\Delta_{SP} = 0.29$  s, assuming a background  $v_P/v_S = 1.73$ ,  $v_P = 6.0$  km/s, and a ray length of 20 km through the 3-D volume. This anomaly in  $v_P/v_S$  can only be resolved if the sum of the absolute observation errors in the P and S-wave arrivals is smaller than  $\Delta_{SP}$ . With the average picking uncertainty of 0.27 s for automatic S-picks in our application, it is certainly difficult to resolve anomalies in  $v_P/v_S < 5\%$ , if we assume a mean uncertainty of at least 0.1 s in P-arrival times.

Together with the MPX picking tool of *Aldersons* (2004), our approach offers the possibility to generate sets of high-quality P- and S-phase data suitable for local and regional tomography.

## Acknowledgments

We are grateful to the following networks in the Alpine Region who provided us with digital recordings used in this study: BED (Ludwig-Maximilians-University, Munich), GERESS (Hannover), GRSN/SZGRF (Erlangen), INGV/MEDNET (Rome), Landes-Erdbebedienst (Freiburg i. B.), OGS/CRS (Udine/Trieste), RENASS (Strasbourg), RSNI/DipTeris (Genova), SED (Zurich), SISMALP (Grenoble), SNRS (Ljubljana), TGRS (Nice), ZAMG (Vienna).

The reference picking was performed with the *SeismicHandler* package (*Stammler*, 1993). Most of the plots were generated using the Generic Mapping Tool of *Wessel and Smith* (1995). We thank S. Greenhalgh, J. Pujol, A. Cichowicz, and one anonymous reviewer whose thoughtful remarks and recommendations greatly improved the manuscript. This research was supported by the Swiss National Fund grant 200021-103698.

## Chapter 6

### Discussion and Conclusion

## 6.1 3-D Lithological Model of the Alpine Crust

The non-cylindric structure of the Alpine crust is well documented by several geophysical-geological transects and their interpretations (e.g. *Schmid et al.*, 2004) as summarized in Figure 6.1. The Penninic nappes system (northern derived) overlies the crustal basement in the Western and Central Alps (Fig. 6.1a-c), whereas the Eastern Alps are dominated by the southern derived Austroalpine nappes system (Fig. 6.1d). In addition, the structure of the lower crust denotes substantial differences between Western, Central and Eastern Alps. A wedge of lower European crust is observed in the Western Alps (Fig. 6.1a,b) and on the other hand, lower Adriatic crust is wedged between upper and lower European crust in the Central Alps (Adriatic indenter, Fig. 6.1c). In the Eastern Alps a reversal of subduction occurs: Adriatic lithosphere subducts beneath European lithosphere in NE direction (Fig. 6.1d). This change in subduction regime is mainly based on the upper mantle structure as derived from the high-resolution teleseismic tomography model of *Lippitsch et al.* (2003).

To integrate these obviously non-2D structures into a regional tectonic context, detailed information on the lithology of the entire Alpine crust is required. Composition and physical state (i.e. fluid content and temperature) of the Alpine lithosphere represent key parameters to understand these structural differences. Seismic velocities can be used to discriminate between different mineral compositions. As demonstrated e.g. by *Holbrook et al.* (1992) P-wave velocities of many common crustal rock types overlap and therefore additional information on S-wave velocities is necessary to overcome this ambiguity. In addition, independent measurements of P- and S-wave velocities allow estimates on subsurface temperatures (*Goes et al.*, 2000) and on fluid content (*Popp and Kern*, 1993; *Ito et al.*, 1979). Local earthquake tomography represents a powerful tool to derive such 3-D velocity images of P- and S-wave velocities of the crust. As described in chapter 1, a uniform resolution of the entire Alpine crust requires a very large aperture of the network since the lower crust is only illuminated by regional phases such as Pn and Sn in major parts of the Alps. An appropriate aperture and a high data coverage can only be achieved by merging travel-time data of all available national and regional networks. As demonstrated in chapter 1 and 3 compilations of merged routine phase data is of low overall quality, since routine picks provided by single networks usually include a high degree of inconsistencies and a uniform error assessment in merged data is not available at all. In order to improve the resolution and reliability of the tomographic image, consistent re-picking of seismic phases of local earthquakes has to be performed. Considering the amount of data necessary for regional tomography models, automated re-picking of first arriving P- and S-phases represents the future of tools to derive large data sets of high quality.

A local earthquake data set appropriate for re-picking of seismic phases has to include digital waveform data and information on associated hypocenters (bulletin data) and stations (coordinates, instrument types, etc.). As described in chapter 2, the compilation and merging of such data from more than ten networks in the

## 6.1 3-D LITHOLOGICAL MODEL OF THE ALPINE CRUST

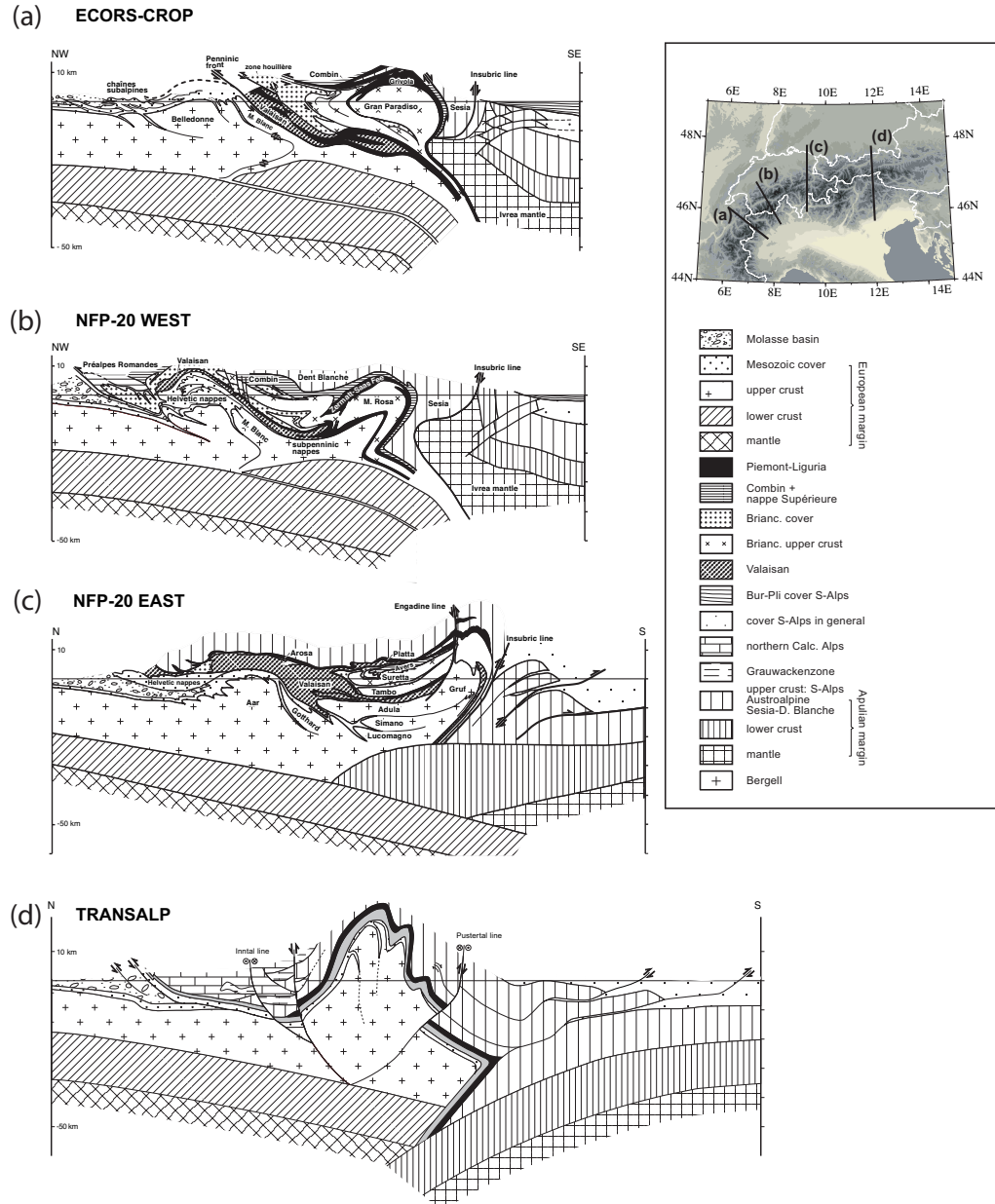


**Figure 6.1:** Crustal cross-sections through the Alps along major geophysical-geological transects. (*Schmid et al., 2004; Kissling et al., 2006*). The upper-right map indicates the locations of the four transects.

Alpine region requires the design of specific procedures. Although a large part of the networks provide online-access to their data bases, a common and complete data exchange of high-frequency sampled digital waveforms in the greater Alpine region is still not available. Data format and accessibility of bulletin and waveform data differs for the majority of networks used in this study. Consequently, the compilation of complete waveform data sets is still a rather laborious process. Furthermore, various network specific problems and inconsistencies are present in waveform data, which have to be identified and, if possible, corrected. Examples of common problems are differences in timing systems (GPS, DCF), systematic time shifts due to filters, reversed polarities of components, inconsistencies in waveform headers, data gaps, etc. The aspired picking-accuracy of 100 ms and less requires the identification and correction of existing systematic timing errors. In addition, problems mainly caused by data transmission introduce different ‘non-seismic’ signals, such as spikes and ‘step-functions’ to the seismograms. The automatic identification of such non-seismic signals represents a major challenge, since most picking algorithms misinterpret them as the actual arrival of a seismic phase.

## 6.2 3-D P-Wave Model of the Alpine Crust from Automated Phase Picking

### Automated Re-Picking of P-Phases

In chapter 3, common problems in routine hand picking were identified and a procedure for consistent hand picking was developed (for a detailed description see Appendix C). This procedure was applied to pick a reference data set of P-wave arrivals, used for calibrating and assessment of the automatic picking software MPX (*Aldersons*, 2004).

The comparison of reference hand picks with automatic picks identified the problem of phase misidentification, particularly present beyond the cross-over distance between Pg and Pn phases. The first arriving, weak Pn phase is often missed by the automatic picker and the secondary Pg or PmP phase is misinterpreted as the first arriving phase instead. A first order discrimination between Pg and Pn phases was achieved by splitting the data set into two epicentral distance ranges ( $\Delta_1 < 100$  km,  $\Delta_2 \geq 100$  km). Different configurations of MPX have to be used for the two subsets.

To overcome the problem of phase misidentification at epicentral distances  $\geq 100$  km a rather conservative setup of MPX has to be applied, which results in a low recovery rate of medium quality Pn arrivals. Most of these phases are rejected by the quality weighting scheme of MPX. In addition, the iterative use of automatic picker and minimum 1-D models is necessary to reduce the number of mispicks caused by phase misidentification and to improve the reliability of automatic phase picks at regional scales.

Finally, all picks associated with travel-time residuals of  $|\delta| > 0.8$  s in the minimum



1-D model were cross-checked against the corresponding waveforms to identify and remove potential gross outlier picks. The average picking error of the final data set is about 0.12 s, which denotes a major improvement in terms of accuracy and consistency compared to any previous regional study of the Alpine crust (e.g. *Solarino et al.*, 1997).

The final high-quality data set, consisting of more than 13'000 P-phase arrivals of 552 well-locatable earthquakes in the greater Alpine region, was used for 1-D and 3-D local earthquake tomography. The regional minimum 1-D model derived in chapter 3 represents the base for the initial model of the 3-D inversion described in chapter 4. Furthermore, the minimum 1-D model and the corresponding station corrections allow a reliable and consistent earthquake location in the Alpine region.

Compared to the procedure used by *Di Stefano et al.* (2006), the distance depending picking approach described in chapter 3 leads to an increased number of automatic picks of high overall assessment quality for the Alpine region. Due to the conservative weighting necessary to avoid phase misidentification at larger distances, more than half of the high and medium quality picks are still rejected by MPX. To further improve the performance of MPX, an automatic assessment of the various phase onsets will have to be included in the picking algorithm, since the currently implemented pattern recognition cannot account for it directly. A detailed description of the fundamental concepts of MPX is provided in Appendix D.

### 3-D P-Wave Model of the Alpine Crust

The high-resolution P-wave model described in chapter 4 represents the first step towards a 3-D lithological model of the Alpine crust. The high-quality data derived from automated re-picking in chapter 3 was used to invert simultaneously for hypocenter locations and 3-D P-wave velocity structure. Our model images large parts of the Alpine orogen between 0 and 60 km depth. Due to the rather coarse station configuration in the north-eastern part of the model, well resolved regions are mainly restricted to the Western and Central Alps. Moreover, the lack of stations in regions dominated by near-surface sedimentary structures (Po plain, Molasse basin) leads to obvious gaps in resolution of the uppermost crust. Since uniform and homogeneous resolution is of higher importance than the maximum possible resolution in local earthquake tomography, a rather coarse grid of 25 x 25 x 15 km turned out to be the finest possible model parameterization without showing a strongly heterogeneous ray coverage.

The ray distribution may allow a finer model parameterization in the center of the model (in particular the ‘cone’ of increased ray density beneath the SED network in Switzerland), however, this would lead to a patchy resolution for the remaining regions associated with a lower ray coverage. As demonstrated by *Kissling et al.* (2001) such unbalanced resolution can cause severe artifacts in the tomographic image and should therefore be avoided. A possible finer parameterization of the model requires an increased ray density on regional scales. Adding data of a single

network will certainly be of no use for the overall resolution capacity. In addition, the minimum resolvable velocity perturbation strongly depends on model parameterization and data error as described in Appendix E.1. The reliable resolution of velocity perturbations in the lower crust with a given average picking error requires an appropriate model parameterization. In our case, an average picking error of 0.12 s in combination with the coarse parameterization allows the resolution of P-wave perturbations in the the lower crust of at least 5%. Therefore, a finer model parameterization either reduces the resolution in terms of perturbation amplitudes or requires the reduction of the average picking error.

Resolution tests with synthetic crustal models showed that the regional 3-D Moho topography can be imaged even within our rather coarse model parameterization. Based on the  $v_P = 7.25$  km/s iso-surface of our 3-D model, a Moho map of the Alpine region was derived as described in chapter 3. The regional structure of the tomography Moho is in good agreement with the CSS model of *Waldhauser et al.* (1998) and the recent receiver function study of *Lombardi et al.* (2008) in the Western and Central Alps. Furthermore, our Moho model might provide some additional information to link the recent CSS model of the Eastern Alps (*Behm et al.*, 2007) with Waldhauser’s model of the Central Alps.

Further first order anomalies like the Ivrea body are clearly resolved and in very good agreement with previous CSS and tomography studies. In addition, several consistent small scale features are visible in our tomographic image. The low-velocity anomalies identified in the upper and mid crust north-west of the Ivrea body are probably associated with European upper crust wedged towards the suture zone. North of the Lago Maggiore (southern Switzerland) a high-velocity anomaly can be observed, whose location correlates with the Tecino-anomaly present in the gravity model of *Kissling* (1984).

In the Central Alps reduced P-wave velocities reach almost to the suture between the European lower crust and the Adriatic lower crustal indenter. A clear continuation of the lower European crust beneath the Adriatic Moho, as proposed e.g. by *Schmid and Kissling* (2000) for the Central Alps (Fig. 6.1c), is not visible in our tomographic image. Resolution tests demonstrate that the presence of unmodified lower European crust below the Adriatic mantle wedge should lead to an observable signature in our tomography model. The absence of such signature may indicate the eclogitization of the subducted European lower crust in the Central Alps as postulated by *Laubscher* (1990) and *Bousquet et al.* (1997).

## Comparison with ISC Routine Phase Data

The differences in terms of resolution and reliability between our high-quality data set derived from automated re-picking and merged routine phase data extracted from the data base of the International Seismological Center (ISC) are demonstrated by the tomographic models in Figure 6.2. The ISC P-phase data was compiled as described in section 2.4. All events (about 10’000) were relocated in the regional minimum 1-D model *s12c* calculated from our high-quality data set in chapter 3. P-phases indicating travel-time residuals  $|\delta| > 5.0$  s are asso-

ciated with outlier picks and were removed from the data set. Subsequently, all remaining phases were used to relocate the events again. Finally we selected well-locatable events with at least 10 P-phase observations and azimuthal gap  $< 150^\circ$ . The remaining data set consists of 95'047 P-phases from 3399 events in the Alpine region. Hence, the ISC data set denotes about six times more events and about seven times more phases than our re-picked data set.

We used the same initial model and the same inversion parameters (damping value 100, five numbers of iterations, RKP-raytracing) for the 3-D inversion of the ISC data set as we used for the re-picked data in chapter 4. Figure 6.2 compares the P-wave tomography model based on re-picked data (left column) with the results of the ISC data set (right column). The bold black contours outline the Resolution Diagonal Element (RDE) of 0.15, which was used as a first order assessment of solution quality in chapter 4.

The uppermost part of the model seems to be rather well resolved by ISC data set (Fig. 6.2, 0 km depth) due to the higher data coverage compared to the re-picked data set (indicated by enlarged area of  $\text{RDE} = 0.15$  in the ISC data). Tectonic units like external massifs (Black-Forest, Vosges mountains), sedimentary deposits (southern Rhine Graben, Po plain, partly Molasse basin), and Alpine orogen are clearly resolved by the ISC data.

In 15 km depth, the tomographic image derived from ISC data indicates a slightly higher noise level. The north-western part of the Ivrea body seems to be blurred and the Central and Eastern Alps denote a patchy velocity structure (Fig. 6.2). The higher noise level of the ISC data becomes obvious in 30 km depth, where the crustal root of the Alps and the northern Apennines are much clearer imaged by the re-picked data set. The apparently reduced resolution of the ISC data in deeper parts of the model might result from the increased number of misidentified Pn phases.

The comparison of the two data sets and their corresponding tomographic images clearly demonstrates the impact of a high-quality data set on the resolution in seismic tomography. Especially the resolution of lower crustal structures with local earthquake tomography requires a consistently picked data set. Inconsistencies in picking and the lack of a common quality assessment cannot be compensated by an increased quantity of phase data. Furthermore it should be noted that the example in Figure 6.2 represents a rather ideal case, since we made use of the regional minimum 1-D model derived from re-picked data to relocate and to filter the ISC data. In addition, we used the 1-D model as initial model for the 3-D inversion. Typically, we would have to start from scratch and in this case the appropriate data selection turns out to be much more difficult. Considering the certainly higher noise level of the ISC data, one would also pick a higher damping value to obtain a smoother model. In this case, the attenuation of recovered amplitudes in the lower crust is even higher and the crustal root beneath the Alps might not be visible at all in the ISC data.

Besides the enhanced resolution, re-picked data also improves the reliability of the tomographic image, since it provides an consistent uncertainty estimate for each

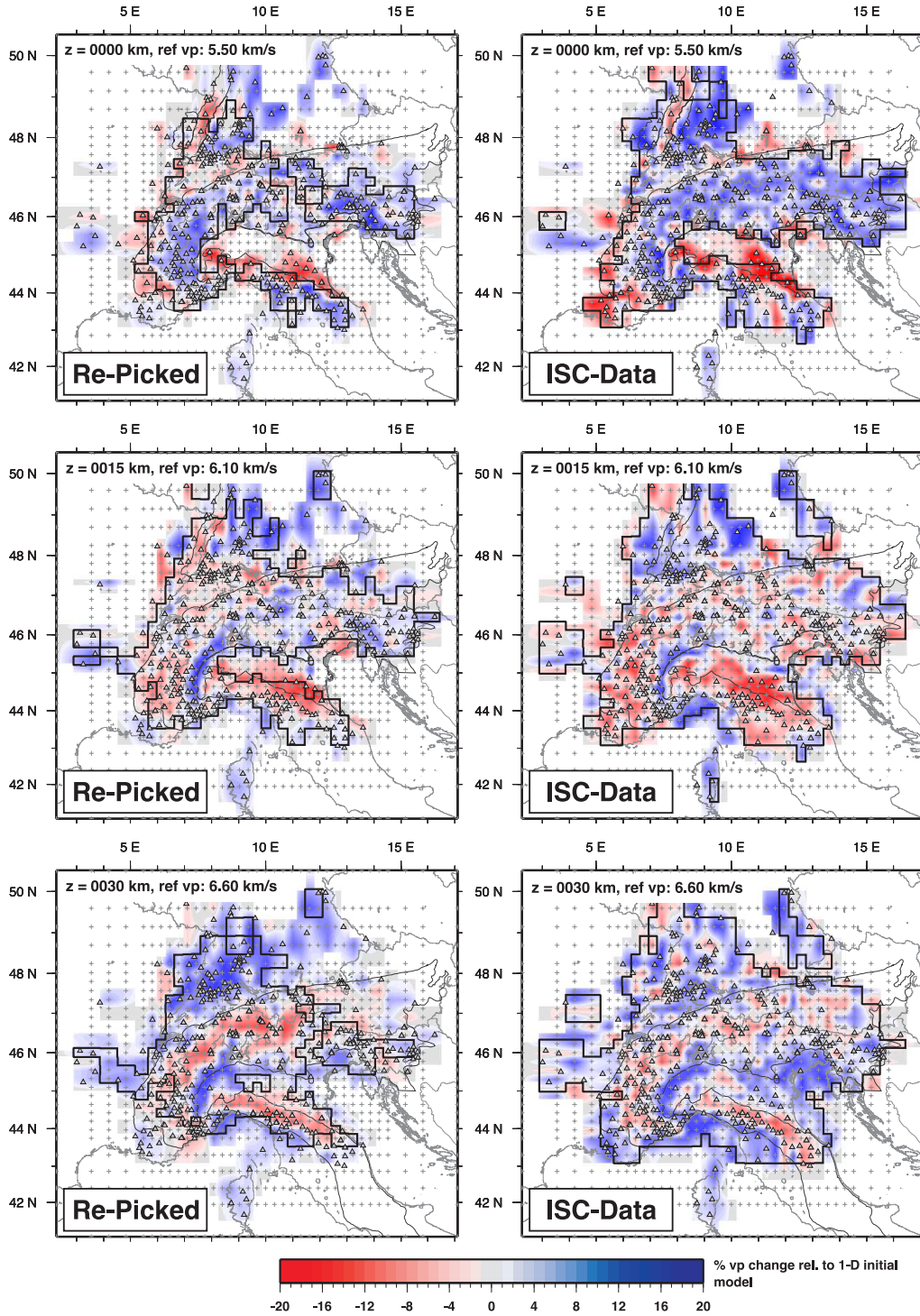


**Figure 6.2:** Comparison of tomographic images based on re-picked phase data (left column) and ISC phase data (right column) at different depths as indicated. The  $v_P$  velocity structure is shown as percentage change relative to the 1-D initial reference model (same for re-picked and ISC). Bold black contours outline Resolution Diagonal Element (RDE) of 0.15.

observation. This allows the performance of rather realistic synthetic test to assess the resolution quality of potential anomalies. Since a common quantitative error assessment is usually not available for compilations of routine picks such as the ISC data, it is difficult to simulate an appropriate error distribution necessary for synthetic resolution tests.

## 6.3 Towards a 3-D S-Wave Model of the Alpine Crust

### Automated Re-Picking of S-Phases

As described in the previous section, automated re-picking represents a powerful tool to derive large and consistent sets of P-phase data suitable for local earthquake tomography at regional scales. The next step towards a 3-D lithological model of the Alpine crust requires similar sets of consistently picked S-phase arrivals. Confirmed by the achievements obtained from re-picked P-waves, an analogous procedure for automated S-wave picking was developed in chapter 5.

The issue of phase identification, as mentioned for P-phase picking before, becomes even more crucial for picking of later arriving S-phases. Therefore, single-component approaches are certainly not sufficient for reliable S-wave picking. Unlike the pattern recognition algorithm implemented in the MPX software of *Aldersons* (2004), a robust automatic quality assessment suitable for S-phase picking has to include additional information on the actual phase type. As discussed in chapter 5, reliable automatic picking of S-phases also requires *a priori* knowledge on the first arriving P-phase. Polarization analysis in a window around the known P-arrival time provides for instance essential information on back-azimuth and incidence angle of the incoming P-wave. Latter two can be used for waveform decomposition through component rotation.

In our approach, we combine two different S-wave detectors with an autoregressive picking algorithm. The two S-wave detectors are based on a short-term to long-term average ratio (STA/LTA) derived from the horizontal components and a polarization analysis technique, respectively. Information provided by the different detectors and the autoregressive picker is combined to an ‘in-situ’ estimate about timing uncertainty and phase identification of the automatic S-pick.

Similar to the procedure applied for automated picking of P-phases, a set of manually picked S-phases was used to calibrate and test the performance of the automatic S-wave picker. It was demonstrated that our automatic approach provides timing accuracy comparable with manually picked S-arrivals. More important, classification of impulsive high-quality S-waves agrees very well with the manual error assessment and only very few poor quality S-arrivals are upgraded by the automatic picker to usable quality classes. Similar to the quality assessment of MPX, medium quality S-arrivals are classified rather conservatively by the automatic picker.

Misinterpretation of phases close to and beyond the cross-over distance between

Sn and Sg turned out to be a major problem for automatic picking of regional S-phases in our data sets. Although misidentification can be reduced by a dynamic configuration of search windows, the number of automatically picked Sn phases remains rather small. The majority of S-phases above 100 km distance are rejected by the automatic quality assessment and for distances larger than 150 km the number of outliers is unacceptable. Therefore, automatic S-wave picks above 150 km epicentral distance are not considered.

The calibrated S-picker was applied to the high-quality data set of the 552 earthquakes used for the 3-D P-wave model in chapter 4. The corresponding ray-coverage of the P-phase data set derived from re-picking is shown in Figure 6.3a. S-waves are only picked on three-component recordings and if an P-phase pick is available. Seismograms indicating clipped amplitudes are immediately rejected. The final data set provided by the automatic S-picker consists of about 2600 first arriving S-phases. The average picking error is about 0.27 s. The corresponding ray-coverage of the S-phase data set derived from re-picking is shown in Figure 6.3b. The S-wave data set denotes about five times less phases compared to the P-wave data and the average uncertainty of S-phase picks is about two times larger than the uncertainty of the P-wave data.

## **Towards a 3-D S-Wave Tomography Model**

The comparison in the previous section identifies a significant discrepancy between P- and S-phase data in terms of quantity and quality. As demonstrated by Figure 6.3b a 3-D S-wave local earthquake tomography of the Alpine crust based on our automated re-picked data is not yet possible. A reason for the sparse ray-coverage of S-waves compared to P-wave data is the obviously lower number of three-component stations in the Alpine region. As shown in chapter 2 only 50% of our waveform data consists of three-component recordings. In addition, amplitudes of seismograms recorded by analog telemetry systems are often clipped shortly after the onset of the P-wave and therefore of no use for S-wave studies. In particular, a future regional Alpine S-wave model requires more reliably identified and picked Sn phases at larger epicentral distances. Pn phases can be picked rather accurately up to distances of more than 500 km and provide a good resolution in the lower crust as shown in chapter 4. Likewise, the S-wave velocity structure of the lower crust can only be resolved by regional Sn phases. As demonstrated in chapter 5, the uncertainty of automatically picked Sn phases in the Alpine region is still rather large and therefore of not much use for local earthquake tomography.

The lack of reliable Sn phases is also present in manually picked data. Figure 6.4 shows travel-time residuals of P and S-phases associated with manual routine picks derived from the Swiss Seismological Service (SED) for well-locatable events between 1999 and 2004. Travel-time residuals are calculated using a minimum 1-D model of Switzerland and surrounding areas. In contrast to P-phases, only few S-phase picks are observed in the routine data for epicentral distances larger than 100 km. The absence of routine S-picks above 100 km is obviously related

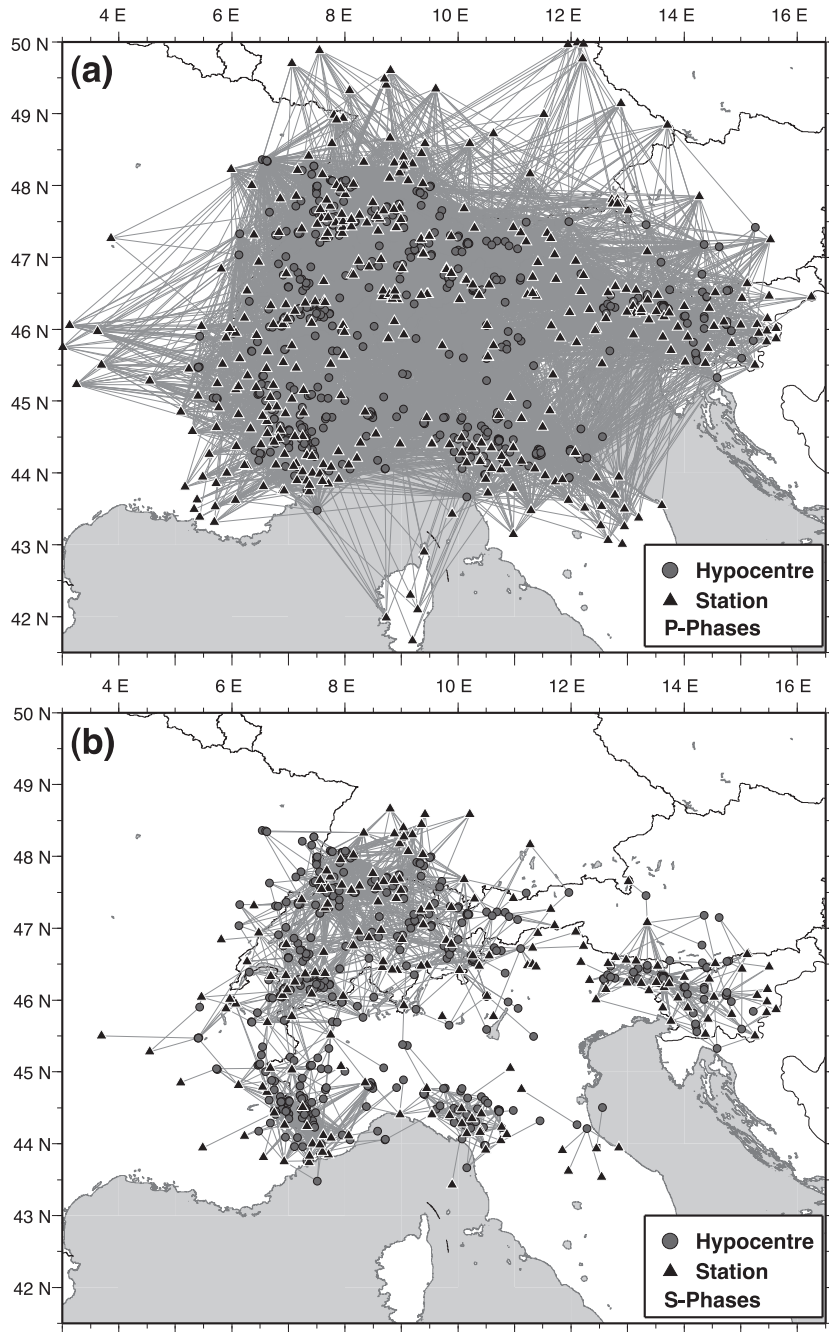


**Figure 6.3:** Ray-coverage of final data sets derived from automated re-picking approaches. **(a)** Final ray-coverage of re-picked P-waves as described in chapter 3. **(b)** Final ray-coverage of re-picked S-waves as described in chapter 5.



with the difficulty of identifying the usually weak and emergent Sn phases. Therefore, possible future approaches have to improve the identification and picking of regional Sn-phases to overcome this gap. The performance of polarization

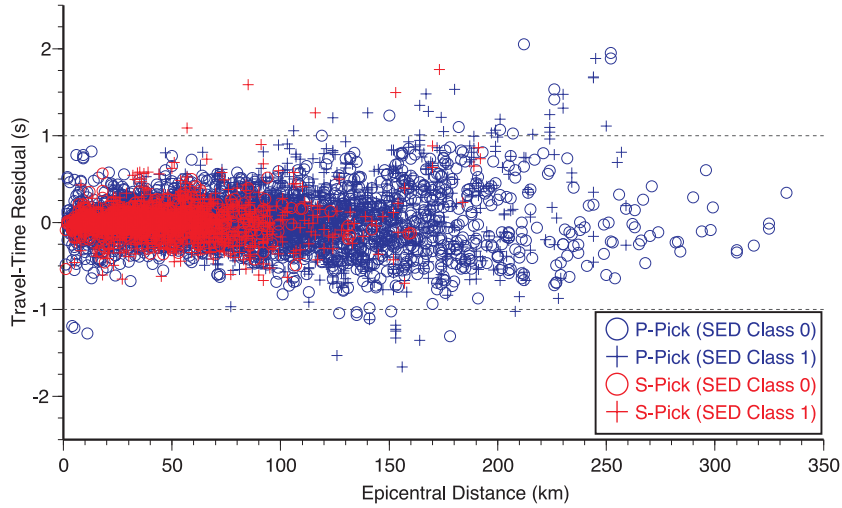


**Figure 6.4:** Travel-time residuals of manually picked P- and S-phases compared to their epicentral distance. Picks correspond to routine phase data derived from the Swiss Seismological Service (SED). Circles denote picks associated with error of  $\pm 0.05$  s (class 0), crosses are associated with error of  $\pm 0.25$  s (class 1). Blue indicates P-phases, red indicates S-phases. Residuals are calculated using a minimum 1-D model of Switzerland and surrounding areas.

detectors might be improved by the use of complex traces (*Vidale, 1986; Bai and Kennett, 2001*) and a moving autoregressive modeling window as suggested by *Bai and Kennett (2000)* could reduce the number of misidentified Sn phases. The implementation of characteristic functions (S-wave detectors, autoregressive modeling) into routine picking tools could also facilitate and improve the visual identification and picking of S-waves.

Although the data set derived from automated re-picking of S-phases in chapter 5 is not yet sufficient for a regional 3-D model of the Alpine crust, it already allows local studies of upper crustal structure in parts of denser ray-coverage (e.g. Switzerland, south-western Alps, northern Apennines, south-eastern Alps). Especially the region between southern Germany and northern Switzerland denotes a rather fair coverage of S-phases and in combination with the P-phase data it might be possible to derive a 3-D  $v_P/v_S$  model in this part. Such a model could provide important information on the origin of the deep seismicity observed in the northern Alpine foreland (*Deichmann and Baer, 1990*).

## 6.4 Conclusion

To integrate the non-cylindric structure of the Alpine crust and upper mantle into a regional tectonic context, detailed information on the lithology of the entire Alpine lithosphere is required. Independent measures of seismic P- and S-wave velocities



allow important estimates on composition and physical state of the lithosphere system. Local earthquake tomography can be used to derive such regional 3-D P- and S-wave velocity models, however, resolution and reliability of the tomographic image strongly depend on the quality of the travel-time data.

A uniform resolution of the entire Alpine crust requires compilation and merging of local earthquake data of more than ten national and regional networks in Austria, France, Germany, Italy, Slovenia, and Switzerland. Since routine picks provided by single networks usually include a high degree of inconsistencies and a common quantitative error assessment is not available for merged phase data, re-picking of P- and S-phases has to be performed. Considering the amount of data necessary for regional tomography models, algorithms combining accurate picking with an automatic quality assessment represent the future of tools to derive large data sets suitable for high-resolution tomography.

A local earthquake data set appropriate for re-picking of seismic phases basically has to include digital waveform data and information on the associated hypocenters (bulletin data). Due to the absence of a common standard for data exchange of digital waveforms and bulletin data, the compilation of a complete data set of the Alpine region is still a rather laborious process. Furthermore, the variety of data formats and the correction of different problems present in waveform data require elaborate data processing procedures. Especially the identification of ‘non-seismic’ signals represents a major challenge, since most picking algorithms misinterpret them as the actual arrival of a seismic phase. The final waveform data set consists of more than 70’000 seismograms from about 1500 earthquakes in the greater Alpine region. About 50% of these seismograms are three-component recordings. This data set represents a quite unique compilation of digital waveforms from local earthquakes within the Alpine region.

Reliable phase identification turned out to be the foremost problem of current automatic picking algorithms, in particular, close to and beyond the cross-over distance of Pn/Pg and Sn/Sg, respectively. The weaker and often emergent Moho-refracted phase can be missed and a later phase is picked as the first arriving phase instead. Such mispicks can only be avoided by the use of narrow picking windows and rather conservative automatic weighting procedures. The former requires accurate estimates on the expected arrival time of the actual phase, the latter rejects a high number of medium quality phases and results therefore in a lower hit-rate. Although accurate travel-time curves can be obtained by the iterative use of automatic picker and minimum 1-D models, a further improvement of automatic pickers on regional scales will only be achieved by including sophisticated phase identification techniques.

The automated re-picking using the MPX software led to a high-quality data set of about 13’000 first arriving P-phases with a sufficiently high number of long-distance observations necessary for a uniform resolution of the entire Alpine crust. The average picking error of this data set is about 0.12 s, which denotes a major improvement in terms of accuracy and consistency compared to any previous regional tomography study of the Alpine crust. The 3-D P-wave velocity model

derived from this data set represents the first step towards a 3-D lithological model of the Alpine lithosphere. First order anomalies like the crust-mantle boundary and the Ivera body are well resolved and in good agreement with previous studies. In addition, several small scale features like the Tecino-anomaly are visible in our tomographic image. A clear continuation of the lower European crust beneath the Adriatic Moho in the Central Alps is not observed. The absence of such a signature may indicate eclogitization of the subducted European lower crust in the Central Alps.

The comparison with a tomography model derived from routine picks of the ISC data base clearly demonstrates the achievements of the automated re-picking approach. Though the model based on ISC data comprises almost seven times more P-phases than the re-picked data set, the resolution in the lower parts of the model is significantly blurred. Effects of the much higher noise level of the ISC data are obvious, especially in the lower crust where several artefacts blend in with real structure.

The reliable automatic picking of S-phases represents the next step towards a 3-D lithological model of the Alpine crust. The issue of phase identification, as mentioned earlier, becomes even more crucial for picking of later arriving S-phases and single-component approaches are certainly not sufficient to detect the S-phase arrival in the P-wave coda. In our approach, we combine two different S-wave detectors with an autoregressive picking algorithm. Information provided by the different detectors and the autoregressive picker is combined to an ‘in-situ’ estimate about timing uncertainty and phase identification of the automatic S-pick. The final data set derived from our automatic picker denotes about 2600 S-phases with an average picking error of about 0.27 s. Due to the fewer amount of three-component recordings and the low number of high-quality Sn phases, this data set is not yet sufficient for a regional 3-D S-wave model of the Alpine crust. In areas of increased data coverage like southern Germany and Switzerland, it might be used for local S-wave or  $V_P/V_S$  studies. A further improvement of the S-wave data coverage in the Alpine region will require more three-component data. In addition, enhancement in picking of regional Sn phases is necessary and the S-picking approach developed in this work represents an excellent base for this purpose.

# Appendix A

## Supplementary Material for Chapter 3

### A.1 Sets of Fisher Coefficients for the Greater Alpine Region

**Table A.1:** Set of Fishers linear discriminant coefficients for 9 predictors and one constant derived from a subset of reference events with  $M_l \geq 4.0$ . For a detailed description of predictors see *Di Stefano et al.* (2006).

Predictors	Automatically Assigned Quality Classes				
	Class 0	Class 1	Class 2	Class 3	Class 4
Constant	-17.512	-15.671	-15.063	-15.613	-17.041
WfStoN	0.297	0.311	0.302	0.302	0.290
GdStoN	-0.555	-0.360	-0.367	-0.407	-0.407
GdAmpR	0.676	0.429	0.438	0.480	0.473
GdSigFR	0.251	0.233	0.199	0.164	0.152
GdDeIF	-0.002	-0.003	0.015	0.026	0.031
ThrCFRat	-0.084	-0.200	-0.212	-0.144	-0.079
PcAboThr	-2.326	-2.416	-2.454	-2.338	-0.493
PcBelThr	0.040	0.051	0.061	0.074	0.100
CFNnoiDev	6.141	6.937	7.519	8.128	8.288

**Table A.2:** Set of Fishers linear discriminant coefficients for 9 predictors and one constant derived from a subset of reference picks at epicentral distances  $\Delta < 100$  km (predominantly Pg phases). For a detailed description of predictors see *Di Stefano et al.* (2006).

Predictors	Automatically Assigned Quality Classes				
	Class 0	Class 1	Class 2	Class 3	Class 4
Constant	-12.940	-11.605	-11.926	-13.219	-26.743
WfStoN	0.205	0.201	0.210	0.254	0.242
GdStoN	-0.357	-0.246	-0.198	-0.395	-0.644
GdAmpR	0.272	0.117	0.086	0.280	0.547
GdSigFR	0.260	0.276	0.215	0.218	0.182
GdDeIF	-0.053	-0.033	-0.010	-0.023	-0.023
ThrCFRat	0.128	-0.015	0.026	-0.028	-0.003
PcAboThr	-1.582	-1.748	-1.253	-0.838	6.376
PcBelThr	0.044	0.069	0.143	0.096	0.159
CFNnoiDev	3.591	4.445	4.544	4.787	5.387



# Appendix B

## Supplementary Material for Chapter 5

### B.1 Character of S-Waves at Local Distances

The nature of shear waves and their interaction with the medium they have travelled through must be taken into account for visual as well as for automatic determination of S-wave arrival times. If  $\vec{L}$  defines the direction of propagation of the compressional P-wave, the particle motion of the S-wave is confined to a plane perpendicular to  $\vec{L}$ . The particle motion within this plane can be described by two normal vectors: the horizontal component (SH) and the vertical component (SV). Furthermore, in an isotropic medium the particle motion of P and S body waves is assumed to be linearly polarized.

The correct picking and identification of the first arriving S-phase can be complicated by various factors. As a later arriving phase, it can be superposed by the P coda and is sometimes preceded by later arriving P phases like the PmP reflection from the Moho (Fig. B.1). Due to the coupling between P and SV, velocity interfaces cause conversion of SV to P energy (and vice versa) as demonstrated in Figure B.1. Such converted Sp precursors generated at interfaces close to the surface (e.g., at the basement/sediment boundary) can be misinterpreted as the first S-onset (see also *Thurber and Atre, 1993*).

Beyond the crossover distance the Sn phase refracted at the Moho is expected to be the first arriving S-phase. Usually, this phase is rather emergent and small in amplitude compared to later arriving S-phases like Sg or SmS. Even in synthetic seismograms of Figure B.1 the Sn phase is difficult to identify, and on R and Z component it is not visible at all. Therefore, it is likely to be missed in real data. At larger distances, especially for shallow focal depths, the linear polarization of the Sg phase gradually changes to elliptical polarization (transition to Lg phase), and the corresponding onset becomes more emergent. In addition, seismic anisotropy reduces the degree of linear polarization and leads to splitting of the shear waves (for a review see e.g., *Crampin and Lovell, 1991*; *Weiss et al., 1999*).

The identification of first-arrival S-waves and its picking accuracy can be improved

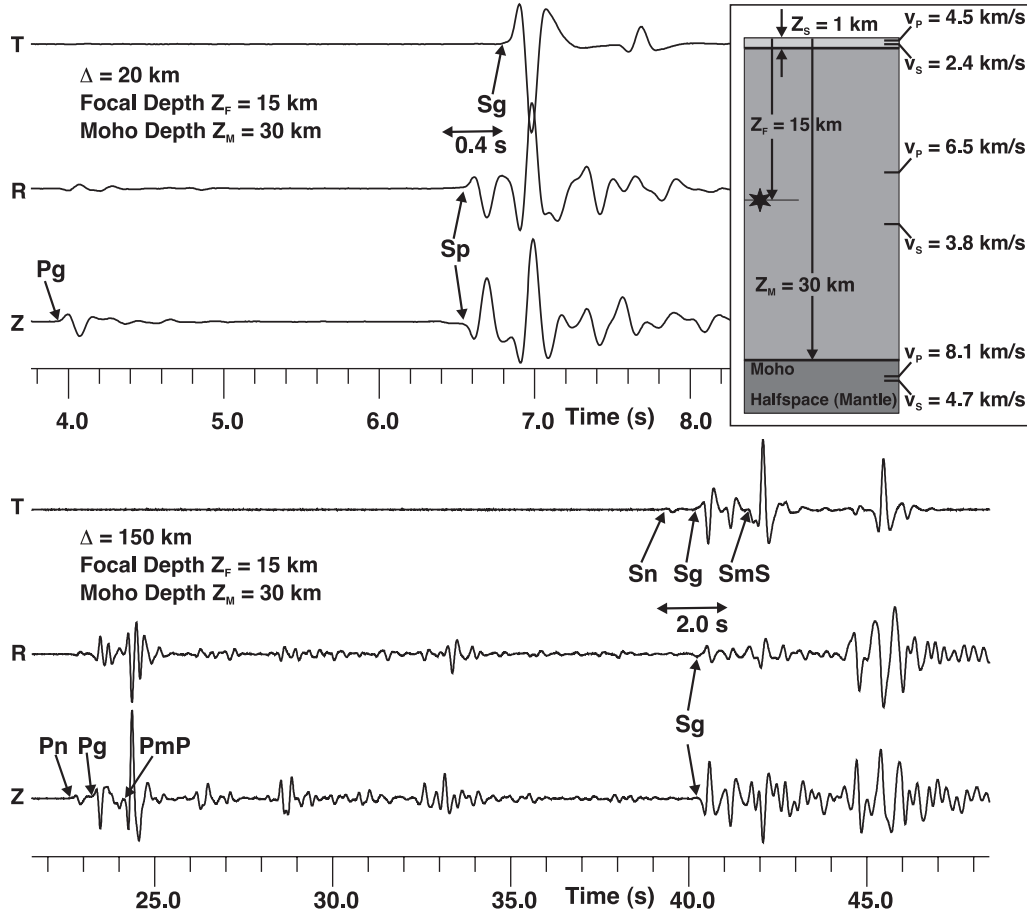


**Figure B.1:** Reflectivity seismograms (*Fuchs and Müller, 1971*) for a simplified 1-D crustal model (upper right inset). Uppermost layer represents a sedimentary basin of reduced P- and S-wave velocities. The uppermost traces show vertical, radial and transverse component at a distance of 20 km. The Sp precursor phase is clearly visible on Z and R component. Lowermost traces correspond to a distance of 150 km. The amplitude of the first arriving Sn phase is rather weak compared to later-arrivals (Sg, SmS) and only visible on the T component. All amplitudes are normalized by station maximum. Seismograms were calculated using the *refmet* code provided by T. Forbriger.

by applying various signal processing techniques. Rotation of components represents a common procedure to enhance the S-wave onset (see e.g., *Plešinger et al.*, 1986). S-waves can also be identified by polarization analysis. Common tools are particle motion diagrams and polarization filters, which e.g., enhance linearly polarized body waves. Finally, appropriate waveform filters, like the Wood-Anderson filter, which essentially integrates the signal, can enhance the low-frequency character of S-waves.

## B.2 Combined Picking Approach (Supplementary Material)

In this section we provide a detailed description of the STA/LTA-detector, the polarization detector, the AR-AIC picker, and the automatic quality assessment. This detailed documentation is intended for any potential user who wants to reproduce our approach (or parts of it). It represents an important complementation to the paper ‘Automatic S-wave picker for local earthquake tomography’ of Diehl et al. 2008.

In the following sections we consider a three component time series (Z,N,E) of  $N$  samples with a sampling interval of  $\Delta t$ . The corresponding amplitudes are represented by  $y_{ji}$ , with  $j = 1, 2, 3$  and  $i = 1, N$ . To facilitate the reader’s orientation, variables used in the description of detectors and picker are summarized in the glossary of Table B.1.

### B.2.1 STA/LTA Detector

In our STA/LTA implementation, we calculate the short-term average for the  $i$ th sample in a window of length  $s$  samples from  $i - s$  to  $i$ :

$$STA_{ji} = \frac{1}{s+1} \sum_{i-s}^i y_{ji}^2 \quad (\text{B.1})$$

The long-term average is calculated in an analogous way over a window of length  $l$  samples:

$$LTA_{ji} = \frac{1}{l+1} \sum_{i-l}^i y_{ji}^2 \quad (\text{B.2})$$

We define the combined horizontal STA/LTA ratio,  $HSL$ , for the N and E-component as:

$$HSL_i = \frac{STA_{2i}}{LTA_{2i}} \cdot \frac{STA_{3i}}{LTA_{3i}} \quad (\text{B.3})$$

Several short-term ( $\Delta st$ ) and long-term ( $\Delta lt$ ) window lengths were tested for our data set. For the Alpine region, a combination of  $\Delta st = 0.20$  s and  $\Delta lt = 2.00$  s

Variable	Description
<b>General Variables</b>	
$tP_{obs}$	Time of <i>a priori</i> (known) P-arrival (e.g., from high-quality autopick)
$tS_{pre}$	Time of predicted S-arrival (e.g., from velocity model)
$t_{MHA}$	Time of Maximum Horizontal Amplitude $y_{MHA}$
$SW1, SW2$	Time of start and end of S-picking window for both detectors
$tS_{me}$	Time of final automatic S-pick (from quality assessment)
$tS_{up}$	Time of upper end of error interval (from quality assessment)
$tS_{lo}$	Time of lower end of error interval (from quality assessment)
<b>Variables used for STA/LTA Detector</b>	
$tS2L_{max}$	Time of maximum STA/LTA value $S2L_{max}$
$thr_1$	Dynamic threshold for STA/LTA detector
$tS_{thr1}$	Time of threshold-based STA/LTA S-pick ('latest possible')
$tS_{min1}$	Time of minimum-based STA/LTA S-pick ('earliest possible')
<b>Variables used for Polarization Detector</b>	
$t_3$	Time of end of window for threshold determination (start: $SW1$ )
$thr_2$	Dynamic threshold for polarization detector
$tS_{thr2}$	Time of threshold-based polarization S-pick ('latest possible')
$tS_{min2}$	Time of minimum-based polarization S-pick ('earliest possible')
<b>Variables used for AR-AIC Picker</b>	
$t_{AC}$	Time of initial pick for AIC configuration (from detectors or $tS_{pre}$ )
$t_{NS}, t_{NE}$	Time of start and end of noise model window
$t_{SS}, t_{SE}$	Time of start and end of signal model window
$AIC^C$	AIC function for component $C$ ( $C=N, E, T, Q$ , or $H$ ); $H=E+N$
$tS_{AC}$	Time of AIC-minimum for component $C$ ( $C=N, E, T, Q$ , or $H$ )
$thr_{AIC}$	Dynamic threshold for AIC quality assessment
$tS_{eC}$	Time of 'earliest possible' AIC-pick for component $C$
$tS_{lC}$	Time of 'latest possible' AIC-pick for component $C$
<b>Variables used for Quality Assessment</b>	
$tS_{av}$	Average time of all considered picks
$\sigma_{pk}$	Standard deviation of all considered picks
$tS_{er}$	Earliest time of all considered picks
$tS_{la}$	Latest time of all considered picks

**Table B.1:** Complete glossary of variables used and returned by the different detectors and pickers.



yields the best compromise between hit rate and false detections.

To restrict the detection to possible S-phases, we have to ensure that no P-wave is present in the S-detection window. The proposed setup of the S-phase search windows assumes that, on the horizontal components, the S-arrival is located prior and close to the largest amplitude. To minimize the effect of inaccurately predicted S-arrivals,  $tS_{pre}$ , we use this information only for the definition of a first coarse window starting at  $tP_{obs} + (tS_{pre} - tP_{obs})/4$  and ending at  $tS_{pre} + \Delta S_{post}$ . In case of early predicted S-arrival times,  $\Delta S_{post}$  has to ensure that the dominant part of the S-wave coda is still included in the coarse search window. The choice of  $\Delta S_{post}$  depends on the largest possible deviation expected between the predicted S and the actual S-arrival (mainly related to the accuracy of the velocity model and the hypocenter). In our data set a value of 5.0 s seems sufficient.

The coarse S-window is used to determine the position of the maximum horizontal amplitude  $y_{MHA}$  at time  $t_{MHA}$  as illustrated in Figure B.2. We expect the actual

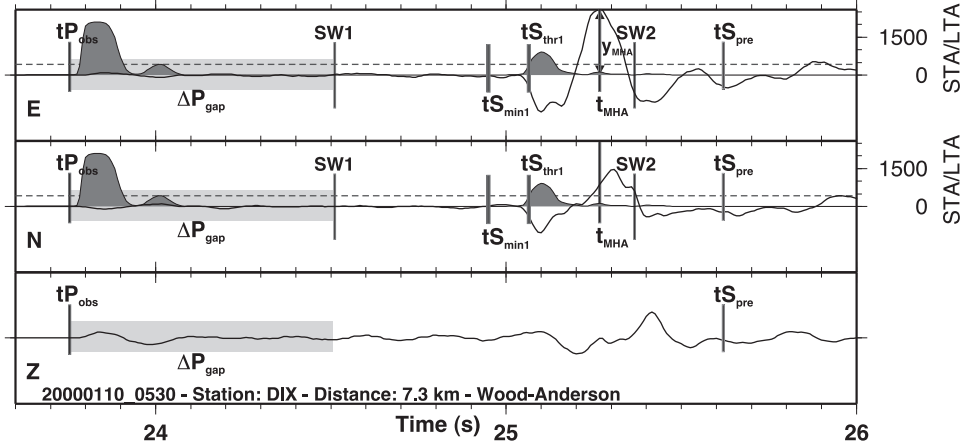


**Figure B.2:** Combined STA/LTA approach used for S-wave detection on horizontal components. Black solid lines represent the Wood-Anderson filtered 3C seismograms (amplitudes normalized by station maximum) of a local earthquake in Switzerland ( $M_l=3.1$ , focal depth of 9 km). The dark gray shaded trace denotes the combined STA/LTA ratio derived from N and E components.  $tP_{obs}$  represents the known P-arrival time and  $tS_{pre}$  indicates the position of theoretical S-arrival predicted from a regional 1-D model. The dashed horizontal line denotes the dynamic threshold  $thr_1$  for the picking algorithm. The S-wave arrival time based on the STA/LTA detector in the potential S-window (SW1 to SW2) is most likely located in the interval between  $tS_{min1}$  (minimum pick) and  $tS_{thr1}$  (threshold pick). See text and Table 5.1 for further description.

S-phase onset to certainly occur prior to  $t_{MHA}$  and therefore,  $t_{MHA} + (2 \cdot t_{up})$  defines the upper end of the search window (SW2 in Fig. B.2). The additional term  $2 \cdot t_{up}$  is required for the picking algorithm, which will be described later. The start of the S-window is derived from  $tP_{obs} + (t_{MHA} - tP_{obs})/2$  and is indicated as SW1 in Figure B.2. For very short epicentral distances, it is still possible that the search window from SW1 to SW2 includes parts of the P-signal. Therefore, a fixed minimum safety gap  $\Delta P_{gap}$  is required between  $tP_{obs}$  and SW1 (represented by light gray band in Fig. B.2). If SW1 falls within this safety gap, it is automatically adjusted to  $tP_{obs} + \Delta P_{gap}$ . We set  $\Delta P_{gap} = 0.75$  s.

The picking algorithm applied to the characteristic STA/LTA function within the search window is similar to the method proposed by *Baer and Kradolfer* (1987). We extended their threshold-based method by a ‘minimum-picking’ approach also suggested by *Cichowicz* (1993), where a (global) minimum of the characteristic function (CF) prior to the threshold-based pick is determined. The iterative application of threshold and minimum-picking techniques provides a direct assessment of the uncertainty of the phase arrival and is closely related to procedures used in manual picking. Instead of adopting a fixed STA/LTA-threshold, we determine the threshold-value  $thr_1$  from the standard deviation  $\sigma_1$  of the STA/LTA function within the search window. If  $S2L_{max}$  denotes the maximum STA/LTA value within the search window,  $thr_1$  is defined by:

$$thr_1 = \begin{cases} 2 \cdot \sigma_1 & : \sigma_1 < S2L_{max}/2 \\ S2L_{max}/2 & : \sigma_1 \geq S2L_{max}/2 \end{cases} \quad (\text{B.4})$$

The dashed horizontal lines in Figure B.2 represent  $thr_1$  for our example. A pick is declared if the actual STA/LTA exceeds the threshold  $thr_1$  and remains above the threshold for a minimum time  $tup$ . For very impulsive S-waves, we have to ensure that  $tup$  can be reached within the picking window. Therefore,  $SW2$  is defined as  $t_{MHA} + (2 \cdot tup)$ . To account for roughness and singularities present in characteristic functions derived from complex seismic signals, *Baer and Kradolfer* (1987) introduced the additional parameter  $tdw$ . The pick flag is not cleared if the CF drops below the threshold for a time interval less than  $tdw$ . We obtained stable results for  $tup = 0.05$  s and, due to the usually rather smooth STA/LTA function, we set  $tdw$  to zero. The corresponding threshold-based pick in Figure B.2 is represented by  $tS_{thr1}$ .

Our ‘minimum-picking’ approach determines the minimum value of the CF prior to  $tS_{thr1}$  and is equivalent to a delay correction usually necessary for threshold-based picks. This minimum can be interpreted as the position of the earliest possible arrival time of the phase detected by the threshold method. To account for local minima and to include possible smaller precursory phases, we introduce an parameter  $tbe$  similar to  $tup$ . If a minimum prior to  $tS_{thr1}$  is detected, we require that the values of the CF remain below  $thr_1/2$  for the period of  $tbe$  backward in time. The corresponding ‘minimum’ pick is represented by  $tS_{min1}$  in Figure B.2. For the STA/LTA detector, we use  $tbe = tup$ .

## B.2.2 Polarization Detector

The implementation of our polarization detector is mainly based on the approach of *Cichowicz* (1993) and its principles are described in the following paragraph. As a first step, we determine the direction of the incoming P-wave. We compute the three-component covariance matrix within a narrow window of length  $\Delta wP$  around the known first arriving P-phase  $tP_{obs}$ . The eigenvector corresponding to the maximum eigenvalue of the covariance matrix represents the direction of the P-wave  $\vec{L}$ . The direction in the reference observation system (ZEN) can be defined by

two angles, the back-azimuth  $\beta$  and the angle of incidence  $\varphi$ . The window length used to calculate the covariance matrix is a critical parameter in this procedure, since it can have a significant influence on uncertainty and reliability of the derived rotation angles. In the presence of multiple arrivals or scattered phases close to the first-arrival, long windows can lead to unstable results. On the other hand, very narrow windows can result in wrong rotation angles if the onset of the analyzed wavelet is emergent. To account for differences in the wavelet characteristics, we simply weight the window length by the *a priori* observation quality of the P-phase. Table B.2 describes the weighting scheme used for P-phase picking in the Alpine region (Diehl *et al.*, 2008). The window length used to analyze a P-phase

P-Quality class $qP$	Error $\varepsilon_{qP}$ (s)	Weight (%)
0	$\pm 0.05$	100
1	$\pm 0.10$	50
2	$\pm 0.20$	25
3	$\pm 0.40$	12.5
4	$> 0.40$	0 (rejected, not considered)

**Table B.2:** Weight assignments based on picking errors for P-waves from local and regional earthquakes within the greater Alpine region (Diehl *et al.*, 2008).

of quality class  $qP$  is:

$$\Delta wP = 2 \cdot \varepsilon_{qP}, \quad (\text{B.5})$$

where  $\varepsilon_{qP}$  denotes the error interval associated with quality class  $qP$ . To separate P from SV and SH-energy, we rotate the observation system (ZEN) into a ray-coordinate system (LQT) using rotation angles  $\beta$  and  $\varphi$  according to Plešinger *et al.* (1986):

$$\begin{pmatrix} L \\ Q \\ T \end{pmatrix} = \begin{pmatrix} \cos \varphi & -\sin \varphi \sin \beta & -\sin \varphi \cos \beta \\ \sin \varphi & \cos \varphi \sin \beta & \cos \varphi \cos \beta \\ 0 & -\cos \beta & \sin \beta \end{pmatrix} \begin{pmatrix} Z \\ E \\ N \end{pmatrix} \quad (\text{B.6})$$

Finally, we calculate the directivity  $D(t)$ , rectilinearity  $P(t)$ , ratio between transverse and total energy  $H(t)$ , and a weighting factor  $W(t)$  within a centered window of length  $\Delta pol$  for each sample of the rotated time series. The length of the polarization filter  $\Delta pol$  used to analyze a seismogram with a given P-phase of quality class  $qP$  is derived from the following expression:

$$\Delta pol = 4 \cdot \varepsilon_{qP} \quad (\text{B.7})$$

Again, we account for differences in waveform characteristics by weighting the length of the polarization filter with the P-phase quality. The covariance matrix is determined from the centered window for each sample.

Directivity  $D(t)$  is defined as the normalized angle between  $\vec{L}$  and eigenvector

$\vec{\epsilon}_{max}$  corresponding to the maximum eigenvalue of the covariance matrix. The directivity operator is expected to be close to zero for the first arriving P-wave ( $\vec{\epsilon}_{max}$  parallel to  $\vec{L}$ ) and close to one for the first arriving S-wave ( $\vec{\epsilon}_{max}$  perpendicular to  $\vec{L}$ ).

Rectilinearity  $P(t)$  is calculated using the formulation of *Samson* (1977):

$$P(t) = \frac{(\lambda_1 - \lambda_2)^2 + (\lambda_1 - \lambda_3)^2 + (\lambda_2 - \lambda_3)^2}{2 \cdot (\lambda_1 + \lambda_2 + \lambda_3)^2}, \quad (\text{B.8})$$

where  $\lambda_1, \lambda_2, \lambda_3$  are the eigenvalues of the covariance matrix at time  $t$ .  $P(t)$  is expected to be close to one for both first arriving P- and S-waves.

The ratio between transverse and total energy  $H(t)$  within the centered window is defined as

$$H(t) = \frac{\sum_j (Q_j^2 + T_j^2)}{\sum_j (Q_j^2 + T_j^2 + L_j^2)}. \quad (\text{B.9})$$

Likewise,  $H(t)$  is expected to be close to one for the first arriving S-wave and zero for the first arriving P-wave.

As an addition to the original method of *Cichowicz* (1993), we calculate a weighting factor  $W(t)$  for each window, which accounts for the absolute amplitude within the centered window with respect to the maximum amplitude derived from the coarse S-window:

$$W(t) = \left( \frac{y_{mwin}}{y_{MTA}} \right)^n \quad (\text{B.10})$$

Here,  $y_{mwin}$  denotes the maximum transverse amplitude within the centered window and  $y_{MTA}$  represents the maximum transverse amplitude in the coarse S-window (determined on Q and T similarly to  $y_{MHA}$ ). The exponent  $n$  increases ( $n > 0$ ) or decreases ( $n < 0$ ) the weighting effect. The usage of such a weighting factor significantly reduces the noise of the CF prior to the S-wave arrival. We obtained the best results for  $n = 0.5$ .

The product of the three squared filter operators  $D(t)$ ,  $P(t)$ ,  $H(t)$  with the weighting factor  $W(t)$  yields the modified characteristic function for S-wave detection  $CF_S$ :

$$CF_S(t) = D^2(t) \cdot P^2(t) \cdot H^2(t) \cdot W(t) \quad (\text{B.11})$$

Figure B.3 shows the LQT components of the same local earthquake from Figure B.2 and the corresponding S-wave operators  $D(t)$ ,  $P(t)$ , and  $H(t)$ . The arrival of the S-wave (gray band) goes along with the simultaneous increase of  $D(t)$ ,  $P(t)$ , and  $H(t)$  and leads to a well-defined signature on  $CF_S$ .

The picking algorithm applied to  $CF_S$  is almost identical to the one used for the STA/LTA detector described above. The S-wave search window starts at  $SW1 =$

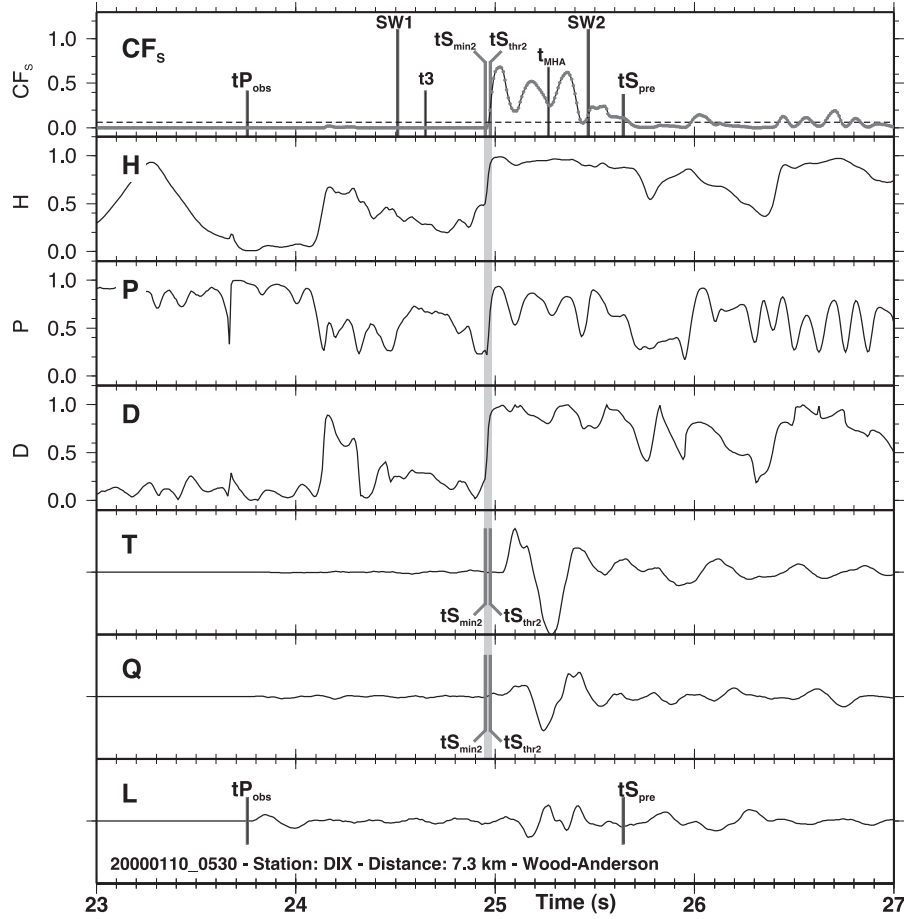


**Figure B.3:** Example for the polarization detector applied to the same local earthquake of Figure B.2. L, Q, T denote the rotated components. The corresponding S-wave operators are  $D(t)$  (directivity),  $P(t)$  (rectilinearity), and  $H(t)$  (transverse to total energy ratio). The uppermost trace represents the amplitude weighted characteristic S-wave function  $CF_s$  and the dashed horizontal line denotes the dynamic threshold  $thr_2$  for the picking algorithm. The arrival of the S-wave (gray band) goes along with the simultaneous increase of  $D(t)$ ,  $P(t)$ ,  $H(t)$ , and  $CF_s$ . Compared to the actual arrival on T, the S-wave detection is shifted by approximate 0.1 s to earlier times. This time-shift is caused by the finite length of the polarization filter.  $CF_s$  is not affected by the P-wave. See text and Tables B.1 for further description.

$tP_{obs} + (t_{MHA} - tP_{obs})/2$  and ends at  $SW2 = t_{MHA} + (2 \cdot tup)$ , where  $tup$  can deviate from the value used for the STA/LTA detector. The threshold  $thr_2$  for the picker (dashed horizontal line in Figure B.3) is derived from the standard deviation  $\sigma_2$  and the mean  $\overline{CF_S}$  of  $CF_S$  between  $SW1$  and  $t3$  according to the procedure proposed by Cichowicz (1993). The position of  $t3$  is defined as  $SW1 + (t_{MHA} - SW1 - \Delta pol)/4$  and the threshold is calculated from:

$$thr_2 = \overline{CF_S} + (3 \cdot \sigma_2) + cw, \quad (\text{B.12})$$

where  $cw$  denotes a ‘water-level’, which stabilizes the picking in case of a large signal-to-noise ratio. Otherwise,  $thr_2$  would approach zero, since  $\sigma_2$  as well as  $\overline{CF_S}$  become small for large signal-to-noise ratios. We use  $cw = 0.06$ ,  $tup = 0.10$  s, and  $tdw = 0.05$  s for the threshold-based picking on  $CF_S$  and the corresponding pick is represented by  $tS_{thr_2}$  in Figure B.3. In addition, we perform the minimum-picking prior to  $tS_{thr_2}$  as described earlier. To account for smaller precursory signals, we choose  $tbe = 2 \cdot tup$ . The position of the minimum-pick is marked as  $tS_{min2}$  in Figure B.3. Compared to the actual arrival on the transverse component,  $tS_{thr_2}$  and  $tS_{min2}$  are shifted by approximate 0.1 s to earlier times (Fig. B.3). This time-shift is caused by the finite length of the polarization filter. For emergent arrivals the time-shift is less significant.

### B.2.3 Autoregressive Picker

Following the definition of *Takanami and Kitagawa* (1988) the time series  $x_n \{n = 1, \dots, N_A\}$  can be divided into two subseries before and after the unknown arrival time, and each of them can be expressed by an AR model:

$$x_n = \sum_{m=1}^{M(1)} a_m^1 x_{n-m} + \varepsilon_n^1, \quad (1 \leq n < n_1), \quad (\text{B.13})$$

$$x_n = \sum_{m=1}^{M(2)} a_m^2 x_{n-m} + \varepsilon_n^2, \quad (n_1 \leq n \leq N_A), \quad (\text{B.14})$$

where  $\varepsilon_n^i$  is Gaussian white noise with zero mean and variance  $\sigma_i^2$ ,  $a_m^i$  is the autoregressive coefficient,  $M(i)$  is the order of the  $i$ -th model, and  $n_1$  corresponds to the unknown arrival time. Equation (B.13) represents the background ‘noise’ model and Eq. (B.14) the corresponding ‘earthquake’ model. The AIC can be considered as a measure of the deficiency of the estimated model and is given by:

$$AIC = -2(\log L_{max}) + 2(M_P), \quad (\text{B.15})$$

where  $L_{max}$  denotes the maximum likelihood function of the two AR models and  $M_P$  is the number of independently estimated parameters. *Takanami and Kitagawa* (1988) show, that the AIC can be reduced to a function of  $n_1$ . Therefore,  $n_1$  corresponding to the minimum  $AIC_{n_1}$  represents the best AIC estimate of the

arrival time.

In practice, we calculate the noise model  $AIC_i^{forw}$  forward in time starting at  $t_{NS}$  and ending at  $t_{SS}$ , assuming the noise part is included in the window from  $t_{NS}$  to  $t_{NE}$  as illustrated in the lower box of Figure 5.4. In addition, the signal model  $AIC_i^{back}$  is calculated backward in time starting at  $t_{SE}$  and ending at  $t_{NE}$ , where parts of the signal are expected to be included in the window between  $t_{SS}$  and  $t_{SE}$ . By simply adding  $AIC_i^{forw}$  and  $AIC_i^{back}$  for common samples of the time series, we obtain the  $AIC_i$  of the locally stationary AR model. If  $i_{min}$  corresponds to the sample of the minimum  $AIC_i$  value, then  $i_{min} + 1$  represents the best estimate of the arrival time. Moreover,  $AIC_i$  from different components can be added to give combined AIC functions, e.g.  $AIC^H$  represents the sum of the horizontal components N and E. In practice, the position and length of the noise, pick, and signal windows, as defined by  $t_{NS}$ ,  $t_{NE}$ ,  $t_{SS}$ , and  $t_{SE}$ , is set by an initial pick and some fixed parameters as described in the following section.

### Configuration of AR-AIC Windows

Due to their fundamental concept, predictive AR-AIC pickers always require an initial pick  $t_{AC}$  to setup a noise model window  $\Delta LN$  and signal model window  $\Delta LS$  separated by the picking window  $\Delta gN + \Delta gS$  (Fig. 5.4). Previous implementations of AR-AIC pickers such as *Sleeman and van Eck* (1999) or *Akazawa* (2004) mainly use triggers from STA/LTA detectors for this purpose. In our procedure,  $t_{AC}$  can be derived from the polarization detector, from the STA/LTA detector, or from a theoretical travel time. The search windows are centered around  $t_{AC}$ , and in the configuration of Figure 5.4, the first arriving P-wave is included in the noise window between  $t_{NS}$  and  $t_{NE}$ . The corresponding AIC functions have the typical shape with well developed minima around the actual onset of the S-wave (Fig. 5.4). The AR-AIC estimated picks  $t_{SAQ}$  and  $t_{SAT}$  agree very well with the arrival observed on the different components. The onset appears more impulsive on the T component, which is also indicated by the sharper minimum on  $AIC^T$  compared to the one observed on  $AIC^Q$  (Fig. 5.4).

The quality of AR-AIC pickers depends mainly on the degree of separation between noise and signal in the analysis window from  $t_{NS}$  to  $t_{SE}$ . This can be critical if, for example, several phases are present within the window (e.g., Pg and Sg at very short epicentral distances or Sn and Sg at larger distances). Therefore, minimum *a priori* information is required to guide the picker to the correct phase and to setup the AR-AIC search windows properly. The examples in Figure 5.4, B.4, and B.5 are used to demonstrate the importance of correctly configured search windows for AR-AIC picking of S-wave arrivals. The configuration in Figure B.4 uses the same initial pick  $t_{AC}$ . However, the picking range, noise, and signal windows are much longer than in Figure 5.4. With this search window configuration, part of the first arriving P-wave is included in the picking window between  $t_{NE}$  and  $t_{SS}$ . The resulting shape of the AIC functions is rather unexpected and no global minimum close to the actual S-wave arrival can be observed. Consequently, the corresponding AR-AIC S-picks are grossly wrong in this example. Figure B.5 illustrates a

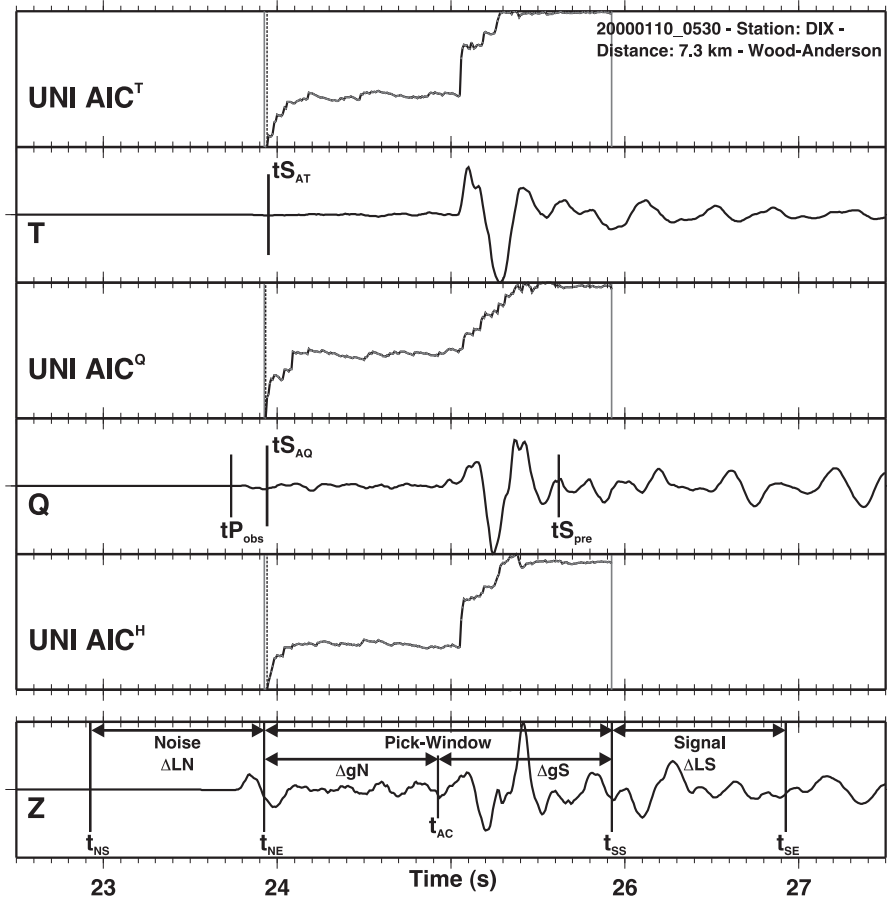


**Figure B.4:** Example for misconfigured AR-AIC search windows (Sg case). Part of the P-wave is included in the picking window between  $t_{NE}$  and  $t_{SS}$ . This configuration leads to a deformed AIC function with the absence of a global minimum around the actual S-wave arrival. The corresponding AR-AIC picks  $t_{SAQ}$  and  $t_{SAT}$  are erroneous, being far-off the actual S-wave arrival.



similar effect of larger epicentral distances, where a weak first-arrival Sn is followed by an impulsive and strong Sg or SmS phase. The emergent Sn phase is missed by the STA/LTA and the polarization detector (Fig. B.5d). Misconfigured AR-AIC search windows as represented by configuration A in Figure B.5a,b will also fail to detect the precursor Sn phase and can result in errors up to several seconds.

### Dynamic Configuration Approach

To avoid such problems, we implemented a sophisticated procedure for a dynamic configuration of AR-AIC search windows. The method used to derive the initial pick  $t_{AC}$  depends on the epicentral distance  $\Delta_{epi}$ . Since theoretical travel times can deviate significantly from the actual S-wave onset due to variation in  $v_P/v_S$  or an incorrect hypocenter (in particular focal depth),  $t_{AC}$  as provided by the phase detectors is usually more reliable for stations close to the epicenter. For larger distances the effect of erroneous focal depths is less severe and the mean  $v_P/v_S$  ratio is less affected by lateral variations of the upper crust. Although the three pickers should work as independently as possible, information from the other detectors are essential for the correct setup of the AR-AIC search windows at small epicentral distances. For larger distances, the phase detectors become less reliable (e.g., smaller signal-to-noise ratio) as shown in Figure B.5d, and therefore independent information from predicted arrivals in an appropriate velocity model can do a better job. The epicentral distance above which the theoretical travel time  $tS_{pre}$  is used for  $t_{AC}$  determination is defined as  $\Delta_{AIC_1}$ . If present,  $tS_{min2}$  (from polarization analysis) is taken as the initial pick for distances  $< \Delta_{AIC_1}$ . If no phase was picked by the polarization detector,  $tS_{min1}$  (from STA/LTA) will be used for  $t_{AC}$ . In the rare case of no phase detection,  $tS_{pre}$  will be used also for small distances.

The width of the picking window centered around  $t_{AC}$  is controlled by  $\Delta gN$  and  $\Delta gS$  (Fig. 5.4). Their lengths depend mainly on the expected deviation between  $t_{AC}$  and the actual phase arrival. A wide window allows picking in case of less accurately predicted travel times, however, mispicks as demonstrated in Figure B.4 and Figure B.5 become more likely. The lengths of  $\Delta LN$  and  $\Delta LS$  depend mainly on the expected maximum wavelengths of noise and signal, respectively.

The information about the first arriving P-wave  $tP_{obs}$  is required to adjust the search windows for small epicentral distances. If  $t_{NS} - tP_{obs} \leq 0$  or  $t_{NE} - tP_{obs} \leq 0$  we set  $\Delta LN = \Delta LS = \Delta gN = \Delta gS = (t_{AC} - tP_{obs})/2$  to ensure proper search window configuration (Fig. 5.4). The approximate crossover distance between Sg and Sn as first arriving S-phase is defined by  $\Delta_{AIC_3}$ . As demonstrated by *Diehl et al.* (2008) for automatic P-phase picking, the first arriving phase is usually less well-defined beyond the crossover distance. Due to this change in the signal character of the first arriving phase, different picking procedures have to be used below and above the approximate crossover distance.

For distances  $< \Delta_{AIC_3}$  the maximum of the STA/LTA value  $tS2L_{max}$  is usually associated with the onset of the first arriving Sg phase. Possible picks derived from the STA/LTA or the polarization detector can be used for the proper configuration

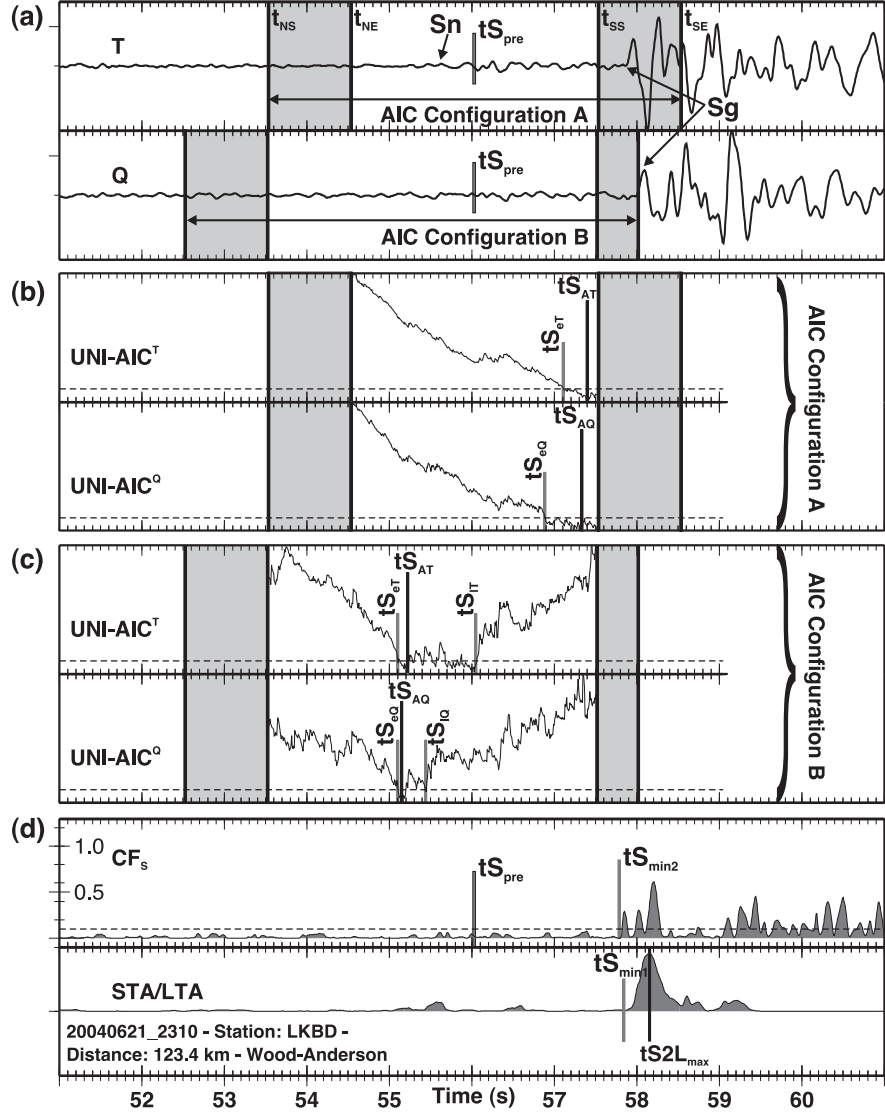


**Figure B.5:** Example for misconfigured AR-AIC search windows (Sn case). (a) Major parts of the Sg-wavelet are included in the signal window between  $t_{SS}$  and  $t_{SE}$  in configuration A. (b) The weak emergent onset of the preceding Sn phase is missed within this static search window configuration A and the corresponding AIC functions show no distinct minimum. (a) By excluding the maximum of the STA/LTA function  $tS_{2L_{max}}$  from the signal window in configuration B, a proper search window configuration for Sn identification is obtained. (c) The flatness of the AIC-function between  $t_{eT}$  and  $t_{lT}$  represents a realistic uncertainty estimate for the weak Sn phase with configuration B. (d) Both the STA/LTA and the polarization detector miss Sn and pick the secondary Sg phase.

of the search windows, even if  $tS_{pre}$  is used as  $t_{AC}$ . For distances less than  $\Delta_{AIC_3}$ , we extend the search windows in a way that includes possible triggers from the detectors.

At distances above  $\Delta_{AIC_3}$  we expect Sn as the first arriving S-phase and the maximum STA/LTA value  $tS2L_{max}$  is usually associated with the arrival of a later (impulsive) phase (Sg or SmS). To avoid phase misidentification as described in Figure B.5, the AR-AIC windows are adjusted in a way such that  $tS2L_{max} - t_{SE} > 0$ . In analogy to P-phase picking for same earthquakes (*Diehl et al.*, 2008) we choose  $\Delta_{AIC_3} = 100$  km. Furthermore, picks are rejected if the minimum AIC is located close to the start or the end of the picking window for several components. A minimum AIC close to the edge of the picking window is usually an indicator for misconfigured AR-AIC search windows.

### B.2.4 Quality Assessment in Combined Approach

Robust uncertainty estimates for automatic S-arrivals can be obtained by combining picking information from different techniques to define lower  $tS_{lo}$  and upper  $tS_{up}$  limit of the error interval. The mean position of this interval  $tS_{me} = (tS_{up} + tS_{lo})/2$  is defined as the S-arrival time. In our approach, the earliest and latest possible pick from the STA/LTA detector ( $tS_{min1}$ ,  $tS_{thr1}$ ), polarization detector ( $tS_{min2}$ ,  $tS_{thr2}$ ), and the different AIC minima ( $tS_{AC}$ , with  $C = N, E, Q, T, H$ ) constitute the lower and upper limits of the corresponding error interval.

In addition, the width of the AIC minimum is usually related to the quality of the onset. Impulsive wavelets like the S-arrival on the T component in Figure 5.4 lead to a distinct AIC minimum, whereas emergent wavelets produce broader minima (Fig. B.5c). The width of the AIC minimum can therefore be used as an additional quality information about the arrival time and is also a good indicator for the presence of possible precursory phases. We define the earliest possible arrival derived from the AIC function as the first sample where AIC drops below  $thr_{AIC}$  and the latest possible arrival as the last sample below  $thr_{AIC}$  (see Fig. 5.4 and B.5c). If  $AIC_{min}$  represents the minimum and  $AIC_{max}$  the maximum AIC value within the picking window,  $thr_{AIC}$  is defined as 10% of the differential AIC:

$$thr_{AIC} = AIC_{min} + (AIC_{max} - AIC_{min})/10 \quad (B.16)$$

The dashed horizontal lines in Figure 5.4 and B.5b,c denote the threshold  $thr_{AIC}$  for the AIC-quality assessment. The corresponding positions of ‘earliest-possible’ and ‘latest-possible’ arrivals are represented by  $tS_{eT}$ ,  $tS_{eQ}$ ,  $tS_{iT}$ , and  $tS_{iQ}$ . The usage of the AIC-quality assessment becomes especially important for appropriate uncertainty estimates at larger epicentral distances. In the following, we define the distance  $\Delta_{AIC_2}$  above which the AIC quality assessment is considered for the overall quality assessment.

### Quality Weighting Scenarios

Since detectors and components are sensitive to different phase types in different

distance ranges, we setup four different weighting scenarios derived from the calibration with the reference data set. The weighting scenarios are also summarized in Table 5.2.

*Scenario 1: S-phase recognized by polarization detector at distances  $\Delta_{epi} < \Delta_{AIC_3}$  (Sg dominated range)*

The polarization detector represents the best indicator for a pure S-wave arrival. In case of a detection, we use the polarization picks  $tS_{thr2}$ ,  $tS_{min2}$ , and the combined AR-AIC minimum  $tS_{AH}$  to derive the uncertainty interval. Furthermore, we consider the AR-AIC picks derived on rotated components (T or Q). Due to the radiation pattern and observation azimuth, the energy of the S-wave can be distributed unevenly between T and Q. Therefore, the S-onset might be of a different quality on different components (see Fig. B.3). In addition, the T component should be less affected by potential Sp energy. To avoid unrealistic large error intervals, we consider only the component, whose AR-AIC minimum  $tS_{AC}$  is closest to the S-wave detection  $tS_{min2}$ . For epicentral distances above  $\Delta_{AIC_2}$ , additional information provided by  $tS_{eH}$  and  $tS_{eT}$  or  $tS_{eQ}$  is used for error interval determination. Finally, we calculate the average pick position  $tS_{av}$ , standard deviation  $\sigma_{pk}$ , earliest pick position  $tS_{er}$ , and latest pick position  $tS_{la}$  from the provided picks. To account for possible precursory S-phases  $tS_{er}$  represents always the position of the lower error interval  $tS_{lo}$ . The upper error interval is derived from  $tS_{up} = tS_{av} + \sigma_{pk}$ .

*Scenario 2: S-phase recognized only by STA/LTA detector at distances  $\Delta_{epi} < \Delta_{AIC_3}$  (Sg dominated range)*

In this case, the phase type is likely to be less well constrained. Besides  $tS_{thr1}$  and  $tS_{min1}$ , AR-AIC minimum picks  $tS_{AC}$  from all components (N, E, Q, T, H) are considered for determination of  $tS_{lo}$  and  $tS_{up}$ . For epicentral distances above  $\Delta_{AIC_2}$ , additional information provided by  $tS_{eC}$  is considered for error interval determination. Again,  $tS_{er}$  represents the position of the lower error interval  $tS_{lo}$  and the upper error interval is derived from  $tS_{up} = tS_{av}$ .

*Scenario 3: S-phase recognized by polarization or STA/LTA detector at distances  $\Delta_{epi} \geq \Delta_{AIC_3}$  (Sn dominated range)*

In the distance range around the crossover between Sg to Sn as the first arriving S-phase, arrivals picked by STA/LTA and polarization detectors are often associated with impulsive later phases. In this scenario the error assessment is solely based on the uncertainty estimates obtained from the AIC function. We calculate the mean and standard deviation from  $tS_{eC}$ ,  $tS_{AC}$ ,  $tS_{IC}$ , with  $C = N, E, Q, T, H$ . The mean position of the S-wave is represented by the average picking position, the error interval is defined by  $\pm\sigma_{pk}$ .

*Scenario 4: S-phase recognized neither by polarization nor STA/LTA detector (at all distance ranges)*

The phase type picked by the AR-AIC picker is rather unreliable. The phase is

rejected by default.

The error interval is used to calculate the mean position of the S-wave arrival and to assign a discrete quality class according to an *a priori* user defined weighting scheme.

Finally, a minimum amplitude signal-to-noise ratio  $S2N_{min}(m)$  is defined for each quality class  $m$ . If the signal-to-noise ratio of the current pick is less than  $S2N_{min}(m)$ , the pick is downgraded to the next lower quality class and its signal-to-noise ratio is checked again for the new class. Since we expect smaller signal-to-noise ratios for potential Sn phases, we define different sets of  $S2N_{min}(m)$  above and below  $\Delta_{AIC_3}$ . Figure 5.5 and B.6 show examples for different automatic S-wave arrival picks and their corresponding error intervals at distances dominated by Sg and Sn, respectively. The mean position and the error intervals of the automatic picks

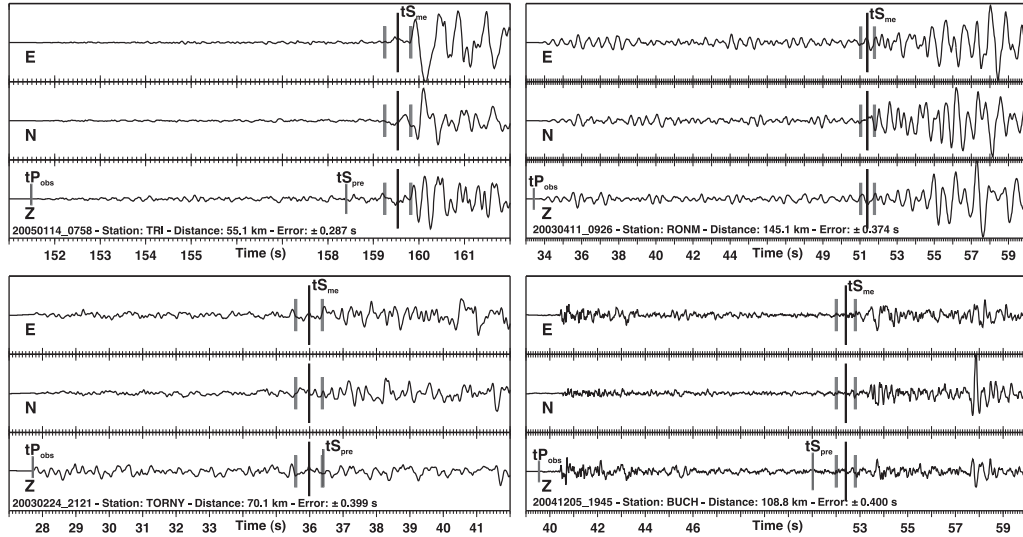


**Figure B.6:** Further examples of automatic S-wave picks at epicentral distances dominated by first arriving Sg phases (left column) and first arriving Sn phases (right column) for different error intervals. The error interval derived from the automatic quality assessment is represented by the vertical gray bars. The vertical long black bars denote the mean position of the S-wave onset. Error interval and mean position agree very well with the actual S-wave arrival observed on the seismograms.

agree very well with the actual S-wave arrival observed on the seismograms.

## B.3 Application to Alpine Region (Supplementary Material)

### B.3.1 Average Picking Uncertainty

The average picking uncertainty of an arrival-time data set can be estimated from the number of picks and the uncertainty interval of each class. Assuming  $L$  quality

weighting classes  $i$  ( $i = 1, \dots, L$ ), each class is associated with an uncertainty interval  $\varepsilon_i$ . The number of picks of the  $i$ th class is described by  $N_i$ . The average picking uncertainty can be estimated from:

$$\varepsilon_{avr} = \frac{1}{\sum_{i=1}^L N_i} \sum_{i=1}^L \varepsilon_i N_i \quad (\text{B.17})$$

### B.3.2 Picking Performance for Tomography

Table 5.3 and 5.5 demonstrate that some S-waves can be picked in principle with an accuracy  $\leq 100$  ms by hand as well as by our automatic algorithm. On the other hand, the highest quality ‘0’ is the less populated class and most of the reference as well as automatic S-picks are classified as ‘1’. Such an unbalanced distribution of errors indicates an optimistic weighting scheme, which is not appropriate for seismic tomography. Since we are usually interested in an uniform ray-coverage (resolution) in 3-D tomography, we are not able to benefit from a minority of high-accurate observations if the majority of data is of a lower quality. On the other hand, the minimum velocity perturbation resolvable depends on data error and on model parametrization. Due to this trade-off, an appropriate parametrization turns out to be rather difficult for such a weighting scheme.

To obtain an appropriate weighting scheme for seismic tomography, we merge class ‘0’ and ‘1’. The simplified weighting scheme contains only two usable (‘0’ and ‘1’) and one reject class (‘2’) as illustrated in Table B.3. The highest quality represents the largest populated class, and the average picking error of the training-

		Automatic Quality Classification			
		0	1	2 (rej)	$\Sigma$ Ref
Reference Quality Classification	0	$N_{00} = 142$ 33 % $\sigma_{00} = 0.10$ s	$N_{01} = 102$ 24 % $\sigma_{01} = 0.31$ s	$N_{02} = 189$ 43 % $\sigma_{02} = 1.22$ s	$N_0^{\text{Ref}} = 433$ $ \varepsilon_0  \leq 0.2$ s
	1	$N_{10} = 13$ 7 % $\sigma_{10} = 0.17$ s	$N_{11} = 35$ 20 % $\sigma_{11} = 0.33$ s	$N_{12} = 128$ 73 % $\sigma_{12} = 1.60$ s	$N_1^{\text{Ref}} = 176$ $ \varepsilon_1  \leq 0.4$ s
	2 (rej)	$N_{20} = 0$ 0 % $\sigma_{20} = 0.00$ s	$N_{21} = 2$ 1 % $\sigma_{21} = \text{Not av.}$	$N_{22} = 186$ 99 % $\sigma_{22} = 0.69$ s	$N_2^{\text{Ref}} = 188$ $ \varepsilon_2  < 0.4$ s
	$\Sigma$ Aut	$N_0^{\text{Aut}} = 155$ $\sigma_0 = 0.12$ s $\overline{\Delta \text{AR}}_0 = -0.01$ s	$N_1^{\text{Aut}} = 139$ $\sigma_1 = 0.31$ s $\overline{\Delta \text{AR}}_1 = 0.11$ s	$N_2^{\text{Aut}} = 503$	

**Table B.3:** Performance of the automatic S-wave picker for simplified weighting scheme (3 quality classes) in matrix presentation as in Table 5.5.

mode adds up to about 0.29 s in this new weighting scheme (only slightly higher than the average error in the original weighting scheme). Such a well-balanced weighting scheme facilitates the model parametrization for tomography. On the other hand, the weighting scheme of Table 5.5 is rather suitable for earthquake location problems, since single high-quality S-arrivals can significantly reduce the uncertainty of the hypocenter determination.

### B.3.3 Parameter Search Procedure

To derive a satisfactory picker-performance for a certain data set, appropriate values of the parameters listed in Tables 5.4 and B.4 have to be evaluated from a trial-and-error procedure. The picker is applied to the reference data for each set of parameters and its resulting performance has to be assessed as described in the body of the article. Guidelines on how the critical parameters have to be evaluated for a certain data set are provided in the body of the article. In this section we give additional information on less critical parameters of Table B.4, which were not discussed in the body of the article.

- $\Delta S_{post}$ : Has to be evaluated from the maximum deviation between predicted arrivals (depending on accuracy of velocity model) and reference picks. The value should be large enough to guarantee that the coarse S-window includes the actual arrival of the S-phase.
- $\Delta P_{gap}$ : The length of the safety gap between  $tP_{obs}$  and  $SW1$  depends on the width of the P-wave signature present in the STA/LTA characteristic function and on the minimum epicentral distance. In principle, a value of 0.75 s would confine the minimum epicentral distance to about 5 to 6 km (for shallow earthquakes). In practice, its value is less critical, since the polarization-detector is pretty reliable for close-by events and in this case, the STA/LTA detector is not considered at all. It might have to be adjusted for special studies such as microseismicity.
- $tdw$  of STA/LTA detector: Due to the rather smooth shape of the characteristic function of the STA/LTA detector,  $tdw$  does not have to account for singularities and can be set to zero. If  $\Delta st$  and  $\Delta lt$  are adjusted to higher resolution, we expect a more complicated characteristic function and it might be necessary to choose a value  $> 0$ .
- $n$ : Controls the effect of absolute amplitude weighting of  $CF_S$ . A value of 0 disables the weighting ( $CF_S$  corresponds to the original definition of *Cichowicz* 1993). Using a value of 0 lead to several false detection (noise) in our application. A high value of e.g. 1.0 could lead to missed Sn arrivals. A value of 0.5 represents the best compromise for our data set.
- $M(1), M(2)$ : The maximum order of the AR-model has not much effect on the AR-AIC performance due to the AR-modeling method implemented in our approach (see *Takanami and Kitagawa* 1988 for details). A value between 10 and 20 is appropriate.
- $\kappa_{min}^1, \kappa_{max}^1$ : Minimum and maximum  $v_P/v_S$  ratio expected in a region for phases sampling mainly the upper crust. Can be used to identify gross mispicks, similar to the use of Wadati diagrams. Usually, we expect values between 1.5 and 2.1.

- $\kappa_{min}^2, \kappa_{max}^2$ : Minimum and maximum  $v_P/v_S$  ratio expected in a region for phases sampling mainly the lower crust. Here we expect a narrower band of  $v_P/v_S$  ratios.
- Waveform Filters: Performance of the picker should be checked for different frequency bands. Based on experience from routine and reference picking, the Wood-Anderson filter facilitates identification of S-wave arrivals. This observation is confirmed by the behavior of the automatic picker, since we obtained the best performance with the application of the Wood-Anderson filter.

Parameter	Description	Value
<b>General Parameters</b>		
$\Delta S_{post}$	Defines upper end of coarse S-wave search window	5 s
<b>Parameters for STA/LTA Detector</b>		
$\Delta P_{gap}$	Safety gap between $tP_{obs}$ and $SW1$	0.75 s
$tdw$	Maximum time $CF$ drops below threshold	0.00 s
<b>Parameters for Polarization Detector</b>		
$n$	Exponent for absolute amplitude weighting of $CF_S$	0.5
<b>Parameters for AR-AIC Picker</b>		
$M(1)$	Maximum order of AR-model (noise)	15
$M(2)$	Maximum order of AR-model (signal)	15
<b>Parameters for Quality Assessment</b>		
$\kappa_{min}^1$	Minimum $v_P/v_S$ ratio defining S-window ( $\Delta_{epi} < \Delta_{AIC_3}$ )	1.500
$\kappa_{max}^1$	Maximum $v_P/v_S$ ratio defining S-window ( $\Delta_{epi} < \Delta_{AIC_3}$ )	2.050
$\kappa_{min}^2$	Minimum $v_P/v_S$ ratio defining S-window ( $\Delta_{epi} \geq \Delta_{AIC_3}$ )	1.600
$\kappa_{max}^2$	Maximum $v_P/v_S$ ratio defining S-window ( $\Delta_{epi} \geq \Delta_{AIC_3}$ )	1.825
<b>Waveform Filters</b>		
$\Delta_{epi} < \Delta_{AIC_3}$ : Wood-Anderson		
$\Delta_{epi} \geq \Delta_{AIC_3}$ : Wood-Anderson + additional 0.5 Hz HP-filter		

**Table B.4:** Additional parameters which have to be adjusted for the described picking approach. The suggested values are derived from a parameter search comparing automatic picks with reference picks of local earthquakes within the greater Alpine region.

## B.4 Outlier Detection (Supplementary Material)

### B.4.1 Outlier-Detection in Test-Mode

To assess the performance of the automatic picker especially in terms of systematic mispicks and outliers present in the test-mode, we display the difference between automatic and reference S-picks ( $\Delta AR$ ) for usable automatic picks against epicentral distance in Figure 5.7. In general, the number of outliers is low and the



corresponding errors are rather large. The number of gross outliers increases in the distance range of the triplication zone (Fig. 5.7). Here, the first arriving weak Sn phases are usually followed by an impulsive Sg and the AR-AIC picker can fail to discriminate the two phases, even if a dynamic adjustment of search windows is applied (example *e1* in Fig. 5.7). Since we use the picks provided by the detectors to setup the AR-AIC windows for smaller epicentral distances, false detection can also result in the wrong phase identification for some Sg phases, as marked by example *e2* in Figure B.5. Here, the polarization detector triggers at a later arriving phase due to the small degree of linear polarization of the preceding earlier phase picked as reference S-arrival.

If the automatic picker is applied to a data set without reference picks (production-mode) we have different possibilities to identify possible outliers. A common way to detect mispicked S-arrivals is the usage of Wadati diagrams as described, for example, by *Kisslinger and Engdahl (1973)* or *Maurer and Kradolfer (1996)*. In Figure B.7a we plot  $\Delta_{SP} = tS_{me} - tP_{obs}$  against the P-wave travel time  $\Delta_P = tP_{obs} - t_0$  for individual (usable) automatic S-picks from the training-mode. For a comparison between automatic and reference S-picks we use the same origin time  $t_0$  as provided by the P-wave minimum 1-D location and compute the corresponding average  $v_P/v_S$  ratios at different distance ranges (0-50 km, 50-100 km, 100-150 km) similar to Wadati diagrams. The corresponding result for the reference S-picks is

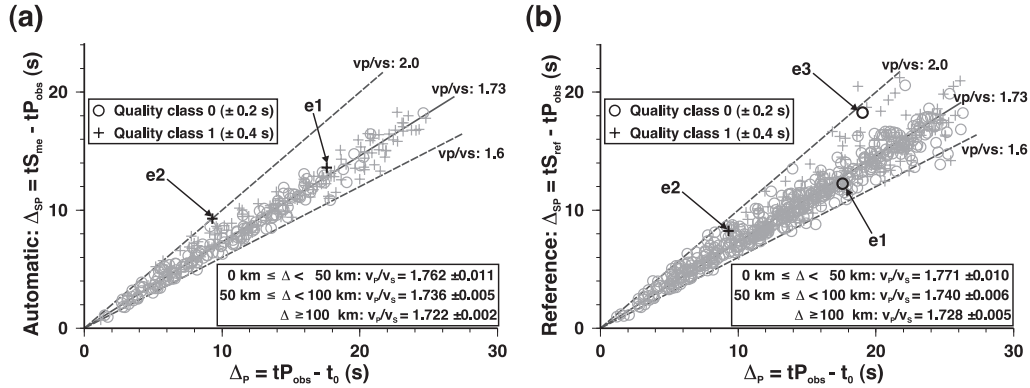


**Figure B.7:** Modified Wadati diagrams based on (a) automatic S-picks from the training-mode and (b) reference S-picks. The fixed origin times  $t_0$  are provided by the P-wave minimum 1-D locations. Dashed lines denote range of extreme  $v_P/v_S$  ratios of 2.0 and 1.6. Solid line represents theoretical  $v_P/v_S$  of 1.73 expected for a Poisson solid. Average  $v_P/v_S$  ratios derived from automatic and reference picks for three different distances ranges are given in the boxes. Example outliers *e1*, *e2*, and *e3* as discussed in the text are marked by black symbols.

presented in Figure B.7b. The average  $v_P/v_S$  ratios show no significant systematic bias between automatic and reference S-picks.

The positions of ‘automatic’ mispicks *e1* and *e2* are marked as black bold crosses in Figure B.7a. Example *e2* indicates a rather high  $v_P/v_S$  ratio close to 2.0. Although wrong by more than one second, *e1* cannot be identified explicitly as an outlier pick.

An increased scatter among the reference picks can be observed in Figure B.7b.

Especially at larger distances several obvious outliers are present in the reference data. In case of example *e3*, the weak earlier  $S_n$  phase was not recognized in the reference hand picking and the later-arrival phase was misinterpreted as the first arriving S-wave, which leads to an error of several seconds. The automatic pick for the same recording was rejected by the automatic quality assessment and is therefore not included in Figure B.7a. This example demonstrates the difficulty and ambiguity in manually picking and identification of S-waves, especially beyond the cross-over distance between  $S_n$  and  $S_g$ . On the other hand, the more conservative quality assessment of the automatic approach significantly reduces the scatter in S-phase arrivals (Fig. B.7a) at the cost of a lower number of usable picks.

### B.4.2 Outlier-Detection in Production-Mode

The production-mode yields 1618 class ‘0’ ( $\pm 0.2$  s) and 973 class ‘1’ ( $\pm 0.4$  s) automatic picks. Hence, 57% of the (non-clipped) potential S-phases could be picked with our approach. If outliers are disregarded, the average picking error adds up to about 0.27 s. Since outliers are associated with errors up to several seconds, they lower the average accuracy of the automatic picks significantly. Therefore, outliers have to be identified and removed from the data set.

As for the test-mode, we derived average  $v_P/v_S$  ratios from modified Wadati diagrams. The results for the three distance ranges agree very well with the values derived from reference S-picks (Fig. B.7b), which suggests that performance of the production-mode is comparable with the test-mode. As demonstrated for the test-mode, the analysis of individual  $S-P$  versus P-wave travel times is not sufficient to detect moderate outliers in the production-mode. Therefore, all automatic S-picks indicating  $v_P/v_S > 1.75$  were cross-checked against waveforms for distances  $> 50$  km in a semi-automatic procedure to assess the number of outliers due to misinterpreted phases. From 450 analyzed automatic picks, 42 (9%) were identified as obvious mispicks or highly questionable automatic picks. Most of these mispicks resulted from phase misinterpretation analogous to example *e1* in Figure B.7 in the distance range of the triplication zone (90-110 km). The 42 clearly identified mispicks represent about 2% of all automatic picks.

# Appendix C

## Users Guide for Consistent Phase Picking at Local to Regional Scales

T. Diehl and E. Kissling

Institute of Geophysics, ETH-Zuerich  
CH-8093 Zurich, Switzerland

June 2008

## C.1 Introduction

Although travel time based earth models and hypocenter solutions strongly depend on the accuracy of used phase data, the description of consistent phase picking receives only little attention in literature. *Simon* (1981), *Kulháněk* (1990), and *Kulháněk* (2002) provide a general overview about seismogram interpretation from local to teleseismic scales. They focus mainly on basic descriptions of phases observable in common seismograms. The assessment of timing uncertainty and phase interpretation, however, is barely discussed. The fundamentals of digital signal processing and their influence on onset properties are described e.g. in *Seidl and Stammer* (1984), *Scherbaum* (2001), and *Scherbaum* (2002). Among the few recent guidelines, the *New Manual of Seismological Observatory Practice* (NMSOP) of *Bormann et al.* (2002) provides an introduction to basic picking principles for local, regional and teleseismic seismograms. Although they already propose to quantify the onset-time reliability, a detailed description for consistent quality assessment is missing, similar to the discussion in *Scherbaum* (2001).

Due to modern digital acquisition systems (timing with GPS or DCF-systems, sampling rates  $\geq 80$  Hz) and the use of modern analyzing software, onsets of seismic signals can be determined with a precision of up to a few tenth of milliseconds. To benefit from this accuracy in applications like high-resolution tomography, a consistent error assessment in terms of timing uncertainty and phase interpretation is crucial. This user guide provides a detailed description of common problems in routine hand picking and presents a hand picking procedure, which includes a consistent quality assessment for timing uncertainty and phase interpretation. It is focused on crustal and upper mantle phases on local to regional distances, but its principles apply likewise to teleseismic observations.

## C.2 Routine Hand Picking

Especially for local and regional earthquake data, phase picking often becomes inconsistent and ambiguous due to rather complex waveform patterns and the close arrival of different phase types within a short time period of the same coda. In general, the shape of a seismic wavelet is affected by the source time function, the radiation pattern, dispersion, attenuation, scattering, interference with other phases, the signal-to-noise ratio at the recording site, and the characteristic of the recording system. The superposition of these components may lead to highly complex waveforms in case of high-frequency local and regional recordings. Moreover, the picking of later phases such as PmP or S-waves becomes even more difficult, since they interfere with the coda of earlier phases. Since the target accuracy of such arrivals is usually within few hundred milliseconds, errors like phase misinterpretations denote blunders and may significantly bias hypocentre locations and velocity models. Furthermore, regional studies usually require the compilation of data from several networks. In such a case, merging routine phase data will add even more inconsistency.

The possible sources for inconsistent hand picking described in the following sections refer mainly to P-wave picking. However, the basic principles of picking and error assessment of phases is also valid for S-wave picking. In addition, section C.2.6 includes problems specific to S-wave picking.

In general, a seismic phase is defined by two visual observations:

1. Change primarily in amplitude:  
The amplitude exceeds the background noise (for a certain amount of time). This can also be denoted as amplitude based signal-to-noise ratio (*ASNR*). We may define a phase, if its amplitude exceeds the background noise at least by a factor of 1.5 ( $ASNR \geq 1.5$ ). Figure C.1 represents a typical example for a phase arrival defined by a change of the *ASNR*.
2. Change primarily in frequency:  
A change of the dominant frequency indicates the arrival of a seismic phase. We can refer to this observation as frequency based signal-to-noise ratio (*FSNR*). Unlike the *ASNR*, it is often much more difficult to quantify visually. Moreover, the dominant frequency of noise and signal can sometimes be very similar. But especially for broad time windows, the *FSNR* can help to determine the approximate position of a phase. Figure C.2 represents a typical example for a phase arrival defined by a change of the *FSNR*.

Once a phase is recognised based on *ASNR* or on *FSNR* or - most likely - a combination of both, we have to determine the precise wavelet onset ('arrival time'). However, its position is usually not completely independent from the associated overall observation uncertainty. Finally, we have to identify the phase type and to do so, we have to answer questions like: May we assign the ray path to the phase (Pg, Pn, PmP) with certainty or is the station near a triplication point? Are we sure that it is the first arrival or is it possible, that an earlier phase is hidden in the noise? In addition, the visual examination of *ASNR* and *FSNR* can be rather subjective and strongly depends on the width of the used time window and also on amplitude scaling. Finally, filtering can affect *ASNR* and *FSNR* significantly. In the following sections, we will give examples for these problems and suggest possible solutions in order to minimize inconsistencies during the picking process. Once identified, it should be possible to minimize their contribution by defining certain rules and procedures, which finally add up to a consistent picking workflow and consistent uncertainty assessment for each observation.

### C.2.1 Phase Picking Part I: Phase Timing and its Error Assessment

The basic quantities associated with a picked phase are usually the absolute arrival time and the corresponding observation error. However, it is difficult or even impossible to give a general definition of a seismic onset, which could be used for the actual measurement of first arrival time from a sampled band-limited signal in the

presence of noise (*Seidl and Stammer*, 1984). Therefore, the visual determination of absolute arrival times often implies a high degree of subjectivity and inconsistency. Consequently, a physical consistent formulation can only be achieved by a probabilistic point of view. Such an approach directly relates the measured arrival time with the corresponding observation error. Considering the onset of a seismic phase as probabilistic function  $P_a(t)$ , the arrival time is expressed as the ‘most likely’ time  $t_A$ , with  $P_a(t_A) = \text{Max}(P_a)$ . On the other hand, the ‘earliest’ possible time for the phase onset is defined as  $t_E$ , where the likelihood for onset is approaching zero. Thus  $P_a(t_E) \geq 0$ . Analogue, the ‘latest’ possible time for the phase onset  $t_L$ , is also defined as  $P_a(t_L) \geq 0$ .

Figure C.1 illustrates the proposed concept for a typical *ASNR*-case in further detail. Although the onset of the phase is rather impulsive and exhibits an almost ideal signal to noise ratio, it is difficult to determine an arrival time consistent with picks of waveforms from same seismic source recorded at other stations. The thick grey band between position ‘1’ and ‘2’ defines the time window that for certain includes the onset of the wavelet. The band outlined by two broken lines denotes the possible threshold of the noise amplitude. In practice, we first determine the position of  $t_L$  and  $t_E$ . For a consistent determination of  $t_L$  and  $t_E$ , we have to setup a common procedure. Since the amplitude exceeds the threshold several times at position ‘2’, the end of the grey band is certainly too late to be picked as  $t_L$ . Therefore, we define the intercept between signal amplitude and a priori noise threshold (here: 1.5 times the noise amplitude) as  $t_L$ . Usually, the consistent determination of  $t_E$  is more difficult. In Figure C.1 we fit a tangent (dashed line ‘a’) to the smoothed slope of the onset. If we shift the tangent from  $t_L$  towards earlier times, the slope decreases. The earliest possible time  $t_E$  corresponds with the first zero slope from  $t_L$  towards earlier time. Therefore, the start of the grey band (position ‘1’) is certainly too early and on the other hand,  $t_A$  would be too late to be picked as  $t_E$ . To ensure  $t_E$  includes the zero slope time in presence of larger background noise, we could shift it to earlier arrival by approximately half a wavelength of the dominant noise. Subsequently, we pick the arrival of the phase at the most likely position  $t_A$ , within the error interval of  $t_E$  and  $t_L$  (e.g. on the seismogram’s leading edge). For the special case of an ideal delta-pulse,  $t_E$  and  $t_L$  would coincide with  $t_A$ . Figure C.2 illustrates the concept for the *FSNR*-case. Again, the thick grey band between position ‘1’ and ‘2’ defines the time window that for certain includes the onset of the wavelet and the band outlined by two broken lines denotes the possible threshold of the noise amplitude. The change in frequency is obvious for arrival times greater than position ‘b’. Therefore, we define  $t_L$  a quarter signal wavelength ( $\lambda/4$ ) after position ‘b’. For arrival times earlier than position ‘a’, the signal frequency (indicated by grey wavelet) is certainly not present. We pick  $t_E$  half a signal wavelength ( $\lambda/2$ ) before position ‘a’. Usually, the observation error is related with a discrete weighting or quality class (e.g. 0-5). However, these classes are often defined only through qualitative attributes, like waveform shape (impulsive or emergent). Such classification is not sufficient for a consistent error assessment. Instead, a quantitative weighting

scheme has to be defined and the assigned weighting class depends only on the measured time error interval ( $t_L - t_E$ ). In addition, the measurement of  $t_L$ ,  $t_E$ , and  $t_A$  allows us to adjust the weighting class definition even after the picking process.

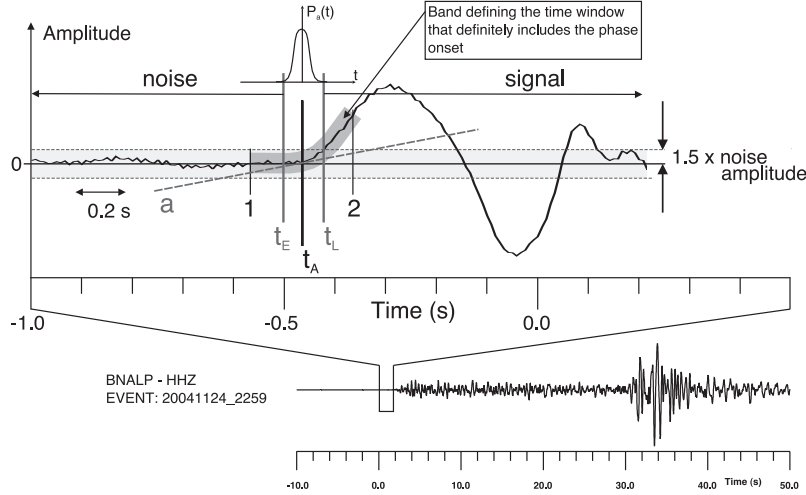


**Figure C.1:** Probabilistic phase picking approach based on change of ASNR: the ‘earliest’ possible pick corresponds to  $t_E$ , the ‘latest’ possible pick corresponds to  $t_L$ . The most likely arrival time  $t_A$  is located within this interval. Primarily amplitude is used for determination of  $t_E$  and  $t_L$ .

### C.2.2 Phase Picking Part II: Phase Identification and its Error Assessment

Although phase misinterpretation can result in significantly large errors, phase identification is typically not supplied with any observation error or uncertainty attribute at all (unlike arrival time of a phase). As demonstrated by synthetic travel time curves in Figure C.3, the first arrival of the local or regional P-wave coda is usually Pg (direct wave as illustrated in inset of Fig. C.3) or Pn (Moho-refracted wave). Whether Pg or Pn is the fastest wave depends on epicentral distance  $\Delta$ , crustal thickness  $z_M$ , and focal depth  $z_F$ . Discrimination between Pg and Pn can become rather difficult in the distance range of phase triplication (see Fig. C.3). The Moho-reflected PmP phase always arrives after Pg and Pn, although its amplitude can become the dominant phase in the coda. The synthetic reflectivity seismograms (*Fuchs and Müller, 1971*) in Figure C.3 (vertical components) denote the expected amplitude ratios between Pg, Pn, and PmP for this simplified crustal model. Especially for large epicentral distances, Pn is sometimes masked in the noise and Pg or PmP can likely be interpreted as the first arrival. As an example, Figure C.4 presents a velocity reduced record section of a local earthquake near Walenstadt, Switzerland with a focal depth of 13 km. Based on waveform characteristics alone, phase interpretation appears rather difficult for

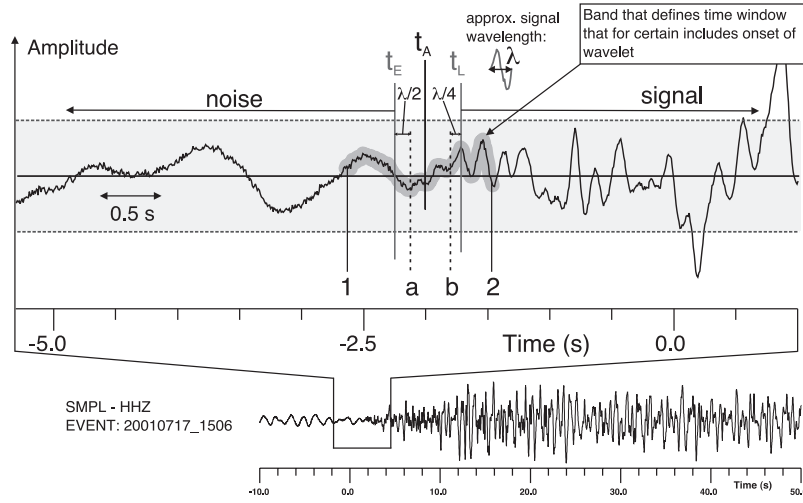


**Figure C.2:** Probabilistic phase picking approach based on change of  $FSNR$ : the ‘earliest’ possible pick corresponds to  $t_E$ , the ‘latest’ possible pick corresponds to  $t_L$ . The most likely arrival time  $t_A$  is located within this interval. Primarily frequency is used for determination of  $t_E$  and  $t_L$ .

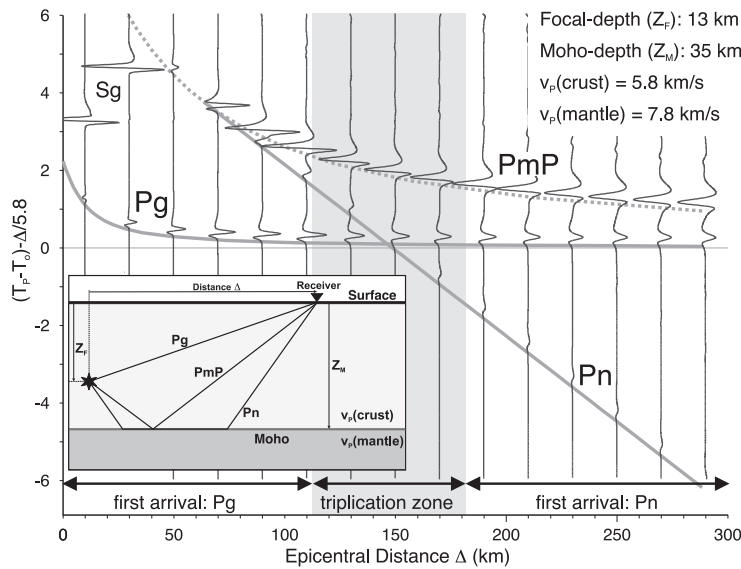


**Figure C.3:** Reflectivity seismograms (vertical components) and synthetic travel time curves (solid and dashed lines) for main phases observed in local and regional earthquakes (one layer over half space). Focal depth is set to 13 km and time axis is reduced by 5.8 km/s. Phase identification is expected to be difficult in the distance range of phase triplication. The position and width of this zone mainly depends on focal depth and Moho topography.



some stations in the distance range of phase triplication (e.g. SPAK and SIERE). In addition, amplitude ratio between Pg and Pn denotes strong variations between some stations (e.g. EMV and HEI) probably due to 3D Moho topography. In this case, Pn is likely to be missed and Pg will be picked as first arrival phase.

Since most applications like hypocenter localisation and travel time tomography are (still) based on first arrivals only, we have to setup an error assessment for phase identification to avoid such inconsistency. The relevance of phase interpretation becomes even more evident for S-wave picking. For use in routine first-arrival studies and subsequent special studies, we define an error assessment for phase identification as shown in Table C.1.

Phase label	Phase is ...	Phase used for routine 1 <sup>st</sup> arrival studies
Pg	Direct (crustal)	Yes (if first arrival)
Pn	Moho-refracted	Yes (if first arrival)
PmP	Moho-reflected	No
P1	Unknown type, but certainly first arrival	Yes
P2	Unknown type, second arrival	No
P3	Unknown type, third arrival	No
P	Unknown type, uncertain if first arrival	No

**Table C.1:** Error assessment used for phase identification. Definition analogue for S-wave.

As illustrated in Figure C.4, the determination of the phase type from the pure waveform characteristics can become quite ambiguous, especially in the range of the crossover distance between Pg and Pn. As a rule of thumb, we define the following waveform characteristics:

- **Pg:** Impulsive high-frequency onset (dispersion tends to sharpen the wavelet front), first arrival close to epicentre.
- **Pn:** Usually small amplitude impulse or emergent onset, lower frequency content (absorption leads to smoothed wavelet front), first arrival for larger epicentral distance, usually followed by strong Pg and PmP phase (delay up to several seconds).
- **PmP:** Usually strong amplitude due to high reflectivity of Moho, wavelet with high-frequency reverberations. Never first arrival.

### C.2.3 Phase Picking Part III: First Motion Polarity and its Error Assessment

Information about first motion polarity is mainly needed for focal mechanism determination. Usually the polarity is denoted as ‘Up’ or ‘Down’. Figure C.1

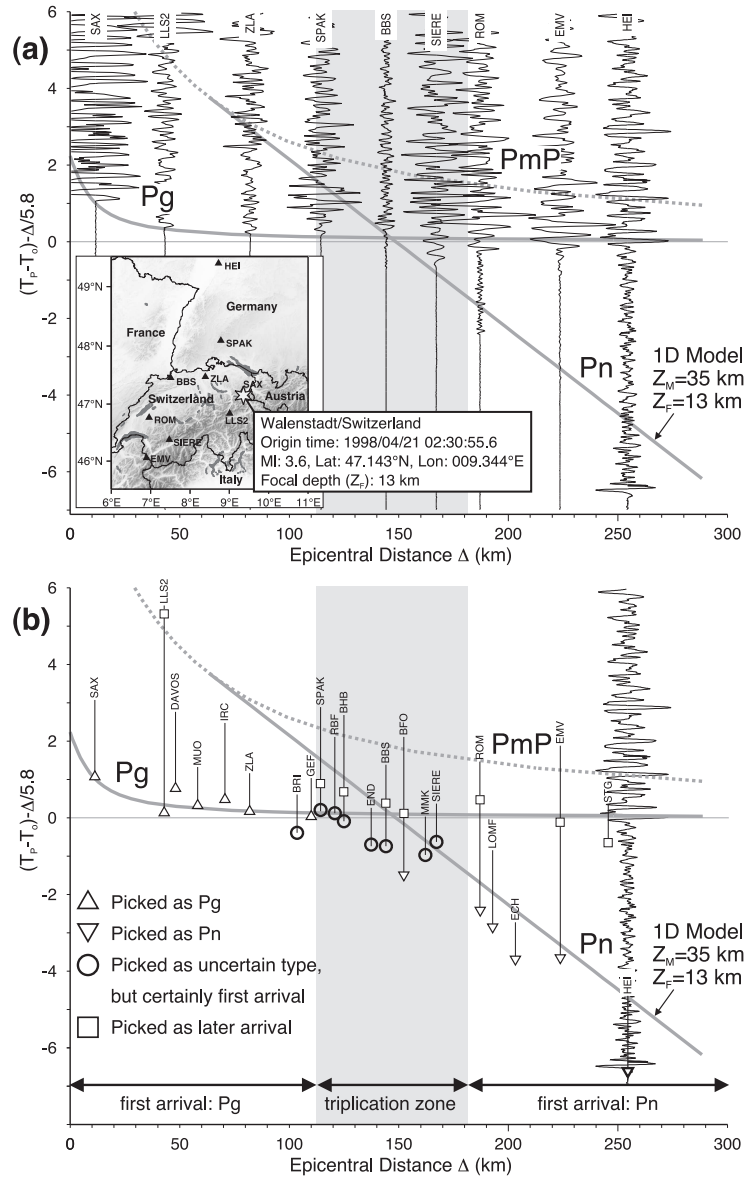


**Figure C.4:** a) Velocity reduced record section of a local earthquake near Walenstadt, Switzerland. Amplitudes are normalised to maximum amplitude of each trace. Synthetic travel time curves for  $P_g$ ,  $P_n$ , and  $P_mP$  are indicated by solid and dashed lines analogue to Figure C.3. Discrimination of phase type from waveform characteristics only might be difficult for stations in triplication range (e.g. SPAK and SIERE). Denote differences in amplitude ratio between  $P_g$  and  $P_n$  for station EMV and HEI. Deviations between expected and observed  $P_n$  arrival are related to 3D Moho topography. b) Velocity reduced phase picks, crosschecked against synthetic travel time curves derived from simplified crustal model.

represents an example for certain polarity identification. On the other hand, it is impossible to determine any polarity for the example of Figure C.2. However, besides these two obvious cases, it is sometimes necessary to use an intermediate quality class for the first motion polarity. Time ‘a’ and ‘b’ in Figure C.5 represent two possible positions for arrival time picks. In this case, the polarity is depending on the location of the pick. If the pick is assigned to position ‘a’, the polarity would be ‘Up’. If position ‘b’ is used, the polarity has to be ‘Down’. In both cases, we are not sure about the actual polarity, therefore we have to introduce an intermediate quality classes ‘+’ or ‘-’. The error assessment used here is summarized in Table C.2.

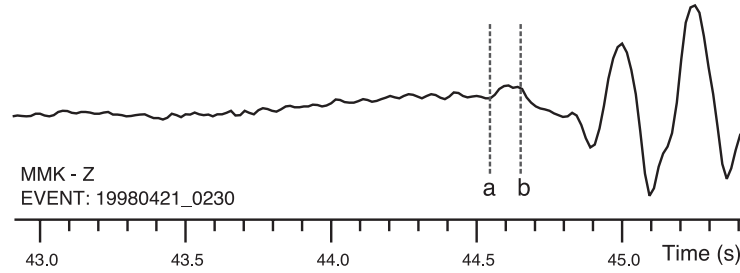


**Figure C.5:** First motion polarity and its error assessment: In this example the first motion polarity is not independent from the pick position. If the pick is assigned to position ‘a’, the polarity would be ‘Up’. If position ‘b’ is used, the polarity has to be ‘Down’. In both cases, we are not sure about the actual polarity, therefore we have to use the intermediate quality classes ‘+’ or ‘-’.

Polarity label	Polarity is ...	Weight
U/D	Up/Down	Polarity is identified with certainty
+/-	Up/Down	Polarity is identified but uncertain
N	None	Polarity cannot be identified

**Table C.2:** Error assessment used for first motion polarity.

#### C.2.4 Size of Time Window and Amplitude Scaling

The influence of time window size and amplitude scaling on picking accuracy and phase identification as described e.g. by *Douglas et al.* (1997) is demonstrated in Figure C.6a-d. In the uppermost example, the used time window is 5 s (Fig. C.6a). The picked onset is labelled as  $P_a$ . For a narrower time window of 1.5 s,  $P_a$  seems a bit too late (Fig. C.6b). Thus, we would pick the phase at position  $P_b$  in this window. The result is even more different, if time window size remains the same, but the amplitude is multiplied by a factor of 5 (Fig. C.6c) and 10 (Fig. C.6d) respectively. An earlier phase is visible, which could be picked as  $P_c$  (Fig. C.6d). But not only the absolute timing of the picked phase depends on window size and

amplitude scaling, also the assigned uncertainty interval. The error interval might be smaller for the narrower time window and the magnified case.

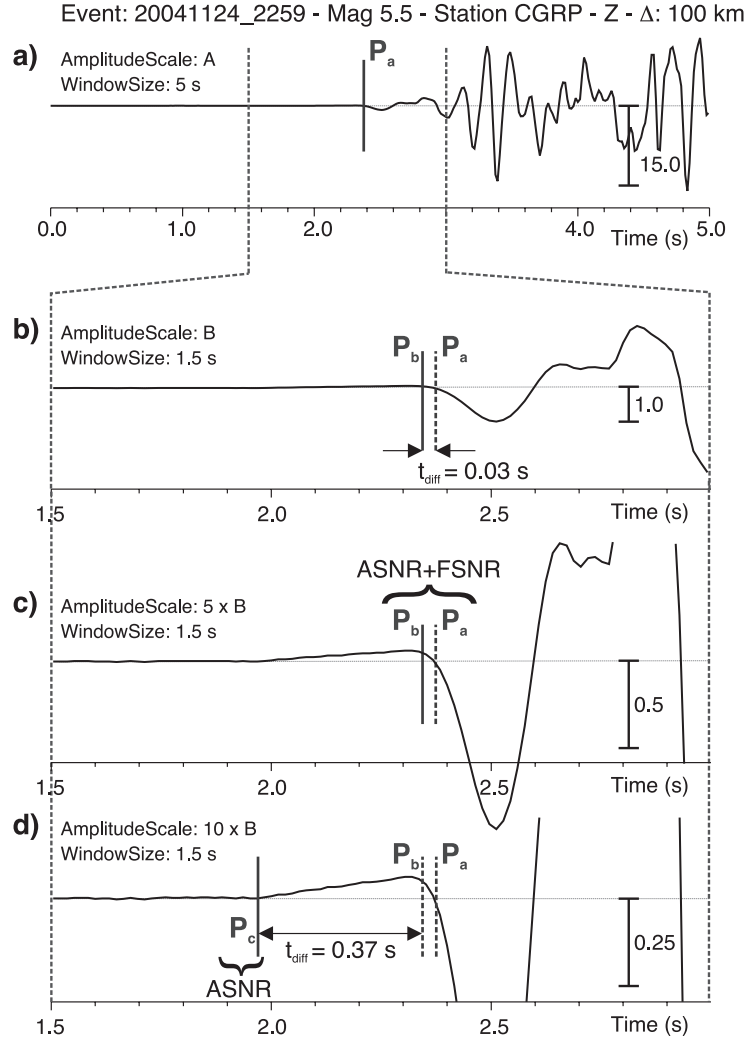


**Figure C.6:** Different phase picking, caused by variable use of time window size (a, b) and amplitude scaling (c, d).

### C.2.5 Aliasing and Waveform Filtering

From signal theory we know, that the correct digital representation of a continuous waveform depends on the sampling frequency. To avoid aliasing, a signal with frequency  $f$  has to be sampled with a sampling frequency  $\Delta f > 2f$ . Thus, the Nyquist frequency is defined as  $f_N = 1/(2\Delta t) = \Delta f/2$ . Any frequencies higher than  $f_N$  are aliased into lower ones. Therefore, we have to ensure that picking accuracy and also phase identification will not be affected by sampling rates, which are rather small. As an example we consider a waveform sampled at  $\Delta f = 20$  Hz or  $\Delta t = 0.05$  s, which corresponds to a Nyquist frequency of  $f_N = 10$  Hz. Concerning

the observation error of a phase pick, the uncertainty intervals can not be smaller than the sampling interval. Therefore, the minimum picking uncertainty is defined as  $\pm\Delta t$ . To avoid possible inconsistency due to significant different sampling rates, we suggest to use only data with  $\Delta f \geq 40$  Hz for local earthquake studies.

Aliasing occurs when the data are sampled, and once this occurs, the data cannot be ‘unaliased’. Therefore, seismic data are usually filtered with an analogue anti-aliasing filter to remove frequencies above the Nyquist frequency before sampling. Furthermore, modern acquisition systems make use of oversampling and decimation techniques (*Scherbaum*, 2001). Such systems imply digital anti-alias filters, which often denote symmetrical or acausal impulse responses to avoid time shifting of the phases (zero-phase). As a consequence, the onset of very impulsive signals (also signal with frequency close to Nyquist frequency) may be obscured by ‘acausal’ precursory oscillations and their true onset becomes hard, if not impossible, to determine. As an example for such precursors, Figure C.7 shows the P-wave recording of a local earthquake near Davos, Switzerland (2006/10/24 13:08,  $M_l=2.6$ ) at the nearby station DAVOX. In principle, this effect can be minimized by an inverse filtering process, described e.g. in *Scherbaum* (2001). However, this nontrivial procedure requires knowledge of the original anti-alias filter coefficients. Especially for large and inhomogeneous data sets, compiling the correct information can be rather difficult or even impossible. An alternative way to deal with this problem is to apply a consistent error assessment to it, as it is described above. The significance strongly depends on the amplitude scaling as discussed in C.2.4 and low-pass filtering or integration of the signal may also help to reduce the amplitudes of such precursors. Since these precursors are present only for very impulsive and high-frequent wavelets, they are expected to be limited to recordings close to the epicentre and/or low sampling rates.

Filters are usually applied to enhance the signal to noise ratio in the presence of noise. However, filtering can significantly change the shape of a wavelet and may also lead to a phase shift of the signal. Therefore, care has to be taken by applying filters during the picking process. Figure C.8 demonstrates the effect of a 2<sup>nd</sup> order Butterworth high-pass filter (1 Hz) on a short period recording. The filter causes a minor change in waveform, but no phase shift is observed. However, the effect on the wavelet can become significant for signals of different frequency content as demonstrated in Figure C.9. Position ‘a’ and ‘b’ represent two possible arrival picks for each waveform. In the worst case, time difference between those two positions could exceed 0.2 s, a value much larger than the uncertainty of each individual pick. Furthermore, the filter process affects the first motion polarity in this example.

### C.2.6 Additional Comments for S-Wave Picking

Most of the previous findings regarding consistent assessment and picking of P-arrivals can also be applied to S-waves. However, picking of S-waves is usually more difficult, since their onset is superposed by the P-wave coda. Furthermore, we have to consider S-wave splitting due to possible seismic anisotropy and the

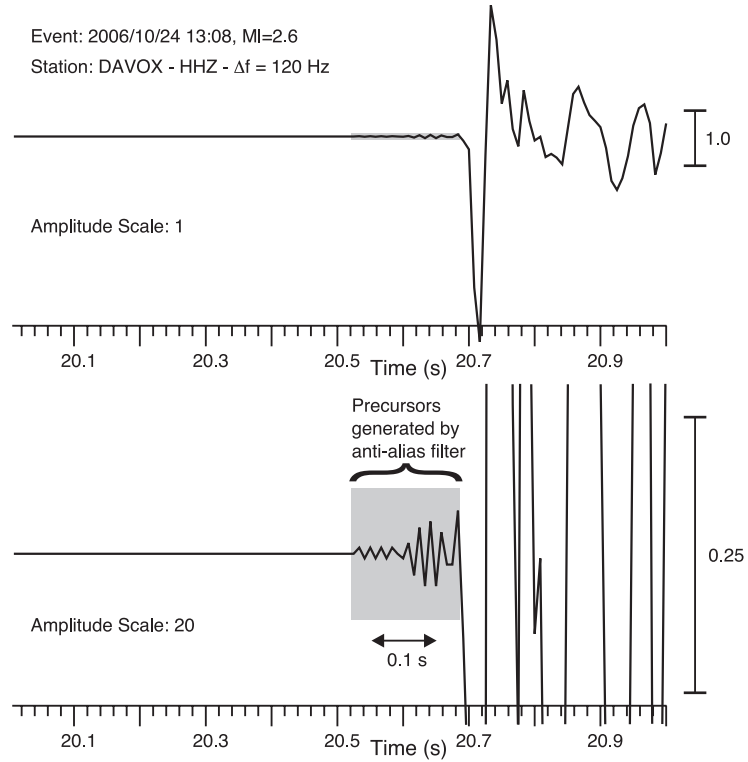


**Figure C.7:** Precursors caused by acausal anti-alias filtering observed at broadband registration of local earthquake near Davos, Switzerland (2006/10/24 13:08,  $M_l=2.6$ ). Sampling frequency is 120 Hz. The precursors become obvious for enlarged amplitude scale (lower trace).

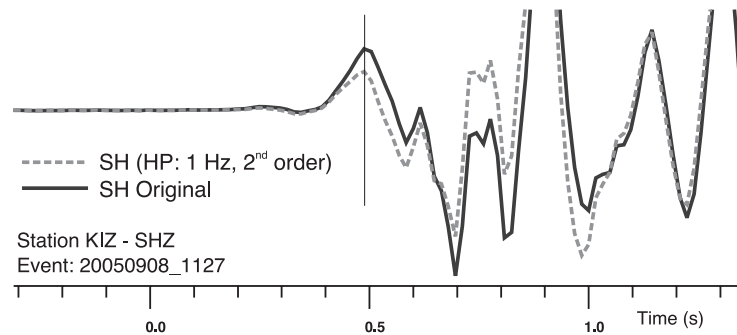


**Figure C.8:** Effect of 2<sup>nd</sup> order Butterworth high-pass filter (1 Hz) on short period waveform. The filter leads to minor change in waveform, but no phase shift is observed.

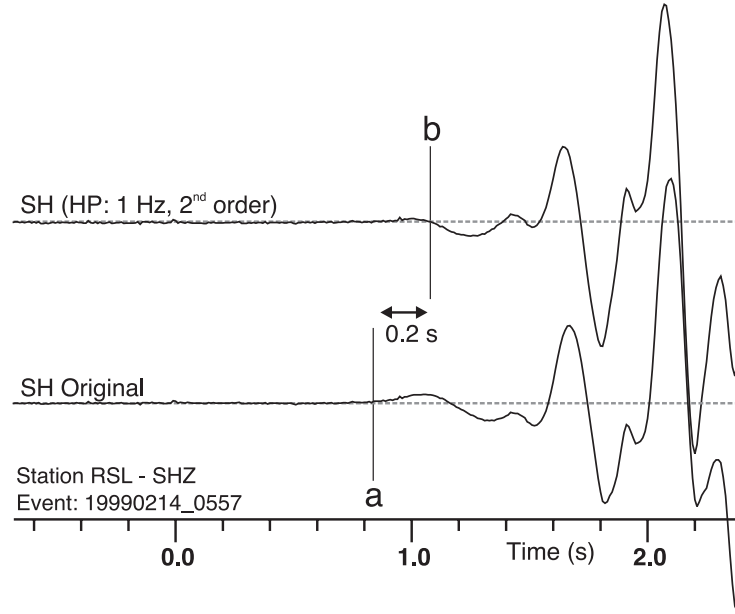


**Figure C.9:** Effect of 2<sup>nd</sup> order Butterworth high-pass filter (1 Hz) on short period waveform. In this example, the filter leads to a significant change in waveform. The earliest low-frequency onset is only hardly observable on the high-pass filtered trace. Position ‘a’ and ‘b’ represent two possible arrival picks for each trace. The time difference between those two positions could exceed 0.2 s.

presence of Sp-converted precursors.

### Polarization of Wavefield

Figure C.10 illustrates the particle motions of P and S-wave in horizontal (a) and vertical (b) planes. The particle motion of the P-wave is parallel or longitudinal to the direction of wave propagation  $\vec{k}$ . The displacement field of the S-wave is transverse to  $\vec{k}$  and can be subdivided into a vertical component (SV) and a horizontal component (SH). The vector  $\vec{k}$  can be described in the cartesian ZNE-system of the seismometer (vertical, north-south, east-west) by two angles: the backazimuth ( $BAZ$ ) and the angle of incidence ( $i$ ). Both angles can be determined from polarization analysis of a three component recording in a window around the P-wavelet. If station and epicenter coordinates are known,  $BAZ$  can also be derived from the orientation of the great-circle including station and epicenter. If focal depth and epicentral distance are known, we can also determine the theoretical angle of incidence in a specified velocity model. Both angles can be used to rotate the ZNE coordinate system into a local ray-system. Within the ray system P, SH, SV components can be partly separated from each other. The horizontal rotation of ZNE by the backazimuth  $BAZ$  results in the ZRT-system as demonstrated in Figure C.10a. The T-component denotes the transverse component, R coincides with the radial component. In the ideal case of a flat layered isotropic medium, the T-component contains only pure SH energy. P- and SV-energy are still mixed on

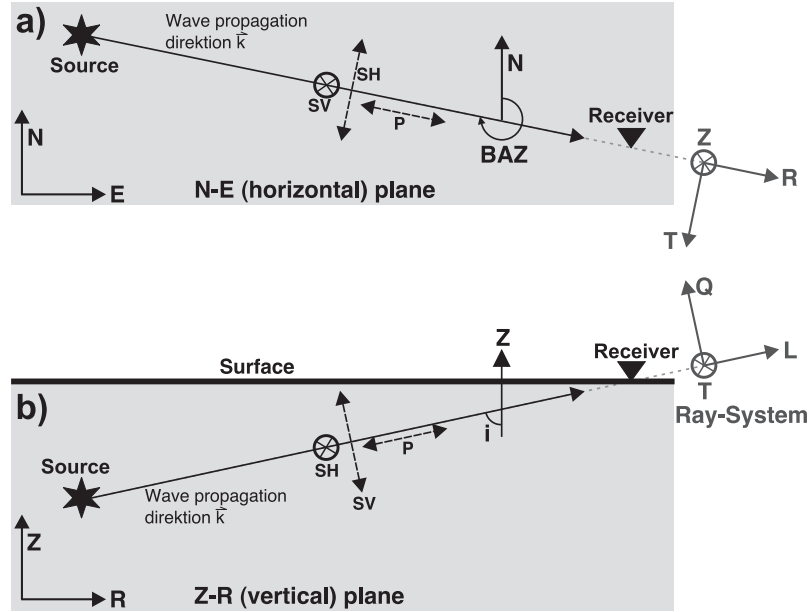


**Figure C.10:** Particle motion for P and S-wave along wave propagation direction. a) Horizontal plane. b) Vertical plane.

Z and R, depending on the incidence angle  $i$ . An additional rotation of ZRT by the incidence angle  $i$  results in a decoupled ray-system LQT. The complete P-energy is recorded on the L-component (longitudinal) and the Q-component contains the SV energy. The T-component remains the same like in ZRT. Since P and SV waves are coupled, SV energy can partly be converted into P waves by transmission of an interface. If such interface is close to the surface and denotes a strong velocity contrast (e.g. basement-sediment interface), Sp precursors are generated which are very close to the initial S-wave. These Sp precursors can be misinterpreted as the onset of the S-wave. The use of a ray-system can be used to identify such precursors. They are usually not present on the T-component, since there is no coupling between SH and P. However, the ratio between radiated SH and SV energy strongly depends on the focal mechanism and the observation azimuth. To avoid the misinterpretation of Sp precursors we recommend the use of a ray system (ZRT or LQT) and to pick the S-wave preferable on the T-component. Furthermore, the use of a ray-system can be helpful for a better discrimination of S-energy from P-coda and the identification of S-wave splitting.



## C.3 Consistent Hand Picking Procedure

The findings discussed in the previous sections will be combined to a standard procedure for consistent reference P- (and S-)phase picking in the following sections. Especially the consistent choice of time window length and amplitude scaling will be discussed in detail, since it represents one of the major sources for inconsistent picking.

### C.3.1 Consistent Waveform Filtering

As demonstrated in section C.2.5, filtering may lead to inconsistent picking. Therefore, we suggest the following procedure for reference picking:

- Be sure, filter does not lead to phase shift of signal. Use e.g. minimum phase filters or 2<sup>nd</sup> order Butterworth filter.
- Broadband (BB) channels (HH, BH):  
Always apply high-pass filter (corner frequency 1 Hz). It will remove the long period noise often present in BB recordings, and in addition, it will simulate the BB signal approximately towards the characteristic of a short-period sensor. Such simulation minimizes the inconsistency due to different sensor types.
- Short-period (SP) channels (EH, SH):  
Apply 1 Hz high-pass filter only if necessary, e.g. in presence of low-frequency noise. Compare original waveform with filtered one before final picking. Also check, if the filter changes first motion polarity.
- Apply possible low-pass or band-pass filters only if necessary e.g. in presence of high-frequency noise. Compare original waveform with filtered one before final picking.

### C.3.2 Consistent Window Size and Amplitude Scaling

The example in Figure C.6 indicates, that there is a strong need for a uniform concept in order to minimize subjectivity in phase picking due to irregular choice of time window size and amplitude scaling. On the other hand, it turns out to be very delicate to define universal rules, especially, if the method should be feasible for picking of large data sets. A consistent choice of time window and amplitude scaling should satisfy two conditions: A fixed time window length and amplitude normalisation with respect to a reference scale. As already mentioned, universal rules for these conditions are difficult to define. Concerning the time window length, the choice depends on the dominant frequency of the signal, but also on the *ASNR*. In the presence of strong noise or in case of a weak and emergent signal, it is often better to use a broader time window to determine the change in frequency and track back the transition from signal to noise. Likewise, it is not

possible to define a universally usable reference phase for amplitude scaling. In addition, many picking tools normalise the amplitude to the maximum amplitude within the selected time window and therefore amplitude scaling depends also from the size and the position of the time window. A possible approach to minimize the inconsistency related to time window choice and amplitude scaling consists of a mixture of iterative selection of window sizes and sliding them stepwise from the noise part towards the signal dominated part. For a further description, we apply this approach to the example shown in Figure C.6. A priori, we define four possible time windows used for picking:

- High-resolution window (HRW): 2 s  $ASNR \geq 3$
- Mid-resolution window (MRW): 5 s  $2 \leq ASNR < 3$
- Low-resolution window (LRW): 10 s  $ASNR < 2$
- Very-low-resolution window (VRW): 15 s

In the first step we choose a broad overview window, which includes the whole P-, or even parts of S-coda (Fig. C.11a). ‘P-PRED’ denotes the theoretical arrival time predicted in the min. 1D model for an a priori hypocentre (e.g. from catalogue). The predicted arrival time can be useful, however, it is not necessary. We pick the approximate position  $P_{approx}$  of the earliest arrival visible in this window. Based on  $P_{approx}$ , the maximum noise and signal+noise amplitude is estimated. To avoid parts of the signal in the pure noise window, we setup a safety gap of  $\pm 0.5$  s around  $P_{approx}$ . We use a length of 3 s for the noise window and 0.5 s for the signal+noise window. We define the noise threshold as  $\pm 1.5$  times the absolute noise amplitude within the noise window. In addition, we calculate  $ASNR$  from the absolute noise and signal+noise amplitudes.

Depending on the resulting  $ASNR$ , we choose the appropriate window size. In Figure C.11b  $ASNR$  is several times larger than 3, therefore we use HRW-size for picking. Between Figure C.11b and C.11e, the time window is shifted stepwise towards earlier times. The maximum amplitude within each time window is used for amplitude scaling. As long as the upper and lower noise threshold (dashed horizontal lines) are close to each other, the time window can be shifted further to earlier times (here, same effect like enlarging the amplitude scale). Finally, in Figure C.11e, the amplitude scaling allows an almost perfect discrimination between noise and the rising signal. In this example, the suggested procedure prevents the missing of the small precursors, but also relates their amplitude to the much stronger amplitude of the following phase.

If we could not clearly distinguish between noise and signal with the actual window size, or if we are not sure whether it is definitely the first arrival (e.g. in the present of strong noise), we repeat the sliding procedure with a larger time window (MRW or LRW). Subsequent, we apply the consistent error assessment as described in section C.2.1 to determine  $t_L$ ,  $t_E$ , and  $t_A$ . For this purpose, displaying the exact upper and lower noise threshold is very useful for the consistent determination of  $t_L$ .

### C.3 CONSISTENT HAND PICKING PROCEDURE

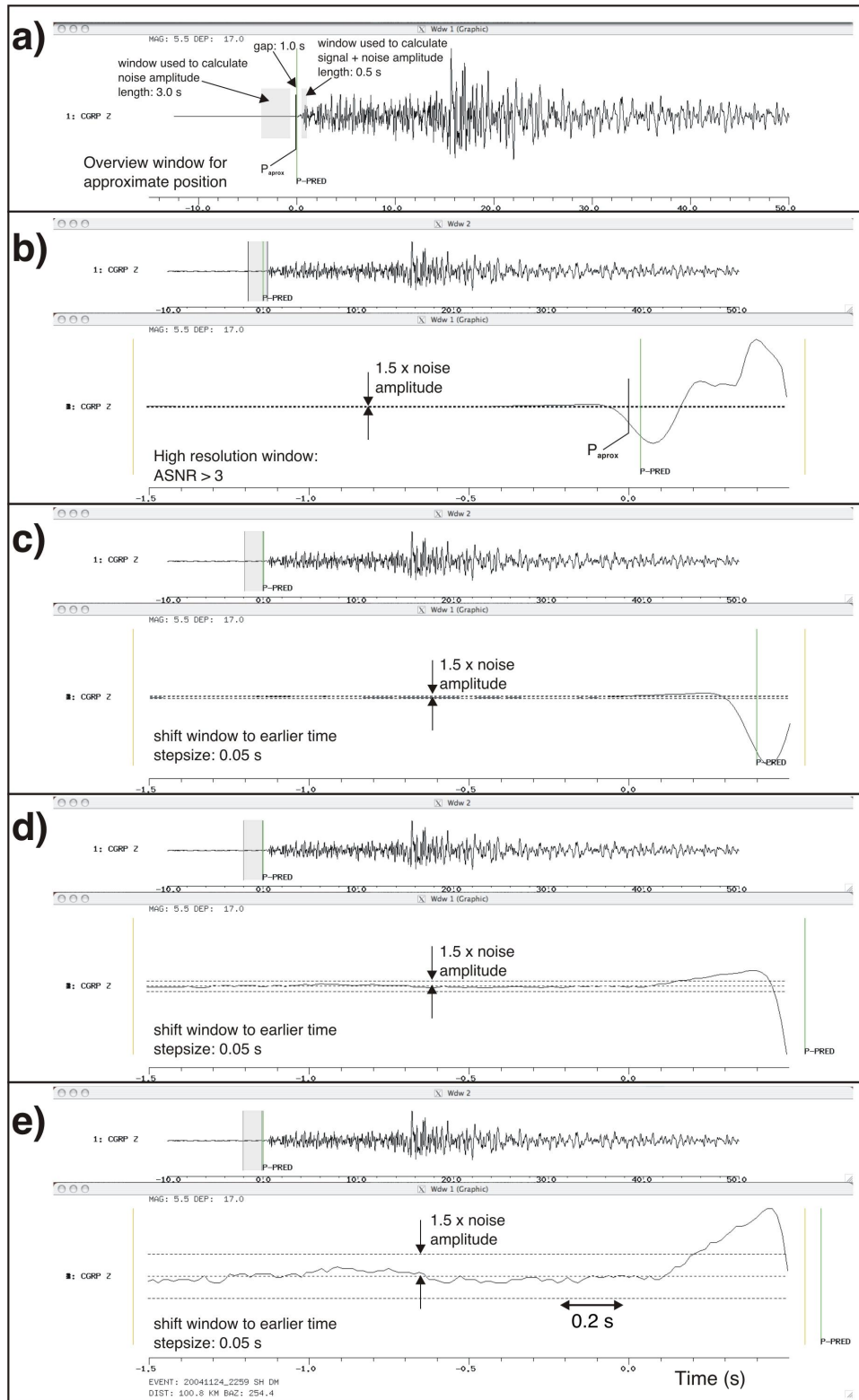


Figure C.11: Sliding time window procedure used for consistent phase picking.

### C.3.3 Consistent Phase Identification

Provided that a hypocentre is found, the actual phase identification can be cross-checked against a simplified crustal model afterwards (analogue to Figure C.4b). Another helpful tool to minimize inconsistency due to phase misinterpretation is the use of synthetic or predicted arrival times, especially during repicking of data. Assumed a reasonable local or regional velocity model is available and a preliminary hypocenter is present (e.g. from bulletin data), we can calculate synthetic first arrival times for each event-station pair, prior to the picking process. The use of synthetic arrivals provides three major advantages. First, they could guide the picker to the right phase (reliability depending on model quality) and therefore minimize phase misinterpretation. Second, they can be used to arrange the seismograms according to their expected arrival time. Thus, we start the picking at the closest station and do not waste too much time with likely low quality arrivals. In addition, it allows us to track the change in waveform from station to (neighbouring) station. Third, it represents a rough test for correct synchronization of the timing system. In case of obvious timing error of a station, we would observe a large discrepancy between synthetic arrival and actual waveform.

# Appendix D

## Users Guide for MPX Picking System

T. Diehl and E. Kissling

Institute of Geophysics, ETH-Zuerich  
CH-8093 Zurich, Switzerland

September 2008

## D.1 Introduction

The MannekenPix (MPX) software of Freddy Aldersons allows the automated (re-)picking of seismic phases from the original waveform data. This users guide represents a helpful extension to the original MPX users guide of *Aldersons* (2005). It gives a short introduction to the basic concept of MPX, explains the main parameters, and illustrates how MPX is calibrated towards a specific waveform data set. A detailed description of the fundamental concept of MPX and its application to the Dead-Sea Region and Italy can be found in *Aldersons* (2004) and *Di Stefano et al.* (2006). Furthermore, *Diehl et al.* (2008) applied the MPX software to the greater Alpine region. They demonstrated how the performance of MPX can be further improved for a regional data set.

In the first section, we give a brief overview on the basic concept of MPX. In the second part, we describe the parameters and how to calibrate these (calibration procedure). In the third section we specifically focus on the applications to the Alpine Region. In the last section we provide a cookbook example on how to perform the MDA with the SPSS software.

It should be mentioned that this guide refers to MPX-version 2.0.11 (December 2005). Furthermore, we thank Freddy Aldersons for providing us with the MPX software and his ‘any-time’ help and support.

## D.2 Basic Concept of MPX

The MPX system combines a picking algorithm with an automatic quality assessment, which is able to adopt the weighting procedure of a human picker. However, it is important to know that the MPX picking algorithm requires an initial (or guiding) pick for each seismogram. Since MPX is usually used for re-picking of known and identified local and regional earthquakes, a routine pick (e.g. from the routine analysis of an agency) or a predicted pick (theoretical arrival time derived from a catalogue location and a standard velocity model) can be used for this purpose. The automated quality assessment is accomplished by estimating the quality-class membership from a set of discriminant waveform characteristics or ‘predictors’ (signal-to-noise ratio, etc.) measured at (and around) the automatic pick. The mapping of the predictor-values to discrete quality classes is done via weighting factors (Fisher coefficients) for each predictor. The Fisher coefficients have to be calibrated with a (hand picked) reference data set in order to adopt the error assessment of the seismologist. Multiple-Discriminant-Analysis (MDA) can be used to find appropriate Fisher coefficients for the reference data set. Figure D.1 summarizes the basic concept of MPX. The kernel of the system is its Wiener-Filter (WF) routine. The WF is used to determine the thresholds for the picking engine, but also for measuring some of the waveform characteristics used for the quality assessment. In addition, it can also be used for waveform filtering. Basically, the WF compares the characteristics of the seismogram in two search-windows located around the initial pick. In the ideal case, the ‘earlier’ window

contains just noise and the ‘later’ contains noise+signal characteristics. The picking engine implemented in MPX is based on the Baer-Kradolfer algorithm (*Baer and Kradolfer*, 1987) extended by a delay correction as described e.g. in *Aldersons* (2004) or *Di Stefano et al.* (2006). The MPX-Workflow can be divided into four main steps:

- Setup reference data set: consistent manual picks for representative subset of waveform data set (tectonic region, magnitude, depth, network, etc). Divide reference data set in two subsets. Part I is used for calibration. Part II is used for testing calibration scheme (see section D.3).
- Calibration-Procedure: adopt automatic picking and quality assessment to reference data part I (see section D.4).
- Test-Procedure (optional): Apply calibration scheme to reference data part II and assess performance.
- Production-Procedure: Initial picks necessary for all seismograms in waveform data set. Apply calibration scheme to complete waveform data set (see section D.5).

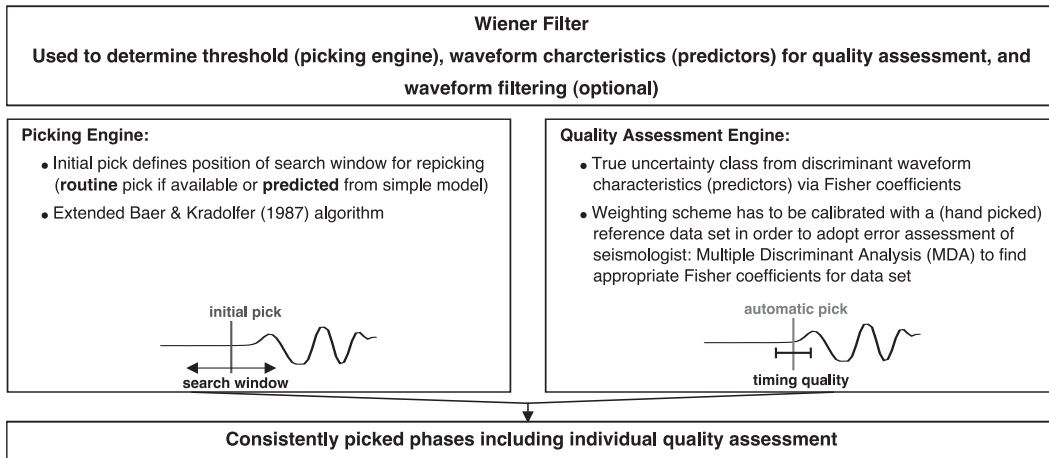


**Figure D.1:** Basic concept of MPX. The Wiener-Filter routine represents the kernel of the picking system. It is used to derive thresholds for the picking engine and waveform characteristics for the quality assessment engine. Optional, it can be used for waveform filtering.

## D.3 Compilation of Reference Data Set

Since the reference data set should present a cross section of waveforms expected in the complete data set (production stage), we have to extract a representative selection of earthquakes and recording stations. Possible criteria are: location (different tectonic regions, different networks), magnitudes (e.g. not only the strongest) and

depth (important e.g. in subduction zones). In general one can tend to higher magnitudes, since these earthquakes are recorded over larger distances and therefore, they will contain a broad spectrum of qualities. In addition, they will include strong and clear later arrivals such as Pg and PmP phases. During the calibration and test procedure we have to ensure that MPX never picks a later arrival as the first arrival. The number of picks depends on the dimension of the study area. However, we suggest at least 1000 picks for calibration and testing.

The picking procedure itself should be performed as consistent as possible, since these picks will be used to calibrate the automatic picker. Therefore, the manual picker should define some general rules for picking and error assessment. In any case, we recommend the picking of the uncertainty intervals for each phase, which later allows a flexible quality (error) class definition. We assign an additional weight for the uncertainty of the phase identification. For more details on reference picking see ‘Users Guide for Consistent Phase Picking’ by *Diehl and Kissling* (2008) or *Diehl et al.* (2008).

## D.4 Calibration Procedure

The calibration of the automatic picking system is based on the comparison between reference picks and automatic picks. Since we want to imitate the manual picker we have to assume, that the reference picks are located at the ‘true’ position and the assigned reference weights represent the ‘true’ uncertainty interval. The picking and quality assessment of MPX is controlled by a set of parameters (summarized in Table D.1), which have to be calibrated in the following procedure. The calibration procedure is divided in 6 major steps:

1. Step: Estimate the accuracy of initial picks (predicted from velocity model or routine picks) by calculating difference between reference and initial picks as demonstrated by *Diehl et al.* (2008).
2. Step: Adjustment of search windows. Choice of initial safety gaps depends mainly on the accuracy of initial picks (analyzed in previous step). Use suggested values as a first guess for the remaining parameters (see D.4.1 for details).
3. Step: Apply MPX to the reference data set. For the initial MPX run, default Fisher coefficients have to be used, since Fisher coefficients appropriate for our reference data set still have to be calculated. For a set of default Fisher coefficients see e.g., *Di Stefano et al.* (2006) or *Diehl et al.* (2008). Use the output of MPX (export-file) and calculate appropriate Fisher coefficients via MDA (e.g. with SPSS). For details on the automatic quality assessment via pattern recognition and MDA see D.4.2 and D.6.
4. Step: Apply MPX to the reference data set with updated (appropriate) Fisher coefficients and/or adjusted search windows.



5. Step: Check of performance by comparison of MPX output with reference data set. See section D.4.3 for details.
6. Step: The calibration procedure is an iterative process. If result of step 5 is not satisfactory, repeat step 2+4+5, 3+4+5 or 2+3+4+5 till satisfactory performance is achieved.

Figure D.2 summarizes the MPX calibration procedure described above.

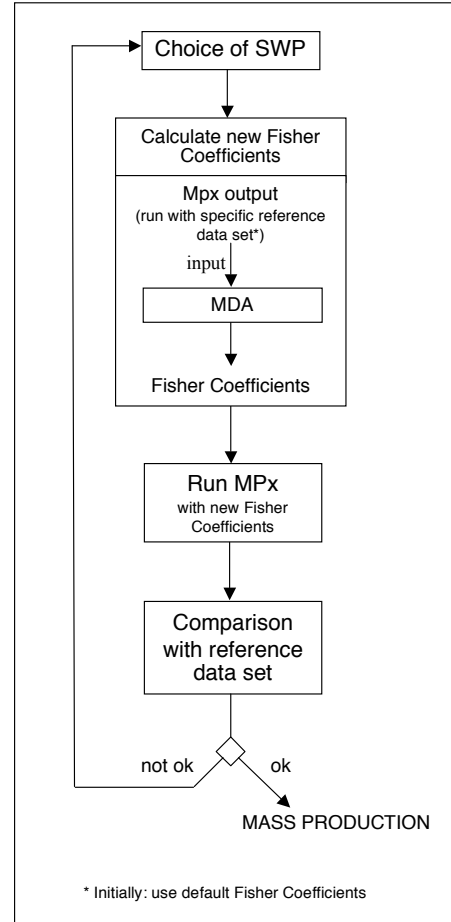


**Figure D.2:** Flow chart illustrating the MPX calibration procedure.

### D.4.1 Adjustment of Search Windows

The search window adjustment controls the picking accuracy, the hit rate and even the phase identification. In the pre-picking stage MPX evaluates the spectral density in a noise (NW) and in a signal+noise (SNW) window via the Wiener Filter routines. The position of these windows are controlled by the initial pick (routine or predicted arrival  $t_{pred}$ ), the length of the windows ( $L_N$  and  $L_S$ ), and the width of the safety gaps ( $g_N$  and  $g_S$ ), which separates NW from SNW as shown in Figure D.3.

MPX Parameter	Achieved by	Dependencies	Example from Alpine Reference Data Set
Fisher coefficients (Predictors x Classes)	MDA, Test with reference data	Waveform characteristics of data set & errors of picking engine	Not shown here
Length of analysing windows $L_N$ and $L_S$ (Wiener Filter length) (sec)	Test with reference data	Frequency content of signal	$L_N = L_S = 2$ s
Set of safety gaps $g_N$ and $g_S$ for predicted pick (sec)	Test with reference data	‘Scatter’ of predicted picks <sup>†</sup> & frequency content	2.5 s, 1.25 s, 0.5 s, 0.08 s
Set of safety gaps $g_N$ and $g_S$ for routine pick (sec)	Test with reference data	Scatter of routine picks & frequency content	Not used
Lower frequency threshold (Hz) (Frequencies below threshold are not considered for SNR determination)	Test with reference data	Frequency content of signal	0.50 Hz

<sup>†</sup> Predicted arrival time depends on simple structural model (usually 1D velocity model). True 3D structure results in ‘scattering’ of true arrival times around predicted pick. Furthermore, imprecise initial hypocenter (usually taken from bulletin information) can cause additional ‘scattering’ on predicted arrival.

**Table D.1:** Summary of MPX parameters which have to be calibrated during the calibration procedure.

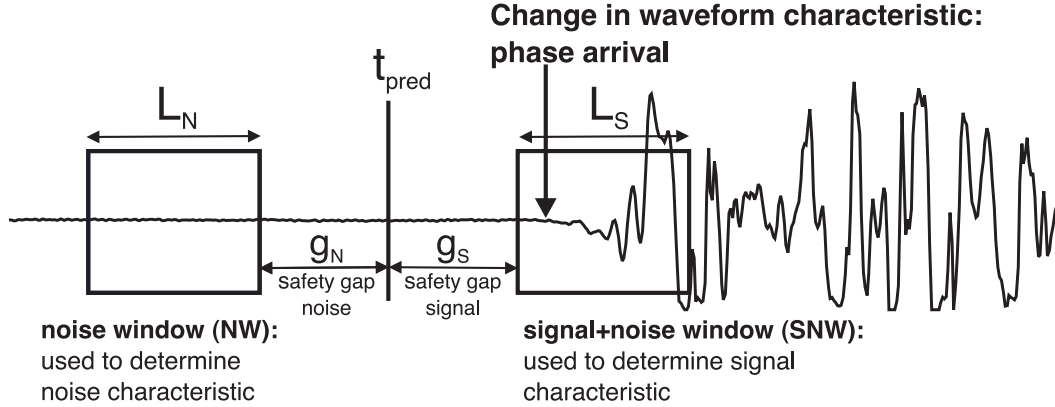


**Figure D.3:** Search window adjustment: The search windows  $NW$  and  $SNW$  are centered around the initial pick (here predicted  $t_{pred}$ ) and are separated by safety gaps  $g_N$  and  $g_S$ .

After this spectral density analysis the picking algorithm is applied to the waveform (picking stage). The MPX picking engine is based on the method of *Baer and Kradolfer* (1987), who calculate a characteristic function  $CFi$  from the envelope of the waveform. The onset is accepted as a pick for a value of  $CFi$  larger than a pre-defined *Threshold1* for a certain amount of time (*TupEvent*). *Threshold1* is automatically determined by MPX based on the spectral analysis done in the pre-picking stage, while *TupEvent* is an *a priori* value defined within MPX (depends on the characteristic frequency of the signal). This procedure of pre-picking and picking is iteratively performed 4 times with wide safety gaps in the first iteration and steadily refining (shrinking) safety gaps for the following iterations. This method allows a very high accuracy of the automatic picking. In order to achieve a satisfying hit-rate and accuracy, we have to adjust the following search window parameters:

#### Window length $L_N$ and $L_S$ for Wiener filter (seconds)

The length of  $L_N$  and  $L_S$  is depending on frequency content of noise and signal. The shorter the better the localisation effect. On the other side, short windows may underestimate lower frequencies. Thus, we have to deal with trade off between localisation and reliability. The signal frequency is mainly driven by epicentral distance (attenuation of higher frequencies).

User Guide Suggestions (*Aldersons*, 2005):

- Local approx. 1-3 s. For epicentral distance  $\Delta < 150$  km:  $\approx 1$  s.
- Regional: approx. 2-5 s. For  $150 < \Delta < 500$  km:  $\approx 2.0$ -2.5 s

#### Set of 4 safety gap parameters $g_N$ and $g_S$ (seconds)

The safety gap is necessary to separate the signal and signal+noise window. During the picking process, the gap is iteratively reduced. Therefore, we have to define four windows. The first gap value, which is used for the first iteration of

the picking process, has to be chosen according to the expected error between initial pick (routine pick or predicted pick) and the true signal. If the difference between initial pick and actual signal is much larger than this gap, the picking engine may not be able to detect the onset properly as shown in Figure D.4b. However, if we use a very wide first safety gap, miss-picks of later phases become

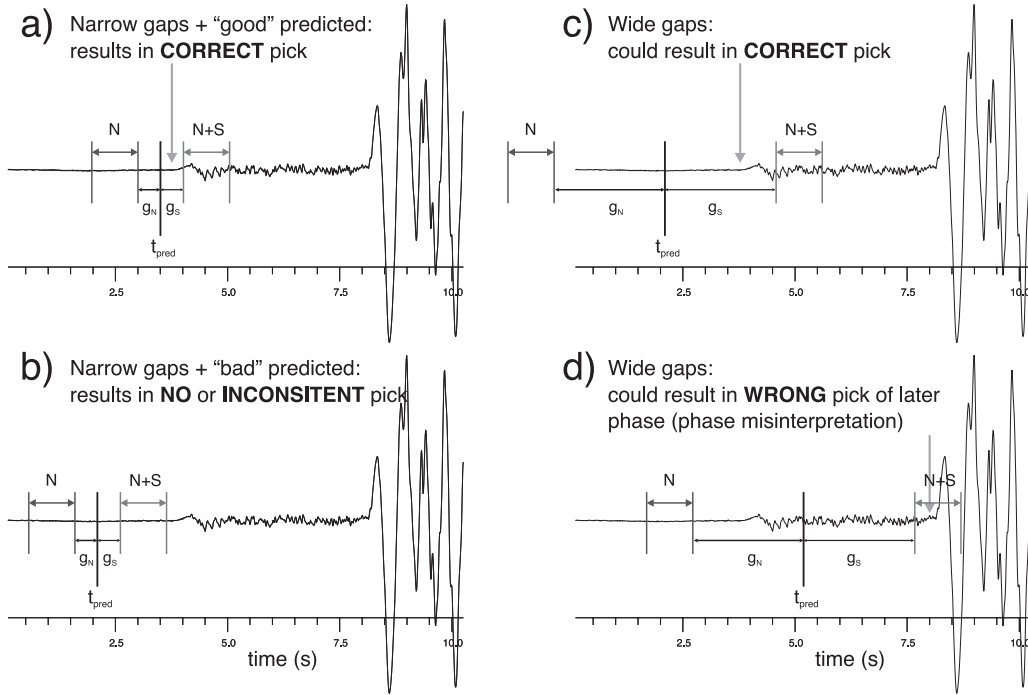


**Figure D.4:** Safety gap adjustment: Trade-off between hit-rate and accuracy. For consistent automatic picks we have to use narrow safety gaps in combination with initial (predicted) picks close to the actual phase onset as shown in a). Initial picks far off the actual phase onset in combination with narrow safety gaps result in no or inconsistent automatic pick (b). Wide safety gaps increase probability of picking impulsive later phases (c).

more likely as demonstrated in Figure D.4d. Therefore, it is necessary to reduce the error between initial and actual phase arrival as much as possible. This can be achieved by improving predicted arrivals (minimum 1-D model + station corrections + improved locations) as demonstrated by *Diehl et al. (2008)* or the use of reliable routine picks. To estimate the order of this error, we have to calculate the standard deviation and the maximum deviations between initial and reference picks. The fourth and last gap value is used for determination of the final pick and it is suggested to be between 40 and 80 ms. The range of its value is limited by two boundary conditions. In theory, a small gap improves the accuracy of the picking. On the other side, in combination with a low frequency wavelet, the picking may get unstable in this case, since a very narrow gap is not able to separate noise and signal+noise properly anymore. Therefore the fourth gap value has to be a compromise between target accuracy and frequency content of the signal. Furthermore, it should not be smaller than the actual sampling rate. Once

we found values for the first and the last gap values, we chose the second and the third value such that the step size from one gap to another is equally distributed. We have to define a set of gap parameters for both types of guiding picks (routine or predicted), since their errors can be rather different.

User Guide Suggestion (*Aldersons*, 2005):

1<sup>st</sup>  $\Rightarrow$  expected error between initial and actual onset (predicted-reference)

2<sup>nd</sup>  $\Rightarrow$  equally distribution of step size (e.g. half of 1<sup>st</sup>)

3<sup>rd</sup>  $\Rightarrow$  equally distribution of step size (e.g. 60 - 120 ms)

4<sup>th</sup>  $\Rightarrow$  compromise between frequency & accuracy: 40 - 80 ms

### Lower frequency threshold (Hz)

The lower threshold for maximum of signal amplitude spectrum. Frequencies below this threshold will not be used in the calculation of the signal to noise ratio. It could be interpreted as a pseudo high-pass filter, without effecting the shape of the waveform.

User Guide Suggestion (*Aldersons*, 2005):

The ‘Lower frequency threshold’ should be set about half the lowest frequency expected for the first onset (0.5 - 2.0 Hz).

## D.4.2 Calibration of the Automated Quality Assessment

### Quality Classification via Pattern Recognition

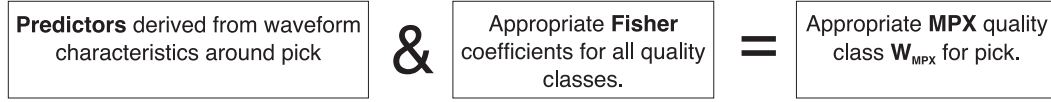
Let us define an *a priori* quality weighting scheme of  $L$  classes for reference picking. Each of these classes is associated with a specific uncertainty interval. The automatic classification of the pick is realised by correlating a set of  $N$  discriminating variables (predictors) to a certain criterion group  $j$  (quality class). The mathematical objective of this so called ‘discriminant analysis’ is to weight and linearly combine the predictors  $P_i$  ( $i = 1, \dots, N$ ) in a way that maximizes the differences between groups while minimizing differences within groups (*Fisher*, 1936, 1938). The weighting coefficients  $F_{ij}$  are called the Fisher coefficients. Thus, the linear discriminant function  $D_j$  for class  $j$  can be written as

$$D_j = F_{0j} + F_{1j} \cdot P_1 + F_{2j} \cdot P_2 + \dots + F_{Nj} \cdot P_N, \text{ with } j = 1, \dots, L-1 \quad (\text{D.1})$$

$F_{0j}$  represents the constant term and is also called ‘independent term’. Thus we have to specify  $M = N + 1$  Fisher coefficients. MPX determines  $N = 9$  predictors for each automatic pick, including parameters like signal to noise ratios, etc. For a detail list of predictors used in MPX see e.g., *Aldersons* (2004) or *Di Stefano et al.* (2006). Subsequently, MPX calculates the  $L$  discriminant functions for a given set of  $M \times L$  Fisher coefficients. Since  $D_j$  has to be maximized we assign the quality class  $j$ , which is related to the largest  $D_j$ . Figure D.5a illustrates the automatic quality classification of MPX: a set of (appropriate) Fisher coefficients applied to the predictor values will return the MPX quality class  $W_{MPX}$  of the pick. A set of

appropriate Fisher coefficients is derived from the reference data set as described in the following sections.

**a) MPX Quality Classification:**



**b) Fisher Coefficients via MDA:**

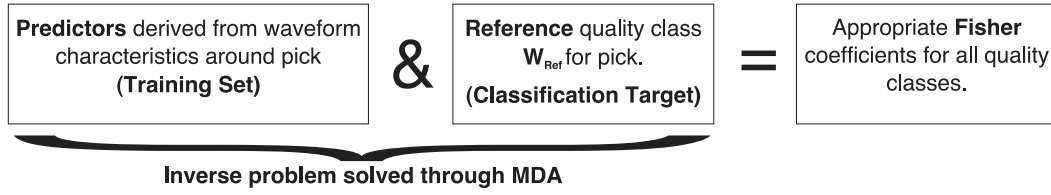


**Figure D.5:** Concept of phase-quality classification with MPX. a) The quality class  $W_{MPX}$  of a phase pick is estimated from predictors measured around the pick weighted by Fisher coefficients. b) An appropriate set of Fisher coefficients is derived via MDA from the reference data set (training set).

### Appropriate Fisher Coefficients via MDA

The principle of the MDA is summarized in Figure D.5b. To calibrate the quality assessment towards a specific data set, we use the predictor values derived by MPX for a subset of reference picks (training set). The MDA then determines Fisher coefficients, which classify the predictors as good as possible towards the reference classes (classification target). The MDA procedure via the statistic package SPSS is described in section D.6 in more detail.

It should be mentioned that misclassification costs are not symmetrically distributed. We rather accept downgrading of picks than upgrading of low qualities. Therefore the application of the MDA to our problem is not straightforward. Since the predictors are strongly related to the waveform characteristics, the result of the MDA significantly depends on the filter used prior to the picking. Thus, the determination of Fisher coefficients for a stable and high accurate weighting scheme strongly depend on the data set used for the MDA. For the Alpine region, it seems to be affected by the epicentral distance of the data, the magnitude range and the used waveform filter as described in *Diehl et al. (2008)*.

### Assessment of Absolute Timing Error with MPX

Since the pattern recognition described by *Aldersons (2004)* is mainly based on signal characteristics in the close neighborhood of the pick, it cannot account directly for the absolute timing error of the extended Baer-Kradolfer picker. However, if we assume that the majority of the reference picks are at the ‘true’ position, an effective automated quality assessment has to account also for the deviation between automatic and reference pick. Figure D.6 illustrates such an apparent misclassified MPX weighting. Although MPX assigns the right quality class  $W_{MPX}$  to the

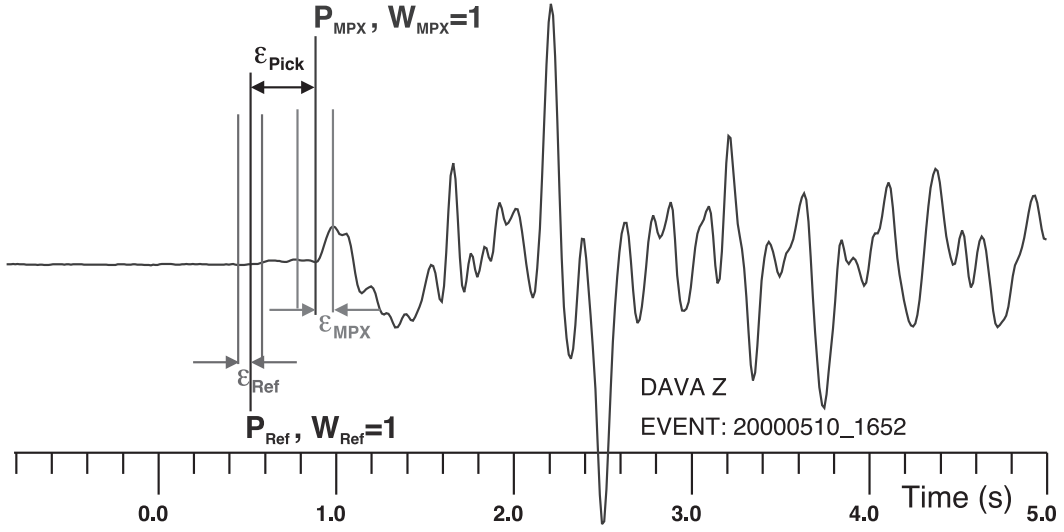


**Figure D.6:** Example for an apparent misclassified weighting. The automatic pick is determined at the later impulsive phase. In contrast, the reference pick is located at the ramp-like first arrival phase. The error  $\varepsilon_{Pick}$  between automatic and reference pick is larger than the automatic assigned error  $\varepsilon_{MPX}$  corresponding to quality class  $W_{MPX} = 1$ . Considering the uncertainty of the later impulsive phase independent from the misidentification as first arriving phase, MPX assigns the correct weighting class  $W_{MPX} = 1$ .

(later) automatic pick  $P_{MPX}$ , it does not account for the absolute picking error  $\varepsilon_{Pick}$  between reference ( $P_{Ref}$ ) and automatic pick ( $P_{MPX}$ ). If we adjust the MDA towards pure waveform classification, the performance of MPX will always be biased by the error between automatic and reference pick  $\varepsilon_{Pick}$ .

Based on the assumption that  $\varepsilon_{Pick}$  is strongly affected by the waveform characteristic (i.e., error of picking algorithm is smaller for impulsive first arrivals), *Di Stefano et al.* (2006) introduced the concept of ‘TrueWeights’. The ‘TrueWeight’  $W_{true}$  represents the quality class corresponding to the picking error  $\varepsilon_{Pick}$ . In order to account for  $\varepsilon_{Pick}$  in the automatic classification, they used  $W_{true}$  instead of the reference weight  $W_{Ref}$  as classification target in the MDA. However, the assumption above may not always be valid. Considering the picking algorithm determines an onset close to the reference pick for a low quality phase by accident. In such a case, the characteristics of a low quality onset would be mapped to a high quality  $W_{true}$ , although the reference weight  $W_{Ref}$  would indicate a low quality phase. This will lead to an increase of low quality picks upgraded to higher quality classes by MPX.

To avoid such contamination, we have to consider not only the picking error  $\varepsilon_{Pick}$  but also the reference weight  $W_{Ref}$  for the ‘TrueWeight’ determination. The picking error  $\varepsilon_{Pick}$  is only used as  $W_{true}$ , if  $\varepsilon_{Pick}$  is larger than the reference error  $\varepsilon_{Ref}$ . Otherwise, we use the reference weight as  $W_{true}$ . The determination of  $W_{true}$  in our approach can be summarized in the following way:

$$\begin{aligned} \text{If } \varepsilon_{Pick} \leq \varepsilon_{Ref} &\Rightarrow W_{true} = W(\varepsilon_{Ref}) = W_{Ref} \\ \text{If } \varepsilon_{Pick} > \varepsilon_{Ref} &\Rightarrow W_{true} = W(\varepsilon_{Pick}) \end{aligned}$$

$W(\varepsilon_{Pick})$  is the quality class that includes the error  $\varepsilon_{Pick}$ .

Considering  $\varepsilon_{Pick}$  in Figure D.6, the ‘TrueWeight’ for the automatic pick is  $W_{true} = 3$ . As a consequence, waveform attributes of rather impulsive phases (like the later phase in Figure D.6), will be mapped to lower quality classes during the MDA. Therefore, the MDA based on  $W_{true}$  instead of  $W_{Ref}$  will downgrade more of the rather impulsive phases, but on average, it will provide a higher accuracy in terms of absolute errors. The application to the Alpine region data set shows, that we have to deal with a strong trade-off between accuracy and MPX classification (Diehl *et al.*, 2008).

### D.4.3 Assessment of Calibration Scheme

To assess the performance of the automatic picking and quality classification for a specific calibration scheme, we have to compare the automatic picks with the reference picks. We have to consider the following errors (see also Fig. D.7):

- ⇒ Timing-Error between reference and automatic pick:  $\varepsilon_{Pick}$
- ⇒ Classification-Error between reference weighting ( $W_{Ref}$ ) and automatic weighting class ( $W_{MPX}$ ).

If we assume that the reference pick represents the ‘true’ first phase onset, a satisfying calibration is achieved if:

- The timing error  $\varepsilon_{Pick}$  between reference and automatic pick is within the automatic assigned error interval  $\varepsilon_{MPX}$  for most of the automatic picks (standard deviation  $\sigma_{ij}$  of all  $\varepsilon_{Pick}$  should be within automatic assigned error interval  $\varepsilon_{MPX}$ , where  $i$ : Reference weight  $W_{Ref}$ ,  $j$ : MPX weight  $W_{MPX}$ ).
- Low reference quality picks are not upgraded to highest quality class by MPX quality assessment. A maximum classification-error between reference weighting ( $W_{Ref}$ ) and automatic weighting class ( $W_{MPX}$ ) of 2 classes ( $W_{Ref} - W_{MPX} \leq 2$ ) for upgrading towards higher classes is tolerated. However, the downgrading of picks is much less critical. Even for an ideal weighting scheme downgrading of higher qualities is required, since automatic picks far off the reference pick should get a lower weight (see also ‘Absolute Timing Error’ in section D.4.2).

Usually we have to deal with a trade-off between these two conditions as discussed in ‘Absolute Timing Error’ of section D.4.2. To assess the performance of MPX classification  $W_{MPX}$  and the picking error  $\varepsilon_{Pick}$  simultaneously, we introduced the ‘TrueWeight’  $W_{true}$ . If we compare the weighting classes derived by MPX ( $W_{MPX}$ ) with the true weights  $W_{true}$  derived from the picking error and the reference class we can assess the picking error and the onset quality classification at once.

To assess the calibration for the complete reference data set, we compare the results of MPX with the reference data set in the so-called ‘Classification-Matrix’ as shown



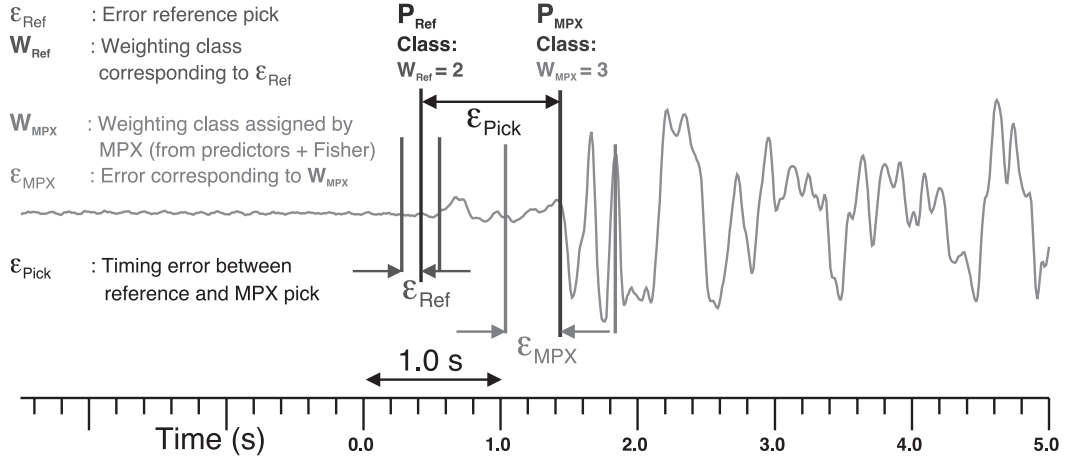


**Figure D.7:** Errors that define performance of automatic picking and quality classification. The uncertainty of the reference pick  $P_{Ref}$  is represented by the error interval  $\epsilon_{Ref}$  and its corresponding quality class  $W_{Ref}$ . Based on predictor values and Fisher coefficients the automatic pick  $P_{MPX}$  is classified as quality class  $W_{MPX}$ . The corresponding error interval is represented by  $\epsilon_{MPX}$ . The deviation between reference and automatic pick is described by  $\epsilon_{Pick}$ .

in Figure D.8. In the case of an ideal calibration (and picking), all reference class ‘0’ picks would be recovered as class ‘0’ by MPX. The same would be valid for class 1,2,3, and 4. The ‘Classification-Matrix’ would be populated only on the diagonal elements as illustrated by grey squares in Figure D.8b. For real data, we observe a smearing of quality classes by MPX. However, we accept downgrading of picks and also moderate upgrading of classes, as long as  $\sigma_{ij}$  remains within the error interval of the upgraded class. We do not accept upgrading of poor picks (e.g. class 3 or 4) to highest quality classes (0,1) as indicated by the black squares in Figure D.8b and we require downgrading of picks far of the corresponding reference pick ( $\epsilon_{Pick} > \epsilon_{Ref}$ ).

## D.5 Examples of Production Modes

*Di Stefano et al. (2006)* used MPX for the re-picking of first arriving P-phases from the Italian National Network (INGV) and demonstrated the improvement in terms of consistency of the phase data. The successful application of the calibrated MPX towards a large data set requires the following: Accurate initial picks, reliable phase identification, and the detection (and removal) of low quality waveform data (non-seismic signals like spikes, etc.). The following case study will describe solutions for the these problems in detail. For further description see also *Diehl et al. (2008)*.

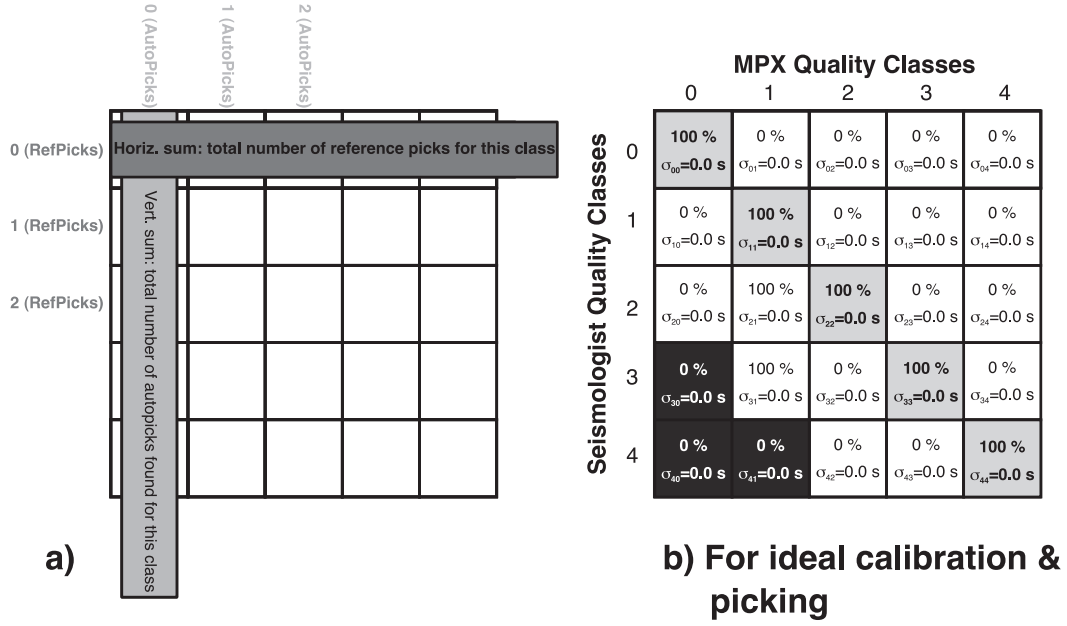


**Figure D.8:** The Classification-Matrix: Smearing of quality classes and standard deviation  $\sigma_{ij}$  of  $\varepsilon_{Pick}$  for each element.

### D.5.1 Application to the Alpine Region

The application of MPX to the greater Alpine region is described in detail by *Diehl et al.* (2008). The main conclusions of this study are:

- Stable and reliable automatic picking requires accurate initial picks. In case of heterogeneous data sets consisting of waveform data from several seismic networks, only predicted arrival times can be used. To improve accuracy of predicted arrivals, the iterative use of automatic picker and minimum 1-D models is necessary as demonstrated by *Diehl et al.* (2008). Precise predicted arrival times reduce the number of phase misidentifications significantly.
- The performance of MPX can be improved by the use of a distance-dependent calibration scheme. In the case of the Alpine region, we used different sets of Fisher coefficients and waveform filters below and above an epicentral distance of 100 km. By splitting the data set into two distance ranges and by using a regional minimum 1-D model, we achieved a first order discrimination between Pg and Pn phases.
- To further improve the performance of MPX, an automatic assessment of the various phase onsets will have to be included in the picking algorithm, since the MDA cannot account for it directly. As any other such algorithms, MPX picks the earliest well-defined signal as the first arriving phase. However, beyond the crossover distance the first arriving Pn is often less well-defined than secondary arriving phases such as Pg or PmP. To correctly identify the picked phase multiple picking approaches, as suggested by *Bai and Kennett*

(2000), have to be considered. They propose the use of attributes provided by short-term to long-term average ratios, autoregressive modeling and polarization analysis to pick and identify series of P- and S-phases.

- Low-quality waveform data (e.g., spikes, data gaps, step functions, etc.) have to be identified and removed prior to the automatic picking. See *Diehl et al.* (2008) for details on how these non-seismic signals can be automatically identified.

## D.6 Cookbook Example: MDA via SPSS Software

We have seen in section D.4.2 that we have to evaluate appropriate Fisher coefficients from the reference data set in order to calibrate the automatic quality classification scheme. This calibration is performed by a *Multiple Discriminate Analysis* (MDA). Basically, the MDA compares the classes assigned to reference picks with the corresponding predictors evaluated by MPX (for the automatic pick). However, the timing of the automatic pick  $P_{MPX}$  usually deviates from the reference pick  $P_{Ref}$ . The error between automatic and reference pick is  $\varepsilon_{Pick}$ . Hence, we have to dial with a trade-off between the timing and weighting scheme calibration: we cannot correlate the predictors of an automatic pick with its corresponding reference weight  $W_{Ref}$  without considering the error of the automatic pick  $\varepsilon_{Pick}$ . Therefore, we have to evaluate the ‘true’ weighting class  $W_{true}$  for  $P_{MPX}$ .  $P_{MPX}$  can be determined by three different methods as described in section D.4.2:

1. Mainly  $\varepsilon_{Pick}$  is used for true weight determination (*Di Stefano et al.*, 2006).
2. Both  $\varepsilon_{Pick}$  and  $W_{Ref}$  are used for true weight determination (*Diehl et al.*, 2008). We recommend this method to account for absolute timing errors.
3. Another mixture between 1. and 2., which is not used so far.

After assigning the true weights to the automatic picks, we perform the MDA to correlate predictors to the target weighting classes by evaluating the best set of Fisher coefficients for each class. The target classes will be represented by the true and not by the reference weights!

In a first step, we apply MPX to our reference data set (or subsets of it) with adjusted search window setup (see D.4.1) and a set of arbitrary default Fisher coefficients. The MDA via the statistic package SPSS uses the output of this (initial) MPX run. Once we estimated a new set of Fisher coefficients via the MDA, we have to update the according values in the MPX command-file and perform another MPX run.

The MDA is practically performed via Excel macros and SPSS in the following way (recommended by F. Aldersons):

- Import MPX export-file to an empty MS-Excel spreadsheet. Import has to start with row 13 and you have to set separators for the first columns by hand. Be sure the importing process was performed correctly (last column has to be labelled as 'AW'). If class definition starts from different values (e.g., from 1 in MPX and from 0 in reference data) you have to adapt this now.
- Open the MS-Excel template spreadsheet (includes certain macros) provided by F. Aldersons ('*MPX2ImportYourDataW0 - 4.xls*'). Be careful, if you use different error classes you have to modify the macro. Error intervals used for reference picking are also specified in the macro!
- Be sure spreadsheet of empty '*MPX2ImportYourDataW0 - 4.xls*' is labelled as 'Sheet1'. Copy & paste the whole (eventually modified) spreadsheet (including two header lines) to the template. In the next step you have to execute the macro:  $\Rightarrow$  Tools  $\Rightarrow$  Macro  $\Rightarrow$  Macros...  $\Rightarrow$  '*PrepareDataForMDA*'. This will create two new spreadsheets: '*MPX2Export*' (contains original export-file) and '*ForMDA*' (contains data necessary for MDA: weights, predictors). The macro calculates 'true' weights with three different methods described above. The 'true' weights will be labeled as 'TrueWM1', 'TrueWM2', and 'TrueWM3' (M1  $\Rightarrow$  Method 1, etc.).
- In the next step, you have to open the SPSS template '*ReadyForImport-MDA.sav*' provided by F. Alderson. Of course, this step requires a installed version of SPSS. Then, copy the content of the Excel 'For MDA' spreadsheet (without the two header lines) and paste it to the SPSS '*ReadyForImport-MDA.sav*' template.
- Now, we can perform the MDA within SPSS. Select from the SPSS menu: 'Analyze'  $\Rightarrow$  'Classify'  $\Rightarrow$  'Discriminant...'. We have to set some parameters for the MDA in the pop-up window (see Fig. D.9). First, choose the target for the MDA ('Grouping Variable'). In our case, it will be the true weight, determined with one of the three methods (TrueWM1-3). We recommend method 'TrueWM2'. We mark this data column in the upper left window of the pop-up menu with the left mouse button and accept this selection by pushing the 'add-arrow' next to the 'Grouping Variable' field. Then, we have to define the range of the 'Grouping Variable' with the 'Define Range...' option. In our example the 'Grouping Variable' ranges from 0 to 4 (class 0 to class 4). Subsequently, we have to define the set of predictors ('Independents') by selecting the nine parameters ('wfilston'-'cfnoidev') from the upper left window of the pop-up menu and add them to the 'Independents' field. Enable the 'Enter independents together' option (if not already enabled). The settings in the main window should agree with the menu shown in Figure D.10. Additionally, we have to fix some settings in the sub-menus 'Statistics...' and 'Classify...'. In 'Statistics...' we have to enable all options

(see Fig. D.11), the settings for sub-menu ‘Classify...’ are presented in Figure D.12.

- Now, we can execute the MDA by pushing ‘OK’ button in the main MDA menu. The results will be displayed in the SPSS viewer. You can extract the Fisher coefficients determined by the MDA from the ‘Classification Function Coefficients’ table. The group prediction of this set of coefficients can be seen in the ‘Classification Result’ table.

After evaluating this set of new Fisher coefficients via the MDA, we insert them in the MPX command-file and perform another MPX run. Subsequently, we have to analyse the export-file again. We have to ensure that our weighting scheme (see also section D.4.3):

- Separates the classes properly (dominance of diagonal elements). If not, merging unresolved classes.
- Does not upgrade lowest quality picks to highest quality classes (smearing).
- Errors  $\varepsilon_{Pick}$  fall within assigned error intervals (trade-off between weighting and timing).

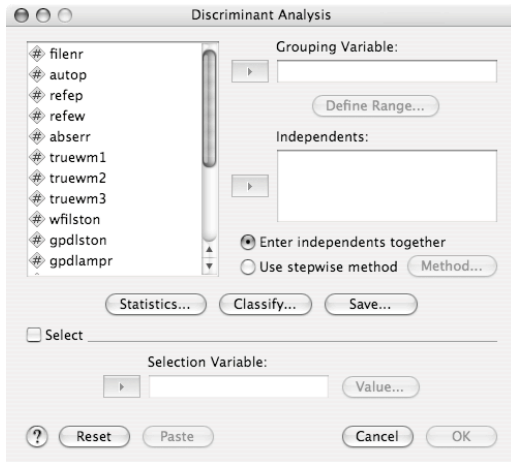


**Figure D.9:** Main SPSS pop-up window to perform MDA (default).

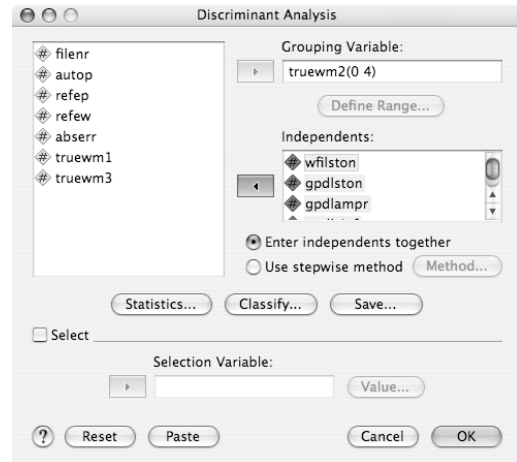


**Figure D.10:** Settings in main SPSS pop-up window to perform MDA.

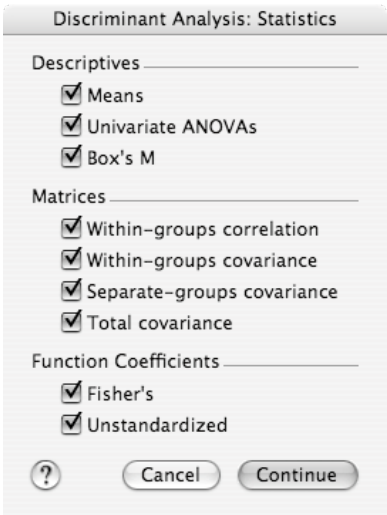


**Figure D.11:** Settings in sub-menu ‘Statistics...’.

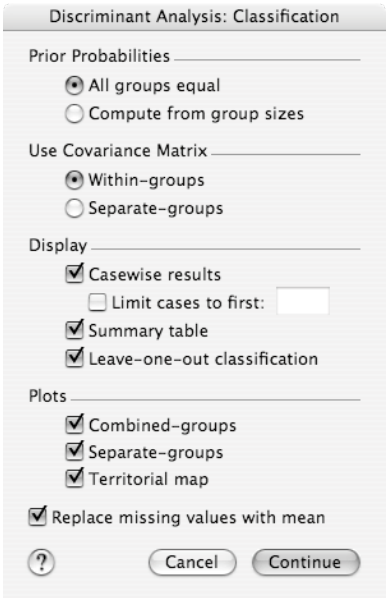


**Figure D.12:** Settings in sub-menu ‘Classify...’.

# Appendix E

## Miscellaneous

### E.1 Parameterization and Resolution in 3-D Tomography

The capability to resolve a velocity perturbation  $\Delta v$  from a background velocity  $v$  in a 3-D volume  $a \times a \times a$  depends on the ray-length  $x$  within the volume (and therefore on  $a$ ), on the background velocity  $v_0$ , and on the measuring error  $t_\varepsilon$  for the travel time  $t$ , as shown in Figure E.1. Let us define  $\Delta t$  as travel time residual between background model and perturbed model. We are able to resolve  $\Delta v$ , if  $t_\varepsilon < \Delta t$ . The travel time residual  $\Delta t$  caused by a perturbation  $\Delta v$  within the

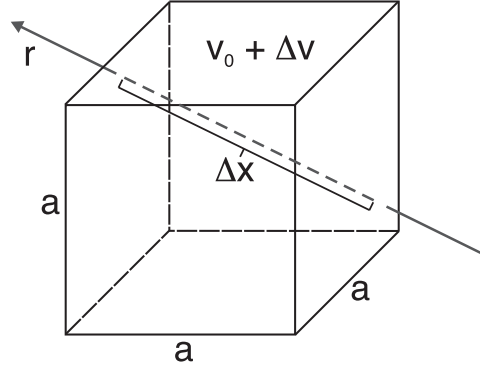


**Figure E.1:** Tradeoff between parametrization, data error, and resolution capability in 3-D tomography. The capability to resolve a velocity perturbation  $\Delta v$  from a background velocity  $v$  in a 3-D volume  $a \times a \times a$  depends on the ray-length  $\Delta x$  within the volume (and therefore on  $a$ ), on the background velocity  $v_0$ , and on the measuring error  $t_\varepsilon$  for the travel time  $t$ . Let us define  $\Delta t$  as travel time residual between background model and perturbed model. We are able to resolve  $\Delta v$ , if  $t_\varepsilon < \Delta t$ .

volume can be described by:

$$\Delta t = \frac{\Delta x}{v_0 + \Delta v} - \frac{\Delta x}{v_0} \quad (\text{E.1})$$

If we express the perturbation  $\Delta v$  in percent of  $v_0$  and denote it  $pvp$  (percent-velocity-perturbation), E.1 can be rewritten as:

$$\Delta t = \frac{\Delta x}{v_0} \left( \frac{-1}{(100/pvp) + 1} \right) \quad (\text{E.2})$$

**Example 1:** A P-wave velocity perturbation of +5 % ( $pvp = 5$ ) within the mid-crust (e.g.  $v_0 = v_0^P = 6.0$  km/s) in a volume of  $25 \times 25 \times 15$  km ( $\Delta x$  e.g. 20 km), results in a P-wave residual of  $\Delta t = -0.16$  s. Such perturbation in a rather large volume can only be resolved, if the data error (mainly picking accuracy) is less than 160 ms. Therefore, we have to find a compromise between volumetric resolution and minimum resolvable perturbation amplitude for the *a priori* uncertainty of our data set. For a given average data error, this implies either lower volumetric resolution with a small threshold of resolvable amplitudes or high volumetric resolution with lower amplitude resolution.

**Example 2:** A S-wave velocity perturbation of +5 % ( $pvp = 5$ ) within the mid-crust (e.g.  $v_0 = v_0^S = v_0^P/1.73 = 3.47$  km/s) along a ray-segment of 20 km results in a S-wave residual of  $\Delta t = -0.28$  s. Assuming no change in  $v_P$  and same ray path, this perturbation in S-wave velocity leads to a reduction in  $v_P/v_S$  of 4.76 % (from 1.73 to 1.65).

To investigate the influence of both picking errors (P and S) on the  $v_P/v_S$  ratio we express the difference between S and P arrival  $t_{SP} = t_S - t_P$  as a function of  $\kappa_0 = v_P/v_S$ . We assume the same ray-path of length  $\Delta x$  for P and S-wave.  $t_{SP}$  can be expressed by:

$$t_{SP} = \Delta x \left( \frac{1}{v_S} - \frac{1}{v_P} \right). \quad (\text{E.3})$$

By replacing  $v_S$  with  $v_P/\kappa_0$  in E.3 we obtain the required relation for a ray path along a straight line:

$$t_{SP} = \Delta x \left( \frac{\kappa_0 - 1}{v_P} \right). \quad (\text{E.4})$$

Along a general ray-path from source  $q$  to the receiver  $r$  E.4 becomes

$$t_{SP} = \int_q^r \frac{\kappa_0 - 1}{v_P} ds, \quad (\text{E.5})$$

which is identical with the forward problem in  $v_P/v_S$  tomography as proposed e.g. by *Thurber and Atre* (1993). A perturbation of  $\kappa_0$  by  $\Delta\kappa$  results in a residual of the  $S - P$  time  $\Delta t_{SP}$ :

$$\Delta t_{SP} = \Delta x \left( \frac{\kappa_0 + \Delta\kappa - 1}{v_P} \right) - \Delta x \left( \frac{\kappa_0 - 1}{v_P} \right) = \left( \frac{\Delta x \cdot \Delta\kappa}{v_P} \right). \quad (\text{E.6})$$



Analog to E.2,  $\Delta\kappa$  can be expressed in percent of  $\kappa_0$  and we denote it  $p\kappa p$  (percent- $v_P/v_S$ -perturbation):

$$\Delta t_{SP} = \left( \frac{\Delta x \cdot \kappa_0 \cdot p\kappa p}{v_P \cdot 100} \right). \quad (\text{E.7})$$

**Example 3:** A  $v_P/v_S$  perturbation of +5 % ( $p\kappa p = 5$ ) within the mid-crust (e.g.  $\kappa_0 = 1.73$ ,  $v_P = 6.0$  km/s) in a volume of  $25 \times 25 \times 15$  km ( $\Delta x$  e.g. 20 km), results in a  $S - P$  residual of  $\Delta t_{SP} = 0.29$  s. This anomaly in  $v_P/v_S$  can only be resolved if the sum of absolute observation errors in P and S-wave arrivals is smaller than  $\Delta t_{SP}$ .



# References

- Akaike, H. (1973), Information theory and an extension of the maximum likelihood principle, in *2nd International Symposium on Information Theory*, edited by B. N. Petrov and F. Csaki, pp. 267–281, Akademiai Kiado, Budapest.
- Akazawa, T. (2004), A technique for automatic detection of onset time of P- and S-phases in strong motion records, in *13th World Conference on Earthquake Engineering*, Vancouver, Canada, paper No. 786.
- Aldersons, F. (2004), Toward three-dimensional crustal structure of the Dead Sea region from local earthquake tomography, Ph.D. thesis, Tel Aviv University, Israel.
- Aldersons, F. (2005), MannekenPIX 1.7 - User Guide, <http://faldersons.net>.
- Allen, R. V. (1978), Automatic earthquake recognition and timing from single traces, *Bull. Seism. Soc. Am.*, *68*, 1521–1531.
- Allen, R. V. (1982), Automatic phase pickers: their present use and future prospects, *Bull. Seism. Soc. Am.*, *72*, S225–S242.
- Aster, R. C., and C. A. Rowe (2000), Advances in seismic event location, in *Automatic phase pick refinement and similar event association in large seismic datasets*, edited by C. H. Thurber and N. Rabinowitz, pp. 231–263, Kluwer Academic Publishing, Amsterdam.
- Baer, M., and U. Kradolfer (1987), An automatic phase picker for local and tele-seismic events, *Bull. Seism. Soc. Am.*, *77*, 1437–1445.
- Bai, C. Y., and B. L. N. Kennett (2000), Automatic phase-detection and identification by full use of a single three-component broadband seismogram, *Bull. Seism. Soc. Am.*, *90*, 187–198.
- Bai, C. Y., and B. L. N. Kennett (2001), Phase identification and attribute analysis of broadband seismograms at far-regional distances, *J. Seismol.*, *5*, 217–231.
- Behm, M., E. Brückl, W. Chwatal, and H. Thybo (2007), Application of stacking and inversion techniques to three-dimensional wide-angle reflection and refraction seismic data of the Eastern Alps, *Geophys. J. Int.*, *170*, 275–298.

## REFERENCES

---

- Berger, J., and R. L. Sax (1980), Seismic detectors: the state of the art, *Tech. Rep. SSR-R-80-4588*.
- Blundell, D., R. Freeman, and S. Mueller (1992), *A continent revealed, the European Geotraverse*, 275 pp., Cambridge University Press, New York.
- Bormann, P., K. Klinge, and S. Wendt (2002), Data analysis and seismogram interpretation, in *IASPEI New Manual of Seismological Observatory Practice (NMSOP)*, vol. 1, edited by P. Bormann, chap. 11, p. 100, GeoForschungsZentrum, Potsdam, ISBN 3-9808780-0-7.
- Bousquet, R., B. Goffé, P. Henry, X. Le Pichon, and C. Chopin (1997), Kinematic, thermal and petrological model of the Central Alps: Lepontine metamorphism in the upper crust and eclogitisation of the lower crust, *Tectonophysics*, *273*, 105–127.
- Carpena, J., and R. Caby (1984), Fission-track evidence for late Triassic oceanic crust in the French occidental Alps, *Geology*, *12*, 108–111.
- Cattaneo, M., P. Augliera, S. Parolai, and D. Spallarossa (1999), Anomalous deep earthquakes in northwestern Italy, *J. Seismol.*, *3*, 421–435.
- Chen, W.-P., and P. Molnar (1983), Focal depths of intracontinental and intraplate earthquakes and their implications for the thermal and mechanical properties of the lithosphere, *J. Geophys. Res.*, *88*, 4183–4214.
- Christensen, N. I. (1996), Poisson’s ratio and crustal seismology, *J. Geophys. Res.*, *101*(B2), 3139–3156.
- Cichowicz, A. (1993), An automatic S-phase picker, *Bull. Seism. Soc. Am.*, *83*, 180–189.
- Crampin, S., and J. H. Lovell (1991), A decade of shear-wave splitting in the Earth’s crust: What does it mean? What use can we make of it? And what should we do next?, *Geophys. J. Int.*, *107*, 387–407.
- Deichmann, N. (1987), Focal depths of earthquakes in northern Switzerland, *Annales Geophysicae*, *5b*, 395–402.
- Deichmann, N. (1992), Structural and rheological implications of lower-crustal earthquakes below northern Switzerland, *Phys. Earth Planet. Inter.*, *69*, 270–280.
- Deichmann, N., and M. Baer (1990), Earthquakes focal depths below the Alps and northern Alpine foreland of Switzerland, in *The European Geotraverse: Integrative Studies*, edited by R. Freeman, P. Giese, and S. Mueller, pp. 277–288, Eur. Sci. Found., Strasbourg, France.

- Deichmann, N., and L. Rybach (1989), Earthquakes and temperatures in the lower crust below the northern Alpine foreland of Switzerland, in *The lower crust: Properties and processes*, edited by R. F. Mereu, S. Mueller, and D. M. Fountain, pp. 197–213, AGU-Monograph 51, IUGG, Volume 6.
- Deichmann, N., M. Baer, J. Braunmiller, D. Ballarin, F. Bay, B. Delouis, D. Fäh, D. Giardini, U. Kastrup, F. Kind, U. Kradolfer, W. Künzle, S. Röthlisberger, T. Schler, J. Salichon, S. Sellami, E. Spühler, and S. Wiemer (2000a), Earthquakes in Switzerland and surrounding regions during 1999, *Eclogae Geol. Helv.*, *93*, 395–406.
- Deichmann, N., D. Ballarin, and U. Kastrup (2000b), Seismizität der Nord- und Zentralschweiz, *Tech. rep.*, Nagra, Wettingen.
- Di Stefano, R. (2005), Subduction-collision structure beneath Italy: high resolution images of the Adriatic-European-Tyrrhenian lithospheric system, Ph.D. thesis, ETH Zurich, no. 16099.
- Di Stefano, R., F. Aldersons, E. Kissling, P. Baccheschi, C. Chiarabba, and D. Giardini (2006), Automatic seismic phase picking and consistent observation error assessment: Application to the Italian seismicity, *Geophys. J. Int.*, *165*, 121–134, doi:10.1111/j.1365-246X.2005.02799.x.
- Diehl, T., E. Kissling, S. Husen, and F. Aldersons (2008), Consistent phase picking for regional tomography models: Application to the greater Alpine region, *Geophys. J. Int.*, in press.
- Douglas, A., D. Bowers, and J. B. Young (1997), On the onset of P seismograms, *Geophys. J. Int.*, *129*, 681–690.
- Earle, P., and P. M. Shearer (1994), Characterization of global seismograms using an automatic-picking algorithm, *Bull. Seism. Soc. Am.*, *84*, 366–376.
- Eberhart-Phillips, D. (1990), Three-dimensional P and S velocity structure in the Coalinga region, California, *J. Geophys. Res.*, *95*, 15,343–15,363.
- Eberhart-Phillips, D. (1986), Three-dimensional velocity structure in northern California Coast Range from inversion of local earthquake arrival times, *Bull. Seism. Soc. Am.*, *76*, 1025–1052.
- Eberhart-Phillips, D., and A. J. Michael (1993), Three-dimensional velocity structure, seismicity, and fault structure in the Parkfield region, central California, *J. Geophys. Res.*, *98*, 737–758.
- Eberhart-Phillips, D., and M. Reyners (1997), Continental subduction and three-dimensional crustal structure: The northern South Island, New Zealand, *J. Geophys. Res.*, *102*, 11,843–11,861.

## REFERENCES

---

- Eva, E., S. Solarino, and D. Spallarossa (2001), Seismicity and crustal structure beneath the western Ligurian Sea derived from local earthquake tomography, *Tectonophysics*, *339*, 495–510.
- Fisher, R. A. (1936), The use of multiple measurements in taxonomic problems, *Ann. Eugenics*, *7*, 179–188.
- Fisher, R. A. (1938), The statistical utilization of multiple measurements, *Ann. Eugenics*, *8*, 376–386.
- Flinn, E. A. (1965), Signal analysis using rectilinearity and direction of particle motion, *Proc. IEEE*, *53*, 1874–1876.
- Fuchs, K., and G. Müller (1971), Computation of synthetic seismograms with the reflectivity method and comparison with observations, *Geophys. J. Roy. Astron. Soc.*, *23*, 417–433.
- Goes, S., R. Govers, and P. Vacher (2000), Shallow mantle temperatures under Europe from P and S wave tomography, *J. Geophys. Res.*, *105*(B5), 11,153–11,169.
- Gomberg, J. S., K. M. Shedlock, and S. W. Roecker (1990), The effect of S-wave arrival times on the accuracy of the hypocenter estimation, *Bull. Seism. Soc. Am.*, *80*, 1605–1628.
- Grand, S. P. (1990), A possible station bias in travel time measurements reported to ISC, *Geophys. Res. Lett.*, *17*, 17–20.
- Greenhalgh, S., M. Mason, and B. Zhou (2005), An analytical treatment of single station triaxial seismic direction finding, *J. Geophys. Eng.*, *2*, 8–15.
- Haslinger, F., and E. Kissling (2001), Investigating effects of 3-D ray tracing methods in local earthquake tomography, *Phys. Earth Planet. Inter.*, *123*, 103–114.
- Haslinger, F., E. Kissling, J. Ansorge, D. Hatzfeld, E. Papadimitriou, V. Karakostas, K. Makropoulos, H.-G. Kahle, and Y. Peter (1999), 3-D crustal structure from local earthquake tomography around the Gulf of Arta (Ionian region, NW Greece), *Tectonophysics*, *304*, 201–218.
- Holbrook, W. S., W. D. Mooney, and N. I. Christensen (1992), The seismic velocity structure of the deep continental crust, in *The continental lower crust*, edited by D. M. Fountain, R. Arculus, and R. W. Kay, pp. 1–43, Elsevier, Amsterdam.
- Husen, S., and E. Kissling (2001), Local earthquake tomography between rays and waves: fast ray tomography, *Phys. Earth Planet. Inter.*, *123*, 127–147.
- Husen, S., E. Kissling, E. R. Flueh, and G. Asch (1999), Accurate hypocentre determination in the seismogenic zone of the subducting Nazca plate in northern Chile using a combined on-/offshore network, *Geophys. J. Int.*, *105*, 687–701.

- Husen, S., E. Kissling, and E. R. Flueh (2000), Local earthquake tomography of shallow subduction in north Chile: A combined onshore and offshore study, *J. Geophys. Res.*, *105*, 28,183–28,198.
- Husen, S., E. Kissling, N. Deichmann, S. Wiemer, D. Giardini, and M. Baer (2003), Probabilistic earthquake location in complex three-dimensional velocity models: Application to Switzerland, *J. Geophys. Res.*, *108*, 2077, doi: 10.1029/2002JB001778.
- Husen, S., R. B. Smith, and G. P. Waite (2004), Evidence for gas and magmatic sources beneath the Yellowstone volcanic field from seismic tomographic imaging, *J. Volcanol. Geotherm. Res.*, *131*, 397–410.
- Ito, H., J. DeVilbiss, and A. Nur (1979), Compressional and shear waves in saturated rock during water-steam transition, *J. Geophys. Res.*, *84*, 4731–4735.
- Jackson, J. (2002), Strength of the continental lithosphere: time to abandon the jelly sandwich?, *GSA Today*, *12*, 4–10.
- Kissling, E. (1984), Three-dimensional gravity model of the Northern Ivrea-Verbano zone, in *Geomagnetic and Gravimetric Studies of the Ivrea Zone*, edited by J. J. Wagner and S. Mueller, Matér. Géol. Suisse, Géophys., *21*, pp. 53–61, Kümmerly & Frey, Geographischer Verlag, Bern.
- Kissling, E. (1988), Geotomography with local earthquake data, *Rev. Geophys.*, *26*, 659–698.
- Kissling, E., W. L. Ellsworth, D. Eberhart-Phillips, and U. Kradolfer (1994), Initial reference models in local earthquake tomography, *J. Geophys. Res.*, *99*(B10), 19,635–19,646.
- Kissling, E., U. Kradolfer, and H. Maurer (1995), VELEST user’s guide - short introduction, *Tech. rep.*, Institute of Geophysics and Swiss Seismological Service, ETH, Zurich.
- Kissling, E., S. Husen, and F. Haslinger (2001), Model parametrization in seismic tomography: a choice of consequence for the solution quality, *Phys. Earth Planet. Inter.*, *123*, 89–101.
- Kissling, E., S. M. Schmid, R. Lippitsch, J. Ansorge, and B. Fügenschuh (2006), Lithosphere structure and tectonic evolution of the Alpine arc: new evidence from high-resolution teleseismic tomography, in *European Lithosphere Dynamics*, edited by D. G. Gee and R. A. Stephenson, pp. 129–145, Geological Society, London, Memoirs, *32*.
- Kisslinger, C., and E. R. Engdahl (1973), The interpretation of the Wadati diagram with relaxed assumptions, *Bull. Seism. Soc. Am.*, *63*, 1723–1736.

## REFERENCES

---

- Kitagawa, G., and H. Akaike (1978), A procedure for the modeling of non-stationary time series, *Ann. Inst. Stat. Math.*, *30*, 351–363.
- Kradolfer, U. (2000), Waves4U: waveform availability through AutoDRM's, *Seis. Res. Lett.*, *71*, 79–82.
- Kulhánek, O. (1990), *Anatomy of seismograms*, Developments in Solid Earth Geophysics 18, 78 pp., Elsevier.
- Kulhánek, O. (2002), The structure and interpretation of seismograms, in *International Handbook of Earthquake and Engineering Seismology. Part A*, edited by W. H. K. Lee, H. Kanamori, P. C. Jennings, and C. Kisslinger, pp. 333–348, Academic Press.
- Laubscher, H. (1990), The problem of the Moho in the Alps, *Tectonophysics*, *182*, 9–20.
- Leonard, M. (2000), Comparison of manual and automatic onset time picking, *Bull. Seism. Soc. Am.*, *90*, 1384–1390.
- Leonard, M., and B. L. N. Kennett (1999), Multi-component autoregressive techniques for the analysis of seismograms, *Phys. Earth Planet. Inter.*, *113*, 247–263.
- Lippitsch, R. (2002), Lithosphere and upper mantle structure beneath the Alps by high-resolution teleseismic tomography, Ph.D. thesis, ETH Zurich, no. 14726.
- Lippitsch, R., E. Kissling, and J. Ansorge (2003), Upper mantle structure beneath the Alpine orogen from high-resolution teleseismic tomography, *J. Geophys. Res.*, *108*(B8), 2376, doi:10.1029/2002JB002016.
- Lomax, A., J. Virieux, P. Volant, and C. Thierry-Berge (2000), Probabilistic earthquake location in 3D and layered models, in *Advances in seismic event location*, edited by C. H. Thurber and N. Rabinowitz, pp. 101–134, Kluwer Acad.
- Lombardi, D., J. Braunmiller, E. Kissling, and D. Giardini (2008), Moho depth and Poisson's ratio in the western-central Alps from receiver functions, *Geophys. J. Int.*, *173*, 249–264, doi:10.1111/j.1365-246X.2007.03706.x.
- Maggi, A., J. Jackson, D. McKenzie, and K. Priestley (2000), Earthquake focal depths, effective elastic thickness, and the strength of the continental lithosphere, *Geology*, *28*, 495–498.
- Maurer, H., and U. Kradolfer (1996), Hypocentral parameters and velocity estimation in the western Swiss Alps by simultaneous inversion of P- and S-wave data, *Bull. Seismol. Soc. Am.*, *86*, 32–42.
- Michellini, A., and T. V. McEvilly (1991), Seismological studies at Parkfield, I, Simultaneous inversion for velocity structure and hypocenters using cubic B-splines parameterization, *Bull. Seism. Soc. Am.*, *81*, 524–552.



- Montalbetti, J. R., and E. R. Kanasevich (1970), Enhancement of teleseismic body phases with a polarization filter, *Geophys. J. R. Astr. Soc.*, *21*, 119–129.
- Paul, A., M. Cattaneo, F. Thouvenot, D. Spallarossa, N. Béthoux, and J. Fréchet (2001), A three-dimensional crustal velocity model of the southwestern Alps from local earthquake tomography, *J. Geophys. Res.*, *106*(B9), 19,367–19,390.
- Pfiffner, O. A., P. Lehner, P. Heitzmann, S. Müller, and A. Steck (1997), *Deep structure of the Alps: Results of NRP20*, Birkhäuser Verlag, Basel.
- Plešinger, A., M. Hellweg, and D. Seidl (1986), Interactive high-resolution polarization analysis of broad-band seismograms, *J. Geophys.*, *59*, 129–139.
- Podvin, P., and I. Lecomte (1991), Finite difference computation of travel times in very contrasted velocity models: a massively parallel approach and its associated tools, *Geophys. J. Int.*, *105*, 271–284.
- Popp, T., and H. Kern (1993), Thermal hydration reaction characterized by combined measurements of electrical conductivity and elastic wave velocities, *Earth Planet. Sci. Lett.*, *120*, 43–57.
- Priestley, K., J. Jackson, and D. McKenzie (2007), Lithospheric structure and deep earthquakes beneath India, the Himalaya and southern Tibet, *Geophys. J. Int.*, *172*, 345–362.
- Reyners, M., D. Eberhart-Phillips, and G. Stuart (1999), A three-dimensional image of the shallow subduction: crustal structure of the Raukumara Peninsula, New Zealand, *Geophys. J. Int.*, *137*, 873–890.
- Röhm, A. H. E., H. Bijwaard, W. Spakman, and J. Trampert (2000), Effects of arrival time errors on traveltimes tomography, *Geophys. J. Int.*, *142*, 270–276, doi:10.1046/j.1365-246x.2000.00145.x.
- Roure, F., P. Heitzmann, and R. Polino (1990), Early neogene deformation beneath the Po plain, constraints on the post-collisional Alpine evolution, in *Deep structure of the Alps*, edited by R. Polino, pp. 309–322, Memoire de la societee geologique Suisse.
- Rowe, C. A., R. C. Aster, B. Borchers, and C. J. Young (2002), An automatic, adaptive algorithm for refining phase picks in large seismic data sets, *Bull. Seism. Soc. Am.*, *92*, 1660–1674.
- Rowe, C. A., C. H. Thurber, and R. A. White (2004), Dome growth behavior at Soufriere Hills Volcano, Montserrat, revealed by relocation of volcanic event swarms, 1995–1996, *J. Volcanol. Geotherm. Res.*, *134*, 199–221.
- Ruud, B. O., and E. S. Husebye (1992), A new three-component detector and automatic single station bulletin production, *Bull. Seism. Soc. Am.*, *82*, 221–237.

## REFERENCES

---

- Samson, J. C. (1977), Matrix and stokes vector representations of detectors for polarized waveforms: theory, with some applications to teleseismic waves, *Geophys. J. R. Astr. Soc.*, *51*, 583–603.
- Satriano, C., A. Zollo, and C. A. Rowe (2008), Iterative tomographic analysis based on automatic refined picking, *Geophysical Prospecting*, *56*, 467–475.
- Scherbaum, F. (2001), *Of poles and zeros; Fundamentals of Digital Seismology*, Modern Approaches in Geophysics, second ed., Kluwer Academic Publisher.
- Scherbaum, F. (2002), Analysis of digital earthquake signals, in *International Handbook of Earthquake and Engineering Seismology. Part A*, edited by W. H. K. Lee, H. Kanamori, P. C. Jennings, and C. Kisslinger, pp. 349–355, Academic Press.
- Schmid, S. M., and E. Kissling (2000), The arc of the western Alps in the light of geophysical data on deep crustal structure, *Tectonics*, *19*(1), 62–85.
- Schmid, S. M., O. A. Pfiffner, N. Froitzheim, S. G., and E. Kissling (1996), Geophysical-geological transect and tectonic evolution of the Swiss-Italian Alps, *Tectonics*, *15*(5), 1036–1064.
- Schmid, S. M., B. Fügenschuh, E. Kissling, and R. Schuster (2004), Tectonic map and overall architecture of the Alpine orogen, *Eclogae geol. Helv.*, *97*, 93–117.
- Seidl, D., and W. Stammer (1984), Restoration of broad-band seismograms (Part I), *J. Geophys.*, *54*, 114–122.
- Simon, R. B. (1981), *Earthquake interpretations: A manual of reading seismograms*, 150 pp., William Kaufmann Inc.
- Sleeman, R., and T. van Eck (1999), Robust automatic P-phase picking: an on-line implementation in the analysis of broadband seismogram recordings, *Phys. Earth Planet. Inter.*, *113*, 265–275.
- Solarino, S., E. Kissling, S. Sellami, G. Smriglio, F. Thouvenot, M. Granet, K.-P. Bonjer, and D. Sleijko (1997), Compilation of a recent seismicity data base of the greater Alpine region from several seismological networks and preliminary 3D tomographic results, *Ann. di Geofis.*, *XL*, 161–174.
- Solarino, S., E. Kissling, M. Cattaneo, and C. Eva (1997b), Local earthquake tomography of the southern part of the Ivrea body, North-Western Italy, *Eclogae geol. Helv.*, *90*, 357–364.
- Spakman, W., S. van der Lee, and R. van der Hilst (1993), Travel-time tomography of the European-Mediterranean mantle down to 1400 km, *Phys. Earth Planet. Inter.*, *79*, 3–74.

- 
- Stammmler, K. (1993), SeismicHandler - programmable multichannel data handler for interactive and automatic processing of seismological analysis, *Comp. Geosci.*, *19*, 135–140.
- Sue, C., F. Thouvenot, J. Frechet, and P. Tricart (1999), Widespread extension in the core of the western Alps revealed by earthquake analysis, *J. Geophys. Res.*, *104*, 25,611–25,622.
- Takanami, T., and G. Kitagawa (1988), A new efficient procedure for the estimation of onset times of seismic waves, *J. Phys. Earth*, *36*, 267–290.
- Takanami, T., and G. Kitagawa (1991), Estimation of the arrival times of seismic waves by multivariate time series models, *Ann. Inst. Stat. Math.*, *43*(3), 407–433.
- Takanami, T., and G. Kitagawa (1993), Multivariate time-series models to estimate the arrival times of S waves, *Comput. Geosci.*, *19*(2), 295–301.
- Thurber, C. H. (1983), Earthquake locations and three-dimensional crustal structure in the Coyote Lake area, central California, *J. Geophys. Res.*, *88*, 8226–8236.
- Thurber, C. H., and S. R. Atre (1993), Three-dimensional  $v_p/v_s$  variations along the Loma Prieta rupture zone, *Bull. Seism. Soc. Am.*, *83*, 717–736.
- Toomey, D. R., and G. R. Foulger (1989), Tomographic inversion of local earthquake data from the Hengill-Grensdalur central volcano complex, Iceland, *J. Geophys. Res.*, *94*, 17,497–17,510.
- Transalp Working Group (2001), European orogenic processes research transects the eastern Alps, *EOS Trans. AGU*, *82*, 460–461.
- Transalp Working Group (2002), First deep seismic reflection images of the Eastern Alps reveal giant crustal wedges and transcrustal ramps, *Geophys. Res. Lett.*, *29*, 92.
- Um, J., and C. H. Thurber (1987), A fast algorithm for two-point seismic ray tracing, *Bull. Seism. Soc. Am.*, *77*, 972–986.
- Vidale, J. E. (1986), Complex polarisation analysis of particle motion, *Bull. Seism. Soc. Am.*, *76*, 1393–1405.
- Virieux, J., V. Farra, and R. Madariaga (1988), Ray tracing for earthquake location in laterally heterogeneous media, *J. Geophys. Res.*, *93*, 6585–6599.
- Waldhauser, F., E. Kissling, J. Ansorge, and S. Mueller (1998), Three-dimensional interface modelling with two-dimensional seismic data: the Alpine crust-mantle boundary, *Geophys. J. Int.*, *135*, 264–278.

## REFERENCES

---

- Waldhauser, F., R. Lippitsch, E. Kissling, and J. Ansorge (2002), High-resolution teleseismic tomography of upper-mantle structure using an a priori three-dimensional crustal model, *Geophys. J. Int.*, *150*, 403–414.
- Wang, J., and T. Teng (1997), Identification and picking of S phase using an artificial neural network, *Bull. Seism. Soc. Am.*, *87*(5), 1140–1149.
- Weiss, T., S. Siegesmund, W. Rabbel, T. Bohlen, and M. Pohl (1999), Seismic velocities and anisotropy of the lower continental crust: A review, *Pure Appl. Geophys.*, *156*, 97–122.
- Wessel, P., and W. H. F. Smith (1995), New version of the Generic Mapping Tool released, *EOS Trans. AGU*, *76*, 329.
- Withers, M., R. Aster, C. Young, J. Beiriger, M. Harris, S. Moore, and J. Trujillo (1998), A comparison of select trigger algorithms for automated global seismic phase and event detection, *Bull. Seism. Soc. Am.*, *88*, 95–106.
- Ye, S., J. Ansorge, E. Kissling, and S. Mueller (1995), Crustal structure beneath the eastern Swiss Alps derived from seismic refraction data, *Tectonophysics*, *242*, 199–221.
- Zelt, C. A. (1998), Lateral velocity resolution from three-dimensional seismic refraction data, *Geophys. J. Int.*, *135*, 1101–1112.
- Zhang, H., C. H. Thurber, and C. A. Rowe (2003), Automatic P-wave arrival detection and picking with multiscale wavelet analysis for single-component recordings, *Bull. Seism. Soc. Am.*, *93*, 1904–1912.

# Acknowledgments

Foremost I would like to thank Edi Kissling for giving me the opportunity to accomplish this study and for patiently supervising me during my PhD. I greatly benefited from our many discussions, and he tremendously enhanced my understanding of seismogram interpretation, phase picking, tomography, and the structure of the Alps. I am deeply impressed by his anytime-support and his tireless enthusiasm for science.

Furthermore, I am very grateful for the support of Stephan Husen, who helped me a lot to structure my sometimes messy thoughts and ideas. I deeply appreciate his thoroughly proofreading of my manuscripts and his many fruitful comments and suggestions. Thanks also for providing me with all your 3D-tomo knowledge and the necessary codes. In addition, I greatly benefited from his huge experience in computing, especially regarding the world of Mac OSX.

I also thank my third adviser Nicholas Deichmann, who introduced me to the world of data-conversion and helped me to overcome the resulting problems with a bunch of his codes. He extended my knowledge of seismogram interpretation, signal processing, and earthquake location, and he convinced me of the benefit of synthetic seismograms! Thanks also for patiently proofreading.

My special gratitude goes to Freddy Aldersons, who not only provided me with his MPX-code, but also with plenty of help to apply it successfully. This work greatly benefited from all his comments and ideas, which also resulted from our numerous discussions on automatic picking.

I thank Prof. Domenico Giardini and Dr. Felix Waldhauser for joining the committee of my PhD-defense and their constructive comments and suggestions.

Collecting the data for this study was a time consuming and sometimes difficult task. But I enjoyed the trips to Grenoble, Genova, and Munich and I thank Francois Thouvenot, Stefano Solarino, and Joachim Wassermann for a their hospitality and their help. Furthermore, I would like to thank Manfred Baer, Wolfgang Brüstle, Wolfgang Lenhardt, Gabriele Ferretti, Christophe Maron, Enrico Priolo, and Mladen Zivcic for providing me with seismograms and information on databases, bulletins, and stations.

## E ACKNOWLEDGMENTS

---

Special thanks go to my ‘predecessors’ Raffaele Di Stefano and Regina Lippitsch, who provided me with data, models, and helped to clarify some of the ‘station-mess’ in the Alpine region.

I really appreciated the help of Thomas Forbriger, who provided me with his ‘refmet’ code and for his numerous reflectivity-advice. Likewise, I thank Manfred Baer and Klaus Stammer for their help and support with their analyzing packages ‘Snap’ and ‘SeismicHandler’.

I thank my two TomoCH-mates Denis Lombardi and Bill Fry for putting up the stations and doing all the data processing work. Thanks Denis for the many seismological and non-seismological discussions, which helped to overcome some of the ‘downs’ in my PhD. Thanks Bill for some nice Ski-Day and bike adventures.

I will really miss the 12:15 mensa with Stefan Fritsche and the traditional coffee-discussion! It was always a great pleasure, unlike the mensa food... Therefore, I would like to thank Thomas and Henriette for initiating the ‘Kebab-Haus-Hoengg’ trips. I also thank you both for your late-night support and your plenty fruitful comments some nights before my defense talk! Thomas, thanks also for pushing me to the summit of Mauna Loa.

Furthermore, I am grateful to the people from the E-lab for their support during the TomoCH and the THALES project, especially to Andre Blanchard, Beat Rinderknecht, Thomas Stalder, and Jonas Zollinger. I thank Philipp Kästli for his anytime IT support. I owe my thanks to my office mates Sibylle, Vincent, Sabrina, Bettina, and Michael for a great and enjoyable time.

Finally, special thanks to my Family and Doro for their constant encouragement and support through the up and downs in all these years. I am more than grateful for it.

# Curriculum Vitae

**Tobias Diehl**

Born June 28th 1976, Ostfildern/Ruit, Germany

Citizen of Germany

- 1987–1996:** High School, Esslingen am Neckar, Germany
- 1997–2003:** Undergraduate Studies in Geophysics and Physics at the University of Karlsruhe, Germany
- 2003:** Diploma in Physics, Thesis entitled: ‘The crustal structure of southeastern Romania derived by the analysis of teleseismic receiver functions’, University of Karlsruhe, Germany
- 2003–2004:** Research Assistant at the Geophysical Institute, University of Karlsruhe, Germany
- 2004–2008:** Doctoral Student, Institute of Geophysics, ETH Zurich, Switzerland